Control of Supramolecular Phenomena via Molecular Motors

Jongejan, Mahthild Gwendolyn Maria

Control of Supramolecular Phenomena via Molecular Motors

Mahthild G. M. Jongejan

The work described in this thesis was carried out at the Stratingh Institute for Chemistry, University of Groningen, The Netherlands

The work described in this thesis was financially supported by NanoNed

Printed by: Ipskamp Drukkers B.V., Enschede, The Netherlands

Pictures on the cover were results observed throughout the Ph.D. research using an optical microscope.

RIJKSUNIVERSITEIT GRONINGEN

Control of Supramolecular Phenomena via Molecular Motors

Proefschrift

ter verkrijging van het doctoraat in de
Wiskunde en Natuurwetenschappen
aan de Rijksuniversiteit Groningen
op gezag van de
Rector Magnificus dr. F. Zwarts,
in het openbaar te verdedigen op
vrijdag 12 november 2010
om 16.15 uur

door

Mahthild Gwendolyn Maria Jongejan

geboren op 10 juni 1980
te Stadskanaal

Promotor:	Prof. dr. B. L. Feringa
Beoordelingscommissie:	Prof. dr. D. J. Broer Prof. dr. J. B. F. N. Engberts Prof. dr. E. J. R. Sudhölter

ISBN: 978-90-9025753-2 (published version)
978-90-816138-1-1 (electronic version)

Contents

Chapter 1 **Amplification of Chirality** 1

1.1 Introduction 2
1.2 Liquid Crystals 3
1.2.1 Intrinsically chiral Liquid Crystalline molecules 4
1.2.2 Chiral doping of an achiral Liquid Crystalline phase 6
1.2.3 Double amplification of chirality 8
1.2.4 Responsive chiral dopant molecules 10
1.2.5 Responsive Liquid Crystals 13
1.2.6 Non-calamitic Liquid Crystal phases 14
1.2.7 Polymeric Liquid Crystals 19
1.3 Gelators 20
1.3.1 Chiral gelator molecules 22
1.3.2 Helicity through templating 26
1.3.3 Responsive gelator molecules 30
1.4 Supramolecular Chirality 31
1.4.1 Stressed systems 31
1.4.2 Hydrogen-bond generating assemblies 32
1.4.3 Non Hydrogen-bond based assemblies 39
1.4.4 Template-driven assembly 41
1.5 2-D Chirality 44
1.6 Aim of research in this thesis 48
1.7 References 49

Chapter 2 **Helical Twisting Powers of Molecular Motors** 57

2.1 Liquid Crystals 58
2.1.1 Introduction 58
2.1.2 Birefringence 59
2.1.3 Cholesteric phases 61
2.1.4 Analysis 64
2.2 Addressable chiral dopants 66
2.3 Results 68
2.3.1 Varying the molecular motor dopant 68
2.3.2 Other mesogens 74
2.4 Conclusions 76
2.5 Acknowledgements 76
2.6 Experimental section 77
2.7 References 84

Chapter 3 **Photoinduced Reorganization of Doped Liquid Crystals: Bridging Molecular Isomerization and Texture Rotation** 87

3.1 Introduction 88
3.2 Variation in dopant structure 89
3.3 Results 90
3.3.1 The effect of changing the Liquid Crystal 91
3.3.2 The effect of the structure of the molecular motor on particle rotation 93
3.3.3 Particle-size dependence on rotation 93
3.4 Conclusions on rotational behavior of glass particles 98
3.5 The anchoring of a phase 99
3.5.1 Planar-planar (P-P) anchoring 101
3.5.2 Homeotropic-homeptropic (H-H) anchoring 101
3.5.3 Planar-homeotropic (P-H) hybrid anchoring 102
3.5.3.1 Variation of LC layer thickness 104
3.6 Theoretical study 105
3.7 Conclusions on calculations 116
3.8 Acknowledgements 117
3.9 Experimental 117
3.10 References 118

Chapter 4 **The Liquid Crystalline Behavior of a Polyisocyanate Functionalized with a Molecular Motor and a Chiroptical Switch** 121

4.1 Introduction 122
4.2 Lyotropic Liquid Crystalline setup 126
4.2.1 The lyotropic LC system 126
4.2.2 Surface effects 128
4.2.3 The effect of solvent 129
4.3 The use of the liquid IR cell 130
4.3.1 Concentration effects 131
4.3.2 The cholesteric phase of (*2'S*)-(*M*)-*trans*-PHIC 132
4.3.3 Effect of UV irradiation on the cholesteric phase of (*2'S*)-(*M*)-*trans*-PHIC 133
4.4 Layer Thickness 134
4.4.1 Time-dependence of sample orientation 136
4.5 Irradiation experiments 137
4.5.1 UV cycles 137
4.5.2 VIS cycles 138
4.5.3 Thermal control experiment 141
4.5.4 CD spectra 143
4.6 Conclusions 144

4.7 Acknowledgements 145
4.8 Experimental section 145
4.9 References 146

Chapter 5 **Surface Phenomena of a Functionalized Polyisocyanate** 149

5.1 Introduction 150
5.2 Aggregation behavior in solution 152
5.2.1 DLS 152
5.2.2 UV-VIS and CD spectroscopy 154
5.2.3 DSC 156
5.2.4 Temperature-dependent NMR analysis 157
5.3 Behavior on the surface 161
5.3.1 Substrate effect 161
5.3.2 Solvent effects 164
5.3.3 Structural effects 167
5.3.4 Temperature effect 167
5.3.5 Age and concentration effect 169
5.3.6 Irradiation effect 170
5.3.7 Effects of introduction of a thermotropic LC 175
5.4 Conclusions 178
5.5 Acknowledgements 178
5.6 Experimental 179
5.7 References 180

Chapter 6 **Aggregation Phenomena of a Water-soluble Molecular Motor** 183

6.1 Introduction 184
6.1.1 Aggregate types 185
6.1.2 A switchable amphiphilic molecular motor 187
6.2 Results and discussion 190
6.2.1 Photochemical and thermal isomerization 190
6.2.2 CMC determination 192
6.2.3 Langmuir-Blodgett measurements 195
6.2.4 DSC measurements 196
6.2.5 UV/VIS of molecular motor in vesicles 201
6.2.6 Cryo-TEM 202
6.3 Conclusions and Outlook 202
6.4 Acknowledgements 203
6.5 Experimental 203
6.6 References 213

Nederlandse Samenvatting 217
Acknowledgements 223

Chapter 1

Amplification of Chirality

This introductory section will demonstrate the various different ways in which amplification of chirality can be achieved. Biological systems have been well known for this type of behavior, however, it can also be observed in the cases of liquid crystals, gelators, hydrogen-bonding stacks, or surfaces (2-D chirality). In this chapter we look at several of the more interesting examples of these synthetic amplifications of chirality along with some of the (potential) applications which have been found for these systems.

1.1 Introduction

From α-amino acids to sugars, the chirality of nature's building blocks is as essential to their form and function as is their molecular composition. Life is built on supramolecular structures where spatial interaction and non-covalent bonds are as critical to the stability of biological systems as molecular connectivity and its chirality that dominates spatial interactions and molecular recognition.

The molecular chirality of life's building blocks, such as the α-amino acids and sugars, is expressed in the larger supramolecular structures which living cells form, not least DNA and proteins. Indeed nature's control of supramolecular chirality is enviable and has driven scientists to continue to strive to emulate these abilities. Control of chirality at the molecular level is already well advanced both in asymmetric synthesis and in catalysis with often complex organic molecules prepared in >99% enantiomeric excess (e.e.). This is remarkable considering the relatively simple structure of the ligands employed in catalytic reactions when compared to the complex supramolecular architectures of enzymes. However, although nature uses sophisticated and complex structures, it does so with remarkable efficiency, using only a very limited number of chiral building blocks to achieve this. What scientists have achieved synthetically, natural systems have achieved through the use of molecular chirality and its amplification in large supramolecular constructions. It is this fact which has driven scientists in recent years to harness the potential of supramolecular chiral induction and amplification.

The significant recent advances reported by Soai *et al.*[1-3] in the field of autocatalysis[4], have shown that trace amounts of one enantiomer of a product of a reaction can act to direct the enantioselectivity of the reaction. In the *iso*propylzinc addition to an aldehyde the presence of trace amounts of one enantiomer of the alcohol product results in high enantiomeric excess in the product. Chiral induction in autocatalysis can also be induced via chiral surfaces e.g. inorganic crystals or chiral silica.[5] Chiral amplification can also be achieved through the use of metal complexes in dynamic combinatorial libraries, which induce a preferential formation of chiral assemblies, typically the most thermodynamically stable structures are favored .[6]

The most tangible aspect of chirality is its effect on optical absorption, specifically the preferential absorption of left or right handed circularly polarized light (CPL). The difference in absorption of left and right CPL has been employed to induce chirality in materials through selective photochemistry. However, the intrinsic weakness of the effect limits the e.e. that can be achieved.[7]

The considerable increase in attention in recent years in all aspects of chiral amplification is remarkable, however, amplification of chirality in liquid crystalline, gelator and supramolecular systems will form the focus of this chapter. The field of induction of chirality in polymeric systems is treated in detail elsewhere, e.g. the review by Yashima *et al*.[8]

1.2 Liquid crystals

Liquid crystals were first observed by Reinitzer (while analysis/theory were developed by Lehmann) in the 1880's[9,10] when studying cholesterol derivatives which showed unusual optical properties, which were unknown for a liquid (i.e. birefringence). Since the first report, and after somewhat of a long lull, a large variety of mesogenic molecules have been synthesized, some of which have found applications in liquid crystal display (LCD) systems. Indeed LCD technology has dominated liquid crystal research, however, especially in recent years LCs are attracting considerable interest for application in sensor and receptor systems.[11]

Liquid crystals are a mesophase between the liquid and crystalline state, which shares properties of both phases. It is often referred to as the *fourth state of matter*. Mesogens (liquid crystal forming molecules) have weak anisotropic intermolecular interactions that facilitate increased positional or orientational order compared with liquids, however, the degree of organization is much lower than in a solid. The combination of intermolecular organization and the dynamic properties of a liquid allows for liquid crystalline behavior to be controlled readily through external stimuli such as temperature, light, magnetic fields and other non-mesogen molecules.

The structure of the mesogen determines the observed liquid crystalline phase of which calamitic (rod-like molecules) and discotic (disc-like molecules) liquid crystals have received most attention. If the mesogen is chiral, it will assemble in a chiral arrangement (helix). However, it is known that for achiral liquid crystals the addition of a low concentration of a chiral molecule (the chiral dopant) can induce assembly of the mesogens around this central molecule to form a chiral aggregate. In this section we will discuss chiral liquid crystal molecules and chiral dopants.

Achiral liquid crystalline phases show directional ordering along one axis. This directional ordering can be biased, for instance by the use of an induction layer (i.e. rubbed polymer surface). However, in the case of a chiral mesogen there are two ordering directions. The first aligns the molecules along one director. The second result in the ordering of planes of molecules in such a manner as to generate a helical twist amongst the mesogen molecules (see Scheme 1.1).

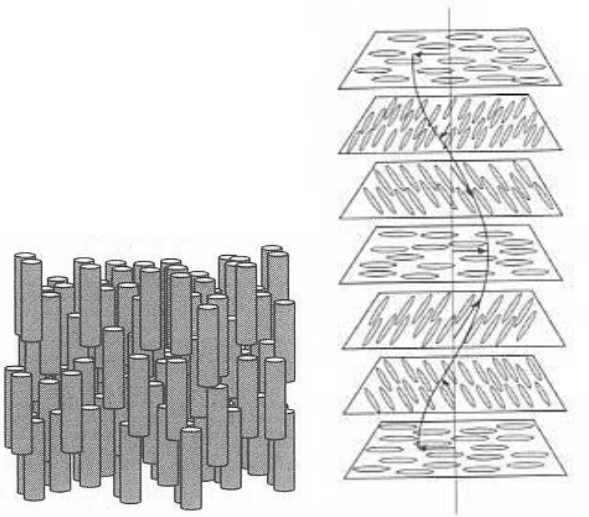

Scheme 1.1: The nematic liquid crystalline phase with directional ordering in one direction upon the addition of chiral non-racemic dopant forms a chiral Nematic phase (Cholesteric) with its helical twist amongst the layers of mesogens.

The tighter the turns in these helices, the smaller the pitch becomes, and the higher the helical twisting power capabilities of a mesogen or dopant are. The helical twisting power (HTP) is determined from the pitch (length of a 360 degree turn in the helix) which can be determined using the Grandjean-Cano method (equation 1).

$$\beta_M = 1/(\text{e.e.} * c * p) \qquad [1]$$

where β_M is the molar helical twisting power, p is the pitch, c is the concentration (mol/mol), and e.e. is the enantiomeric excess

1.2.1 Intrinsically chiral liquid crystalline molecules

The liquid crystalline system can consist of molecules which aggregate in a non-random manner to yield a chiral liquid crystalline phase or alternatively a doped chiral system can be used. There are several mesogens available which are based on natural substances. The cholesterol-based mesogens used by Reinitzer are the first examples of chiral liquid crystal molecules.[9] More recent examples are the helical β-peptides reported by Gellman *et.al*.[12] These compounds form cholesteric phases in water (in contrast to the majority of LCs, which require organic solvents). The concentration required to generate a cholesteric phase shows a strong dependence on the length of the β-peptides. For the tetramer 25 wt % was required to induce typical birefringence, whereas only 19 wt % of the heptamer was required.

Chiral nematic phases can also be formed from suspensions of rod-like viruses. Grelet *et al.* have studied the effect of the overall left-handed helicity induced by a right-handed molecular helix, and have proposed a plausible hypothesis to rationalize their results (Scheme 1.2).[13]

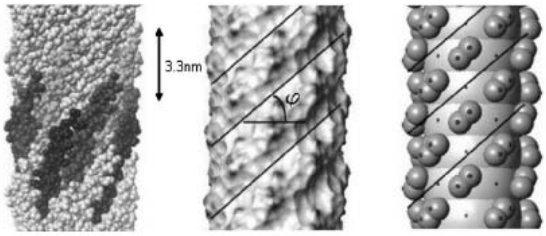

Scheme 1.2: Representation of the resulting superstructure formed from a co-assembly of various right-handed rod-like virus strands. Adapted from ref 13.

The general organization of the phase appears to be controlled by the balance between the contributions of opposite handedness (helicities of the aggregates) where the left-handed helix is energetically more favorable due to better packing of the viral particles and the electrostatic inter-particle repulsion. Other biologically active molecules, such as helical flagella, can generate a helical superstructure,[14] however in recent years synthetic systems have been designed which also yield cholesteric phases.

Bruce and Whitwood[15] have described a mesophase using perfluoroalkyl modified mesogens, which was achieved without the typical micro phase separation. Fluorinated molecules which have been reported to form a liquid crystalline phase, include the amphiphilic enantiomers of alanine and serine with partially fluorinated-*n*-octyl chains (1H,1H,2H,2H-perfluoro-*n*-octyl chains).[16] In water these form intrinsically chiral nematic phases with very high helical twisting powers. In fact the helical twisting power can be approximately 11 times larger for the fluorinated amphiphiles than for their perhydro counterparts. For the fluorinated alanine derivative a HTP of -157.8 μm^{-1} was found, while the nonfluorinated HTP was around -4 μm^{-1}. Similarly for the serine derivative the fluorinated analog has a HTP of -13.7 μm^{-1} while in the case of the hydrogenated compound the value is around -1.8 μm^{-1}. These differences in HTP have been attributed to the pivot effect (enhancing the chiral torque of the stereogenic center compared to that of the hydrogenated compound. This effect is assumed to be related to the overall bulkiness and stiffness of the fluoroalkyl bilayer; However, the electronic polarizability at the stereogenic center through the highly electronegative fluoroalkyl chain may also cause the enhanced HTP valuesof the fluoroalkyl chain.

1.2.2 Chiral doping of an achiral liquid crystalline phase

A large variety of chiral molecules can induce a helical ordering amongst achiral nematic liquid crystals (LCs).[17] Here we mention several examples of such dopants. Upon doping of a nematic phase with small amounts (usually between 1 and 10 wt%) of a non-racemic chiral compound the cholesteric phase is generated. Common nematic liquid crystals (Figure 1.1) which are used for these doping experiments are: the blends E7, ZLI-1167, ZLI-389, and the liquid crystals pCH7, K15 (also known as 5CB) and MBBA.

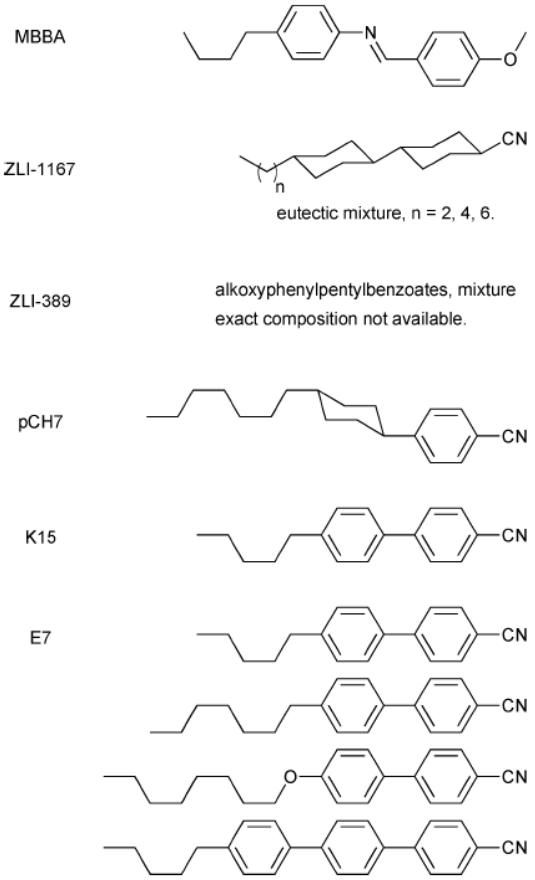

Figure 1.1: Structures of various commonly used liquid crystals (blends)

1,1'-Binaphthyl compounds, typical chiral dopants, can exist in either a cisoid or transoid conformation. Depending on the substituents at the 2 and 2' positions the cisoid or transoid conformation can be energetically favored. These compounds have helical twisting powers which are dependent on the dihedral angle of the binaphthyl moiety.

BINOL derivatives show an increase in the HTP upon bridging. In the case of (S)-BINOL the HTP goes from + 32 to +85 μm^{-1} (in K15) for the bridged derivative. [18,19] One of the classical examples of a chiral guest that can lead to high induction of helical ordering amongst LC molecules is TADDOL (Figure 1.2) and its derivatives.[20,21] This class of chiral dopants can achieve amongst the highest HTPs measured ($\leq$ +405 μm^{-1} in K15).

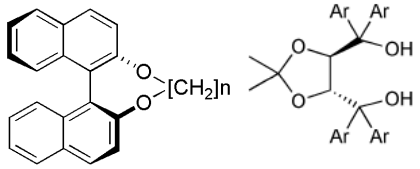

Figure 1.2: The structures of (left) a (S)- BINOL which yields *P* helicity in the LC phase and (right) TADDOL (α,α,α',α'-tetraaryl-2,2-dimethyl-1,3-dioxolan-4,5-dimethanol) and its derivatives ($\beta_M \leq 405\ \mu m^{-1}$). Ar = phenyl, 2-naphthyl etc.

In recent years it has been observed that many metal/chiral-ligand complexes (which were originally designed to be used as catalysts) can yield higher HTPs. In these studies metals such as copper, chromium and ruthenium have been used (Figure 1.3).[22,23] Their helical twisting power capabilities in MBBA range between - 180 to +102 μm^{-1}.

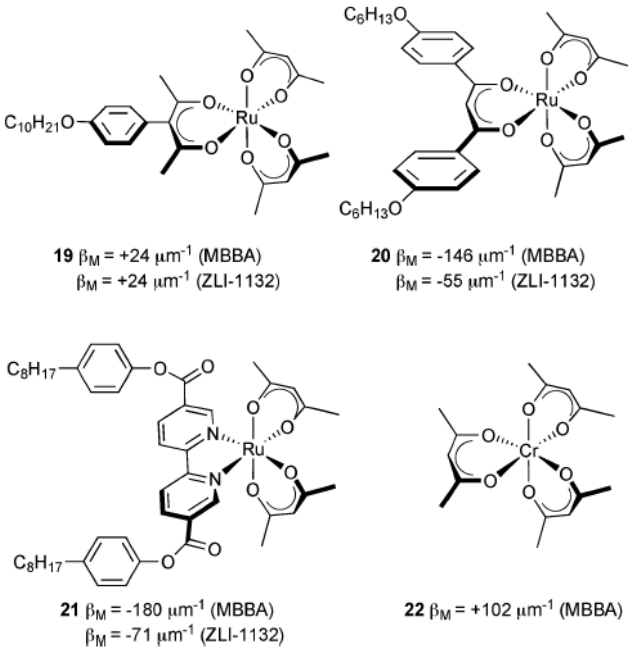

Figure 1.3: Structures of metal/ligand complexes used as chiral dopants

Other metals such as cobalt and rhodium have also been used, although the maximum HTP is almost the same (+100 μm^{-1}).[24] However, the highest helical twisting power reported for a metal/ligand complex in a liquid

crystal so far has been that for the bis-chelated imine-alkoxytitanium complexes (Figure 1.4) described by Parker *et.al*.[25]

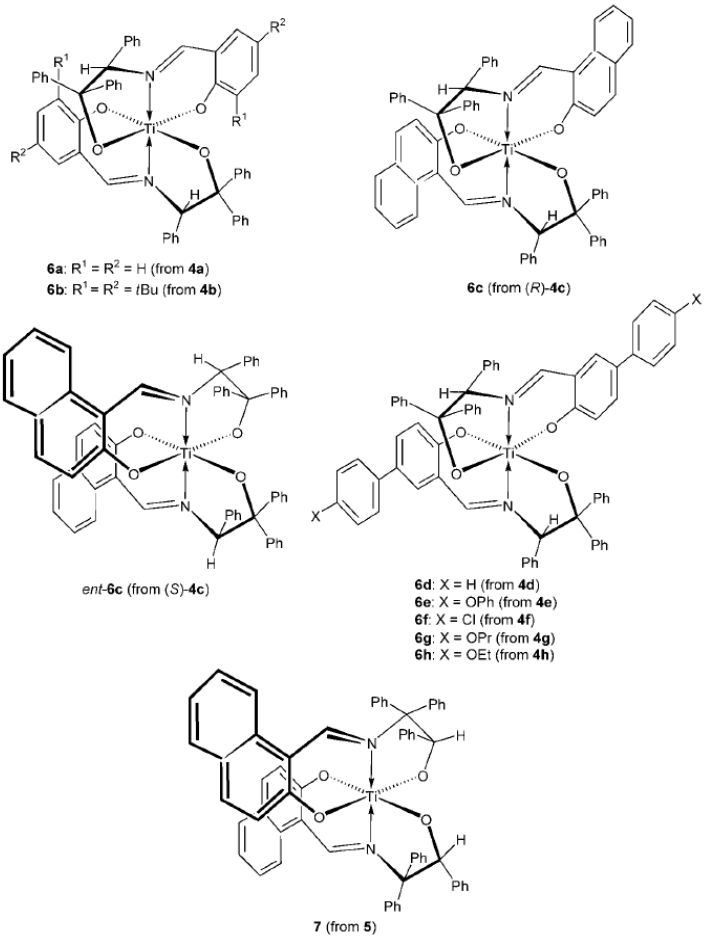

Figure 1.4: Structures of the titanium-based metal/ligand complexes used as chiral dopants.

The range of HTP values lies between 450-740 μm^{-1} in MBBA, which is exceptionally high by normal dopant standards.[25] Chirality is not the only criterion for a molecule to induce helicity. Chiral amines do not usually show helical induction, as sufficient interaction between the dopant and LC molecules is also required. However, chiral amines which were functionalized with LC moieties yield an HTP from 0 to more than 40 μm^{-1} (in K15).

1.2.3 Double amplification of chirality

Double amplification of molecular chirality in achiral liquid crystals has been demonstrated. One example is the double amplification using chiral

amines in the presence of phosphoric acids (Figure 1.5, top). The phosphate-ammonium interactions amplify the chirality of the amine and thus effect a conformational change in the receptor. This is expressed as a change from a nematic to a cholesteric phase. The shortest pitch achieved (therefore the highest helical twist) was ± 10 μm.[26]

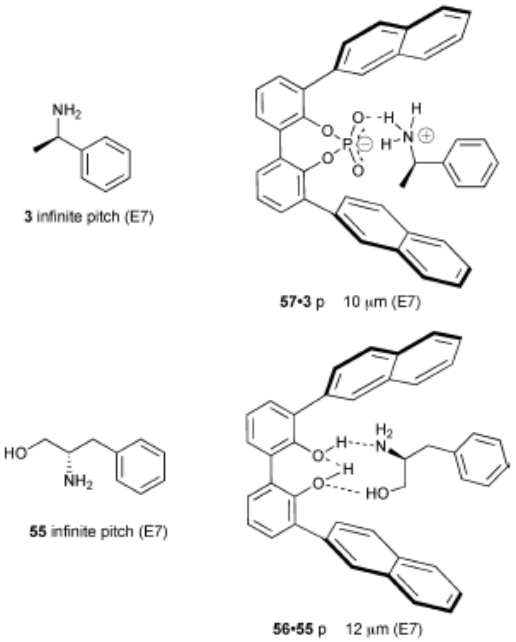

Figure 1.5: The phosphate-ammonium (top), and the biphenol-amino alcohol complexes (bottom). Adapted from ref 26.

Double amplification using amino alcohols and disubstituted biphenols also results in helical induction (Figure 1.5 bottom), albeit less pronounced, with the small pitch values ranging from + 21 to -12 μm in liquid crystal blend E7.[27] The biphenol-based receptors have the ability to form noncovalent complexes with amines via hydrogen bonding. The mixing of a chiral amine and a conformationally flexible biphenol resulted in diastereoselective binding, which enhanced the helical twisting power of the amine. These biphenols exist in two chiral conformations (P and M helices), which rapidly interconvert in solution at room temperature (Scheme 1). Diastereoselective binding of a chiral amine could result in an excess of one of the axially chiral conformers. Based on this principle it was envisioned that it would be possible to transfer the chirality of an amine to an LC phase by complexation to an achiral biphenol derivative in a doped LC system (Scheme 1.1b), taking advantage of the often relatively high helical twisting powers of chiral biphenyls.

.

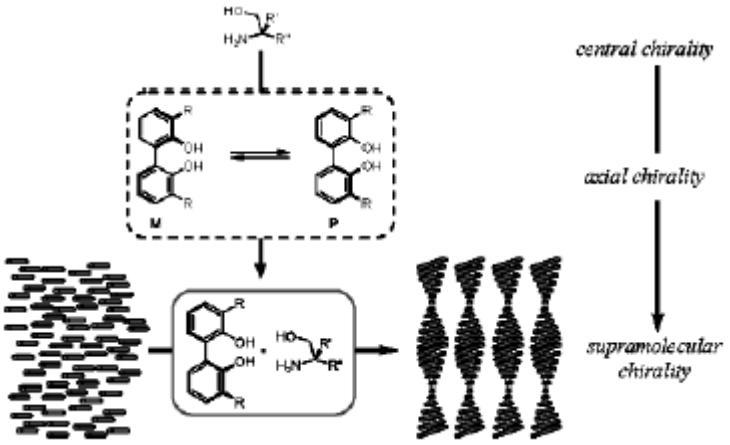

Scheme 1.1b Cartoon of the double amplification mechanism in the case of amino alcohols. From ref 27.

1.2.4 Responsive chiral dopant molecules

Many chiral molecules can be used to influence the packing of liquid crystalline molecules, however these molecules cannot be removed subsequently from the LC matrix, and the change is irreversible. Reversible control of liquid crystalline behavior by post doping modification, e.g. by UV or VIS photolysis, has attracted some interest in recent years. Ichimura *et al*.[28,29] have employed azobenzene compounds with central chirality to achieve HTPs of up to 15 μm^{-1}. Typically the *trans* isomer has a higher HTP than the *cis* isomer.

C_2-symmetric binaphthyl azo-switch based chiral dopants,[30,31] alter configuration upon irradiation with UV light. By subsequent irradiation with visible light the switches return to the original geometry both in solution and the LC matrix. As the photochromic dopant molecule changes configuration within the LC matrix, the liquid crystalline molecules around it rearrange, thereby not only affecting the shape of the dopant molecule but also the ordering in the entire LC matrix. Compound **67** in Figure 1.6 (phase 1052[32]) has the highest helical twisting power at PSS_{Vis} of +155 and PSS_{UV} +108 μm^{-1}.

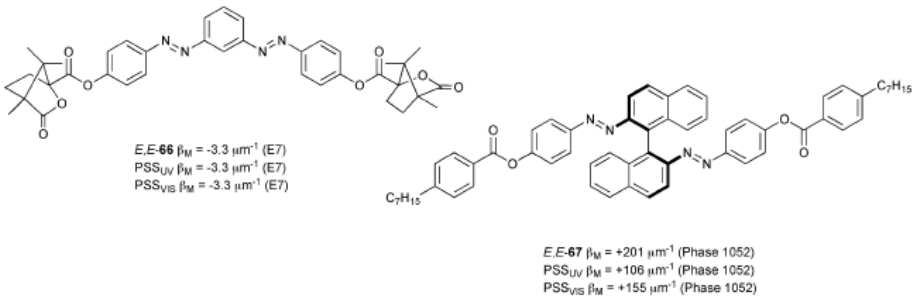

Figure 1.6: Two structurally different diazo-switch molecules used as responsive chiral dopant molecules in the liquid crystal matrix (E7 or Phase 1052). HTP values are given for each molecule pure (E,E#) and after UV and VIS light irradiation. Switch **66** (left) is by Ichimura while **67** (right) is by Gottarelli.

Responsive systems, which show photoswitchable HTP, have been reported, including diazo-, diarylethene- and fulgide-based switches.[17] Although, the HTP of the dopant can be changed by irradiation with visible or UV light, a complete change in sign (and hence the helicity of the entire phase) is difficult to achieve. The first molecular systems to show an inversion of the helicity of a cholesteric phase were based on sterically overcrowded alkenes.[33] The design of the overcrowded alkene was later modified to form first generation motors[34] and later second generation motors, which can act as switches (when these possess a symmetrical lower half, Figure 1.7) as well as rotary motors (desymmeterized lower half), which have proven to be effective switchable chiral dopants. For liquid crystal applications the overcrowded alkenes with a symmetrical lower half are preferred, as only two conformations rather than four are possible upon continued cycles of photo and thermal irradiation of the phase simplifying the analysis. However, the four configurations and constant rotation could be promising for applications.

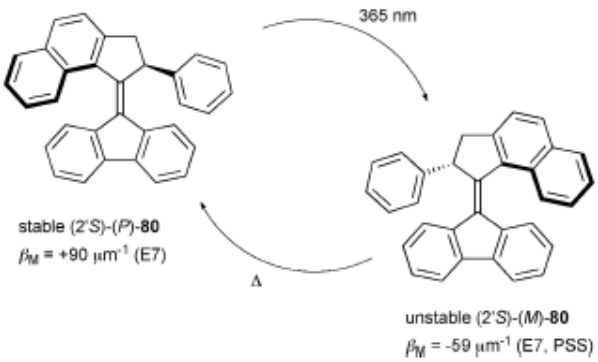

Figure 1.7: An example of a molecular motor (second generation with symmetric lower half) and its two forms after irradiation and thermal isomerization, which is used as a dopant in E7. Adapted from ref 37.

Irradiation of the overcrowded alkene-based molecular rotary motors results in switching of its intrinsic helicity, which in turn changes the pitch length of the LC helices. Consequently a change in the wavelength of reflected light is achieved, which can be observed as a change in color as the order of magnitude of the pitch length is in the same region as the wavelength of visible light.[35] Owing to the large magnitudes and opposite signs of the HTP of the two states of the switch, the whole of the visible spectrum can be accessed. The photochemistry is fully reversible, however, the systems employed are slow to recover after they respond to light, i.e. the recovery of the thermally stable form is slower than the time required to reach the unstable state photochemically. Nevertheless an increase in the recovery rate is possible by synthetic tuning of molecular properties. The color change has already been used as a colorimetric test to determine the enantiomeric excess of a chiral compound.[36]

In addition to a change in color upon irradiation and the change of pitch (lengthening), a rotation of the entire liquid crystalline surface was observed.[37,38] The force generated due to the reorientation of all the mesogens is sufficient to rotate glass micro particles (Figure 1.8). Though the rotation process seems to temporarily stagnate when the phase appears to become nematic (equal amounts of M and P helical overcrowded alkenes present), the process is resumed once there is an excess of M or P helix. The phase will continue to turn until the phase has reached the final helical conformation once PSS is reached. The reverse rotary motion is observed upon thermal helix inversion of the central double bond of the overcrowded alkene.

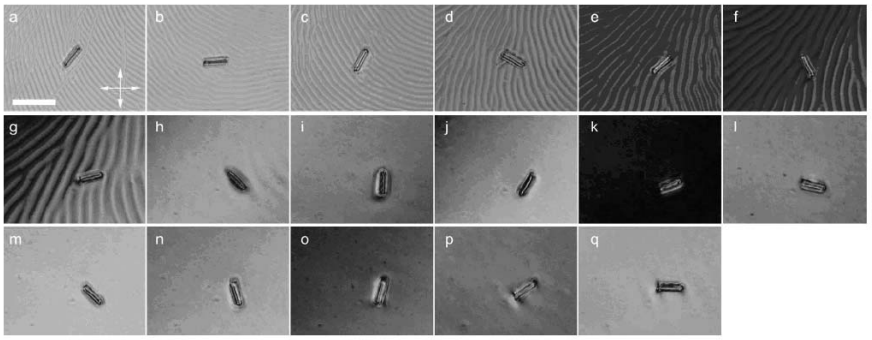

Figure 1.8: Optical micrographs of a glass rod on an LC film doped with the motor shown in Figure 1.7, during irradiation with UV light (λ = 365 nm). The rod and the cholesteric phase rotate in a clockwise fashion. The interval between the pictures is 15s (except for q which is taken 11s after p). The rod made approximately 2.5 full turns during the depicted process (the process continues upon further irradiation. This is not depicted in this scheme). The scale bar is 50μm. The crossed arrows indicate the directions of the crossed polarizers. The glass rod is 28μm long and 5μm in diameter. From ref 37.

1.2.5 Responsive liquid crystals

In addition to photochromic chiral dopants, photochromic mesogens have been investigated also.[39] Diarylethene switches have been prepared which incorporate a mesomorphic group. The diarylethenes retain their photochromic switching behavior (the mesomorphic group does not absorb in the same regions as the photochromic unit) and form liquid crystalline states; thereby yielding a perfectly switchable mesogen and photoswitchable liquid crystal phases. However, in contrast to switchable dopants, these photoswitchable liquid crystals do not yield a chiral liquid crystalline phase.

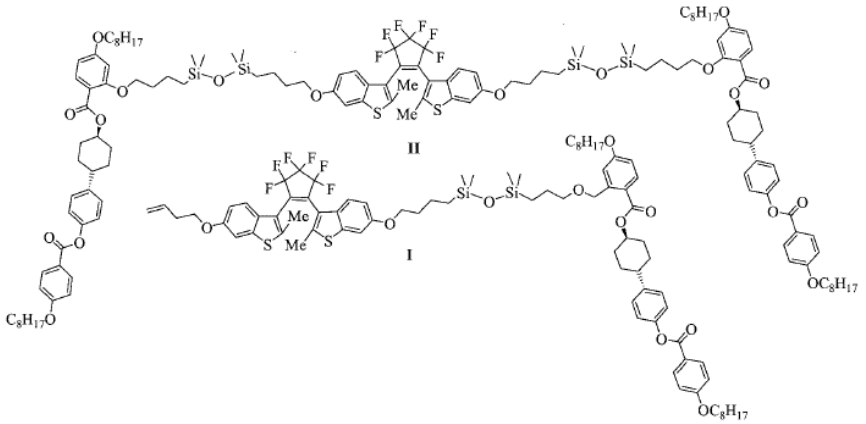

Figure 1.9: Structures of two different diarylethene-based light responsive liquid crystals.

One of the few examples of a responsive liquid crystal, which yields a chiral liquid crystalline phase are the diphenylbutadiene-based mesogenic dimers (figure 1.10).[40] The mesogen consists of a cholesterol moiety linked to the butadiene chromophore via a flexible alkyl chain.

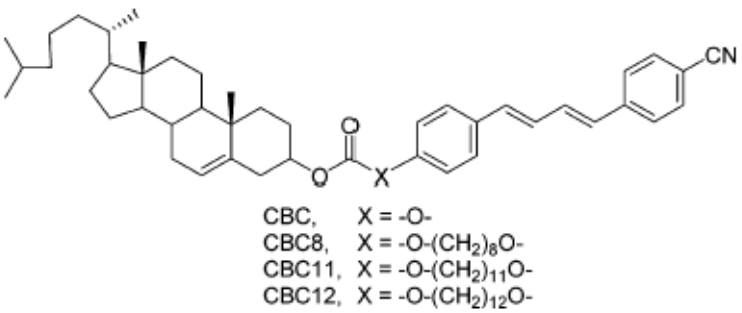

Figure 1.10: The structures of the biphenylbutadiene-based mesogenic dimers.

These liquid crystals show thermal and photochemical switching. The type of chiral liquid crystalline phase observed can be influenced by a change in

temperature. CBC 8 (Figure 1.10) forms a chiral Nematic phase at 152 ºC, while at 121 ºC it forms a chiral smectic A phase. At 135 ºC the twist grain-boundary of the chiral A phase can be observed.

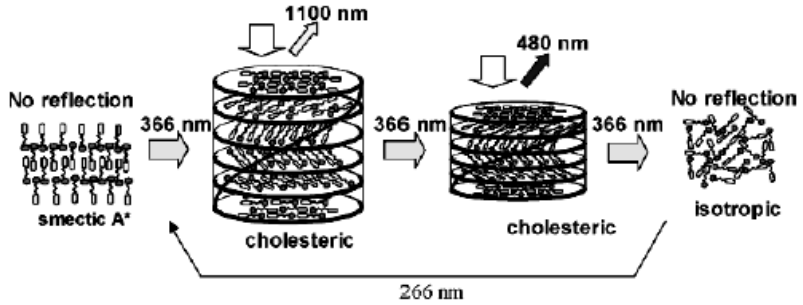

Figure 1.11: Transition from the chiral smectic to the chiral nematic and then to the isotropic phase. From ref 40.

The photoinduced *cis*/*trans* isomerization of the butadiene moiety brings about an isothermal phase transition from the smectic to the cholesteric phase. The pitch of the cholesteric phase can be controlled by the *cis* to *trans* ratio that is induced. Already after 15 s (λ = 366 nm) CBC 12 undergoes a transition from the chiral smectic A to the chiral nematic phase. After 9 min of irradiation the isotropic phase is reached (Figure 1.11). Through careful manipulation of the phase the pitch of the phase can be controlled. Using energy modulated irradiation, patterns or images can be generated. Upon converting these phases to chiral nematic glasses these images can be stabilized (figure 1.12).

Figure 1.12: Image stored in a cholesteric glass generated via energy-modulated irradiation of a smectic film at 105 ºC. From ref 40.

1.2.6 Non-calamitic liquid crystal phases

Although calamitic (rod-like molecules) nematic liquid crystals have attracted most attention due to their commercial availability, there are other molecules which possess liquid crystalline properties. Discotic liquid crystals are formed from disc-like molecules rather than rod-like molecules of the nematic phase. These molecules are known to stack in columns yielding a cholesteric phase as, for example, in the case of discotic triazine triamides, which self-assemble to form helices (Scheme 1.3).[41]

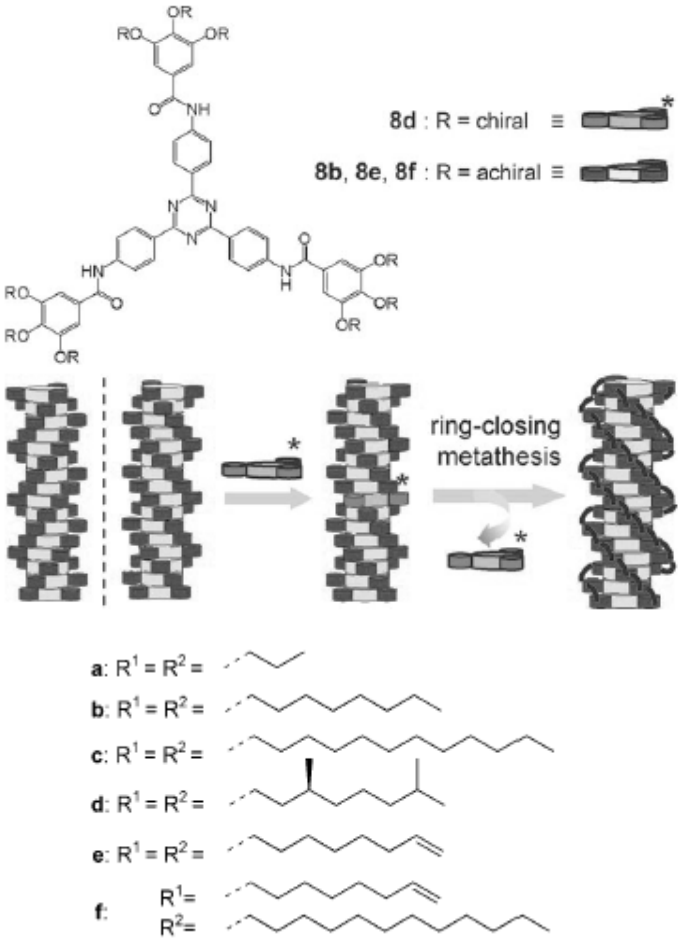

Scheme 1.3: The helical stacks formed through the assembly of discotic triazine trisamides. In the case of **8f** there are two different R groups, R_2 is on the *para* position and R_1 on the *meta* positions. Image adapted from ref 41.

The proposed mechanism is that the aggregate is based on stabilization through cooperative π-stacking, hydrogen bonding and van der Waals interactions. The central triphenyltriazine moieties can form a one-dimensional aggregate through π-stacking. A triple helical network can be induced via the hydrogen bonds of the amides, which propagates along the first aggregate axis and enforces a helical shape. Through subsequent ring-closing metathesis the helical shape can be fixed covalently.

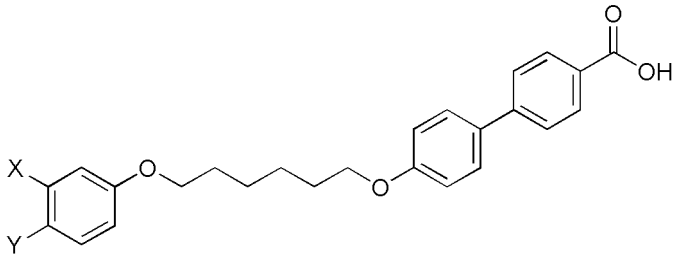

Figure 1.13: The general structure of the achiral C6 biphenyl carboxylic acids which form chiral smectic phases. BPCA-C6-P*m*OH X = OH Y= H; BPCA-C6-P*m*OCH3 X= H, Y= OCH3; BPCA-C6-P X = H, Y = H; BPCA-C6-P*p*OH X = H, Y= OH.

Achiral C6 biphenyl carboxylic acid compounds (Figure 1.13) can also form supramolecular helical structures which result in chiral smectic phases (SmC, Figure 1.14),[42] upon the transition from SmA to the SmC phase. The self-assembled twisted dimers with the phenyl end groups are essential to form stable helical superstructures. The dimers may pack in a clinic or anticlinic manner depending on the substituents on the *meta*- and *para*-positions (Figure 1.15); however this does not affect the helical packing. Even if a mixture of BPCA-C6-P*m*OCH_3 (Figure 1.13: X=OCH_3 Y=H) and BPCA-C6-P (Figure 1.13: X=H Y=H) is used, which cannot hydrogen bond with neighboring layers, a helical structure is still generated. The dimers formed possess a twisted rather than a bend conformation (based on computer simulations). The only C6 molecule not to generate the dimers (BPCE-C6-P*m*OH) had no twist. The chemical origin of these helices is the interaction of head-to-head dimers with the phenyl moieties at both ends.

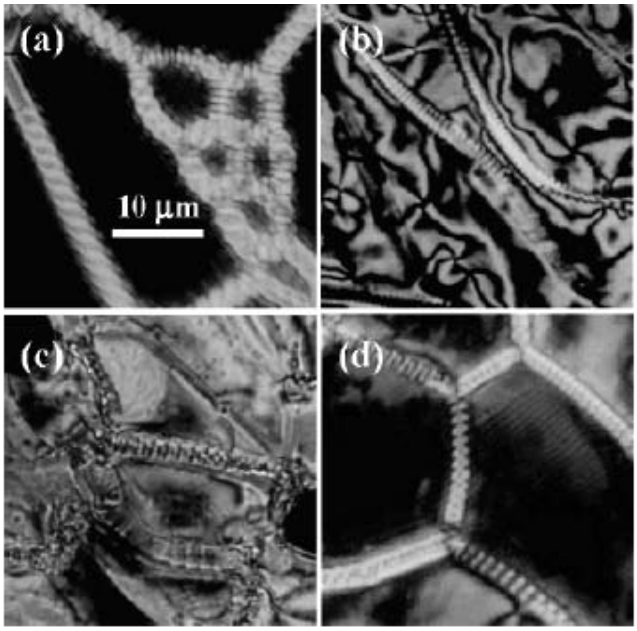

Figure 1.14: Optical micrographs of the various chiral smectic phases generated

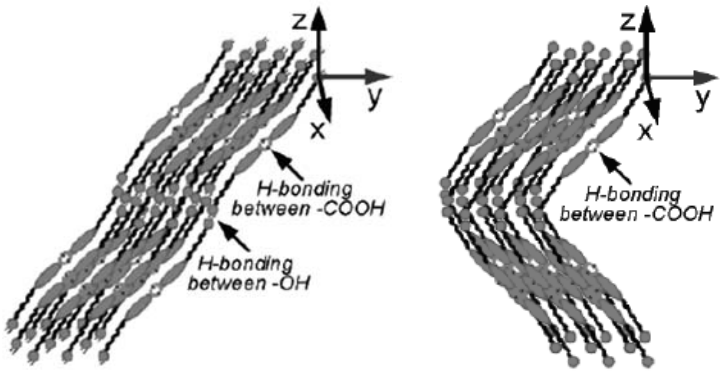

Figure 1.15: Schematic representations of the molecular arrangements in the chiral smectic layers: left) BPCA-C6-P*m*OH and BPCA-C6-P*p*OH (synclinically tilted SmC phase); right) BPCA-C6-P and BPCA-C6-P*m*OCH_3 (anticlinically tilted SmC phase). Taken from ref 42.

Supramolecular chiral assemblies of thermotropic cubic materials which are not based on rod-like aromatic chiral molecules were first reported by Kato *et al*. Folic acid derivatives (Figure 1.16) were synthesized which contained an oligo(glutamic acid) moiety and lipophilic alkyl chains.[43,44]

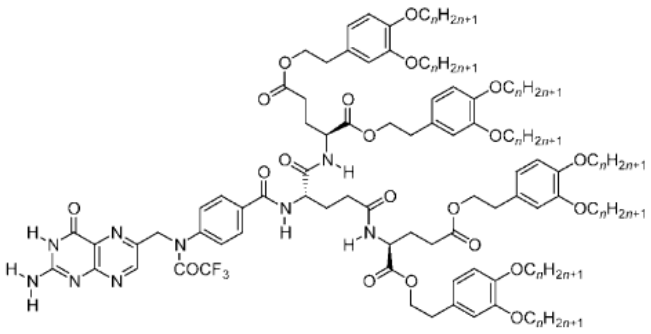

1a (n = 6), **1b** (n = 11), **1c** (n = 18)

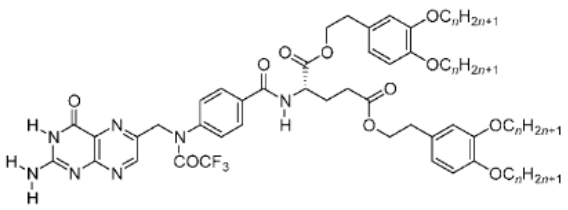

2a (n = 6), **2b** (n = 11), **2c** (n = 18)

Figure 1.16: The structure of folic acid derivatives used in self assembly.

The folic acid derivatives assemble into helical structures in the presence of sodium triflate (Scheme 1.4). These results suggest that compounds **1** self-assemble in chloroform to form disklike tetramers, which should stack to form columnar assemblies through ion–dipolar interactions between sodium salts and the carbonyl groups of the pterin rings. These folic acid derivatives show new chiral mesomorphic behavior by forming both a chiral hexagonal columnar and a chiral cubic Pm3n liquid crystalline phase instead of the typical cholesteric phase. All of the folic acid derivatives tested form stable thermotropic liquid crystalline phases. However, by altering the alkyl chain length the liquid crystalline behavior is altered. In the case of a *n*-hexyl chain only a columnar phase was observed, while in the case of an *n*-undecyl or *n*-octadecyl chain both a columnar and a cubic phase were observed. This work[44] represented the first example of a cubic phase which exhibited supramolecular chirality which was induced by a nonchiral ion.

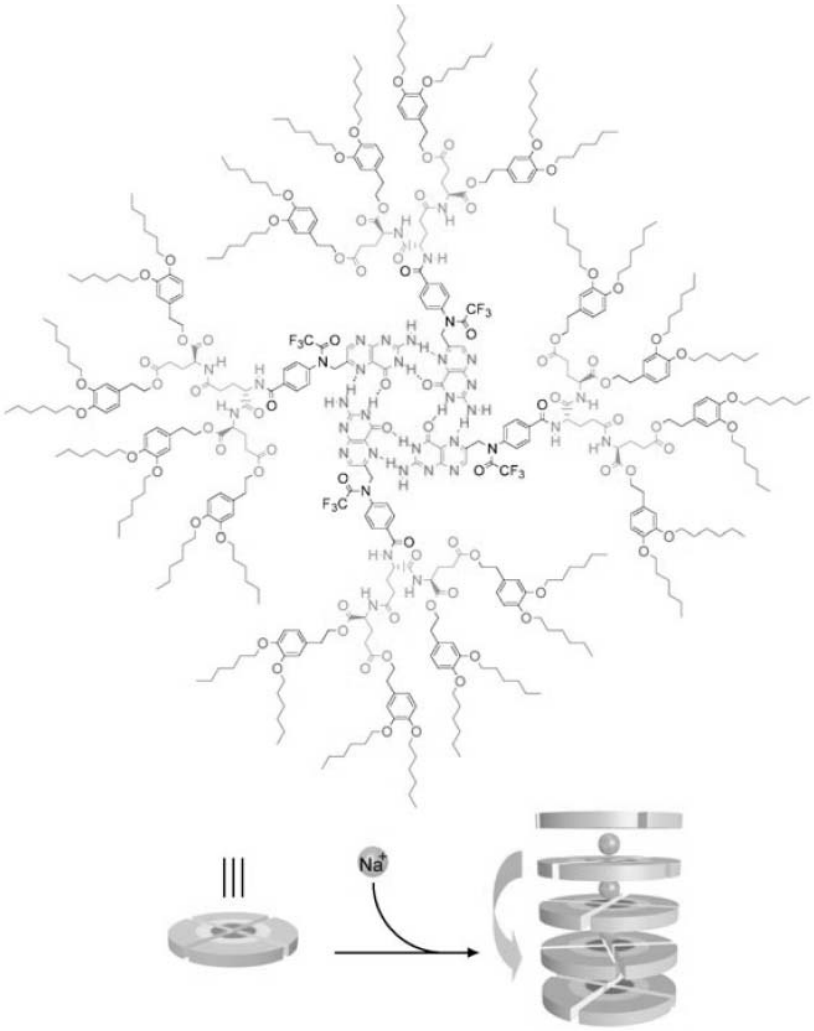

Scheme 4. Schematic representation of self-assembled **1a**/$NaOSO_2CF_3$ in chloroform solution state.

Scheme 1.4: The assembly of the folic acid derivatives with the sodium triflate moiety to generate helical stacks in chloroform. From ref 44.

1.2.7 Polymeric liquid crystals

Chiral carboxylic acid dopants, enable charged poly(phenylacetylene) to form a cholesteric liquid crystalline phase.[45,46] The charged poly(phenylacetylene), in water, acts as a lyotropic liquid crystal. At low concentrations there is already a helical induction, however, only at higher concentrations is the cholesteric phase observed (Scheme 1.5). This high concentration (8 wt % poly-1-HCl in water with an amount of chiral dopant) is the point at which the cholesteric phase observed.

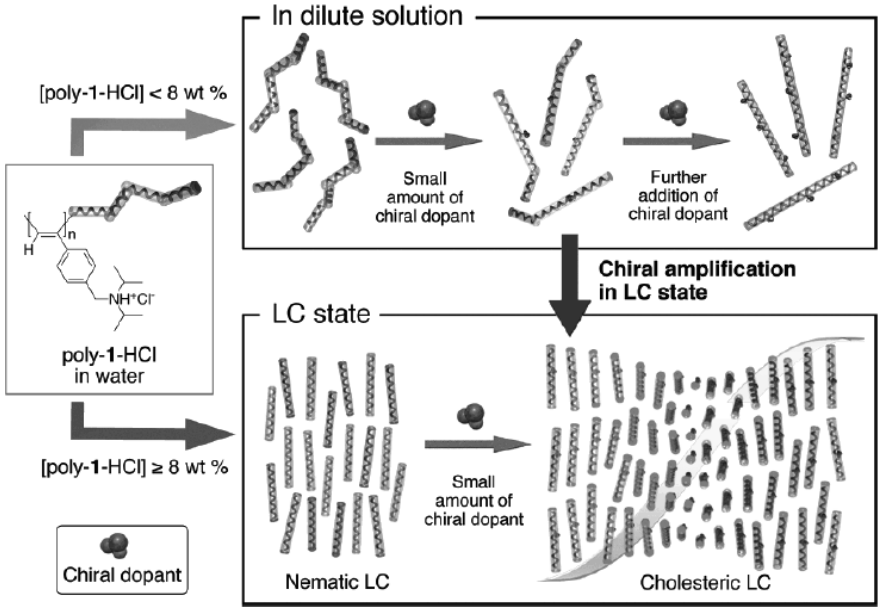

Scheme 1.5: The effect of the addition of chiral carboxylic acids to the polymer poly-1-HCl in water at different weight percentages of the polymer. From ref 46.

The chiral amplification (at lower concentrations) was determined using CD spectroscopy. X-ray diffraction was employed to demonstrate the change in the overall structure of poly-1-HCl after chiral induction.

1.3 Gelators

Organogelators, known already for over one century (Thomas Graham 1861)[47] although only defined as a phenomenon much later by Flory (1970's)[48], are formed by molecules that can self-assemble in a solvent in such a way as to influence the behavior of the system as a whole. Flory defined a gel as a substance, which has a continuous structure on the macroscopic scale that is permanent (time scale of an analytical experiment) and with solid-like rheological behavior. Colloidal aggregates are formed, which are linked into complex three-dimensional networks that immobilize the liquid component. These networks are formed through either hydrogen bonding interactions, π-π stacking, electrostatic interactions or more typically a combination thereof. Gelators are typically classified as being hydrogen-bond or nonhydrogen-bond-based. The structural diversity of molecular gelators available is remarkable and include steroid and fatty acid derivatives, α-amino acids, and organometallic compounds, as well as two-component systems.[49-51] A comprehensive review by Terech and Weiss of these organogelators is already available.[52]

The ability of a gelator to gelate solvents is critically dependent on its molecular structure, and gelators for all types of solvents ranging from organic solvents to water are known. Typically gelator molecules stack to form fiber like superstructures.[53] Depending on the configuration of the gelator employed, the gelators can stack in a chiral superstructure. However, the chirality does not necessarily require that the gelator molecule itself is chiral. By the addition of a chiral solvent or other chiral additive, achiral gelators can form chiral supramolecular architectures. The transcription of "information" from the molecular level to the macroscopic scale (in terms of materials properties) is a major driving force for research in this field. In the following sections we will examine several complex gelator mixtures and the helical and double helical morphologies that have been observed for these systems.

1.3.1 Chiral gelator molecules

The formation of chiral gels, in the case of chiral gelator molecules, depends on the gelator and the choice of solvent. Chiral low-molecular-weight gelators (LMWG) can, and typically do, generate chiral fibrous architectures within a gel. One example of a LMWG is based on a binaphthalene (a molecular motif often employed for its ability to induce chirality in liquid crystals) functionalized with two urea moieties.[54] These moieties assemble in a chiral manner through hydrogen bonding and π-π interactions.

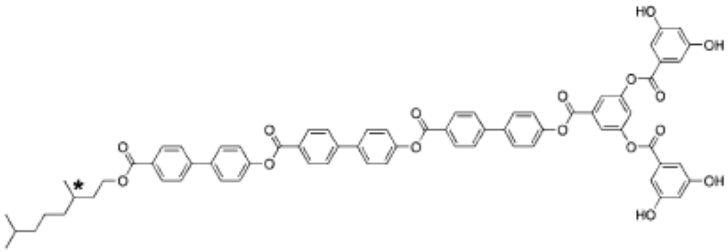

Figure 1.17: The structure of a gelator based on a DRC, from ref 55.

Dendron rod coils (DRCs, Figure 1.17), which self-assemble in organic solvents form ribbon-like structures.[55] The self-assembly is driven by head-to-head hydrogen bonds and the respective orientation of the tails (R or S) determines the prefered packing. The R enantiomer packs to form a ribbon (left handed helix) with the opposite helicity of the S enantiomer, as can be seen by atomic force microscopy (AFM, Figure 1.18).

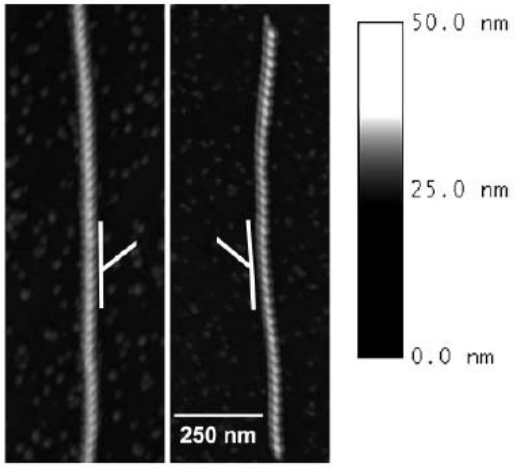

Figure 1.18: AFM images of R-DRC (left image) and S-DRC (right image). The horizontal and vertical scale bars are identical for both images. The white lines indicate the handedness of the formed fibers.

Comparison of one and two component dendritic systems has been employed in an attempt to elucidate some of the possible molecular recognition pathways that lead to gel formation.[56] The gelator consist of L-lysine-based dendritic headgroups connected via an amide bond to an aliphatic diamine chain (Figure 1.19), which self-recognize and form supramolecular polymer-like[57] structures.

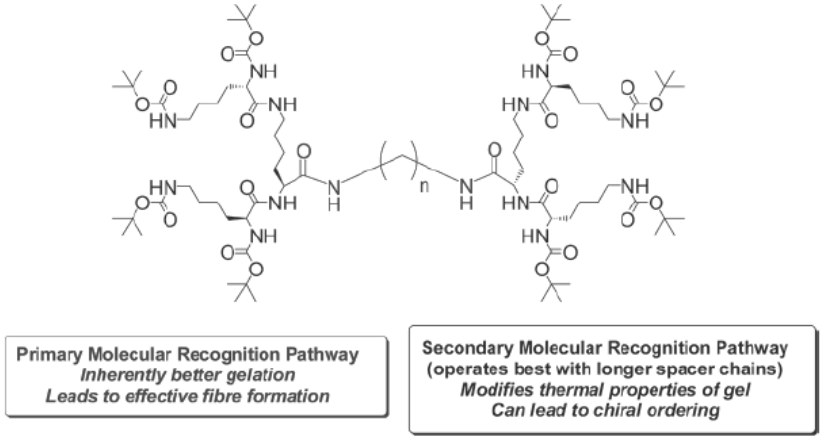

Figure 1.19: Structure and properties of a dendritic polymer-like gelator. The bridging section is the primary recognition pathway, while the outer amide functionalities are considered to provide the secondary molecular recognition pathway.

These dendrimers self-assemble in toluene. The assembly of these single component systems is efficient as there are both covalent and hydrogen bonding interactions present. However, the preset chiral information in the dendritic headgroups does not always transcribe into chiral nanoscale assemblies. Indeed a two-component assembly, in which a dendritic headgroup and an aliphatic spacer, attached non-covalently through acid-amine interactions,[58] employed hydrogen bonding exclusively. This two-component system yields a chiral ordered assembly consistently. The fiber formation is accompanied by chiral ordering since the molecular recognition pathway is entirely dependent on the hydrogen bonding interactions between the two components.

Achiral tetra(thiafulvalene-crown-ether)-substituted phthalocyanine building blocks (Figure 1.20) have been found to stack in solution and on surfaces forming helical tapes (Scheme 1.6).[59] The crown ether moieties (TTF) can interact with each other and with the phthalocyanine moiety (Pc). If only homo-interactions would be observed a standard stack (no helicity) aggregate would be the result. However, the TTF-Pc interaction causes the molecules to assemble in a bilayer type assembly, which scrolls up to form a helical tape.

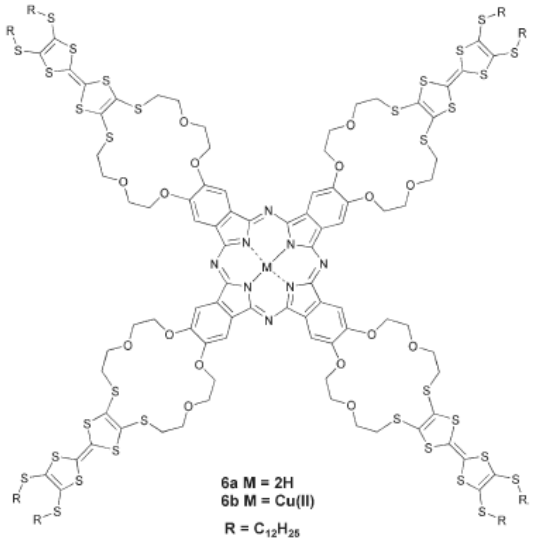

Figure 1.20: The structure of a tetra(thiafulvalene-crown-ether)-substituted phthalocyanine building block

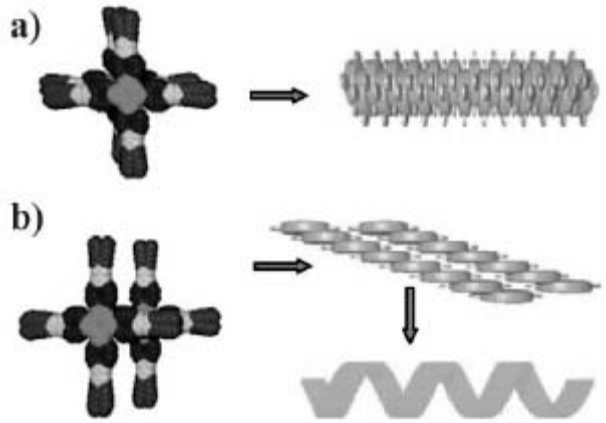

Scheme 1.6: (a) TTf-TTF and Pc-Pc interactions dominate in generating columnar stacks (not observed). (b) Pc-TTF and TTF-TTF interactions dominate in forming bilayer type structures which then scroll up into helical tapes (observed). From ref 59.

Double-helical foldamers (artificial oligomers that also adopt well-defined folded conformations) can be formed through the interstrand interactions between side-chains.[60] 4-Decyloxy-substituted oligomers (structure in scheme 1.7, R =$OC_{10}H_{12}$), for example nonamers, cooperate to form both helices and double helices. However, in the case of benzyloxy, the equilibrium favors the double helical form, which arises through interactions of two separate strands (Scheme 1.7) producing a three-turn

helix. This is favorable owing to the extensive interstrand π-π interactions between the benzyloxy side chains.

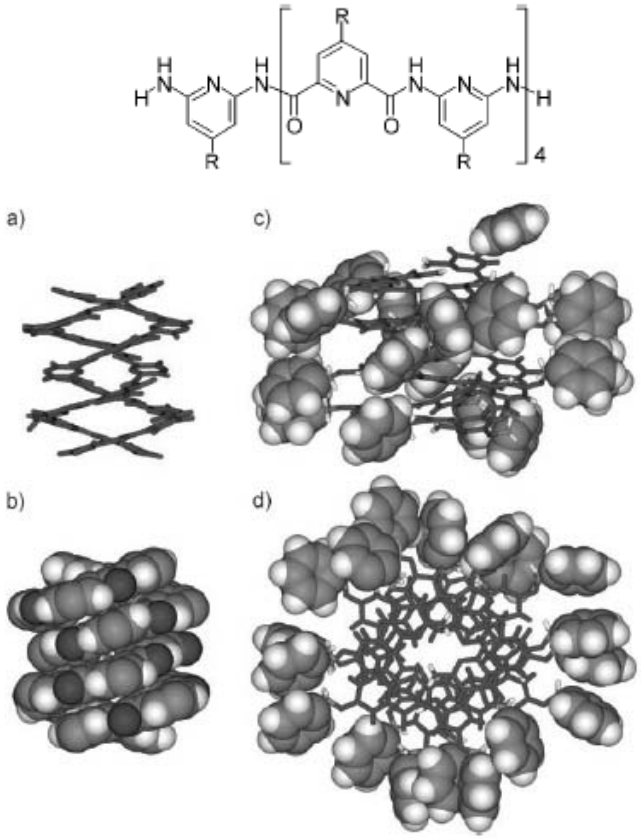

Scheme 1.7: Shows assembly for benzyloxy-substituted nonamer (structure top, R = OBn) a) the stick model; b) the space filling model; c) side view of the assembly; d) top view of the assembly with a space filling model for the side groups and stick model for the backbone. Adapted from ref 60.

Chiral crown ether-functionalized phthalocyanines (Scheme 1.8 A), in chloroform, form gels through π-π stacking, the fibers of which form helical stacks.[61] Although they form a right-handed helix initially (based on CD-spectroscopy), TEM images (Scheme 1.8 B) suggest that the assemblies formed are left-handed twisted bundles due to the supercoiling of two of these fibers to generate a larger left-handed superhelix (Scheme 1.8 C). Upon the addition of alkali-metal ions, which bind in the crown ether moieties, the aggregates disassemble completely.

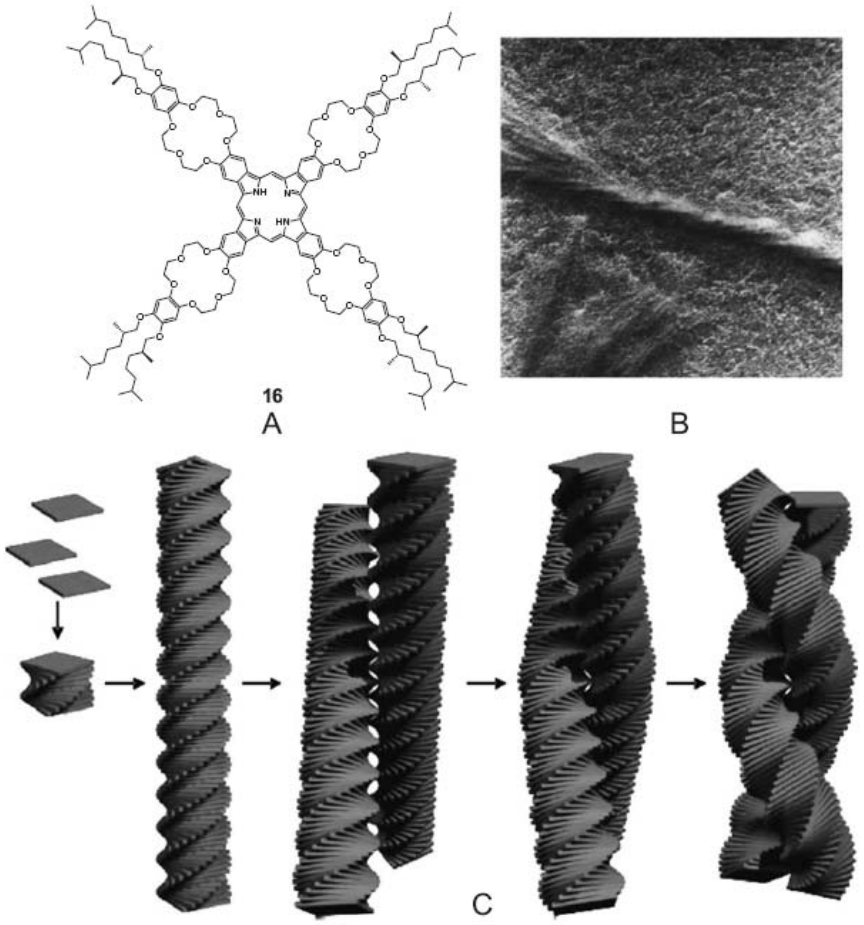

Scheme 1.8: A) The structure of the crown ether-functionalized phthalocyanine. B) TEM image of left-handed twisted bundles formed by A. C) Proposed hierarchical organization of the molecules A, first the right-handed helix that then supercoils to form a left-handed superhelix. Adapted from ref 61.

1.3.2 Helicity through templating

Nucleotide bolaamphiphiles (Figure 1.21) can self-assemble through the template function of an oligonucleotide. The longer oligoadenylic acids (n = 10, 20, 40) are able to induce helical morphologies in single nanofibers. The evidence presented suggests that through the complementary A-T base pair interactions the molecules align in a helical sense.[62] Both ends of the bolaamphiphiles are thus edged (Scheme 1.9). The bolaamphiphiles stack along one axis while the double strands of oligonucleotides wrap around it along the same axis yielding helical nanofibers.

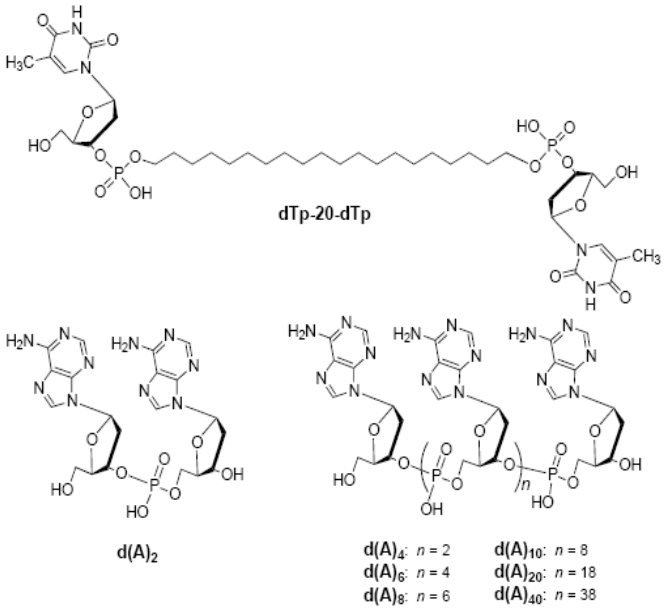

Figure1.21: The structure of the bolaamphiphile **dTp-20-dTp**, and the series of oligoadenylic acids (**d(A)$_n$**) used.

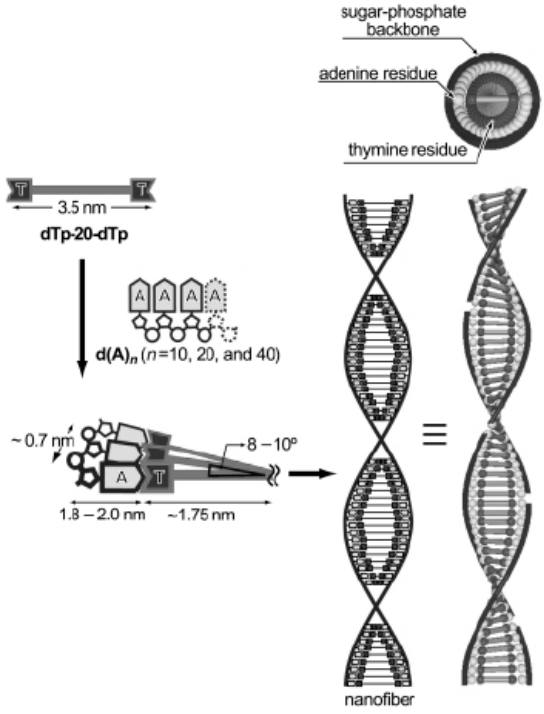

Scheme 1.9: The helical assemblies formed by the bolaampiphiles shown in Figure 1.21. The red units represent the thymine and the yellow units represent the adenine residues. From ref 62.

The use of organic compounds in building inorganic structures has received increasing attention, as these templates form novel supramolecular structures.[63] Helical organogel fibers can be used to induce both right- and left- handed silica structures.[64] Neutral and cationic amide-based gelators and neutral urea-based gelators have been employed to achieve this also (Figure 1.22). These gelators consist of a chiral diaminocyclohexane skeleton, a common motif in aggregation of helical fibers.

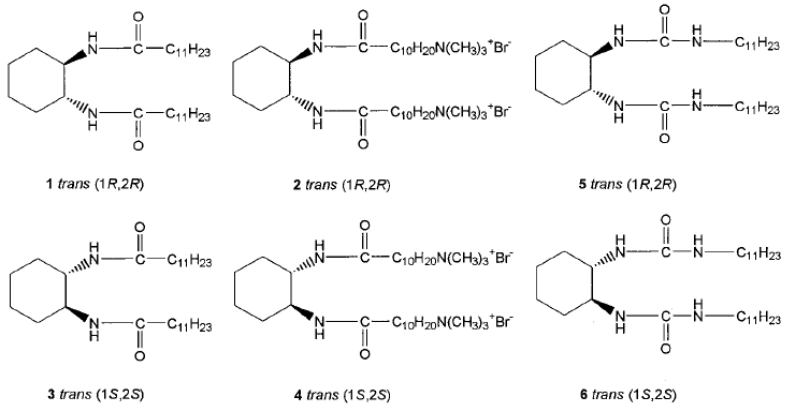

Figure 1.22: The structures of several neutral and cationic amide-based gelators and neutral urea-based gelators

The helical structure of the organogelators is transcribed to silica particles (Figure 1.23). By utilizing a right-handed organogel helix as a template for the silica structure is formed which appeared to be right-handed also. The same holds for the left-handed organogel.

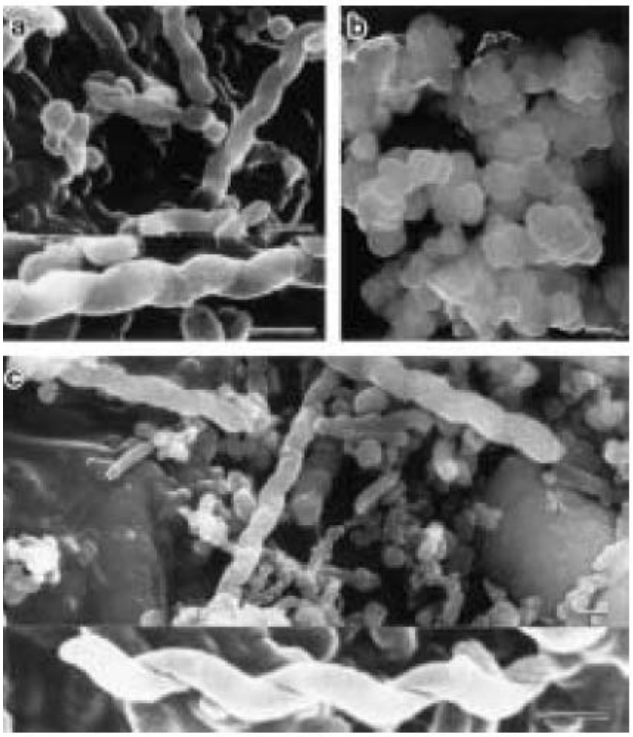

Figure 1.23: SEM pictures of the silica structures obtained from a) 1+2 (1:1 wt %) b) 1+2 (9:1 wt%) and c) 3+4 (1:1 wt %) after calcination (bar 200 nm).

More recently, Shinkai *et al.* have shown that this templating effect can be extended further to sulfonated polyaniline (SPAN) superstructures created in chiral diaminocyclohexane-based organogel systems (Figure 1.24).[65]

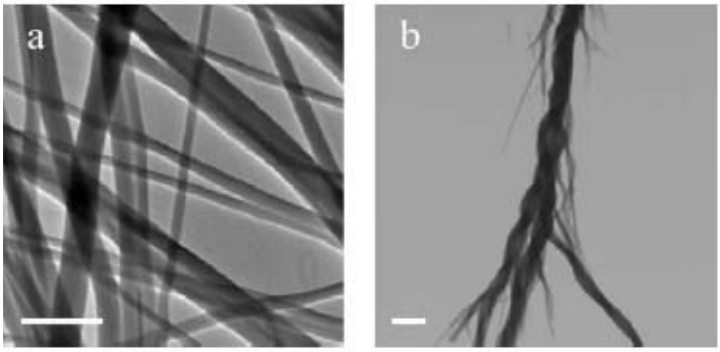

Figure 1.24: TEM images of the SPAN:X:Y xerogel prepared from DMSO, where X is a neutral and Y is a cationic diaminocyclohexane-based organogelator (a), and the film cast from a dilute solution in DMSO (b). No staining was used. The scale bar = 1 μm. the mole ratio of SPAN:X:Y is 2:1:5.

1.3.3 Responsive gelator molecules

Low molecular weight gelators (LMWG) often exhibit highly specific self-assembly features.[52] LMWG, with multiple hydrogen bonding groups, and a diarylethene photoresponsive unit (which imparts photochemical controlled functionality) have been reported.[66] The coassembly of isotactic chiral and achiral molecules enables the transfer and propagation of chirality in the coaggregate structure. The photochemical ring-closure of the diarylethene moiety can lock the chiral information (Scheme 1.10). The switches are present in two rapidly interchanging conformations (with P and M helicities), which upon ring closure lead to RR or SS enantiomers in equal amounts. Aggregation of the chiral open switch **1o** (Figure 1.25) leads to selection of only one of the helical forms of **1o** in the gel state.[67] After ring closure in the gel state a 96% diastereomeric excess in the gelator molecules was observed while in solution no stereoselection is observed. For the coassembly shown in Scheme 1.10, a gel is formed containing 0.6 mM **3o** and 0.6 mM of either **1o** or **2o**. The coassemblies of **3o** with **1o** or **2o** is accompanied by a preference for one of the helical conformations of **3o**.[68] Large asymmetric inductions were observed confirming that the presence of **1o** forces **3o** into a preferred conformation: a sergeant-soldier[69] effect is operating, and up to 8-fold chiral amplification with **3o** was observed.

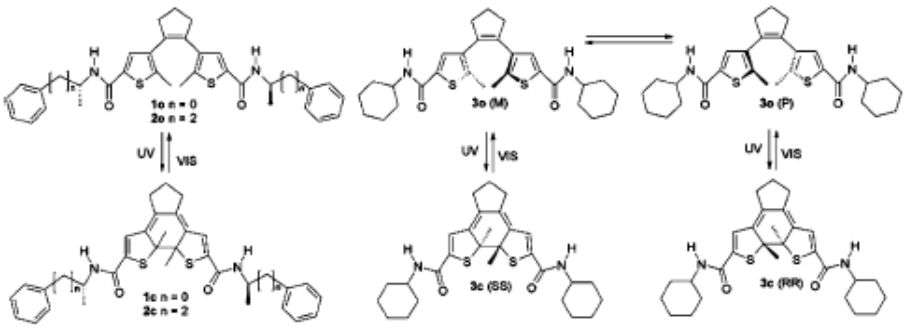

Figure 1.25: The structures of the chiral diarylethene switches used for selection and amplification upon aggregation via hydrogen bonding; o = open form, c = closed form, UV: λ = 313nm, VIS λ > 420 nm. From ref 68.

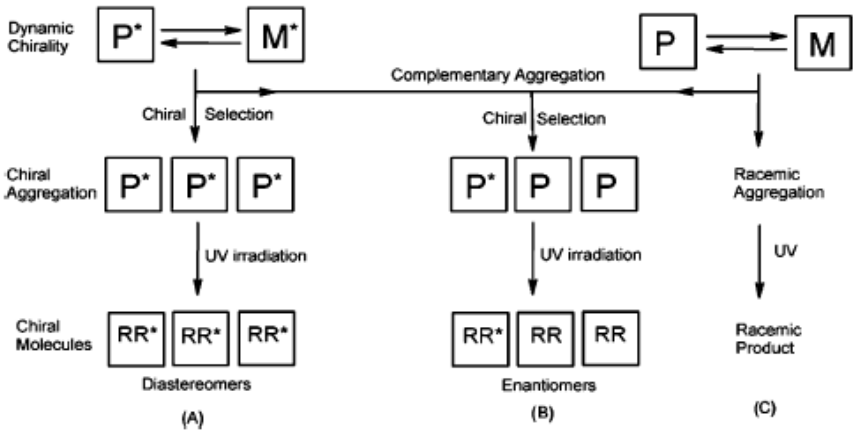

Scheme 1.10: Schematic representation of the amplification of supramolecular chirality and subsequent transfer to molecular chirality. (A) In a dynamic equilibrium (P* versus M*), upon aggregation one of the helical conformations, P* is preferred due to chiral auxiliary groups involved in hydrogen bonding, leading to high diastereomeric excess after UV irradiation (RR*). (C) For achiral compounds, no selection during aggregation from the dynamic equilibrium occurs; hence a racemic product is formed after irradiation. (B) Coaggregation of both molecules leads to a selection process and preferential formation of single (RR) enantiomers after UV irradiation. From ref 68.

1.4 Supramolecular chirality

Supramolecular chemistry, as defined by Lehn, unlike molecular chemistry relies on non-covalent interactions. Highly complex supramolecular structures are generated through molecular recognition-driven self-assembly. The assembly can be the result of complementary hydrogen-bonding, electrostatic interactions, hydrophobic interactions or π-π stacking.[70] These complex preorganized assemblies have been designed as receptors for molecular recognition, catalysis and transport of a variety of substrates.[71,72] Noncovalent positioning of these assemblies, especially when these are chiral, can aid in templating.[73-75]

1.4.1 Stressed systems

One manner of inducing chirality in a larger self-assembled system is through the spontaneous symmetry breaking of the aggregate. This will always induce chirality, however the sign may be unpredictable. For example, by stirring an enantiomeric excess can be induced during crystallization, though these systems behave unpredictably.[76] Homoassociates of zwitterionic diprotonated porphyrins aggregate (generating liquid-crystal structures at higher concentrations) in aqueous solution and can undergo spontaneous symmetry breaking.[77] Initially J-aggregates are formed through the electrostatic and hydrogen-bonding

interactions of the positively charged porphyrin rings and the anionic sulfate groups (Scheme 1.11). The elementary chiral fluctuation originates from the preferred long symmetry axis of the J-aggregate. Depending on the direction of the vortex motion of the stirrer, the sign of the chirality of the homoassemblies could be selected. Thus it appears that the chiral selection takes place at the supramolecular level. This was the first example for which it was proven unequivocally that stirring can induce chirality.[78]

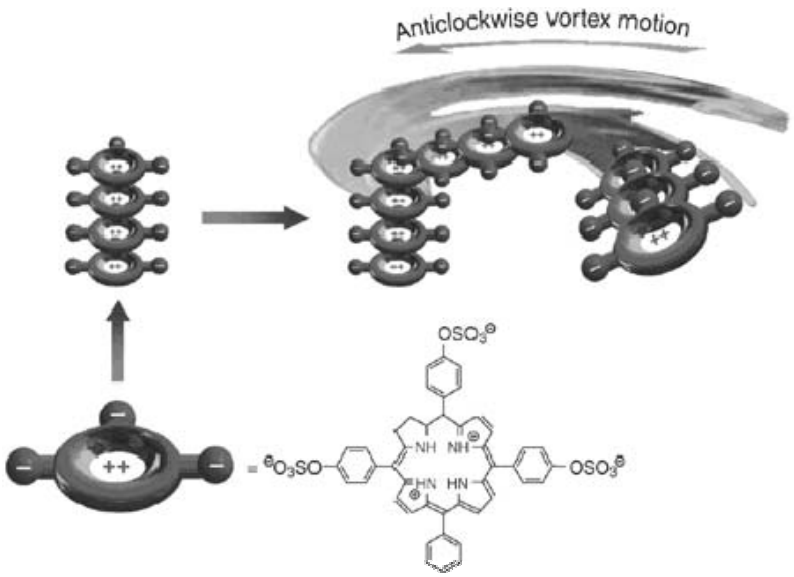

Scheme 1.11: The J-aggregates formed upon self-assembly of the porphyrin molecules, and the consequent induction of chirality via the stirring direction. In this case the rotational motion is counterclockwise. From ref 77b.

1.4.2 Hydrogen-bond generated assemblies

Reinhoudt *et al.* have shown that through the use of peripheral chiral information structural isomerism in noncovalent hydrogen-bonded assemblies can be influenced.[79] Double rosette assemblies[73] were formed based on calix[4]arene dimelamines and barbiturates/cyanurates. The double rosette is assembled entirely through hydrogen bonding interactions (Scheme 1.12). The resulting dynamic assemblies stack in three different forms: staggered (D_3 symmetry), symmetrically eclipsed (C_{3h} symmetry), or unsymmetrically eclipsed (C_s symmetry). The isomeric distribution between these forms depends on steric, electronic and solvation effects. It was observed that the addition of chiral molecules, such as barbituric acid and isocyanuric acid derivatives, determine the isomeric distribution during the the assembly process.

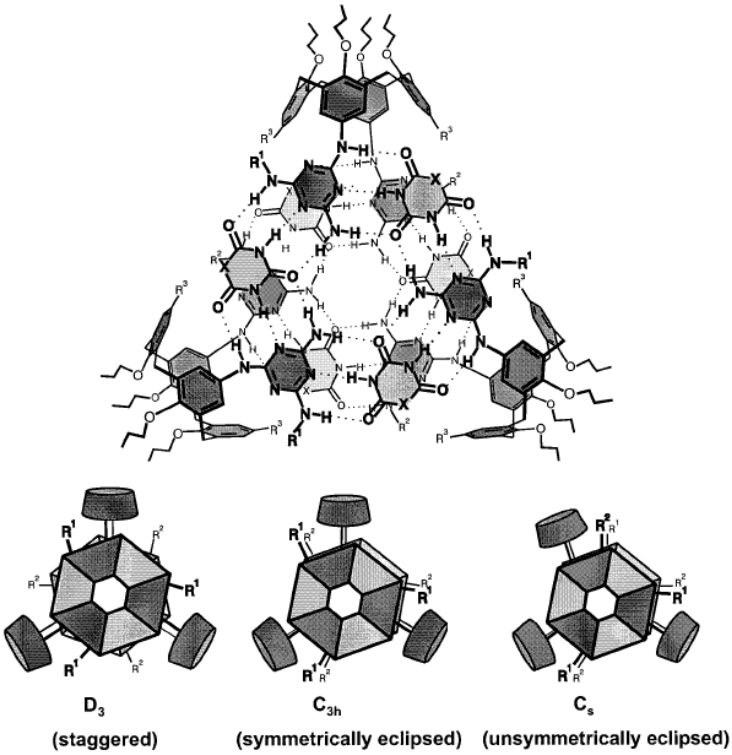

Scheme 1.12: Double rosette assemblies of calix[4]arene dimelamines and barbiturates/cyanurates. From ref 79.

More recently it was shown that tetrarosette helices can be formed through hydrogen bonding of tetramelamine (Scheme 1.13) and cyanurate.[80] The extent of chiral amplification that is obtained through a sergeant-soldier effect is dependent on the structure of the assembly. Initially it was observed that a solution containing a ratio of 90:10 racemic cyanurate and a pure P helix tetramelamine gave a relative CD intensity of 10%. However, after reaching thermal equilibrium the relative CD intensity increased to 52%. This increase occurred nonlinearly, which is expected in the case of chiral amplification. The chiral amplification is attributed to the exchange between the two cyanurates enantiomers within the assemblies generating a preference for the formation of the P diastereomer rather than the heteromeric assembly.

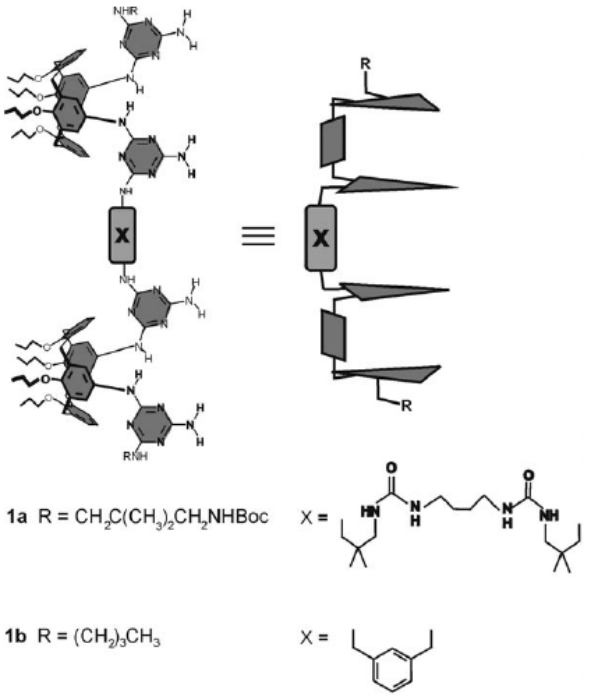

Scheme 1.13: The structure of the building blocks used for the tetrarosette assemblies. From ref 80.

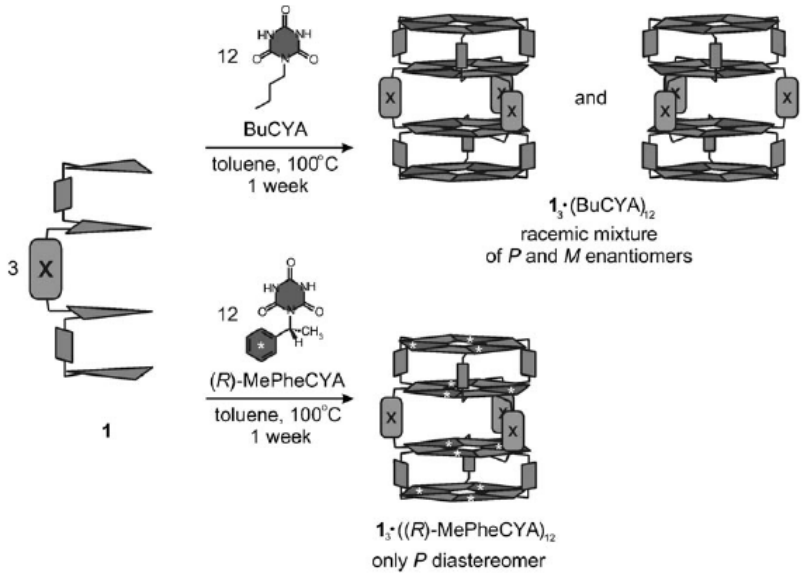

Scheme 1.14: Self-assembly of tetrarosette structures using both chiral and achiral templates. From ref. 80.

The tetrarosette assemblies, which are induced by a stereogenic center have a difference in Gibbs energy which is 40 times greater than in the case of the mentioned double rosettes (vide supra).[79,81] This is a result of a decrease in the dissociation rate constant of the tetramelamine building blocks. When the spacer rigidity is altered so is the chiral amplification. The more rigid the spacer that is used in the tetramelamine building block the lower the chiral amplification. Scheme 1.14 shows the chiral induction based on the addition of a chiral molecule. Scheme 1.15 shows the effect of exchange from one achiral additive to another or to a chiral additive. The achiral additive can be replaced readily by the chiral additive resulting in the exclusive assembly of a P-diastereomer rather than a racemic mixture. This means that the template molecule used in the tetrarosette assembly need not be chiral. The helical shape of the assemblies can be altered at a later stage by adding the correct chiral additive through exchange.

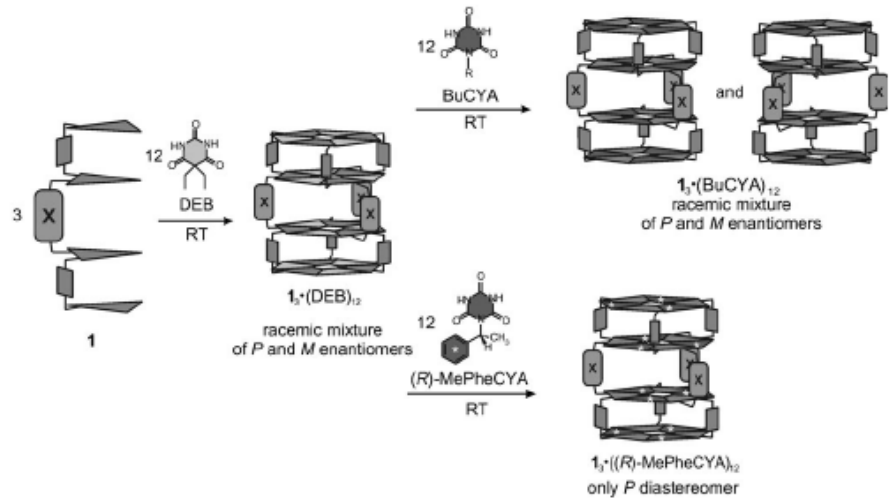

Scheme 1.15: Self-assembly of the tetrarosettes using an achiral template (DEB) and then exchanging this molecule for another achiral molecule (BuCYA) or a chiral template ((R)- MePheCYA). From ref 81.

Molecular recognition of dyads through cooperative self-assembly can be induced leading to discrete helical structures.[82] In this study several diaminopyridine-flavin based dyads were used for their specific three-point hydrogen bonding interactions, which resulted in tetrameric complexes.

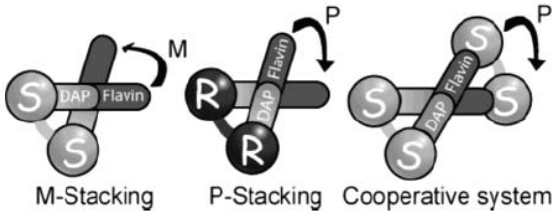

Scheme 1.16: Self-assembly of diaminopyridine-flavin based dyads towards a cooperative tetrameric complex From ref 82.

Depending on whether (R-) or (S)-diaminopyridines were being used in combination with achiral flavin, M or P stacking could be achieved. An assembly of (R)-diaminopyridines with (S)-flavins was attempted also, however, the Cotton effect was weak. This is an indication of frustrated self-assembly. In the case of two (S)-flavin segments in combination with two S-diaminopyridines, a cooperative effect resulted in a strong bisignate Cotton effect (Figure 1.26). The cooperative system was the most stable assembly generated and showed a P-helicity which is the opposite to the M-stacking assembly.

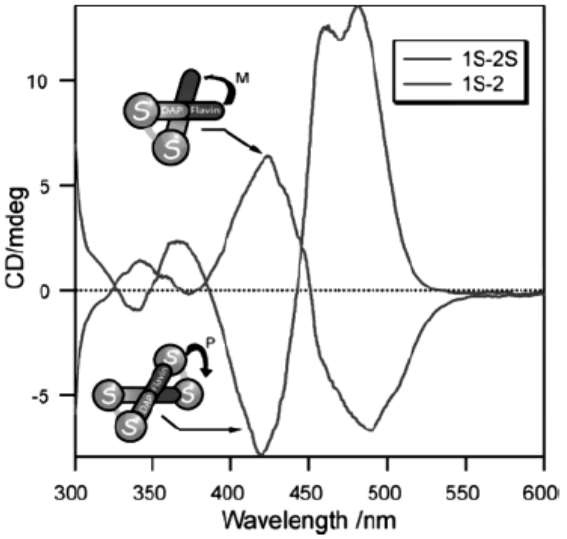

Figure 1.26: CD spectrum of the S-DAP/racemic flavin assembly and the S-DAP/S-flavin assembly, showing an inversion of the Cotton effect and the difference in amplitude of the CD signal (at -10 ºC in *n*-hexane). From ref 82.

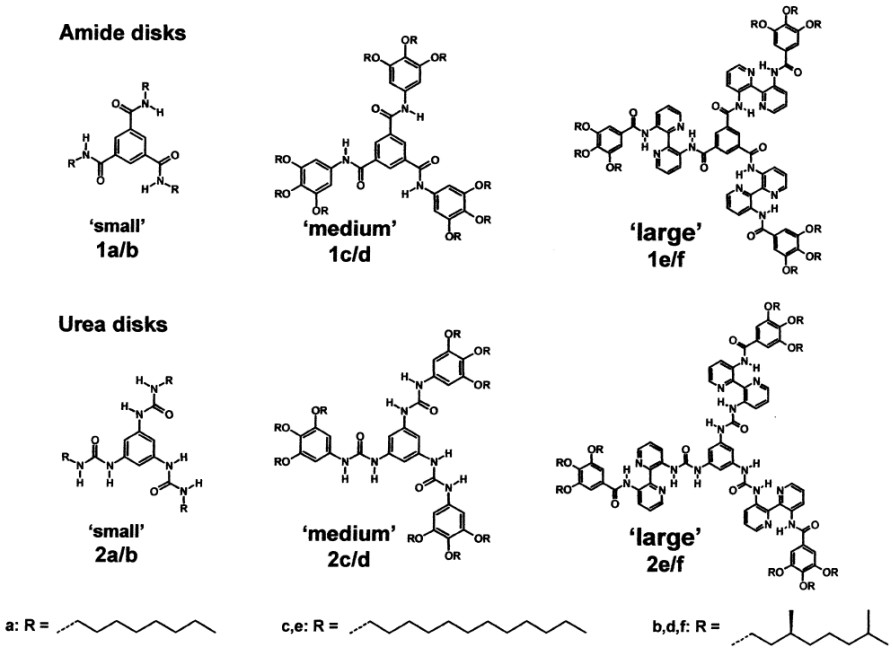

Figure 1.27: The structures of various trisamides and trisureas.

Meijer and coworkers[83] have shown that when C_3-symmetric building blocks such as discotic trisamides and trisureas (Figure 1.27), can self assemble into larger helically-shaped supramolecules. These discotic molecules form liquid crystals as can be seen from the polarization microscope image (Figure 1.28). At certain concentrations these compounds also form gels in apolar solvents (except for the medium sized amide discs).

Figure 1.28: Optical micrograph of a typical focal conic defect in a chiral liquid crystalline phase

Further studies[84] have shown that upon mixing achiral urea molecules and chiral amides, initially mixed aggregates were formed (Scheme 1.17). With

time the discs rearrange in the supramolecular assembly generating two different stack types: one which contains exclusively the achiral disc while the other stack consists of chiral disc molecules only. This shows that even though one of the disc types is in excess (85% achiral to 15% chiral) it is thermodynamically favorable for the monomers to form homoaggregates.

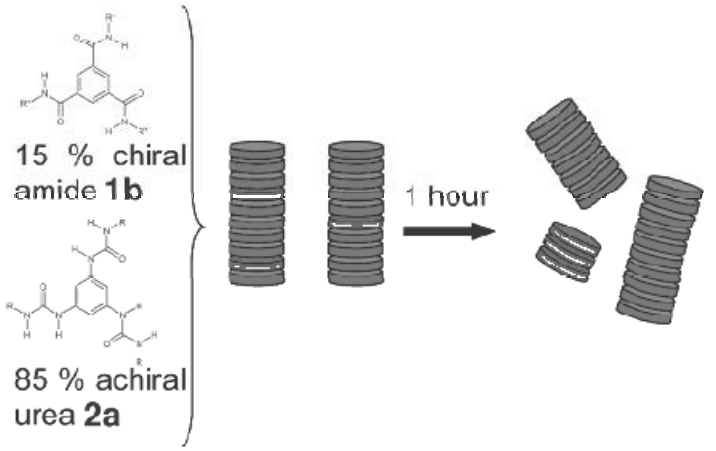

Scheme 1.17: The columnar stacks formed directly after mixing of the chiral amide and the achiral urea and after 1 hour when thermal equilibrium has been reached.

Ghadiri *et al.* have designed cyclic peptide cylinders, which stack through hydrogen bonding forming a type of synthetic channel made up of a dimer of cylinders (Scheme 1.18).[85] The peptides used can assemble into dimers in two different ways. The cross-strand phenyl interactions (edge-to-face phenyl interactions, cation-π, π-π, and quadrupole-quadrupole interactions) between the two moieties can be used to favor one of the two possible dimeric species. By leaving the peptide cavity essentially unaltered and changing the four phenylalanine side chains to two phenylalanines and two phenylalanines substituted with an additional methylene group an extreme difference in lattice morphology is observed. These small changes in structure of similar cyclic peptides have shown the subtlety of crystal growth. These cylindrical dimers are useful models for crystallization nuclei as sixteen functional groups are present in close proximity through self-assembly. This enhances control over lattice contacts by preforming a cluster of functionality.

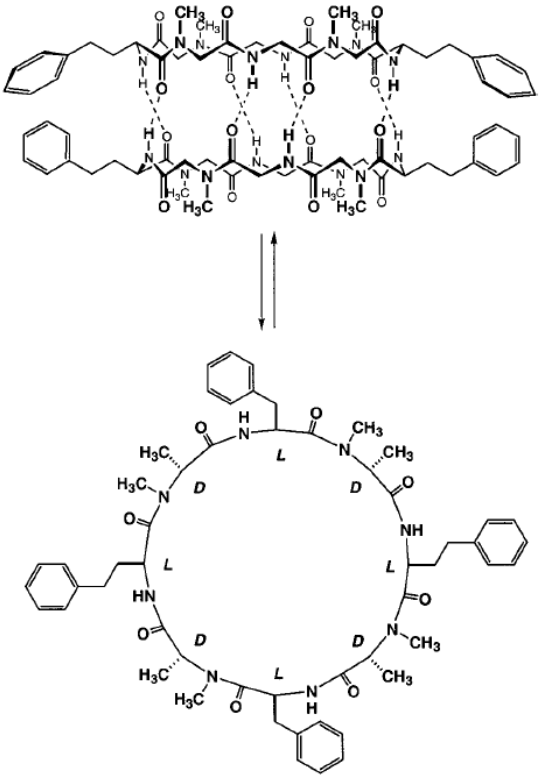

Scheme 1.18: The dimers formed through hydrogen-bonding between two cyclic peptides. From ref 85.

1.4.3 Non hydrogen-bond based assemblies

Chiral zinc porphyrins and chlorins designed to mimic natural bacteriochlorophylls,[86] have been shown to self-assemble in solution generating structures of opposite chiralities for the different enantiomers (Figure 1.29). The molecular chirality of the hydroxyethyl groups is transferred to the superstructure.

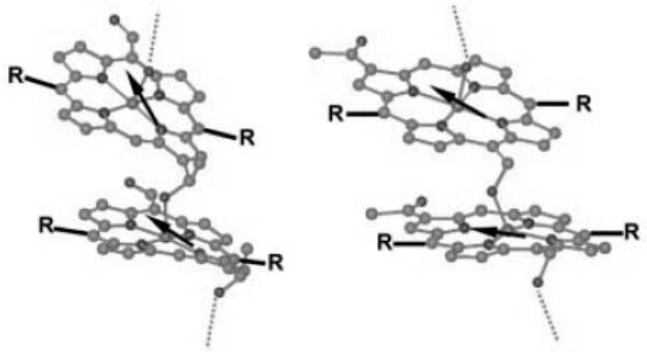

Figure 1.29: Two self-assemblies of two different chiral zinc porphyrins. **10-Zn** (left) and **15-Zn** (right); R = 3,5-di-*tert*-butylphenyl; Position R substituents the same for both zinc porphyrins. **10-Zn** has a CHO group on position 15 and a $CHOHCH_3$ at position 3. **15-Zn** has a $COCH_3$ at position 13 and a CH_2OH group on position 5. From ref 86.

Of particular interest is the observation that the separate enantiomers self-assemble less readily than the racemate at the same concentrations. In the case of the chlorosomes both enantiomers of the 3-hydroxyethyl group are present within various homologues.

Membranes can be formed through the aggregation of amphiphilic molecules. Through the use of chiral counterions (tartrate) a helical twist can be induced in the membrane (Scheme 1.19).[87] Upon increasing the ratio of L-tartrate the pitch of the helical twist is altered which allows for control of the helical pitch of the ribbons formed.

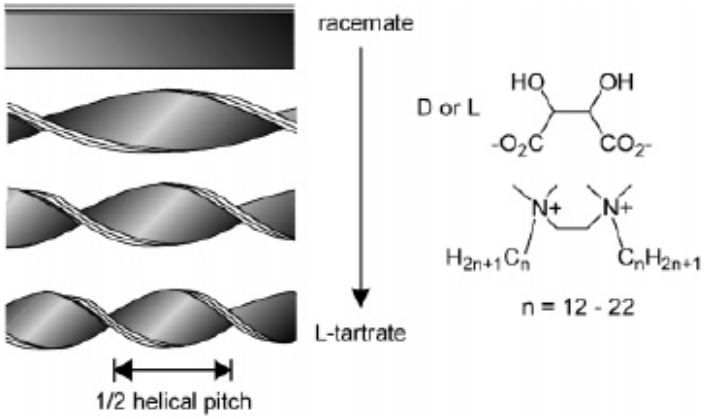

Scheme 1.19: Structure of the amphiphiles with a tartrate counterion and a schematic representation of the twisted bilayers that these compounds form in water. From ref 87.

1.4.4 Template-driven assembly

Mixtures of tetraanionic H_2TPPS (*meso*-tetrakis-(4-sulfonatophenyl)porphyrin) and tetracationic CuT4 (*meso*-tetrakis-(*N*-methylpyridinium-4-yl)porphinato-copper(II)) porphyrins form hetero-assemblies.[88] In the presence of a suitable chiral template (e.g. α-amino acids, poly-L-glutamate) a kinetically inert chiral porphyrin heteroassembly can be formed. Owing to the remarkable stability of these assemblies (due to the shielding effect of the cationic unit amongst the anionic units) the aggregates can survive template chirality disruption or even the complete removal of the chiral template from solution (Scheme 1.20).

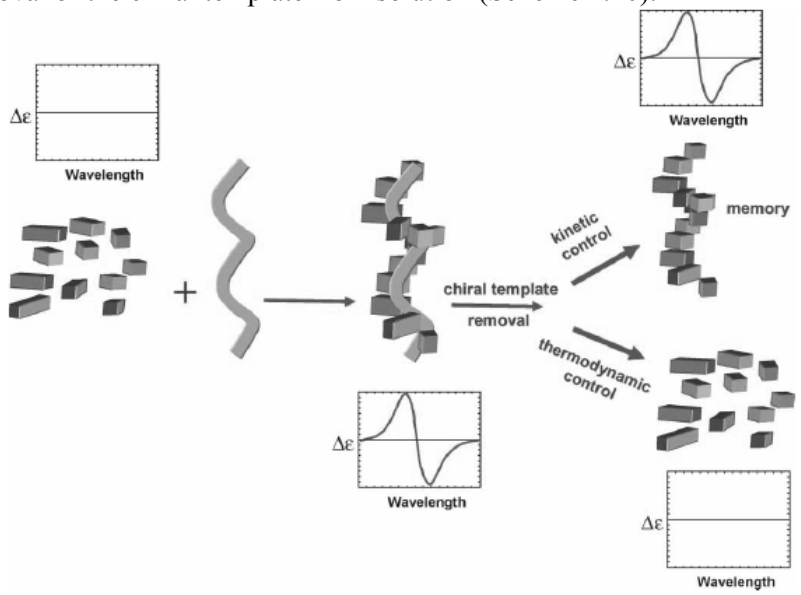

Scheme 1.20: Chiral assembly of a combination of porphyrins using a chiral template. After removal of the chiral template the porphyrin assembly retains the same chirality owing to a chiral memory effect. From ref 88.

The result is that an unaltered heteroassembly with an imprinted chiral structure remains. This structure is an excellent mold for the generation of its own structure in solution.

A chiral porphyrin assembly can further be generated which shows a memory effect, through the use of a chiral poly(phenylacetylene) template.[89] This means that even after reversal of chirality in the original template strand the chiral porphyrin assembly is unaltered (Scheme 1.21). In this case (S)- BINOL was added to a solution of poly(phenylacetylene)-HCl in water. This results in an amplification of the helicity of the BINOL as observed in the formation of chiral polyphenyl acetylene. As a result, the induced helix possesses charged pendant groups on the outside of the helix which can serve as a template for further supramolecular arrays of achiral,

oppositely charged porphyrins (tetraanionic *meso*-tetrakis-(*N*-methylpyridinium-4-yl)porphinato-copper(II)). The result is a chiral J-aggregate. Upon addition of (R)-BINOL the helicity of the helical polymer template is inverted. The supramolecular chirality of the H_4TPPS^{2-} homoaggregate, however, remains unchanged. This is another example of a chiral memory effect in a supramolecular assembly.

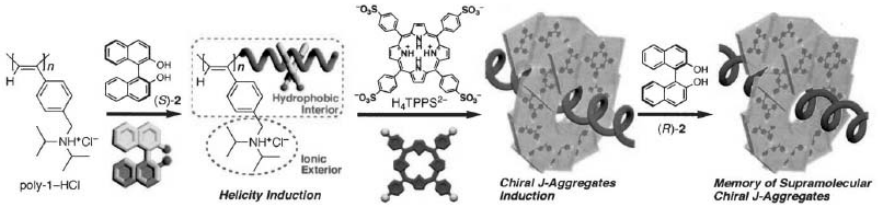

Scheme 1.21: The assembly of a chiral polymer template which is used to induce chirality in the assembly of tetraanionic porphyrins. After chiral inversion of the template the porphyrin assembly retains the same helicity. From ref 89.

Utilizing nucleotide appended oligo(p-phenylenevinylene) (OPV), molecular recognition-driven self-assembly was induced through complementary hydrogen bonding.[90] This resulted in the formation of right-handed helical stacks which closely resemble the DNA double helix in water. The oligodeocyadenylic acids are known to form right-handed helices through the formation of A-T base pairing. The OPV derivative, when mixed with one or two equivalents of the adenylic acid, formed homo or binary self-assemblies (Scheme 1.22) following the helical conformation of the oligodeocyadenylic acid template.

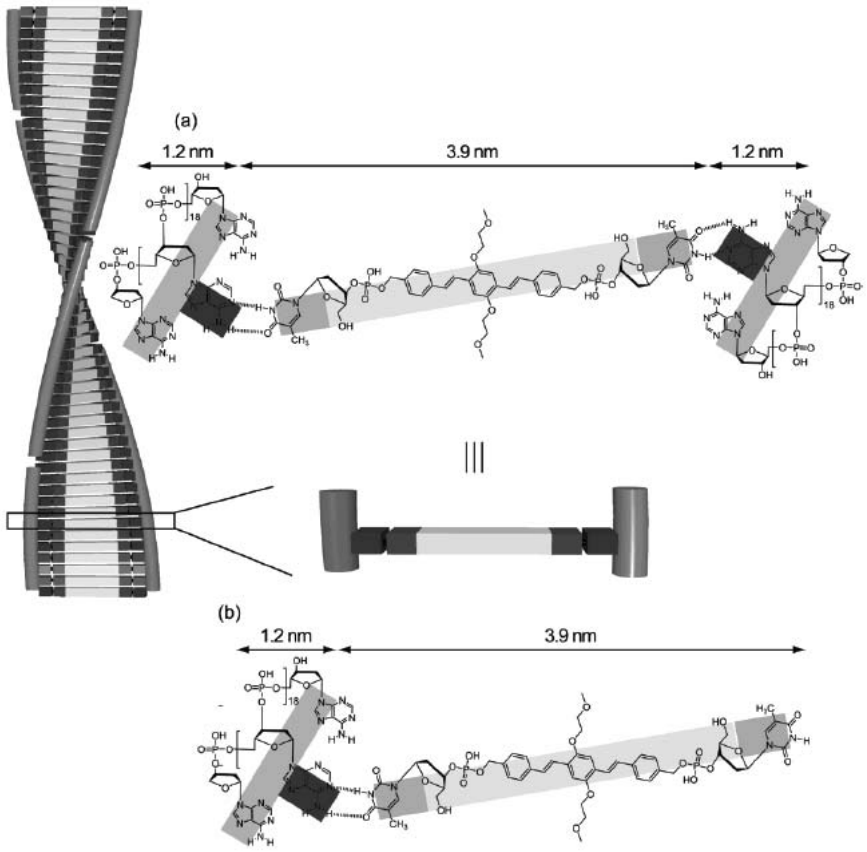

Scheme 1.22: Structures generated by the self-assembly of (a) 1:1 bola to 20-meric adenylic acid (b) 2:1 bola to 20-meric adenylic acid. Possible elongation mechanisms for the helical stacks. From ref 90.

1.5 2D chirality

The examples of chiral induction and amplification presented thus far have been in the liquid state. However, chirality can also originate at the liquid-solid interface. Indeed achiral molecules can assemble in a 2D chiral organization on various surfaces, with HOPG being the most extensively studied. This is a relatively new field of chiral amplification referred to as 2D chirality.[91,92]

Prochiral molecules, such as 4-[trans-2-(pyrid-4-yl-vinyl)] benzoic acid (PVBA), assemble on a Cu (1 0 0) in a chiral manner.[93] The molecules (when the coverage remains below a critical value of 0.05 PVBA molecules per Cu atom) when confined to a surface will assemble into two enatiomeric forms (λ- and δ-PVBA, Figure 1.30). Mesoscopic chiral resolution occurs which manifests itself through the formation of two enantiomorphous domains. Above the critical coverage the mesoscopic resolution is lost and both λ- and δ-PVBA molecules are assembled together forming one homogeneous phase.

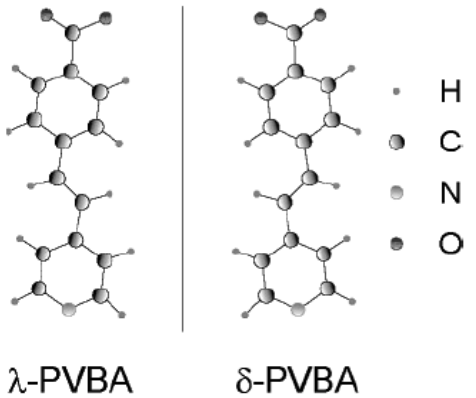

Figure 1.30: The two forms in which the prochiral PVBA is physisorbed to the surface in two enantiomeric orientations.

Assemblies formed by achiral oligo(*p*-phenylene vinylene)(OPV) derivatives (Figure 1.31) on graphite are of particular interest.[94,95] These achiral molecules assemble to form extensive domains of chiral rosettes on surfaces (Figure 1.32). The windmill blades appear as bright rods in the STM images. These correspond to the conjugated backbone of OPV. In many cases the phenyl moieties are fully resolved. The dark areas correspond to the dodecyloxy chains. One rosette is constructed from six OPV molecules, and the rosettes show the same direction of propagation and rotation. Depending on the length of the achiral OPV (**OPV1** or **OPV2**) being used the direction of rotation can be inverted. The resulting pattern is a result of hydrogen-bonding, inter-chain van der Waals interactions and the free volume. This is mainly affected by the backbone to alkyl chain length ratio.

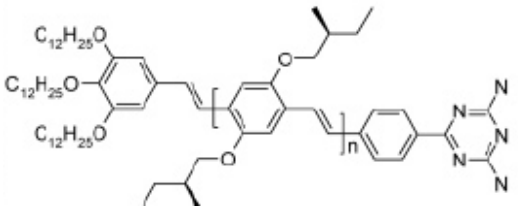

Figure 1.31: The structure of OPV. **OPV1** n=1; **OPV2** n=2; **A-OPV4T** n=2 and there are no methyl groups on the side chains (achiral)

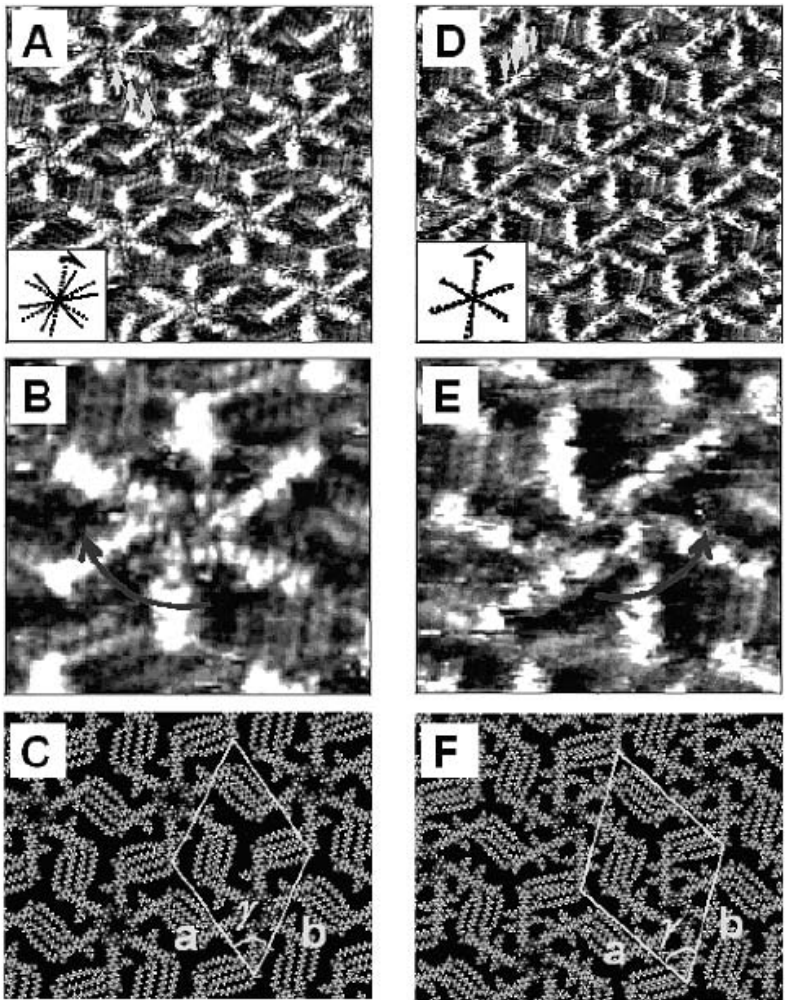

Figure 1.32: STM image of a monolayer of OPV physisorbed at the 1-phenyloctane/graphite interface (A) **OPV1** (image size: 14.4 - 14.4 nm^2) and (D) **OPV2** (image size: 18.4 - 18.4 nm^2). Yellow arrows point to the phenyl rings of the OPV backbone. The inset shows the propagation direction of rosette rows (solid line) and the main symmetry axes of graphite (dashed line). (B, E) A magnification of an **OPV1** and **OPV2** rosette. The red arrow indicates the "rotation direction" of the windmill. (C, F) Tentative model of the unit cell of **OPV1** and **OPV2** (A unit cell is indicated in yellow).

Rosette helicity of **A-OPV4T** (Figure 1.31) can be influenced depending on the type of solvent used during deposition.[96] Chiral solvents, such as (R)-1-phenyl-1-octanol and (S)-1-phenyl-1-octanol, generate rosettes of opposite helicities. The (S)- enantiomer generates clockwise-rotating rosettes while (R)- enantiomer generates mostly counterclockwise rosettes. Interestingly, the rosettes at the solvent/HOPG interface align with time (Figure 1.33). Thus an irregular hexamer forms a rosette in a period of 142 seconds.

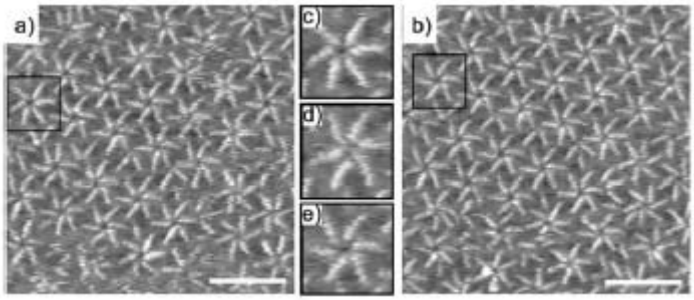

Figure 1.33. a) First and b) last frame of a sequence of STM images of an **A-OPV4T** (Figure 1.31) monolayer at the (R)-1-phenyl-1-octanol–HOPG interface recorded at the same area. The time gap between the frames is 142 seconds. The scale bar is 10 nm. The area of interest is indicated by the black square. An enlargement of that area is shown in c) after 0 s, in d) after 95 s, and in e) after 142 s. Over time, the irregular cyclic hexamer indicated in the square evolves into a CCW rosette.

Racemic heptahelicenes generate two types of domains on a Cu (1 1 1) surface. Each enantiomer forms its own domain which is either right- or left-handed in nature.[97] These domains (when the heptahelicenes are racemic) are present in equal ratios. However, upon the use of miniscule enantiomeric excesses (0.08 % e.e.) of the M helix heptahelicene homochirality is induced (Figure 1.34).

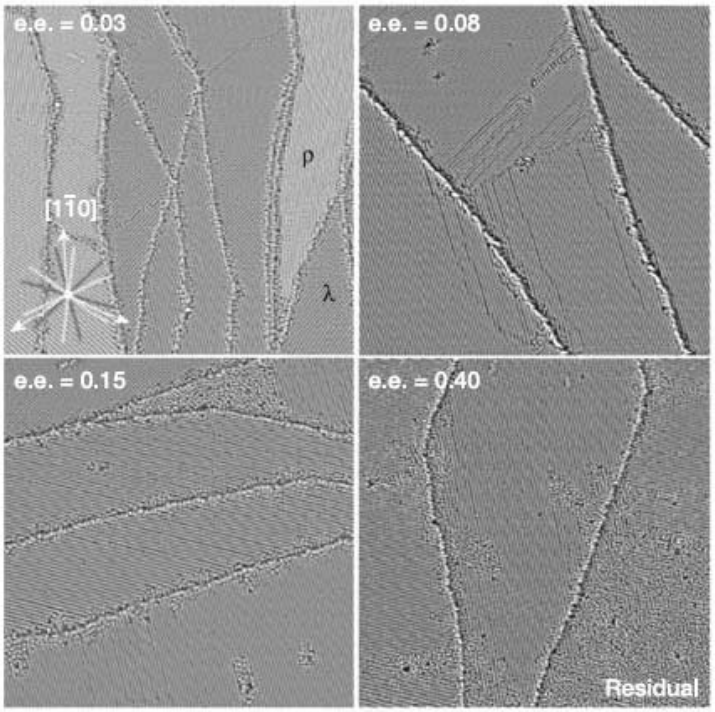

Figure 1.34: STM images demonstrating effect of increasing the enantiomeric excess on the emergence of homochirality. At e.e. = 0.08, the ρ domains have completely disappeared and only λ domains remain. Remaining areas increase upon higher enantiomer excess.

This homochirality is most probably induced by a boundary-driven amplification mechanism. The boundaries which form between the ρ and λ domains are energetically unfavorable. The enantiomeric excess results in a chiral bias at these domain boundaries thereby dictating the preferred orientation of the molecules in the domains (Scheme 1.23). Therefore the sign of the enantiomer that is in excess determines the handedness of the domains.

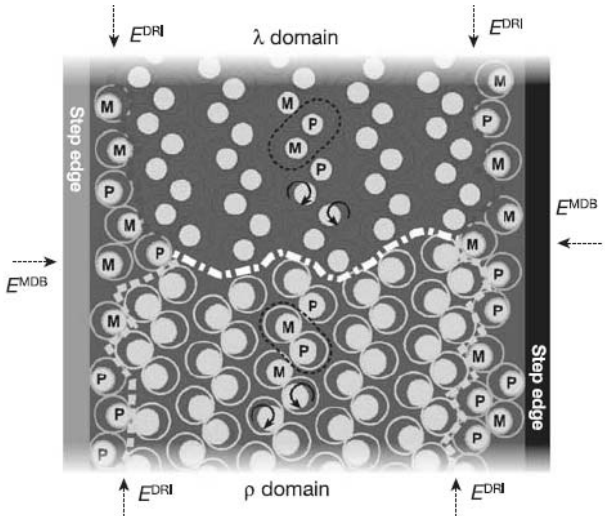

Scheme 1.23: Schematic representation of the chiral amplification mechanism. The dashed lines (E^{MDB}) represents the ρ and λ domain boundary which is energetically unfavorable. The enantiomeric excess at the edges (E^{DRI}) results in a chiral bias which then favors one domain orientation. From ref 97.

1.6 Aim of research in this thesis

In this chapter it was highlighted that it is possible to amplify chirality from the molecular to the supramolecular level in various ways. All of the research presented in this thesis centers around chiral amplification at different hierarchical levels in particular by using an enantiomerically pure molecular motor, to induce chirality on a larger scale.

In **Chapter 2** various structurally different molecular motors were used as chiral dopants in liquid crystalline phases to determine the sensitivity of the system towards minor changes in dopant structure.

In **Chapter 3** the molecular motor doped liquid crystalline system was studied further to determine why rotational reorganization of the liquid crystalline phase is observed upon irradiation.

Chapter 4 focuses on lyotropic liquid crystalline systems. In this case molecular motor functionalized polymer chains are used as the liquid crystalline mesogen. Chirality is thus transferred from the motor functionality to the polymeric chain and throughout the liquid crystalline phase.

Chapter 5 focuses on the behavior of these polymeric systems on a surface. The presence of the molecular motor or chiroptical switch moiety influences the type of aggregate formed upon deposition on a surface. Toroidal structures are observed for the functionalized systems.

In **Chapter 6** the first water-soluble molecular motor (which is still addressable with UV irradiation) is reported. The molecules assemble into micellar structures. Depending on the configuration of the molecular motor (stable vs. unstable), a different CMC (critical micelle concentration) is observed.

1.7 References

1. Sato I., Urabe H., Ishiguro S., Shibata T. & Soai K. Amplification of Chirality from Extremely Low to Greater than 99.5% *ee* by Asymmetric Autocatalysis. *Angew. Chem. Int. Ed.* **42**, 315-317 (2003).

2. Soai K. & Kawasaki T. Discovery of Asymmetric Autocatalysis with Amplification of Chirality and Its Implication in Chiral Homogeneity of Biomolecules. *Chirality* **18**, 469-478 (2006).

3. Blackmond D.G. Mechanistic study of the Soai autocatalytic reaction informed by kinetic analysis. *Tetrahedron: Asymmetry* 584-589 (2006).

4. Feringa B.L & van Delden R.A. Absolute asymmetric synthesis: The origin, control and amplification of chirality *Angew. Chem. Int. Ed.* **38**, 3418-3438 (1999)

5. Sato I., Kadowaki K., Urabe H., Jung J.H., Ono Y. Shinkai S. & Soai K. Highly enantioselective synthesis of organic compound using right- and left-handed helical silica. *Tet. Lett.* **44**, 721-724 (2003).

6. González-Álvarez A., Alfonso I. & Gotor V. Highly diastereoselective amplification from a dynamic combinatorial library of macrocyclic oligoimines. *Chem. Comm.* 2224-2226 (2006).

7. Huck N.P.M., Jager V.F., de Lang B. & Feringa B.L. Dynamic control and amplification of molecular chirality by circular polarized light. *Science* **273**, 1686-1688 (1996).

8. Maeda K. & Yashima E. Dynamic Helical Structures: Detection and Amplification of Chirality. *Top. Curr. Chem.* **265**, 47-88 (2006).

9. Reinitzer F. *Monatshefte* **9**, 421 (1888).

10. Lehmann O. *Z. Phys. Chem.* **4**, 462 (1889).

11. Shiyanovskii S.V. Lavrentovich O.D., Schneider T., Ishikawa T., Smalyukh I.I., Woolverton C.J., Niehaus G.D. & Doane K.J. Lyotropic Chromonic Liquid Crystals for Biological Sensing Applications. *Mol. Cryst. Liq. Cryst.* **434**, 587-598 (2005).

12. Pomerantz W.C., Abbott N.L., Gellman S.H. Lyotropic Liquid Crystals from Designed Helical β- Peptides. *J. Am. Chem. Soc.* **128**, 8730-8731(2006).

13. Tombolato F., Ferrarini A.& Grelet E. Chiral Nematic Phase of Suspensions of Rod-like Viruses: Left-Handed Helicity from a Right-Handed Molecular Helix. *Phys. Rev. Lett.* **96**, 258302 (2006).

14. Barry E., Hensel Z. Dogic Z., Shribak M. & Oldenbourg R. Entropy-Driven Formation of a Chiral Liquid-Crystalline Phase of Helical Filaments. *Phys. Rev. Lett.* **96**, 018305 (2006).

15. Metrangolo P., Präsang C., Resnati G., Liantonio R., Whotwood A.C. & Bruce D.W. Fluorinated liquid crystals formed by halogen bonding. *Chem. Comm.* 3290-3292 (2006).

16. Acimis M. & Karaman E.B. Comparison of helical twisting powers of fluorinated amphiphilic enantiomers with their hydrogenated counterparts. *J. Colloid Interf. Sci.* **300**, 1-6 (2006).

17. Eelkema R. & Feringa B.L. Amplification of Chirality in liquid crystals. *Org. Biomol. Chem.* **4**, 3729-3745 (2006).

18. Gottarelli G., Hibert M., Samori B., Solladie G., Spada G.P. & Zimmerman R. Induction of the cholesteric mesophase in nematic liquid crystals: mechanism and application to the determination of bridged biaryl configurations *J. Am. Chem. Soc.* **105**, 7318-7321 (1983).

19. Gottarelli G., Spada G., Bartsch R., Solladie G. & Zimmerman R.G. *J. Org. Chem.* **51**, 585 (1986).

20. Kuball H.G., Weiss B., Beck A.K. & Seebach D. *Helv. Chim. Acta* **80**, 2507 (1997).

21. Seed A.J., Walsh M.E., Doane J.W. & Khan A. *Mol. Cryst. Liq. Cryst.* **410**, 201 (2004).

22. Hoshino N., Matsuoka T., Okatmoto K. & Yamagishi A. *J. Am. Chem. Soc.* **125**, 1718 (2003).

23. Yoshida J., Sato H., Yamagishi A. & Hoshino N. *J. Am. Chem. Soc.* **127**, 8453 (2005).

24. Drake A.F., Gottarelli G. & Spada G.P. *Chem. Phys. Lett.* **110**, 630 (1984).

25. Braun M., Hahn A., Engelmann M. Fleischer R., Frank W., Kryschi C., Haremza S., Kürschner K. & Parker R. Bis-Chelated Imine-Alkoxytitanium Complexes: Novel Chiral Dopants with High Helical Twisting Power in Liquid Crystals. *Chem. Eur. J.* **11**, 3405-3412 (2005).

26. Eelkema R. & Feringa B.L. Phosphoric Acids as Amplifiers of Molecular Chirality in Liquid Crystalline Media. *Org. Lett.* **8**, 1331-1334(2006).

27. Eelkema R. & Feringa B.L. Macroscopic Expression of Chirality of Amino Alcohols by a Double Amplification Mechanism in Liquid Crystalline Media. *J. Am. Chem. Soc.* **127**, 13480-13481 (2005).

28. Ruslim C. & Ichimura K. *Adv. Mat.* **13**, 37 (2001).

29. Ruslim C. & Ichimura K. *J. Mater. Chem.* **12**, 3377 (2002).

30. Pieraccini S., Gottarelli G., Labruto R., Masiero S., Pandoli O. & Spada G.P. The Control of the Cholesteric Pitch by Some Azo Photochemical Chiral switches. *Chem. Eur. J.* **10**, 5632-5639 (2004).

31. Pieraccini S., Masiero S., Spada G.P. & Gottarelli G. A new axially-chiral photochemical switch. *Chem. Comm.* 598-599 (2003).

32. Nematic LC phase 1052 is a mixture with a structure similar to ZLI-389. The exact composition and phase transition temperatures are not available.

33. Feringa B.L., Huck N.P.M. & Doren H.A. *J. Am. Chem. Soc.* **117**, 9929 (1995).

34. Koumura N., Zijlstra R.W.J., van Delden R.A., Harada N. & Feringa B.L. *Nature* **401**, 152 (1999).

35. Eelkema R. & Feringa B.L. Reversible Full-Range Color Control of a CHolesteric Liquid-Crystalline Film by using a Molecular Motor. *Chem. Asian J.* **1**, 367-369 (2006).

36. Eelkema R., van Delden R.A. & Feringa B.L. *Angew. Chem. Int. Ed.* **43**, 5013 (2004).

37. Eelkema R., Pollard M.M., Vicario J., Katsonis N., Ramon B.S., Bastiaansen C.W.M., Broer D.J. & Feringa B.L. Molecular machines: Nanonmotor rotates microscale objects. *Nature* **440**, 163 (2006).

38. Eelkema R., Pollard M.M., Katsonis N., Vicario J., Broer D.J. & Feringa B.L Rotational Reorganization of Doped Cholesteric Liquid Crystalline Films. *J. Am. Chem. Soc.* **128**, 14398-14407 (2006). Marangoni…

39. Frigoli M. & Mehl G.H. Room Temperature Nematic Photoswitchable Liquid Crystals - Molecular Modularisation of Functional Elements. *Eur. J. Org. Chem.* 636-642 (2004).

40. Abraham S., Mallia A., Vijayaraghavan Ratheesh K., Tamaoki N. & Das S. Reversible Thermal Photochemical Switching of Liquid Crystalline Phases and Luminescence in Diphenylbutadiene-based Mesogenic Dimers. *J. Am. Chem.. Soc.* **128**, 7692-7698(2006)

41. Ishi-i T., Kuwahara R., Takata A., Jeong Y., Sakurai K. & Mataka S. An Enantiomeric Nanoscale Architecture Obtained from a Pseudoenantiomeric Aggregate: Covalent Fixation of Helical Chirality Formed in Self-Assembled Discotic Triazine Triamides by Chiral Amplification. *Chem. Eur. J.* **12**, 763-776 (2006).

42. Jeong K., Knapp B.S., Ge J.J., Jin S., Graham M.J., Harris F.W. & Cheng S.Z.D. Origin of Self-Assembled Helical Supramolecular Structures in Achiral C6 Biphenyl Carboxylic Acid compounds. *Chem. Mater.* **18**, 680-690 (2006).

43. Kato T., Matsuoka T., Nishii M., Kamikawa Y., Kanie K., Nishimura T., Yashima E. & Ujiie S. Supramolecular Chirality of Thermptropic Liquid-Crystalline Folic Acid Derivatives. *Angew. Chem. Int. Ed.* **43**, 1969-1972 (2004).

44. Kamikawa Y., Nishii M. & Kato T. Self-Assembly of Folic Acid Derivatives: Induction of Supramolecular Chirality by Hierarchical Chiral Structures. *Chem. Eur. J.* **10**, 5942-5951 (2004).

45. Nagai K., Maeda K., Takeyama Y., Sakajiri K. & Yashima E. Helicity Induction in Charged Poly(phenylacetylene)s Bearing Various Acid Functional Groups in Water and Its Mechanism. *Macromolecules* **38**, 5444-5451 (2005).

46. Nagai K., Sakajiri K., Maeda K., Okoshi K., Sato T. & Yashima E. Hierarchical Amplification of Macromolecular Helicity in a Lyotropic Liquid Crystalline Charged Poly(phenylacetylene) by Nonracemic Dopants in Water and Its Helical Structure. *Macromolecules* **39**, 5371-5380 (2006).

47. Graham T. *Phil. Trans. Roy. Soc.* **151**, 183 (1861).

48. Flory P.J. *Discuss Faraday Soc.* **57**, 7 (1974).

49. Waguespack Y.Y., Banerjee S., Ramannair P., Irvin G.C., John V.T. & McPherson G.L. An organogel Formed by the Addition of Selected Dihydroxynaphthalenes to AOT Inverse Micelles. *Langmuir* **16**, 3036-3041 (2000).

50. Willemen H.M., Vermonden T., Marcelis A.T.M. & Südholter E.J.R. *Langmuir* **18**, 7102-7106 (2002).

51. Friggeri A., Gronwald O., van Bommel K.J.C., Shinkai S. & Reinhoudt D.N. *J. Am. Chem. Soc.* **124**, 10754-10758 (2002).

52. Terech P. & Weiss R.G. *Chem. Rev.* **97**, 3133-3159 (1997).

53. Brizard A., Oda R. & Huc I. *Low Molecular Mass Gelators*., pp. 167-218 (Springer- Verlag, Berlin Heidelberg, 2005).

54. Wang C., Zhang D. & Zhu D. A Chiral Low-Molecular-Weight Gelator Based on Binaphthalene with Two Urea Moieties: Modulation of CD Spectrum after Gel Formation. *Langmuir* **23**, 1478-1482 (2006).

55. Messmore B.W., Sukerkar P.A. & Stupp S.I. Mirror Image Nanostructures. *J. Am. Chem. Soc.* **127**, 7992-7993 (2005).

56. Huang B., Hirst A.R., Smith D.K., Castelletto V. & Hamley I.W. A Direct Comparison of One- and Two-Component Dendritic Self-Assembled Materials: Elucidating Molecular Recognition Pathways. *J. Am. Chem. Soc.* **127**, 7130-7139 (2005).

57. Brunsveld L., Folmer J.B., Meijer E.W. & Sijbesma R.P. *Chem. Rev.* **101**, 4071-4097 (2001).

58. Partridge K.S., Smith D.K., Dykes G.M. & McGrail P.T. *Chem. Commun.* 319-320 (2001).

59. Sly J., Kasák P., Gomar-Nadal E., Rovira C., Górriz L., Thordarson P., Amabilino D.B., Rowan A.E. & Nolte R.J.M. Chiral Molecular tapes from novel tetra(thiafulvene-crown-ether)-substituted phthalocyanine building blocks. *Chem. Comm.* 1255-1257 (2004).

60. Haldar D., Jiang H., Leger J.-M. & Huc I. Interstrand Interactions between Side Chains in a Double-Helical Foldamer. *Angew. Chem. Int. Ed.* **45**, 5483-5486 (2006).

61. Engelkamp, S. Middelbeek and R. J. M. Nolte, *Science*, **284**, 785 (1999)

62. Iwaura R., Yoshida K., Masuda M., Ohnishi-Kameyama M., Yoshida M. & Shimizu T. Oligonucleotide-Templated Self-Assembly of Nulceotide Bolaamphiphiles: DNA-like Nanofibers Edged by a Double-Helical Arrangement of A-T Base Pairs. *Angew. Chem. Int. Ed.* **42**, 1009-1012 (2003).

63. van Bommel K.J.C., Friggeri A. & Shinkai S. Organic Templates for the Generation of Inorganic Materials. *Angew. Chem. Int. Ed.* **42**, 980-999 (2003).

64. Jung J.H., Ono Y. & Shinkai S. Sol-Gel Polycondensation in a Cyclohexane-Based Organogel System in Helical Silica: Creation of both Right- and Left-Handed Silica Structures by Helical Organogel Fibers. *Chem. Eur. J.* **6**, 4552-4557 (2000).

65. Li C., Hatano T., Takeuchi M. & Shinkai S. Polyaniline superstructures created by a templating effect of organogels. *Chem. Comm.* 2350-2351 (2004).

66. For information on LMWG see for instance: Terech P.& Weiss R.G. *Chem. Rev.* **97**, 3133-3159 (1997) or Molecular Gels: Materials with Self-

Assembled Fibrillar Networks (P. Terech, R.G. Weiss, Eds.), Springer, New York, 2005.

67. de Jong J.J.D., Lucas L.N., Kellogg R.M., van Esch J.H. & Feringa B.L. *Science* **304**, 278-281 (2004).

68. de Jong J.J.D., Tiemersma-Wegman T.D., van Esch J.H. & Feringa B.L. Dynamic Chiral Selection and Amplification Using Photoresponsive Organogelators. *J. Am. Chem. Soc.* **127**, 13804-13805 (2005).

69. For examples of the sergeant soldier effect see for instance: Memoires and Switches, special issue, guest editor M.Irie, *Chem. Rev*. 100, (2000) or *Molecular Switches* (B.L. Feringa, Ed.) Wiley VCH, Weinheim 2001.

70. Elemans J.A.A.W., van Hameren R., Nolte R.J.M. & Rowan A.E. Molecular materials by Self-Assembly of Porphyrins, Phthalocyanines, and Perylenes. *Adv. Mat.* **18**, 1251-1266 (2006).

71. Lehn J.-M. *Supramolecular Chemistry: Concepts and perspectives*. VCH, Weinheim (1995).

72. Lehn J.-M. Toward Self-Organization and Complex Matter. *Science* **295**, 2400 (2002).

73. Whitesides G.M., Simanek E.E., Mathias J.P., Seto C.T., Chin D., Mammen M. & Gordon D.M. Noncovalent Synthesis: using Physical-Organic Chemistry to make Aggregates. *Acc. Chem. Res.* **28**, 37-44 (1995).

74. Fyfe M.C.T. & Stoddartt J.F. *Acc. Chem. Res.* **30**, 393 (1997).

75. Prins L.J., Reinhoudt D.N. & Timmerman P. The Cooperativity Concept. *Angew. Chem. Int. Ed.* **40**, 2382-2426 (2001).

76. Jacques J., Collet A. & Wilen S.H. *Enantiomers, Racemates, Resolutions*. Wiley, New York (1981).

77. a) Ribo J.M. & Crusats J. Chiral Sign Induction By Vortices During The Formation of Mesophases in Stirred Solutions. *Science* **292**, 1435-1436 (2001); b) Feringa B.L. Chemistry: A New Twist on Chirality, *Science*, **292**, 2021-2022 (2001)

78. There are very few examples of this type of amplification of chirality. In most instances the experiments have been irreproducible.

79. Prins L.J., Jolliffe K.A., Hulst R., Timmerman P. & Reinhoudt D.N. Control of Structural Isomerism in Noncovalent Hydrogen-Bonded Assemblies Using Peripheral Chiral Information. *J. Am. Chem. Soc.* **122**, 3617-3627 (2000).

80. Mateos-Timoneda M.A., Crego-Calama M. & Reinhoudt D.N. Amplification of Chirality in Hydrogen-Bonded Tetrarosette Helices. *Chem. Eur. J.* **12**, 2630-2638 (2006).

81. Prins L.J., Timmerman P. & Reinhoudt D.N. *J. Am. Chem. Soc.* **123**, 10153-10163 (2001).

82. Nakade H., Jordan B.J., Xu H., Han G., Srivastava S., Arvizo R.R., Cooke G. & Rotello V.M. Chiral Translation and Cooperative Self-Assembly of discrete Helical structures Using Molecular Recognition Dyads. *J. Am. Chem. Soc.* **128**, 14924-14929 (2006).

83. van Gorp J.J., Vekemans J.A.J.M., & Meijer E.W. C_3-Symmetrical Supramolecular Architectures: Fibres and Organic Gels from Discotic Trisamides and Trisureas *J.Am.Chem. Soc*. **124**, 14759-14769 (2002)

84. van Gestel J., Palmans A. R. A.,. Titulaer B, Vekemans J. A. J. M. & Meijer E. W., *J. Am. Chem. Soc*., **2005**, 127, 5490–5494

85. Bong D.T. & Ghadiri M.R. Self-Assembling Cyclic Peptide Cylindrs as Nuclei for Crystal Engineering. *Angew. Chem. Int. Ed.* **40**, 2163-2166 (2001). Ghadiri review

86. Balaban T.S., Linke-Schaetzel M., Bhise A.D., Vanthuyne N. & Roussel C. Green Self-Assembling Porphyrins and Chlorins as Mimics of the Natural Bacteriochlorophylls c, d, and e. *Eur. J. Org. Chem.* 3919-3930 (2004).

87. Berthier D., Buffeteau T., Léger J.-M., Oda R. & Huc I. From chiral counterions to twisted membranes. *J. Am. Chem. Soc.* **124**, 13486-13494 (2002).

88. Lauceri R. & Purrello R. Transfer, Memory and Amplification of Chirality in Porphyrin Aggregates. *Supramolecular Chemistry* **17**, 61-66 (2005).

89. Onouchi H., Miyagawa T., Morino K. & Yashima E Assisted Formation of Chiral Porphyrin Homoaggregates by an Induced Helical Poly(phenylacetylene) Template and Their Chiral Memory. *Angew. Chem. Int. Ed.* **45**, 2381-2384 (2006).

90. Iwaura R., Hoeben F.J.M., Masuda M., Schenning A.P.H.J., Meijer E.W. & Shimizu T. Molecular-Level Helical Stack of a Nucleotide-Appended Oligo(p-phenylenevinylene) Directed by Supramolecular Self-Assembly with a Complementary Oligonucleotide as a template. *J. Am. Chem. Soc.* **128**, 13298-13304 (2006).

91. Ernst K-H. Supramolecular Surface Chirality. *Top. Curr. Chem*. **265**, 209-252 (Springer-Verlag, Berlin Heidelberg, 2006).

92. Katsonis N. Lacaze E. & Feringa B.L. Molecular chirality at fluid/solid interfaces: expression of asymmetry in self-organized monolayers *J. Mater. Chem*. **18**, 2065-2073 (2008).

93. Vidal F., Delvigne E., Stepanow S., Lin N., Barth J.V. & Kern K. Chiral Phase Transition in Two-Dimensional Supramolecular Assemblies of Prochiral Molecules. *J. Am. Chem. Soc.* **127**, 10101-10106 (2005).

94. Miura A., Jonkheijm P., de Feyter S., Schenning A.P.H.J., Meijer E.W. & de Schryver F.C. 2D Self-Assembly of Oligo(p-phenylene vinylene) Derivatives: From Dimers to Chiral Rosettes. *Small* **1**, 131-137 (2005).

95. de Feyter S. & de Schryver F.C. Self-Assembly at the Liquid/Solid Interface: STM Reveals. *J. Phys. Chem. B.* **109**, 4290-4302 (2005).

96. Katsonis N.,Xu H., Haak R.M., Kudernac T., Tomović Ž., George S., van der Auweraer M., Schenning A.P.H.J., Meijer E.W., Feringa B.L. & de Feyter S. Emerging Solvent-Induced Homochirality by the Confinement of Achiral Molecules Against a Solid Surface. *Angew. Chem. Int. ed*. **47**, 4997-5001 (2008)

97. Fasel R. & Ernst K-H Amplification of Chirality in Two-Dimensional Enantiomorphous Lattices. *Nature* **439**, 449-452 (2006).

Chapter 2

Helical Twisting Powers of Molecular Motors

*It has been previously observed that chiral liquid crystalline phases can be generated upon the addition of enantiopure molecular motors to achiral mesogens. In this chapter the effect of small structural changes of the dopant structure on the helical induction is studied. The comparative study suggests that the magnitude of the Fjord angle is crucial to the helical twisting power. There appears to be an optimum; of the molecular motors measured in this study the phenyl substituent (**2.2**) yielded the highest HTP (93 μm^{-1}).*

2.1 Liquid crystals

In 1888 a botanist named Reitzner discovered that cholesterol benzoate had two melting points.[1] A theory on the origin of this second melting point was first developed by the physicist Lehmann.[2] Further studies led to the discovery that these materials with two melting points, reflected singularly polarized light and had the ability to rotate the polarization direction of light. Subsequent research showed that this phenomenon could not only be observed for cholesterol derivatives but also for other natural compounds such as myelin. The term cholesteric liquid crystals, was first suggested by the physicist Georges Friedel in 1922. For the first eighty years after their discovery these materials were purely of scientific interest.[3] Only after materials, which were liquid crystalline (phase between the two melting points) at room temperature were discovered, their popularity increased.[4]

2.1.1 Introduction

This new liquid crystalline (LC) phase is now often referred to as the "fourth state of matter". Mesogens (liquid crystal molecules) have weak anisotropic interactions which can cause either positional or directional orientation. Though the degree of organization is less than is the case for a crystalline system, its ordering is significantly higher than that in a liquid. Therefore liquid crystals tend to be slightly opaque and slightly viscous to highly viscous materials. As a consequence of the high orientational and dynamic nature of liquid crystals these systems are susceptible to external stimuli such as magnetic and electric fields and temperature.[5] Also small chiral additives can have a large impact on the type of liquid crystalline phase that is formed. This is why the field of research of LCs as biological sensors is growing rapidly.[6]

Liquid crystalline systems can be generated from organic molecules (lyotropic or thermotropic) or from a mixture of organic and inorganic molecules (metallotropic)[7]. In this thesis we focus on the organic molecule based LC systems. Thermotropic LCs consist of mesogenic molecules which, within a certain temperature range, generate an LC phase. In the case of lyotropic systems[†] a solvent is required as well as a certain temperature range to generate an LC phase. In this chapter we focus on thermotropic LC systems. There are two main groups of liquid crystalline phases formed depending on the shape of the mesogens: discotic and calamitic. There are also other phases possible such as blue phases.[8] Discotic phases are generated by disc-like molecules (Scheme 2.1). This phase shows positional ordering. Rigid, rod-like mesogens form calamitic phases.[9] The calamitic phases can be subdivided into two categories: the smectic and nematic phases. In the nematic phase there is directional

[†] For more details on lyotropic LC systems; see chapter 4 of this thesis

ordering along one director. In the smectic phase there is not only directional order, but there is an added positional order as these liquid crystalline systems are ordered in layers (schemes 2.2).

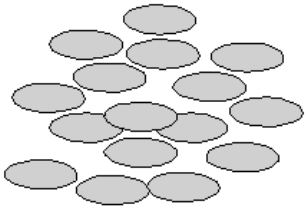

Scheme 2.1. A schematic representation of a discotic phase.

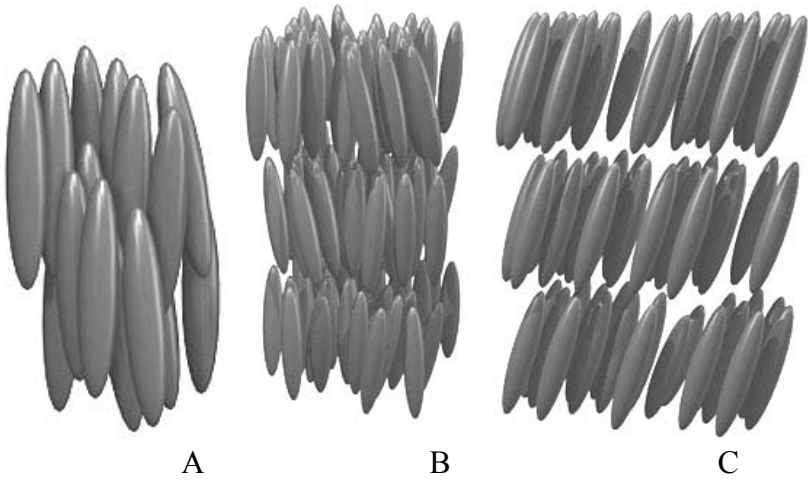

Scheme 2.2: A schematic representation of the calamitic phases: A) nematic phase, B) smectic A phase, C) smectic C phase[10]. The rods represent the local direction of the director.

Depending on the type of surface upon which the liquid crystalline material is deposited different features will appear. This is due to the different interactions which are possible between the substrate and the mesogen. This will be dealt with in detail in chapter 3.

In this study we focus on rod-like achiral mesogens which have a high anisotropy and therefore align in one direction (along the director). These form the aforementioned nematic phases.[5]

2.1.2 Birefringence

Mesogenic phases have an alignment order (vide supra, Scheme 2.2). Therefore, depending on the direction of a measurement, as one direction will correspond to the alignment of the phase while another will not, the

properties will vary accordingly. This anisotropy of the molecules causes such phenomena as birefringence. This means that the molecules have two indices of refraction. Light polarized parallel to the director has a different index of refraction than that polarized perpendicularly to the director.
When light enters a nematic liquid crystalline phase the light will be split into two components. These are referred to as the fast (ordinary ray, denoted o in Scheme 2.3) and slow (extraordinary ray, denoted e in Scheme 2.3) component as these rays travel at different velocities through the sample (Scheme 2.3). As a result the light is split into two components which are out of phase with each other. As the rays leave the sample they recombine. The polarization state has changed owing to this phase difference between the waves.[11]

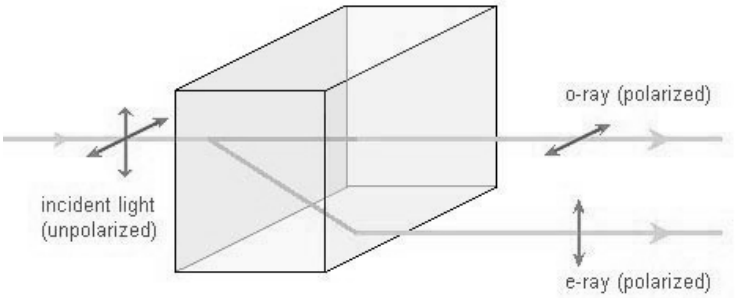

Scheme 2.3 Depiction of the two components, the ordinary and extraordinary ray into which light passing through an LC phase will be split. Adapted from ref 10.

The birefringence of a material is also dependent on the thickness of the sample as the shift (phase difference between the o and e waves) accumulates as it propagates through the sample. As a result any polarization state can be obtained with the right birefringence and thickness of the sample.

The birefringent nature of a liquid crystal sample causes the incoming linearly polarized light of a microscope to become elliptically polarized. When this elliptically polarized ray reaches the second polarizer (at a 90º degree angle with respect to the first polarizer), there is now a component that can pass through and the region appears bright. If the sample is very thin, the ray components (o and e) do not get very far out of phase. However, in the case of thicker samples, large differences are possible. For example, if the phase difference is equal to 360 degrees, the wave returns to its original polarization state. This is blocked by the second polarizer. The size of the phase shift determines the intensity of the transmitted light. However, if the first polarizers transmission axis is parallel to either of the ray components, no change in the polarization state occurs (no elliptical polarization). Thus there is no component that can pass through the second polarizer. As a result these regions will appear dark under the polarized microscope.

Owing to the fact that the birefringence and length (of the light pathway) are not constant over the entire liquid crystalline sample some areas will appear light and others appear dark. The light and dark areas denote regions of different director orientation, birefringence, and thickness. As the birefringence is highly dependent on the anisotropy of the mesogens this phenomenon is highly temperature-dependent. Upon reaching the nematic to isotropic phase transition all birefringence disappears.

2.1.3 Cholesteric phases

The cholesteric or chiral nematic phase[12] can be generated either from a chiral nematic mesogenic molecule or upon the addition of an enantiomerically pure, or enantio-enriched, chiral dopant to an achiral mesogen.[13] As mentioned previously the nematic phase has directional ordering along one specific director. In the case of a cholesteric phase, the mesogens show a twist along the director, generating a helical ordering at the macroscopic level (Scheme 2.4). The axis of the helical organization is perpendicular to the director. A variety of chiral dopant molecules have been used to induce this helicity among various mesogens, of which the TADDOL derivatives have proved to be some of the most efficient.[14] The length of a 360 degree turn along the axis of the helical organization is referred to as the pitch. This helical supramolecular structure is responsible for many of its unique optical properties such as selective reflection of circularly polarized light, high optical rotatory power, circular dichroism and electro-optic effects.[15]

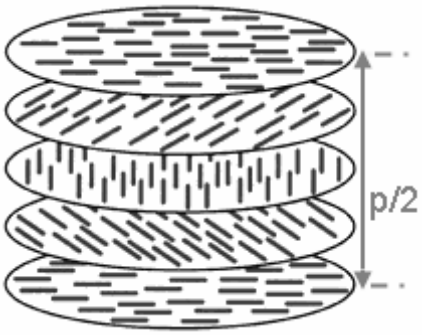

Scheme 2.4. Schematic representation of the cholesteric phase. The rods represent the director orientation throughout the phase. The length for a 360 degree rotation in the director is called the pitch (p). Adapted from ref 23

An incident unpolarized light beam parallel to the helix axis of the cholesteric phase is split into two opposite circularly polarized components. One component is transmitted whereas the other is reflected. Both the transmitted and reflected light is circularly polarized by the cholesteric

phase. The reflected light will be polarized in agreement with the screw sense of the helical orientation of the cholesteric phase. The transmitted light will have the opposite polarization (Scheme 2.5). If the pitch length is in the order of magnitude of a specific wavelength within the visible region, this wavelength will be reflected and this is responsible for the specific reflection of a particular color of light. Cholesteric LC phases therefore not only reflect but transmit light as well. Depending on the type of wavelength being studied and the exact make-up of the mesogen and chiral dopant, some of the wavelengths will be partially absorbed. Unlike conventional color filters, a cholesteric film combines several optical properties in one layer: it is not only a filter but also a reflector and a polarizer. However, the range of pitches possible in the visible range is limited (most pitches are too small). The reflected light is circularly polarized with the same handedness as the incident light, which is the exact opposite of a normal dielectric mirror that changes the handedness. For example, when looking at an LC phase with a left handed helicity, either of two things can happen with circularly polarized light. If the incident light is left handed in nature it will be reflected by the phase. If it is right handed in nature it will be transmitted without significant loss through the phase. Consequently, as only circularly polarized light with one handedness is reflected, the reflected intensity of ambient unpolarized light from a CLC is never greater than 50%.[16]

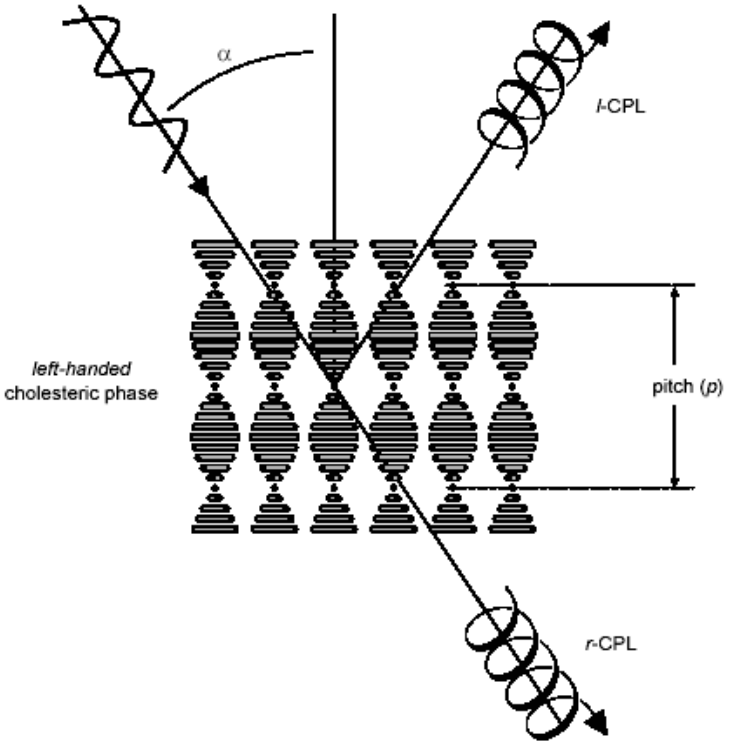

Scheme 2.5. Schematic representation of the optical properties of a cholesteric phase.

The most striking features are the exceptionally large optical rotatory power and the iridescent colors due to the selective reflection displayed by a uniformly oriented cholesteric phase, when the helix axis is perpendicular to the observation plane. The mean reflection wavelength λ_0 is related to the pitch p and the mean refraction index n by:

$$\lambda_0 = np \qquad 1$$

However, the color observed is dependent on the viewing angle. The angle dependency of the wavelength of the reflection is given by:

$$\lambda(\alpha) = n \cdot p \cdot \cos\left(\sin^{-1} \frac{\sin \alpha}{n} \right) \qquad 2$$

Where α is the angle of the incident ray relative to the normal, n is the average of the ordinary (n_0) and the extraordinary (n_e) refractive indices: $n = (n_0 + n_e)/2$. Equation 2 simplifies to equation 1 when $\alpha = 0^o$.[17] The spectral width of the reflection band $\Delta\lambda$ is defined as:

$$\Delta\lambda = p\Delta n \qquad 3$$

where $\Delta n = n_e - n_0$ is the birefringence.

2.1.4 Analysis

The cholesteric phase is characterized by the appearance of a fingerprint region. The pitch length of the helical orientation amongst the mesogen can be calculate using three different methods. As mentioned in the previous section, the pitch can be determined from the selective reflection of light. Distances can also be measured on the cholesteric fingerprint texture. The distance from crest to crest represents a 180° rotation, therefore half the pitch length. However, this method of determining the pitch is rather inaccurate in the presence of defects. It is also highly dependent on the alignment surface used. [18] Another commonly used method for the determination of the cholesteric pitch is the Grandjean-Cano method. This method involves a cholesteric sample aligned between a flat (usually polyimide-functionalized) glass slide (allowing the cholesteric helix to be oriented perpendicular to the surface) and a convex lens of known dimensions. Thus, the thickness of the LC layer is almost zero at the contact point with the lens and gradually increases towards the rims. The qualitative result will be the appearance of concentric circles (Figure 2.1) also known as concentric disclination lines. The pitch length is then calculated using formula 4.

$$p = \frac{(r_{n+1})^2 - (r_n)^2}{R_{lens}}, (n = 1,2,3) \qquad 4$$

where r is the radius of one of the concentric disclination lines shown in Figure 2.1, R_{lens} is the radius of the sphere from which the covex lens is cut.

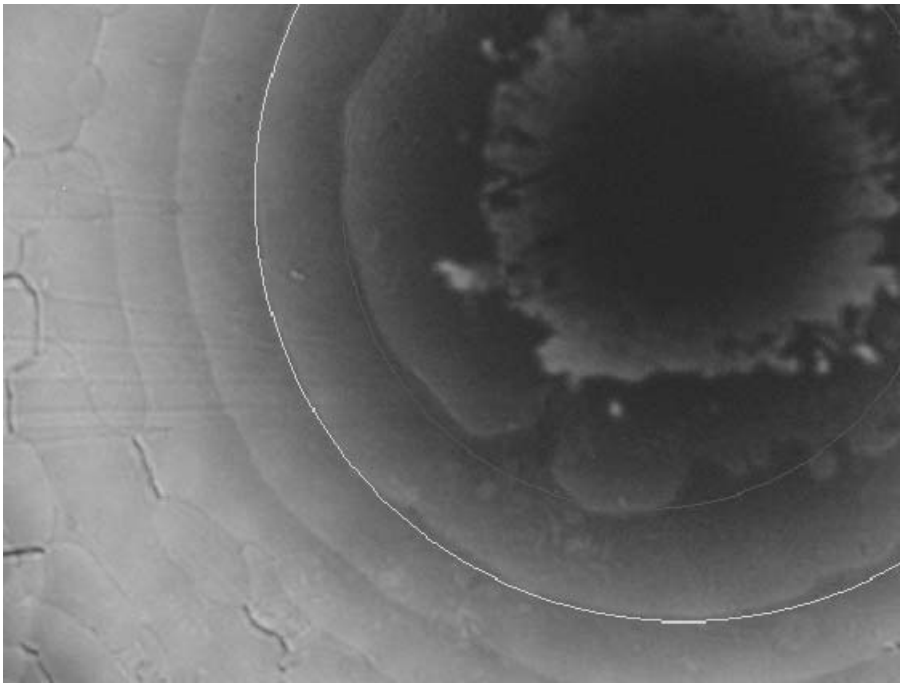

Figure 2.1: An optical micrograph of a cholesteric phase with a lens on top of it (using the Grandjean-Cano technique). The concentric circles (concentric disclinations) which are used for determination of the pitch length are not perfectly symmetric therefore measurements must be carried out in all directions from the center of the lens to minimize errors.

Once the pitch of the cholesteric helix is determined the helical twisting power (HTP) of the sample can be determined. When preparing a liquid crystalline system using an enantiomerically pure dopant the concentration of the dopant and the enantiomeric excess of the chiral dopant are necessary to determine the HTP. The HTP (β) can be determined using the following formula:

$$\beta = \frac{1}{p \cdot c \cdot ee} \qquad 5$$

Where ee is the enantiomeric excess which is given the value 1 for an enantiopure sample and c is the concentration of the dopant either in weight or moles. Usually molar HTP is calculated (β_M) using moles/moles rather than a weight percentage, allowing for better comparison. The concentration of the chiral dopant is usually between 1 and 10 wt%. The limit on added chiral dopant is 20 wt%. Outside this concentration range the relation above no longer holds, as phase separation and domain formation occur.

The HTP is a measure of how well a certain chiral dopant induces the chiral packing in the LC phase. The better the chiral induction, the lower the concentration that is required for generating a tighter pitch. In this chapter we will look at a variety of chiral molecules and their abilities to induce a cholesteric helix in a variety of liquid crystal mesogens.

2.2 Addressable chiral dopants

As liquid crystalline systems are finding more applications, both in the LCD industry, or as possible biological sensing and data storage devices, further developments are necessary.[19, 20] In the desire for further control of these doped liquid crystalline systems, switchable dopants have been used such as those by the groups of Gottarelli and Ichimura.[20] At the moment the unidirectional molecular motors developed in our group have proven to be among the most efficient switchable dopants for liquid crystal mesogens (LC).

In the previous literature the major origin for a high chiral induction of a certain dopant has been attributed to the structures of the dopant and mesogen being alike. Also in general rather twisted rigid chiral molecules have been successful dopants.[21] An interesting group of dopants are those that change configuration upon coming in contact with external stimuli (heat and light). The two configurations affect the LC phase differently resulting in an externally addressable LC phase.[22] It has been demonstrated that molecular motors (see Scheme 2.6 for rotational cycle) can be used as chiral dopants, and that upon irradiation of the sample the liquid crystalline phase undergoes a rotational reorganization which is observed as a rotational reorganization of the surface texture.[23] In fact, objects (such as glass rods) placed upon the phase can be rotated. In this study we look at the effect of using subtly different molecular motor dopants, and varying LC mesogens to ascertain which chiral structure would be the best dopant (the one which shows largest changes in the cholesteric phase between the helical twisting powers for the stable and unstable (isomers at PSS).

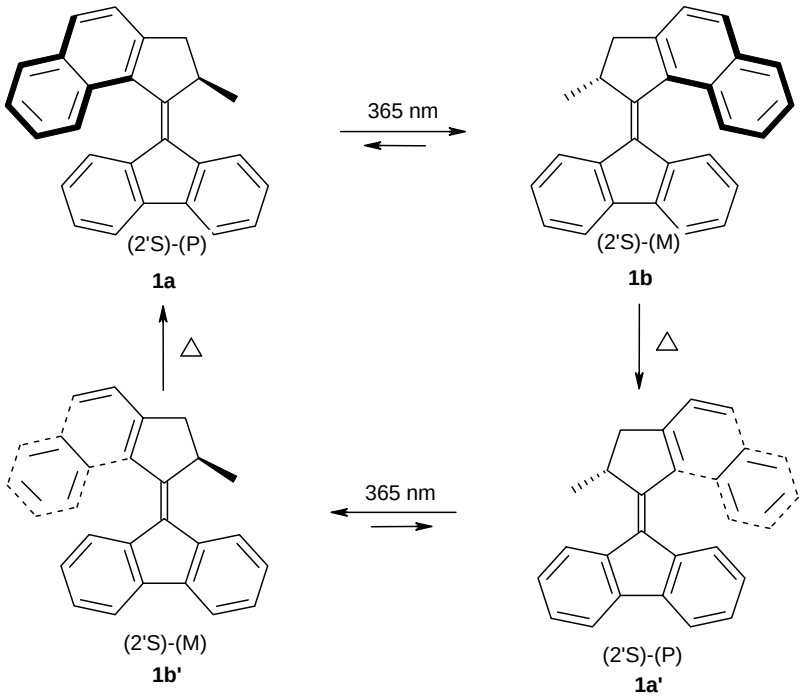

Scheme 2.6 Unidirectional rotational cycle of molecular motor **1.**

In the present study second generation molecular motors are used owing to better chiral induction.[26] The molecular motor **1** is an overcrowded alkene with a stereogenic center in its upper half and a symmetrical lower half. Through the use of sequential UV irradiation and thermal isomerization steps a rotational cycle (scheme 2.6) can be completed. In the first step the molecular motor **1a** (stable form) is irradiated with UV light which induces a photochemical isomerisation of the central double bond which is accompanied by an intrinsic helix inversion (from *P* to *M*) within the molecule. The methyl substituent has now been forced to move from the pseudo axial (**1a**) to the pseudo equatorial (**1b**) position. Owing to the strain associated with the pseudo equatorial orientation, the motor is referred to as the unstable form. Subsequently, to relieve strain a thermal helix inversion takes place and the stable form (**1a'**) is generated again. As a symmetrical lower half is being used both stable forms **1a** and **1a'** are equivalent. Under continuous irradiation the transformation sequence of stable – unstable – stable – unstable, etc. can be repeated continuously, thereby, allowing the molecules to act as a unidirectional rotary motor.

The main aim of this work is to study the influence of minor structural changes in the motor molecule on the ability to induce helical ordering amongst the mesogens; and thereby to attempt to clarify which interactions between the LC and the dopant are crucial for good helical induction. In the literature[21] many dopants have been used of varying designs (i.e.

TADDOLs, catalysts, azobenzenes), however no clear understanding exists of what is essential for the most effective interactions between the dopant and mesogen. The ability to predict the helical twisting power (HTP), through the use of molecular dynamics calculations, is a vastly growing field of research.[16,17] It is also not clear yet how sensitive the LC system is to slight changes in the structure of the dopant. Therefore, a screening of several, structurally different, molecular motors in various liquid crystals was carried out to determine the effect of changing only a substituent (Scheme 2.7), adding an electronically different atom (i.e. sulfur or oxygen) or changing the type of liquid crystal being used on the HTP.

2.3 Results

2.3.1 Varying the molecular motor dopant

The HTPs of the various motor dopants were measured using the Granjean-Cano method (section 2.1.4), before and after UV (λ=365 nm) irradiation until PSS was reached. All systems were irradiated for 15 min at which point the PSS was achieved (no further changes were observed). The data are summarized in Table 2.1. The enantiomers with *P* and *M* helicity show HTPs of the same magnitude but of different sign. However, upon irradiation the photoisomerization is not complete, instead the photostationary state is reached (PSS). The ratio between the stable and unstable motor isomers reached at the photostationary state is specific for each molecular motor. When testing several motor dopants where only the substituent R is altered (Scheme 1, **2.1**-**2.6**) within the same LC blend (E7, Scheme 2.8) it was observed that subtle changes in the motor molecule structure already had a large influence on the magnitude of the HTP.

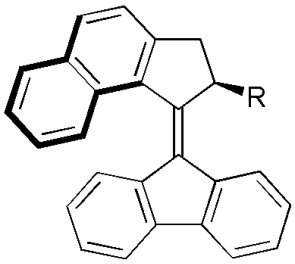

	R
2.1	methyl
2.2	phenyl
2.3	*p*-bromophenyl
2.4	*iso*-propyl
2.5	*tert*-butyl
2.6	methoxy

Scheme 2.7: General structure for the chiral dopants used. The structure depicted above represents the molecules with intrinsic *P* helicity.

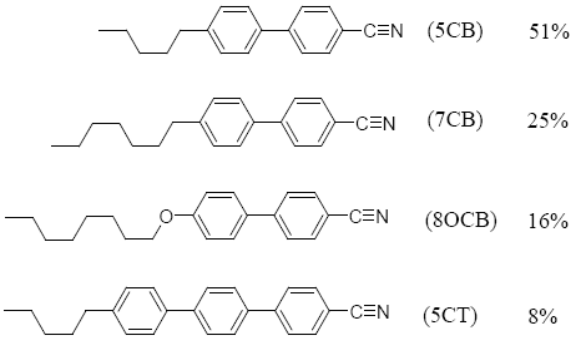

Scheme 2.8: The liquid crystal blend E7. Percentages of each compound are indicated.

For the series of motor molecules (**2.1** to **2.6**) in which the substituent R was systematically changed, a trend was observed, where, as the size (steric bulk) of the substituent increased, the HTP decreased (Table 2.1). This was observed going from the methyl (**2.1**) to the *iso*-propyl (**2.4**) to the *tert*-butyl (**2.5**) substituent. It was previously shown that when the substituent increases in size the thermal isomerization times decrease, the central double bond length increases and the torsional angle [‡] increases (for depiction of some alterations in angles depending on steric bulk at the chiral center in the motor molecules, see Scheme 2.9).[24] Though in principle the steric bulk of a phenyl substituent is larger than a methyl group, it had the highest HTP of all the molecular motors measured up till now. This is probably due to the fact that the phenyl moiety can turn away (sp^2-hybridized carbon instead of sp^3) and thereby appears to be smaller. Therefore it can be seen as the smallest substituent.

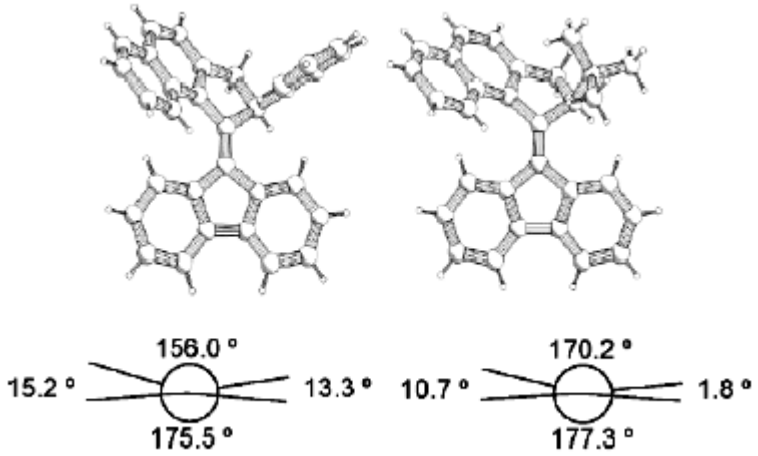

Scheme 2.9. X-ray structures of the (*S*) enantiomer of the molecular motors **2.2** (left) and **2.5** (right), shown with internal angles.

[‡] The torsional angle is between the naphthalene and fluorenone groups.

Another plausible explanation for the high HTP observed for **2.2** is that there is an added interaction possible between the molecular motor and the LC molecules through π-π stacking and that this might therefore increase the helical induction capabilities. The *p*-bromophenyl moiety (**2.3**) has a much lower HTP than the non-substituted phenyl moiety. The bromine atom is far larger than hydrogen; therefore sterically unfavorable interactions with the rest of the motor can occur. Bromine is also an electronegative substituent and might pull electron density from the aromatic ring making it less efficient for π-π stacking interactions with the mesogens. The two phenyl substituted motors, however, do have the highest HTPs and also the largest differences between HTP values before and after irradiation.

The results obtained for the methoxy-substituted motor **2.6**, were poorly reproducible. This might be due to low solubility or poor miscibility, which made it difficult to know the exact concentration of the dopant molecule in the LC phase. Therefore no hard conclusions can be drawn as to where this substituent belongs in the series studied here. The relatively high PSS value (-50 vs. 42 in table 2.1), though, suggests that the PSS reached is one of the highest (i.e. most effective photoisomerization to the unstable form).

Motor in E7	R	β_M stable P helicity	β_M unstable at PSS[b]	Difference β_M
2.1	CH_3	55	-22	77
2.2	C_6H_5	93	-59	149
2.3	C_6H_4Br	59	-45	104
2.4	$CH(CH_3)_2$	43	-32	75
2.5	$C(CH_3)_3$	6	-[c]	-
2.6	OCH_3	42	-50	92[d]

Table 2.1. Helical twisting powers [a] (μm^{-1}) for motor molecules (Scheme 1) in LC blend E7. The HTP values are given for the P enantiomer for the stable sytem and mostly M at PSS. [a] Errors in the HTP are ca. 10%[§] for the stable and 20% for the HTP at PSS. [b] β_M unstable is measured at the apparent PSS. [c] *tert*-butyl HTP at PSS not determined as the motor's thermal barrier is too low. [d] Solubility issues result in poor reproducibility. HTP at PSS is measured at the apparent PSS.

[§] Errors are determined based on calculations of the standard deviation between measurements of the pitch length using the Grandjean-Cano method. The deviation is larger in the PSS measurements owing to generally poorer quality (more defects) in the concentric disclinations.

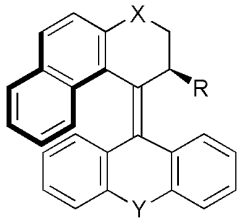

	X =	Y =	R =
3.1	O	-	H
3.2	O	-	CH_3
3.3	CH_2	-	CH_3
3.4	-	O	CH_3
3.5	O	O	CH_3

Scheme 2.10: General structure for further chiral dopants used (with intrinsic P helicity).

After comparing several 5-5 membered ring systems (**2.1**-**2.6**) 6-membered ring systems were measured in order to determine which structures are more suitable as chiral dopants (i.e. higher HTP) in LC phases. Motor **3.2** (scheme 2.10), with an oxygen 6-membered ring, yielded a clear cholesteric phase with HTPs (Table 2.2) which are somewhat lower than those found for the corresponding 5-membered ring motor without an oxygen (**2.1**). Remarkably, when exchanging the oxygen bridging atom in the upper half to a CH_2 group (**3.3**), the HTP becomes so small that no fingerprint region could be observed. The CH_2 group is slightly larger than the oxygen, thereby changing the size of the six-membered ring. Depending on the size of the six-membered ring the Fjord angle (the angle between the upper and the lower half seen along the connecting double bond) will be altered. It was previously shown that the Fjord angle has an effect on the thermal isomerization ($t_{1/2}$ = 1300y for **3.3** and 4 min for **2.1**).[25] These results point to the crucial importance of the Fjord angle between the upper and lower halves for the ability to induce chirality. The switch molecule (**3.1**, with two hydrogens on the α-carbon) has almost the same HTP as the molecular motor version **3.2**. This would suggest that the methyl substituent does increase the HTP capability but it is not the most important contributor. The angle between the naphthalene and the lower half seems to be more crucial. Motor **3.5** did form a cholesteric phase, however, upon contact of the phase with the lens (used for pitch determination), discontinuations formed which made it impossible to determine where the Grandjean-Cano lines were located and thus to calculate a pitch. When there is no oxygen in the upper half (**3.4)** a HTP can be measured. This suggests that the oxygen in the lower half is not detrimental to the formation of a cholesteric phase.

Motor in E7	β_M stable	β_M unstable at PSS[b]
3.1 [c]	26	-
3.2	30	-33
3.3 [d]	0	0
3.4 [d]	37	n.d.[e]
3.5	-	-
4	4	22
5	-	-
6	9	-

Table 2.2. Helical twisting powers [a] (μm^{-1}) for non five ring-five ring motor molecules (scheme 3 and figures 2.11 and 2.12) in LC blend E7. [a] Errors in the HTP are ca. 10% for the stable HTP and 20% for the HTP at PSS. [b] β_M unstable is measured at the apparent PSS. [c] **3.1** is a switch rather than a molecular motor. [d] See ref [26]. [e] Not determined.

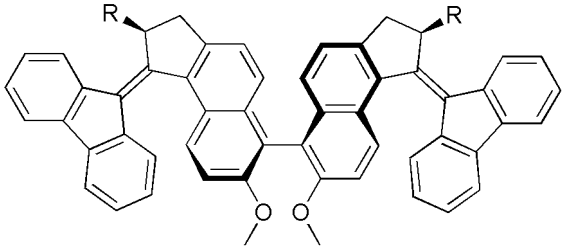

4

Scheme 2.11: Structure of the bicycle motor (**4**) with an R-S configuration.

The bis motor molecule **4**, (scheme 2.11) contains three chiral features i.e. stereogenic centers, helical structures and biaryl chirality (atropisomerism). Each motor molecule has R or S stereochemistry at the methyl moiety, the relation between the naphthalene and the lower half determines whether or not the intrinsic helicity is *P* or *M* and the bond connecting the two motor molecules can have one of two atropisomeric configurations. Owing to the exact configuration the two molecular motors have opposed intrinsic helicities: both *P* and *M* are present. Therefore it was thought that these might induce conflicting orientations amongst the mesogens resulting in a net zero helical induction. The HTP for the stable isomer is much lower than for the single molecular motor, implying that indeed, the two opposite intrinsic helicities show opposite effects, but not enough to cancel helical induction entirely. Judging from the HTP observed for the unstable form (which is much higher) this destructive interference is less at the PSS. At the PSS some of the molecular motors will have undergone photoisomerization while others will not. Therefore the LC system will contain a large variety of chiral features after irradiation. Contrary to the stable system, there might be some molecules where only one of the motors has undergone photoisomerization, in which case both molecular motors

will have the same intrinsic helicity, thus inducing some helical ordering amongst the mesogens and generating a HTP.

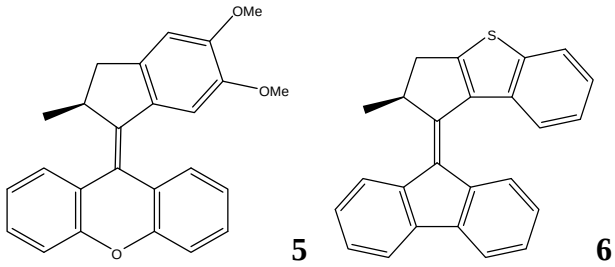

5 **6**

Scheme 2.12. The structures of two different motor molecules used as a dopant; **5** dimethoxy motor; **6** thiophene motor[27].

The dimethoxy motor (**5**, scheme 2.12) did not at first seem to generate a cholesteric phase in the normal concentration range. However, when a glass rod was deposited on the surface, traces of a cholesteric phase could be observed. This could mean that no fingerprint region is visible by eye as the pitch is too large. The available images were not good enough to be used to determine a pitch.

It seems that the angle between the naphthalene and the lower half might be of crucial importance. By keeping a similar lower half, but by altering the upper half from a naphthalene **3.4** (scheme 2.10) to a dimethoxy substituted phenyl group (**5**) no HTP is observed anymore. This is another strong indication for the importance of the angle made between the upper and lower half for inducing chirality into the system. The helical twisting power for the stable conformation of the thiophene motor (**6**, scheme 2.12) is relatively low. The rigidity of the thiophene moiety alters the Fjord region again. As a direct result the $t_{1/2}$ for thermal isomerization is lowered to 70 ms.[27] Interestingly, though the Fjord angle is at its best for accelerated thermal isomerization, it has a negative effect in the ability to induce chirality amongst the mesogens. Therefore, there appears to be an optimal value for the Fjord angle with respect to HTP which is not the same as the optimal Fjord angle for accelerated thermal isomerization. The maximum seems to be for the five-five membered ring naphthalene structures with smallest R substituent (sp^2).

2.3.2 Other mesogens

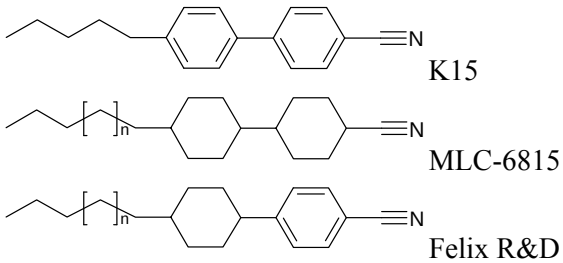

Scheme 2.13: Structures of the other commercially available mesogens used in this study besides E7.[**]

Various LC mesogens other than E7 (which was used for the remainder of the measurements in this chapter) presented in Scheme 2.13 were selected owing to their different temperature ranges in which these can be used, and differing chemical compositions. K15 (Scheme 2.13) is made up of one single molecule (not a blend), as a result the temperature range over which it is liquid crystalline is only 11 degrees (temperature range between 24 - 35ºC for the nematic phase). It is known that certain aryl components in LC mesogens can fluoresce upon irradiation. E7, however, contains a triphenyl, and therefore this blend fluoresces more than other LC's used. As a consequence not all of the light intensity produced will reach the molecular motor dopant to cause isomerization and instead generate fluorescence in the LC phase. Both MLC-6815 and Felix are blends containing various chain lengths. As a consequence the temperature range in which the nematic phase is observed is larger. MLC-6815 has a temperature range from <20 – 67ºC, while Felix R&D has a temperature range between 29.7 - 55ºC. MLC-6815, however, contains no phenyl moieties, therefore of the presented LC mesogens in Scheme 2.13 this is the mesogen which is least likely to absorb UV light during irradiation at 365 nm, thus possibly allowing for better transmittance of the irradiation to the molecular motor molecule.

[**] Exact ratios of the components within an LC blend are usually not disclosed by the manufacturer.

Motor in K15	β_M stable	β_M unstable at PSS[b]	Difference β_M
2.2	150[c]	-75	225
2.5	106	-58	164
4	6	28	34

Table 2.3. Helical twisting powers [a] (μm^{-1}) for three motor molecules measured in LC K15. [a] Errors in the HTP are 10% for the stable HTP and 20% for the HTP at PSS. [b] β_M unstable is measured at the apparent PSS. [c] Previously reported value by R. Eelkema[14] is 137μm^{-1} however, upon multiple measurements the value was consistently found to be slightly higher.

LC	β_M stable	β_M unstable at PSS[b]	Difference β_M
E7	55	-22	77
MLC	53	-19	72
Felix	53	-10	63

Table 2.4. HTP (μm^{-1}) [a] of motor **2.1** in different liquid crystals (Scheme 6). [a] Errors in the HTP are 10% for the stable HTP and 20% for the HTP at PSS. [b] β_M unstable is measured at the apparent PSS.

When K15 was used as the mesogen instead of E7 (Scheme 2.8) the magnitude of the HTPs of the molecular motors increased significantly. A possible explanation is that E7 is a blend, which contains a variety of LC molecules which will have better or worse interactions with the dopants and each other. The K15 molecules, as this is a pure mesogen, presumably will have more optimized intermolecular interactions than a mixture, and this would explain the better helix induction. The relative efficiency of the dopants, however, remains the same (Table 2.3). Other liquid crystal blends were also used, but, these gave values for the HTP comparable to those in E7 (Table 2.4). The slight decrease in the HTP at PSS compared to the values for the *P* isomer, falls within the experimental error so no conclusions can be drawn from these data. For future applications it is important to emphasize that K15, though it gives higher HTPs, it has a temperature range in which it can be used which is rather small compared to, for example, E7 (temperature range between -10 - 60ºC). Owing to the make up of liquid crystal blends, however, other properties such as fluorescence may become more pronounced affecting the photostationary state of the molecular motor and thus influencing the observed magnitudes of the observed HTPs at PSS.

2.4 Conclusions

The LC/chiral dopant system is very sensitive towards minor changes between the interactions resulting from the alterations in geometry. It was not anticipated that the exchange of a bridging atom from oxygen (**3.2**) to a CH_2 group (**3.3**) in the upper half could have such dramatic effects on the helix-inducing capabilities of the dopants (30 to 0 μm^{-1}). However, as was previously observed, the change in the torsional and Fjord angles, based on the molecular motor structures, is crucial for optimizing the HTP. There appears to be an optimum for the Fjord angle with respect to the HTP. The 5-5 membered molecular motors gave the highest HTP's and have Fjord angle dimensions between those of the more rigid system **6** or the six membered ring systems (**3.1**-**3.5**). Of the 5-5 membered ring systems, molecular motor **2.2** gave the highest HTP, and it has the smallest torsional angle of the **2.1**-**2.6** motors.
It is also clear that the solubility of the dopant in the LC is crucial. When there were problems of this type no HTP could be determined. This does not necessarily mean that these molecular motors could not induce a helical organization if these were better compatible with the liquid crystal (i.e. other not tested mesogens). It is certain, however, that all segments of the molecular motor seem to be relevant for transmitting chirality as both changes in the upper and lower halves of the motor have induced changes in the HTP values. More research will be needed to clarify what geometries of the molecule yield the highest helical induction in the LC. The best molecular motors measured would be **2.2** and **3.2**. Molecular motor **2.2** is best owing to its large difference between the HTP values for the P isomer and at PSS allowing for a large range of addressable colors throughout the process to reach PSS. However, owing to the very high thermal barrier of molecular motor **3.2** is very useful as it can be stopped at any moment throughout photoisomerization to give a desired pitch length. Using visible light irradiation the process can be reversed. Thus this molecular motor would be more practical in future applications.

2.5 Acknowledgements

I would like to acknowledge all those who prepared, and supplied molecules for me allowing the measurement of their HTP values: Dr. Javier Vicario, Dr. Mike Pollard, Dr. Edzard Geertsema, and the students I guided, Jos Kistemaker and Sander de Jong.

2.6 Experimental section

General remarks

Molecular motors **2.1-2.5**, **4**, **5**, and **6** were synthesized according to literature procedures.[28,27] Molecules **3.1, 3.2** and **2.6** were prepared as described in the synthesis section.
All chiral dopants were obtained enantiopure via preparative HPLC. All enantiomers were checked after resolution on an analytical HPLC to determine that these indeed consisted of a single enantiomer only. Specific resolutions used can be found in the references indicated or under the synthesis heading.
All chemicals were used without further purification except toluene which was freshly distilled prior to use. Glass slides were purchased from Knittel Glaser (76*26*1 mm).
For the spin coating a commercially available polyimide (Optmer AL1051, JSR, Belgium) was used. For the irradiation experiments a Spectroline model ENB-280C/FE lamp was used. LC hosts used are K15 (98% Aldrich, weight 249.36), E7 (Merck; average weight 274.244), MLC-6815 (gift from Merck: average weight 288.38), and Felix R&D (96322/EoiD, Hoechst, weight 253.374). An Olympus BX 60 microscope, equipped with crossed polarizers and a Sony 3CCD DXC 950P digital camera, attached to a personal computer with Matrox Inspector 2.1 imaging software was used.
Reagents were purchased from Aldrich, Merck or Fluka and were used as provided unless otherwise stated. All solvents were reagent grade and were dried and distilled before use according to standard procedures. Chromatography: silica gel, Merck type 9385 230-400 mesh, TLC: silica gel 60, Merck, 0.25 mm. Mass spectra (HRMS) were recorded on an AEI MS-902. ^{1}H and ^{13}C NMR spectra were recorded on a Varian Gemini-200 operating at 200.55 MHz for the ^{1}H nucleus, and at 50.44 MHz for the ^{13}C nucleus, in $CDCl_3$, unless stated otherwise. Chemical shift values are denoted in δ values (ppm) relative to residual solvent peaks ($CHCl_3$, ^{1}H δ=7.26, ^{13}C δ=77.0 ppm). HPLC analyses were performed on a Shimadzu 10AD-VP using a chiral OD column. A preparative Gilson HPLC system consisting of a 231XL sampling injector, a 306 (10SC) pump, a 811C dynamic mixer, a 805 manometric module (with a 119 UV-VIS detector), a 202 fraction collector, and a chiral OD column were used to separate the isomers. Kinetic (UV-Vis) measurements were performed on a Hewlett-Packard HP 8453 FT spectrophotometer equipped with a Huber Polystat cc1 and a Quantum Northwest temperature control, running Agilent UV-Visible ChemStation.

Synthesis of Switch 3.1 and molecular motor 3.2

Molecules **3.1** was synthesized according to similar procedure as **3.2.**

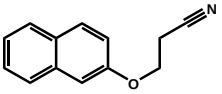

3-(Naphthalen-2-yloxy)propanenitrile (3.2a). To a solution of 2-naphthol (23.8 g, 165 mmol) in acrylonitrile (45 g, 848 mmol) Triton B (2.7 ml, 6.1 mmol) was added and the mixture was stirred for 18 h under reflux conditions. The reaction mixture was then cooled to 0 ^{o}C and filtered. The residue was washed with a 5% aq. sodium hydroxide solution (75 ml) and water (40 ml) and dried over $MgSO_4$ affording 21.5 g (109 mmol, 66%) of nitrile **1**. ^{1}H NMR (200 MHz, $CDCl_3$) δ 7.79 (d, J=7.9 Hz, 1H), 7.77 (d, J=8.8, 1H), 7.74 (d, J=8.2 Hz, 1H), 7.46 (t, J=7.3 Hz, 1H), 7.37 (t, J=7.5 Hz, 1H), 7.17 (dd, J=2.4 , 8.9 Hz, 1H), 7.12 (d, J=2.1 Hz, 1H), 4.31 (t, J=6.4 Hz, 2H), 2.89 (t, J=6.4 Hz, 2H); ^{13}C NMR (50 MHz, $CCHCl_3$) δ 155.5 (C), 134.1 (C), 129.6 (CH), 129.2 (C), 127.6 (CH), 126.7 (CH), 126.5 (CH), 124.0 (CH), 118.4 (CH), 117.2 (C), 106.9 (CH), 62.4 (CH_2), 18.4 (CH_2).

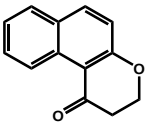

2,3-Dihydro-1H-benzo[f]chromen-1-one (3.2b). Nitrile **3.2a** (42.1 g, 213 mmol) was added to aq. 85% H_2SO_4 solution (425 ml) in 15 min and the mixture was stirred for 2 h. The reaction mixture turned from yellow to red. The mixture was then poured onto 1 kg of ice and after melting a solid was filtered off. The liquid was extracted with ether (2x 150 ml) and ethyl acetate (2x 150 ml). The solution was dried over $MgSO_4$ and the solvent was subsequently removed under reduced pressure and the solid was washed with saturated aq. $NaHCO_3$ (300 ml) and water (250 ml). Drying afforded 21.1 g (106 mmol, 50%) of ketone **2**. ^{1}H NMR (200 MHz, $CDCl_3$) δ 9.47 (d, J=8.7 Hz, 1H) 7.85 (d, J=9.0 Hz, 1H), 7.70 (d, J=8.0 Hz, 1H), 7.62 (t, J=7.8 Hz, 1H), 7.40 (t, J=7.5 Hz, 1H), 7.05 (d, J=9.0 Hz, 1H), 4.56 (t, J=6.6 Hz, 2H), 2.87 (t, J=6.6 Hz, 2H).

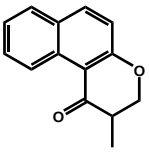

2-Methyl-2,3-dihydro-1H-benzo[f]chromen-1-one (3.2c). n-Butyllithium (6.25 ml, 10 mmol) was added to a stirred mixture of di*iso*-propylamide (1.4 ml, 10 mmol) in THF (50 ml) at -78 ^{o}C. To this yellow mixture, ketone **3.2b** (2.0 g, 10 mmol) in THF (50 ml) was added dropwise in 15 min. Methyliodide (25 ml, 0.3 mol) was added and the solution turned red. The mixture was allowed to warm to room temperature and stirred overnight. The yellow mixture was poured on a saturated aq. NH_4Cl

solution (300 ml) and extracted with ethyl acetate (3x 150 ml). The combined organic layers were washed with brine, dried over $NaSO_4$ and the solvent was removed under reduced pressure affording 1.17 g (5,5 mmol, 55%) of ketone **3**. ^{1}H NMR (200 MHz, $CDCl_3$) δ 9.48 (d, J=8.7 Hz, 1H), 7.91 (d, J=9.0, 1H), 7.75 (d, J=8.8 Hz, 1H), 7.63 (ddd, J=1.5 , 7.0 , 8.6 Hz, 1H), 7.42 (ddd, J=1.1 , 6.9 , 8.0 Hz, 1H), 7.09 (d, J=9.0 Hz, 1H), 4.60 (dd, J=5.1 , 11.2 Hz, 1H), 4.27 (dd, J=10.0 , 11.7 Hz,1H), 2.94 (dqd, J=5.1 , 7.0 , 10.6 Hz, 1H), 1.28 (d, J=7.0 Hz, 3H); ^{13}C NMR (50 MHz, $CCHCl_3$) δ 196.0 (C), 163.5 (C), 137.2 (CH), 131.7 (C), 129.5 (CH), 129.2 (C,C), 128.3 (CH), 125.8 (CH), 124.7 (CH), 118.6 (CH), 111.9 (C), 72.1 (CH_2), 41.2 (CH), 11.3 (CH_3).

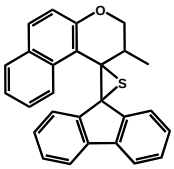

Dispiro[2,3-dihydro-2-methyl-1*H*-naphtho[2,1-b]-pyran-1,2'-thiirane-3',9'-(9'H-fluorene)] (3.2d). Under a nitrogen atmosphere ketone **3.2c** (1.1 g, 5.2 mmol) and P_2S_5 (10 g, 22.5 mmol) in toluene (140 ml) were heated to 70 ^{o}C until the conversion of ketone **3** into thioketone was complete (TLC, silica, pentane/DCM 2/1, $R_{f,ketone}$= 0.3, $R_{f,thioketone}$= 0.8). The hot solution was filtered and the green filtrate was directly applied to quick flash column chromatography (silica, pentane/DCM 2/1). The collected fraction of thioketone was immediately added to a solution of 9-diazo-9H-fluorene (3.0 g, 15.6 mmol) in toluene (140 ml) and the reaction mixture was heated at reflux for 72 h. The solvents were removed under reduced pressure and the residue was purified by column chromatography (silica, pentane/DCM 10/1 → 1/2) affording 1.25 g (3.17 mmol, 61%) of episulfide **5**. ^{1}H NMR (200 MHz, $CDCl_3$) δ 9.21 (d, J=8.8 Hz, 1H), 7.79 (t, J=7.7 Hz, 2H) 7.66-7.55 (m, 4H), 7.43 (ddt, J=1.2 , 3.1 , 7.4 Hz, 2H), 7.31 (dt, J=1.2 , 7.5 Hz, 1H), 7.07 (dt, J=1.0 , 7.5 Hz, 1H), 6.77 (d, J=8.8 Hz, 1H), 6.49 (dt, J=1.1 , 7.6 Hz, 1H), 6.06 (td, J=0.8 , 7.8 Hz, 1H), 3.64 (m, 2H), 3.16 (m, 1H), 1.17 (CH, J=6.9 Hz, 3H); ^{13}C NMR (50 MHz, $CCHCl_3$) δ 155.20 (C), 143.27 (C), 143.16 (C), 141.93 (C), 139.97 (C), 134.38 (C,C), 129.45 (CH), 129.33 (C,C), 128.80 (CH), 128.29 (CH), 127.46 (CH), 126.35 (CH), 126.01 (CH), 124.09(CH), 123.50 (CH), 123.25 (CH), 122.55 (CH), 120.46 (CH, CH), 119.35 (CH), 118.09 (CH), 117.65 (C), 72.44 (CH_2), 40.09 (CH), 19.19 (CH_3); HRMS (EI): calcd for $C_{27}H_{20}OS$, 392.12349; found, 392.12448.

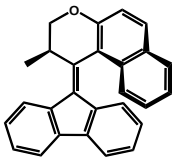

1-(9H-Fluoren-9-ylidene)-2-methyl-2,3-dihydro-1H-benzo[f]chromene (3.2). Under a nitrogen atmosphere a stirred solution of

episulfide **3.2d** (1.2 g, 3.1 mmol) and PPh_3 (2 g, 7.6 mmol) in toluene (200 ml) was heated at reflux overnight. The mixture was allowed to cool to room temperature and after addition of MeI (50 ml) it was stirred for 1 h. Filtration and removal of the solvent under reduced pressure gave a yellow oil which was purified by column chromatography (silica, pentane/DCM 10/1) affording 1.0 g (2.9 mmol, 95%) of **6**. ^{1}H NMR (200 MHz, $CDCl_3$) δ 8.01-7.91 (m, 1H), 7.90-7.75 (m, 4H), 7.70 (d, J=7.6 Hz, 1H), 7.45-7.33 (m, 2H), 7.28 (dt, J=0.9 , 7.4 Hz, 1H), 7.10-7.20 (m, 3H), 6.72 (dt, J=0.7 , 7.6 Hz, 1H), 6.53 (d, J=8.0 Hz, 1H), 4.43 (m, 2H), 4.22 (m, 1H), 1.45 (d, J=7.0 Hz, 3H); ^{13}C NMR (50 MHz, $CDCl_3$) δ 153.4 (C), 140.6 (C), 139.5 (C), 138.3 (C), 137.9 (C,C), 132.6 (C), 131.9 (C), 131.8 (CH), 129.0 (C), 128.3 (CH), 127.3 (CH), 127.1 (CH), 127.0 (CH), 126.8 (CH), 126.5 (CH), 125.2 (CH), 125.0 (CH), 124.4 (CH), 123.5 (CH), 119.9 (CH), 118.9 (CH), 118.1 (CH), 113.7 (C), 72.3 (CH_2), 33.0 (CH), 15.8 (CH_3); HRMS (EI): calcd for $C_{27}H_{20}O$, 360.15141; found, 360.15025.

Motor **3.2**: PSS (unstable:stable) 99:1, k^0 =8.76 x10-7; ΔG 106; $t^0_{½}$ = 220 h

Synthesis of molecular motor 2.6

General procedure similar to that in the literature[29](the only difference is the presence of the bromine), however different solvent systems were required.

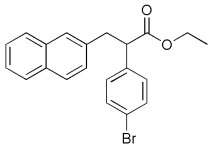

Ethyl2-(4-bromophenyl)-3-(naphthalen-2-yl)propanoate (2.6a)

3 g 2-(bromomethyl)naphthalene was recrystallised before use. In a three-neck flask a mixture of 35 mL *tert*-butanol and 34 mL di-isopropyl ether was stirred at 40 °C under nitrogen flow. The potassium salt of *tert*-butanol (KOtBu) 1.57 g (11.3 mmol, 1.2 eq) was added, along with 2.06 g (9.3 mmol) 2-(bromomethyl)naphthalene and 2.26 g (9.3 mmol) ethyl 2-(4-bromophenyl). The progress reaction was followed by TLC (ethyl acetate:*n*-heptane=1:1).

After 23 h of stirring, the conversion was determined by ^{1}H-NMR (30-50%) and 0.5 equiv. extra potassium salt of *tert*-butanol was added. Because the bromide did not fully dissolve 85 mL di-isopropyl ether was added. The stirring was continued for 24 h, whereupon another 0.5 equiv. of potassium salt of *tert*-butanol was added. After 90 min, 20 mL *tert*-butanol and 50 mL di-isopropyl ether was added.

For the 1H-NMR sample, an aliquot of the reaction mixture was acidified using a 2 M aq. HCl solution. The mixture was then extracted with dichloromethane, dried ($MgSO_4$) after which the solvent was evaporated to give a dark yellow oil.

The reaction mixture was heated at reflux while stirring over 55 h and cooled to room temperature afterwards. Most of the solvent was evaporated yielding a viscous orange liquid. This was acidified with 12 mL aq. 2M HCl (2.5 equivalents). The resulting mixture was extracted with 40 mL dichloromethane and the organic layer was extracted with 2x 20 mL water. The organic layer was dried with Na_2SO_4 and the solvent was evaporated to give an orange solid (2.66 g, 6.95 mmol; 75%).
^{1}H NMR ($CDCl_3$, 300 MHz) δ : 7-8 (m, 7H), 4.18 (q, 1H), 4.08 (m, 4H), 3.55 (d, 2H), 3.18 (q, 2H), 1.26 (t, 3H)

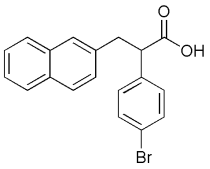

2-(4-Bromophenyl)-3-(naphthalen-2-yl)propanoic acid (2.6b) Ester **2.6a** 1.34 g (3.50 mmol) was stirred overnight in a mixture of 0.67 g LiOH (28 mmol), 5 mL methanol and 15 mL water. The mixture was then acidified with a 10% aq. HCl solution. It was extracted with 50 mL ether twice and the organic layers were washed twice with 50 mL brine after which they were dried on $MgSO_4$. The solvent was evaporated to give a white solid. ^{1}H NMR ($CDCl_3$, 300 MHz) δ : 7.95 (s, 1H), 7.91 (s, 1H), 7.75 (s, 1H), 7.70 (s, 1H), 7.62 (d, 1H), 7.55 (s, 1H), 7.47 (s, 1H), 7.45 (s, 1H), 7.41 (s, 1H), 7.24 (d, 3H), 4.83 (q, 1H), 3.65 (t, 2H)

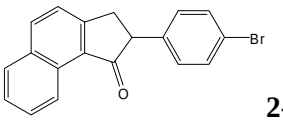

2-(4-Bromophenyl)-2,3-dihydro-1H-cyclopenta[a] naphthalen-1-one (2.6c) Ketone **2.6b** (0.393 g, 1.11 mmol) was dissolved in 25 mL DCM, the mixture was stirred and heated at reflux with 4 mL $SOCl_2$ and 2 drops of dimethylformamide (DMF). After one hour the mixture was cooled to room temperature. The solvent was evaporated to give a yellow oil. The oil was dissolved in toluene, cooled to 0 ^{o}C and stirred. Subsequently 0.55 g $AlCl_3$ (4.12 mmol) was added in one portion, and the mixture was stirred for one hour after which it was slowly added to 75 mL of a stirred, saturated aq. $NaHCO_3$ solution. This was stirred for 60 h while CO_2 escaped via a valve. The mixture was then extracted twice with 50 mL ether and the organic layers were dried using $MgSO_4$. The solvents were evaporated to give a yellow oil. According to ^{1}H-NMR, the reaction did not proceed to completion and the reaction was started again with the oil. 50 mL of DCM, 3 drops of DMF and 8 mL $SOCl_2$ were added and the mixture was heated at reflux at a higher temperature for 15 h. During this step a side product was formed, caused by a small amount of bromomethyl naphthalene. This reacted with the toluene to form 8-methyl-11H-benzo[a]fluorene. ^{1}H- NMR ($CDCl_3$, 300 MHz) δ: 9.19 (d, 1H), 8.13 (d,

2H), 7.96 (d, 2H), 7.68 (t, 1H), 7.59 (t, 2H), 7.45 (d, 1H), 7.11 (d, 1H), 3.96 (dd, 1H), 3.31 (dd, 2H)

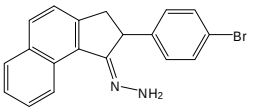

(E)-(2-(4-Bromophenyl)-2,3-dihydro-1H-cyclopenta[a]naphthalen-1-ylidene)hydrazine (2.6d) 0.84 g (2.48 mmol) of **2.6c** was heated at reflux in a mixture of 5 mL hydrazine monohydrate, 5 mL ethanol and 2 mL ether for 3 d under nitrogen flow. Water (50 mL) was added and the mixture was extracted twice with 50 mL DCM. The organic layers were dried with Na_2SO_4 and the solvent was evaporated to yield a yellow-orange oil (0.61 g; 1.74 mmol; 70%)
^{1}H NMR ($CDCl_3$, 300 MHz) δ: 9.25 (d, 1H), 7.95 (d, 2H), 7.91 (d, 2H), 7.63 (t, 1H), 7.56 (t, 2H), 7.45 (d, 1H), 7.13 (d, 1H), 6.83 (2H), 3.68 (dd, 1H), 3.38 (s, 1H), 3.32 (s, 1H)
m/z (EI+, %): 350 (M, 27), 183 (100), 166 (59)

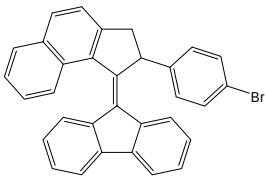

9-(2-(4-Bromophenyl)-2,3-dihydro-1H-cyclopenta[a]naphthalen-1-ylidene)-9H-fluorene (2.6) A solution of 200 mg (0.6 mmol) of **2.6d** in 10 mL DMF was cooled to -50 ^{o}C. An excess of [bis(trifluoroacetoxy)iodo]benzene was added. After stirring for 15 s, an excess of fluorenone thioketone was added and the cooling was removed. The temperature of the mixture slowly reached room temperature overnight. The mixture was then washed with 10 mL aq. NH_4Cl to remove a bit of DMF, then extracted twice with 10 mL ether, dried using $MgSO_4$ and the solvent was evaporated to yield a red brown oil which still contained DMF. The oil was purified using column chromatography (SiO_2, *n*-heptane:ethyl acetate 9:1) to yield 0.142 g of episulfide. This episulfide was dissolved in 20 mL toluene and 0.2 g triphenylphosphine and the mixture was heated at reflux for 20 h. The mixture was then cooled and 1.1 equivalent of methyl iodide was added. 20 mL water was added and the mixture was extracted twice with 20 mL ethyl acetate. The organic layers were washed twice with 10 mL water, dried with $MgSO_4$ and evaporated to yield a yellow-brown oil. This oil was purified using column chromatography (SiO_2, *n*-heptane:DCM 9:1). This yielded 0.015 g (0.03 mmol; 5%) of product which was then recrystallized from ethanol.
^{1}H NMR ($CDCl_3$, 400 MHz) δ : 7.96 (t, 2H), 7.89 (d, 1H), 7.81 (d, 1H), 7.78 (d, 1H), 7.51 (t, 1H), 7.43 (q, 3H), 7.32 (d/q, 3H), 7.25 (t, 1H), 7.14-7.08 (m, 3H), 6.86 (t, 1H), 6.80 (d, 1H), 5.30 (d, 1H), 3.98 (q, 1H), 3.16 (d, 1H)

^{13}C NMR ($CDCl_3$, 50 MHz) δ : 146.2 (C), 145.4 (C), 143.2 (C), 140.4 (C), 140.1 (C), 139.6 (C), 137.6 (C), 137.2 (C), 133.6 (C), 133.0 (C), 132.1 (CH), 131.6 (CH), 129.6 (CH), 129.2 (CH), 127.7 (CH), 127.4 (CH), 127.3 (CH), 126.5 (CH), 126.1 (CH), 125.8 (CH), 124.4 (CH), 123.8 (CH), 119.9 (CH), 119.4 (CH), 56.2 (CH), 44.2 (CH_2)
m/z (EI+, %): 336 (100)

Motor **2.6**: PSS (unstable:stable) 90:10, $t^0_{1/2}$ = 18 min

LC Sample preparation

Standard glass slides were thoroughly cleaned (using TPOL and *iso*-propanol to remove all traces of grease and dust) and dried, prior to spin coating (3000 rpm, 60 seconds) with a thin film of polyimide. These films were then allowed to adhere to the glass surface overnight in a vacuum oven at 170 ºC.

HTP measurements

Samples were prepared by weighing out a certain amount of motor molecule and then adding enough LC to generate a 0.5 to 1 wt% solution (motor molecule relative to the LC). Toluene was slowly added until a homogeneous solution was formed. A segment of glass slide was taken and the polyimide coated slide was then rubbed in one direction using a fine cotton cloth. Then 10 µL of the resulting solution was placed on the surface and allowed to spread to generate as thin a layer as possible. This slide was then placed under the microscope for observation. Pitches were determined by placing a convex lens, of known radius, on the surface of the phase. The pitch lengths could be measured using the Matrox Inspector 2.1 software.
In order to be able to observe both the stable and unstable forms it was essential to perform irradiation experiments. These were performed using a UV lamp with a wavelength of 365 nm. The irradiations were always performed directly on the slide and for an average duration of 15 min or until no further change in the phase was observed (PSS reached).
The percentage error for the HTP was assumed to be the same as the percentage error in the pitches that were determined. The standard deviation of each measurement varies slightly depending on the quality of the Grandjean-Cano pictures taken for the sample. Therefore an average error is give for these HTP measurements.

2.7 References

[1] F. Reinitzer, *Monatshefte* **1888**, 9, 421
[2] O. Lehmann, *Z. Phys. Chem* **1889**, *4*, 462
[3] T.J. Sluckin, D.A. Dunmur, H. Stegenmeyer, *Crystals that Flow: Classic Papers from the History of Liquid Crystals,* (G.W. Gray, J.W. Goodby, A. Fukuda, eds.), Taylor &Francis, London, **2004**
[4] a) H. Kelker, B. Scheurle, *Angew. Chem. Int. Ed*. **1969**, *8*, 884 b) G.W. Gray, K.J. Harrison, J.A. Nash, *Electronics Lett*., **1973**, *9*, 130
[5] *Handbook of Liquid Crystals Vol. 2A: Low Molecular Weight Liquid Crystals* (D. Demus, J.W. Goodby, G.W. Gray, H.W. Spiess, V. Vill, eds.) Wiley-VCH, Weinheim, **1998**.
[6] For low molecular weight vapor phase sensing see: R. Shah, N.L. Abbott, *Science*, **2001**, *293*, 1296-1299; For protein sensing see: Y.Y. Luk, M.L. Tingey, D.J. Hall, B.A. Israel, C.J. Murphy, P.J. Bertics, N.L. Abbott, *Langmuir*, **2003**, *19*, 1671-1680; For non toxic system in cells see: Y.Y. Luk, S.F. Campbell, C.J. Murphy, N.L. Abbott, *Liq. Cryst*. **2004**, *31*, 611; For example of device for pesticide sensing see: J.L. Adgate, A. Barteková, P.C. Raynor, J.G. Griggs, A.D. Ryan, B.R. Acharya, C. J. Volkmann, D.D. Most, S. Lai, M.B. Bonds, *J. Environ. Monit*., **2009**, *11*, 49-55 | 51
[7] See for instance J.D. Martin, C.L. Keary, T.A. Thornton, M.P. Novotnak, J.W. Knutson, J.C.W. Folmer *Nature Materials* **2006**, *5*, 271–275.
[8] For further information on blue phases, see, for instance: H. J. Coles, M. N. Pivnenko, *Nature*, **2005**, *436*, 997-1000
[9] *Handbook of Liquid Crystals Vol 1: Fundamentals* (D. Demus, J.W. Goodby, G.W. Gray, H.W. Spiess, V. Vill, eds.) Wiley-VCH, Weinheim, **1998**.
[10] Pictures courtesy of Sci tech encyclopedia.
[11] http://plc.cwru.edu/tutorial/enhanced/files/lc/biref/biref.htm
[12] I. Dierking, *Textures of Liquid Crystals*, Wiley-VCH, Weinheim, **2003**
[13] a) M. Braun, A. Hahn, M. Engelmann, R. Fleischer, W. Frank, C. Kryschi, S. Haremza, K. Kürschner, Parker, *Chem. Eur. J.* **2005,** *11*, 3405-3412. b) G. Heppke, D. Lötzsch, F. Oestreicher, *Z. Naturforsch.* **1986,** *41A*, 1214.

[14] a) H.G. Kuball, B. Weiss, A.K. Beck, D. Seebach, *Helv. Chim. Acta* **1997**, *80*, 2507. b) A.J. Seed, M.E. Walsh, J.W. Doane, A. Kahn, *Mol. Cryst. Liq. Cryst*. **2004**, *410*, 729-736
[15] a) Bobrovsky, A.Y.;Boiko, N.I.; Shibaev, V.P. *Polym. Sci. A* **1998**, *40*, 232; b) Peter, P.M. *Nature* **1998**, *391*, 745; c) N Tamaoki,.; Y. Aoki, , M. Moriyama, M. Kidowaki, *Chem. Mater*. **2003**, *15*, 719 d) Demus, D.; Goodby, J. "Physical Properties of Liquid Crystals" Weinheim, Wiley-VCH: New York, 1999
[16] Research has been done to go beyond this 50%. See, for instance: a) M. Mitov, N. Dessaud, *Nature Materials*, **2006**, *5*, 361-364. b) M. Mitov, N. Dessaud *Liq. Cryst*. **2007**, *34*, 183-193.
[17] H. Coles in *Handbook of Liquid Crystals, Vol. 2A: Low Molecular Weight Liquid Crystals I* (eds. D. Demus, J. Goodby, G.W. Gray, H.-W. Spiess, V. Vill), Wiley-VCH, Weinheim **1998**.
[18] W. Shang, M.M. Labes, *Mol. Cryst. Liq. Cryst*. **1994**, *239*, 55
[19] N. Tamaoki, *Adv. Mater*. **2001**, *13*, 1135 b) S.V. Shiyanovskii, O.D. Lauvrentovich, T. Schneider, T. Ishikawa, I.I. Smalyukh, C.J. Woolverton, G.D. Niehaus, K.J. Doane, *Mol. Cryst. Liq. Cryst*. **2005**, *434*, 587-598

[20] See references 15 a and b and for instance: R.A. van Delden, T. Mecca, C. Rosini, B.L. Feringa*, Chem. Eur. J.* **2004**, *10*, 61-70
[21] For reviews on LC dopants see e.g: R. Eelkema, B.L. Feringa, *Org. Biomol. Chem*. **2006**, *20*, 3729-3745; G.P. Spada, G. Proni, *Enantiomer* **1998**, *3*, 301-314.
[22] a) C. Ruslim, K. Ichimura, *J. Mat. Chem.* **2002**, *12*, 3377; b) S. Pieraccini, G. Gottarelli, R. Labruto, S. Masiero, O. Pandoli, G.P. Spada *Chem. Eur. J.* **2004**, *10*, 5632; c) N. Tamaoki, *Adv. Mater*. **2001**, *13*, 1135
[23] R. Eelkema, M..M. Pollard, J.Vicario, N. Katsonis, B. Serrano Ramon, C.W.M. Bastiaansen, D.J. Broer, B.L. Feringa, *Nature*, **2006**, *440*, 163
[24] See Table **1** pg 5129 in: J. Vicario, M. Walko, A. Meetsma, B.L. Feringa, *J.Am.Chem.Soc*, **2006**, *128*, 5127-5135
[25] M.M. Pollard, A. Meetsma, B.L. Feringa, *Org. Biomol. Chem*. **2008**, *6*, 507
[26] R. Eelkema, *Ph.D. Thesis*, University of Groningen, **2006**
[27] T. Fernández Landaluce, G. London, M.M. Pollard, P. Rudolf, B.L. Feringa, *J. Org. Chem*. **2010**, *75*, 5323-5325
[28] For syntheses, see: ref 23 and E.M. Geertsema, *Ph.D. Thesis*, University of Groningen, 2003
[29] M.K.J. Ter Wiel, *Ph.D. Thesis*, University of Groningen, **2004**

Chapter 3

Photoinduced Reorganization of Doped Liquid Crystals: Bridging Molecular Isomerization and Texture Rotation

Previously the rotational reorganization of a molecular motor doped LC phase was observed. In order to determine the origins of this phenomenon various parameters were varied. The observed rotation of the surface texture is dependent on the kinetics of the molecular motor used (i.e. faster rotation for faster isomerizing molecule). The number of rotations is dependent on the layer thickness. Glass rods will rotate irrespective of the dimensions (unless submergence is observed), or concentration of molecular motor used. A computational model was created based on these findings in order to determine whether or not this behavior can be accurately predicted.

Part of this chapter has been published: A. Bosco, M.G.M. Jongejan, R. Eelkema, N. Katsonis, E. Lacaze, A. Ferrarini, B.L. Feringa, *J. Am. Chem. Soc*. **2008**, *130*, 14615-14624

3.1 Introduction

Liquid crystals are considered promising materials, owing to their sensitivity towards various external stimuli (temperature, magnetic and electric fields). Drops of cholesteric phases have been shown to rotate under the influence of external fields of different types.[1] Lehmann discovered in 1900 that a thermal gradient along the axis of helical organization in a cholesteric phase generated a continuous rotation of a cholesteric drop.[2] Similar effects were later observed under the influence of an electric field[3] and a concentration gradient of chiral solutes in a single direction.[4] The origin for these phenomena lies in the lack of mirror symmetry in cholesteric phases.[2,5] These phases originate from chiral mesogens or can be generated from achiral mesogens which are doped with a small amount (usually in the range of 1 to 5 wt%) of an enantiopure chiral molecule[6]. The chiral dopant molecule should have some structural similarities to the achiral mesogen for efficient transfer of chiral information.

In order to have more control over the liquid crystalline phase, photoisomerizable chiral molecules have also been used as dopants.[7] In our research group molecular motors which can undergo unidirectional rotation along the central double bond have been studied extensively. As the molecular motor isomerizes two different configurations are present in varying ratios (**1a** vs **1b** in scheme 3.1). Both isomers induce opposite helicities in the LC matrix. A lower ratio of isomers is expected to result in a lengthening of the observed pitch until a 50:50 ratio is reached where no preferred chiral induction is expected. As the amount of the second isomer increases a tightening of the pitch is expected. Unexpectedly, it has been reported that upon irradiation of a molecular motor doped LC phase a rotational reorganization of the phase is observed by optical microscopy.[8] After the PSS (photo stationary state) is reached (**1b** in Scheme 3.1) subsequent thermal helix inversion can occur, restoring the molecular motor to the degenerate state (**1c** see scheme 3.1). Thus the system is reversible as is the isomerization of the molecular motor. Dependent on whether the molecular motor isomerizes from *P* to *M* or *M* to *P* the direction of the rotational reorganization is altered (clockwise and counterclockwise, respectively). The rotational phenomenon is linked to the varying ratios in which the two isomers (*P* and *M*) are present in the LC phase, resulting in constantly changing the ability to twist the nematic LC (the overall HTP changes). However, it remains unclear what the relationship is between the isomerization of the dopant molecule and the rotational modifications in the texture that are observed. In order to elucidate the mechanism for this rotational reorganization, experiments were carried out varying the type of molecular motor used (i.e. varying chiral induction, and isomerization times), structurally different LC media, varying concentrations, altering the dimensions of the glass rods on the surface, altering the layer thickness and the anchoring of the phase. These data were then used to design a

simulation to offer a rationalization for the rotational behavior of the liquid crystalline phase.

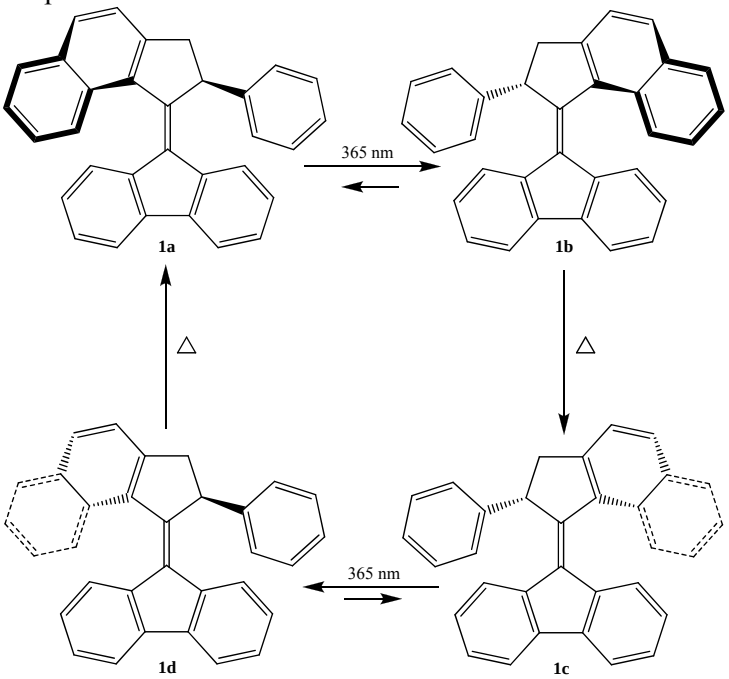

Scheme 3.1 Rotational cycle of a molecular motor.

3.2 Variation in dopant structure

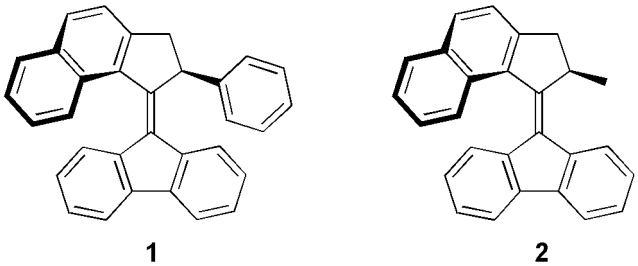

Scheme 3.2 The two molecular motors (**1** and **2**) used to determine the effect of a change in structure on the rotational behavior of the liquid crystalline phase. Both are depicted with *P* helicity (before irradiation).

It was shown previously[9] that rather small changes in the structure of a chiral dopant can have significant effects on the extent of chiral transfer from the chiral dopant molecule to the achiral mesogen. Therefore it was decided to study the effects of structural changes in both the dopant and the achiral mesogen used. Two different molecular motors (Scheme 3.2) and three different LC mesogens were used (Scheme 3.3). The molecular motors were selected on the basis that these gave the higher HTP values reported in chapter 2, and that the thermal barrier was high enough in order

for the phase at PSS to exist long enough for proper determination of the pitch.[9] Molecular motor **2** has a somewhat lower HTP and lower thermal barrier.[10]

MLC-6815 Blend referred to in text as MLC (average molecular weight M = 288.38 , T^{NI} = 340.15ºC)

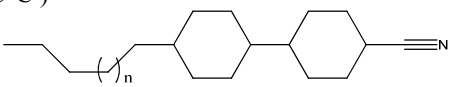

Felix R&D referred to as Semi (average molecular weight M = 253.374 g/mol, T^{NI} = 332 K,340. N.B. it is only nematic starting at 29.7ºC)

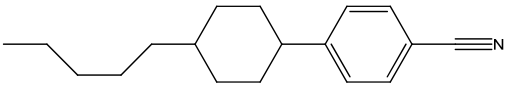

E7 Blend (average molecular weight M = 274.244 g/mol, isotropic-nematic transition temperature T^{NI} = 334 K)

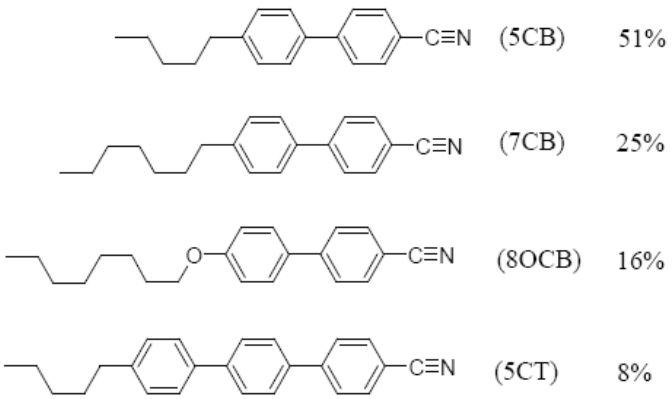

Scheme 3.3 The various LC blends used during the experiments.

3.3 Results

Samples consisted of 1 wt% of a molecular motor dopant relative to a liquid crystal mesogen. These were mixed thoroughly using a small amount of freshly distilled toluene (10μL) and then deposited on a rubbed polyimide surface (on a glass slide). For all experiments (as layer thickness cannot be controlled in this experiment)[†] an equal volume of the mixture was spread

[†] Thicknesses can only be fixed in closed systems, i.e. between two glass slides. In order to be able to observe the rotation of an object on the surface these closed systems could not be used. Therefore there will be some variation in layer thickness throughout the measurements.

on the surface each time (5 μL). Then small glass rods (length in the range of 10-20 μm) were deposited on the liquid crystalline film. Upon initiation of rotation a glass rod was selected for monitoring. The number of rotations and the time required for these rotations was measured. Reaching PSS was taken as the end of rotation.

3.3.1 The effect of changing the Liquid Crystal

Depending on the LC mesogen used, the ability of a chiral dopant to induce chirality amongst the matrix is decreased or increased. The difference in the helical induction (measured using the Grandjean-Cano method) of **2** towards the different LC mesogens was studied, in order to ascertain whether or not there is a trend between lower chiral induction (smaller HTP value) and fewer rotations of the phase. Three commonly available LC mesogens (e.g. blends E7, and the mesogen blends which will be referred to as Semi and MLC-6815), were studied (see Scheme 3.3).

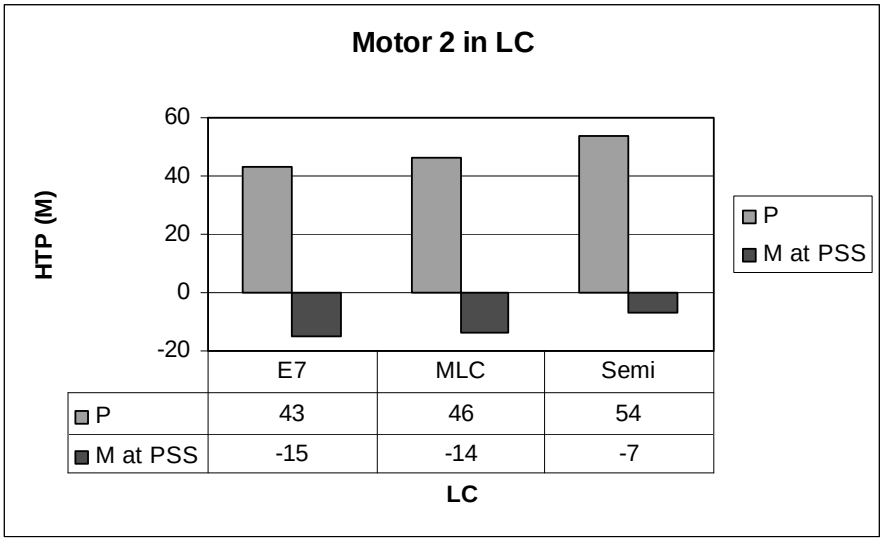

Graph 3.1 The HTP (μm^{-1}) of **2** in three different LC matrices. The values are given for the *P* isomer and for the *M* isomer at PSS (after irradiation of the sample). The reported HTP values have an error margin of 10 %.‡

From Graph 3.1 it is apparent that the HTP value for the *P* configuration for all three samples is similar within the limits of the error margins. However, the values recorded at PSS are very different. Under ideal circumstances, at PSS (if conversion is 100%) the HTP should be the inverse value as the *P* and *M* configurations are degenerate. There should be minor differences in the interactions between the mesogen and the *P* or *M* isomers. Thus, the reasons for the large differences in HTP at PSS must be mainly related to

‡ Error margin is based on the calculated standard deviation measured for the pitch length using the Grandjean-Cano method.

changes in the PSS achieved. This could be due to the different viscosities of the LC matrices which might influence the actual ratio of *M* to *P* isomer reached at PSS. The light of the irradiation source is also partially absorbed by certain mesogens (to give fluorescence), depending on the exact structure, and therefore may vary in intensity. Thus the efficiency of irradiation, although the same source is used, might be different.

Though the amount of isomerization differs per LC used during the irradiation of the phases with 365 nm light, the *cis* to *trans* isomerization of the central double bond occurs in the overcrowded alkene. As a result the surrounding mesogen molecules reorganize altering the surface organization so that the surface texture is observed to rotate. This rotational behavior is observed for all motor **2**/LC combinations.

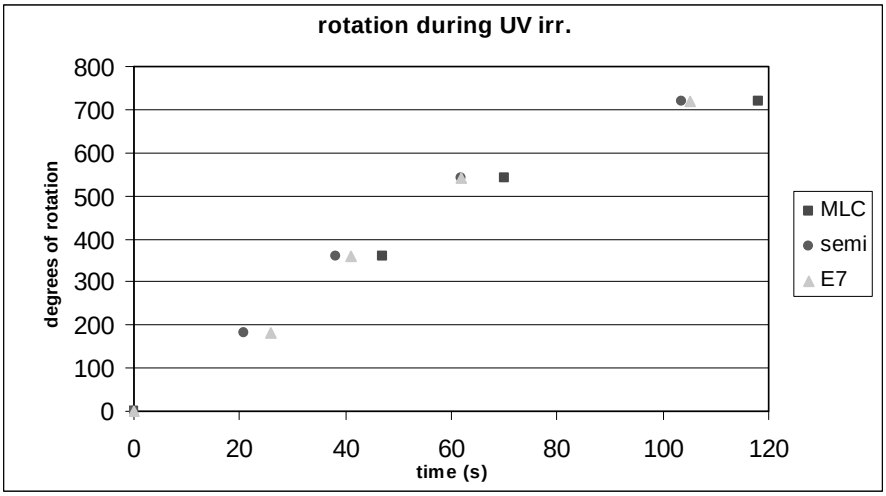

Graph 3.2 Degrees of rotation (measured as described in section 3.3) under UV irradiation of the phase achieved as a function of time for motor **2** in various LC matrices.

	Slope (degrees/s)	R^2
MLC	6.6	0.958
Semi	7.6	0.955
E7	7.5	0.960

Table 3.1 The number of degrees of rotation per second achieved in each LC blend, along with the R^2 values to indicate the validity of the drawn tangent.

The data (Graph 3.2) shows that the degree of rotation achieved in all 2/LC systems is the same. Each completes 720° of rotation. There is a slight difference in the actual rate of rotation between the systems. The correlation suggests that the rate of rotation is slowest for MLC and that Semi and E7 have approximately the same rates. However, the rate is in the same order of magnitude for all the LCs, thus it falls within the error margin. Based on these results all of these LC phases work equally well.

3.3.2 The effect of the structure of the molecular motor on particle rotation

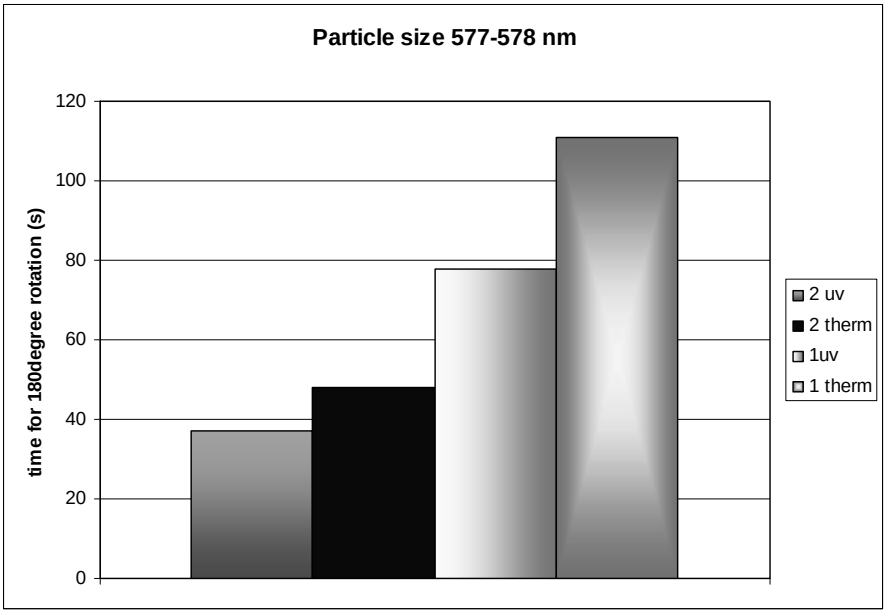

Graph 3.3 Comparing the duration of the first 180° rotation of particles of similar size in **1** and **2** under UV irradiation and thermal back reaction in E7.

When comparing **1** and **2** (the two molecular motors with the highest HTP, **1** is the better chiral inducer, see chapter 2), similarly sized particles always rotate slower in the **1**-LC system (see Graph 3.3). In both cases the rotational reorganization that is caused by thermal isomerization is slower than that resulting from the UV irradiation. This is not unexpected as the thermal inversion in solution for both molecular motors is slower than the corresponding photochemical isomerizations. The rotational behavior seems to be influenced exclusively by the kinetics of the photoisomerization and the thermal isomerizaton of the specific molecular motor being used and not the ability to induce chirality. Compound **2** is known to be a faster motor than **1**.[15] Both phases undergo an equivalent number of degrees of rotation.

3.3.3 Particle-size dependence on rotation

It had been previously observed that deposited glass rods on the surface of the LC phase rotate along with the rotational reorganization of the surface of the LC phase. Not only glass rods but also small salt crystals were rotated. Depending on the size of the glass rod deposited on the surface the behavior could be different. Depending on the size of the pitch of the LC matrix it might be easier to exert force on a similarly sized particle. To determine whether or not this hypothesis is true, various concentrations of

2/ E7 were prepared. The ability for the phase to rotate the particles of a certain size was then determined.

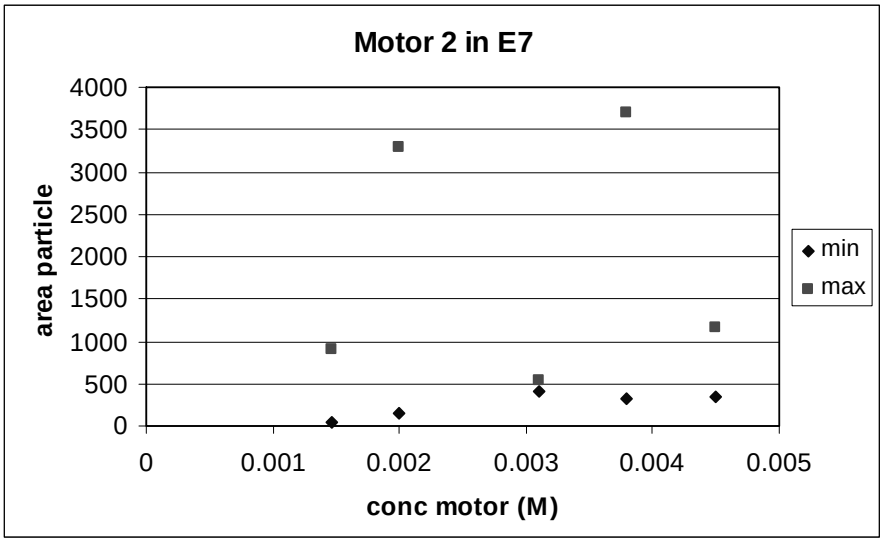

Graph 3.4 Correlation of the particle size in μm^2 (maximum and minimum that were observed to rotate) versus the concentration of **2** used.

A large range of glass particles has been observed to rotate on the LC phase corrugated surface (see Graph 3.4). It became very apparent that the "homogeneous" glass rods in fact contained a large variety of sizes ranging from approximately 100 μm^2 up to more than 4000 μm^2 (dimensions of rods determined by individually measuring their lengths and widths using Matrox software). Rotation was more efficient for rectangularly shaped particles than square ones. As the glass rods supplied were not homogeneous, large particles were not always present on top of the sample studied (i.e. 0.003 M solution showed no rotation of large particles because there were none present). Very large particles (>5000 μm^2) did not rotate at all. These sank directly through the cholesteric phase to the glass surface. However, it can be concluded that a wide range of particle sizes can rotate on the surface and it appears to be relatively independent of the concentration as the largest particle observed to rotate in the case of 0.002 and 0.004 M are similar in dimensions. It must be remembered that potentially larger and smaller particles could be rotated on these surfaces, however, these were not present in the glass rod sample.

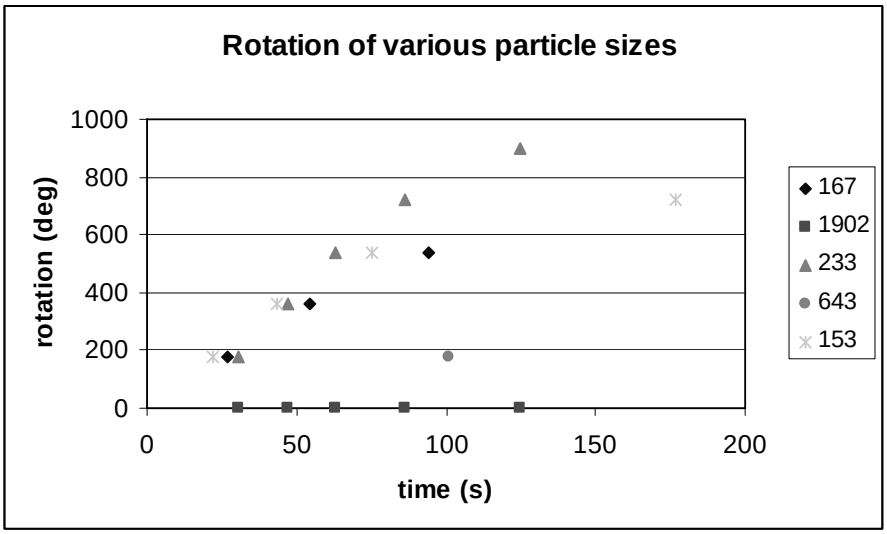

Graph 3.5 The degrees of rotation with time (s) for various sized (surface area in μm^2) glass rods being monitored during the irradiation of the phase under UV irradiation. The sample has a concentration of 0.002M of motor **2** in E7. The pitch is approximately 13 μm. Certain particles stop rotation before the 900º end point in the graph due to spontaneous sinking or envelopment in defects. Apparent PSS is reached at approximately 3 min.

As can be seen from Graph 3.5, using an LC phase with a pitch of approximately 13 μm, various particles could be observed to rotate. The largest, (1902 μm^2) showed no rotation at all. For the first 360º of rotation most of the glass rods seem to move with similar speed. The rod with an area of 643 μm^2 showed only 180º rotation which was much slower than that observed for the other rods. A trend for all observed rotations can be drawn, that with time the rotation slows down. This seems plausible as the rearrangements in the phase upon reaching PSS become smaller.

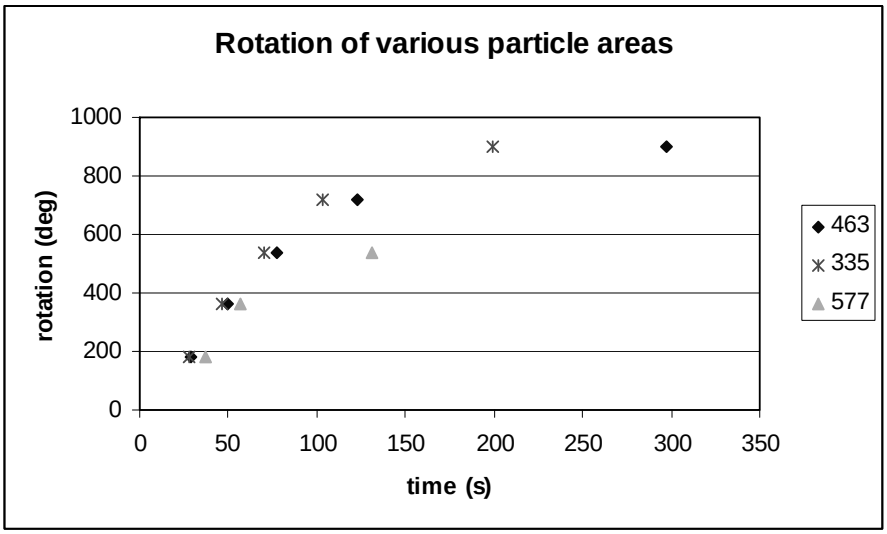

Graph 3.6 The degrees of rotation with time (s) for various sized (area in μm^2) glass rods being monitored during the irradiation of the phase under UV irradiation. The solution has a concentration of 0.0045 M of motor **2** in E7. The pitch is approximately 5 μm. Certain particles stop rotation before the 720º end point in the graph has been reached owing to spontaneous sinking or envelopment in defects.

Compared to Graph 3.5 the data presented in Graph 3.6 were measured at approximately double the concentration of **2**, resulting in a tighter pitch. Again it can be observed (Graph 3.6) that with time the rotation slows down. This trend is irrespective of the pitch of the cholesteric phase (Graph 3.5 at 13 μm and 3.6 at 5 μm). It seems that the glass rods of largest area slow down first i.e. the glass rod with area 577 μm^2. For the first 360º both the 334 and 463 μm^2 rods have similar rotation times, however after this point their rotational behavior changes significantly. It took the smaller rod (334 μm^2) 199 s to rotate 900º, while it took the particle with area 463 μm^2 298 s to accomplish the same movement. This difference of almost 100 seconds is significant. At higher dopant (**2**) concentration (Graph 3.6) the particle with area 334 μm^2 took slightly longer than 200 s to complete rotation. In the case of a lower concentration (Graph 3.5) a particle with area 233 μm^2 took 130 s. The smaller particle is approximately 70% of the size of the larger. This difference is similar to that observed in the time required for rotation. Thus the differences observed are irrespective of the concentration of chiral dopant.

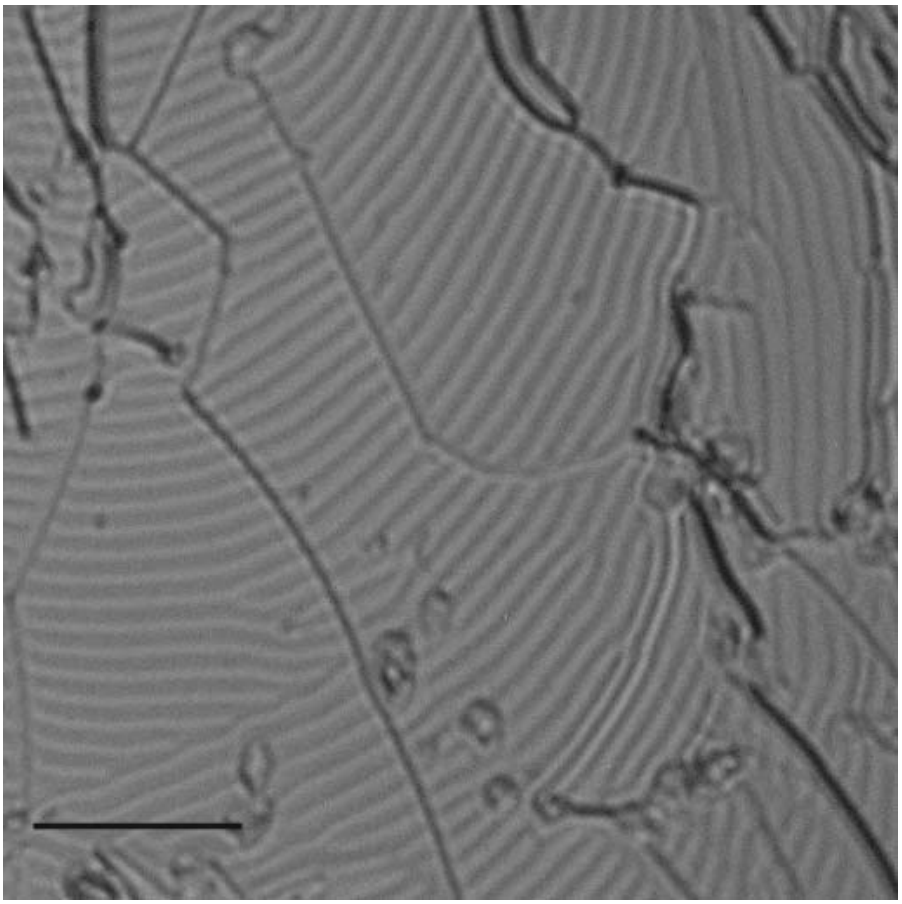

Figure 3.1 Optical micrograph of a 1 wt% solution of **1** in E7 demonstrating the wealth of defects visible on top of the anticipated fingerprint structure. The scale bar represents 100 μm.

The presence of the glass rods affects the surface texture. The larger particles appear to slowly sink towards the bottom of the LC phase towards the substrate. Though initially capable of rotation, it has been observed that after prolonged periods (depending on the size of the rod between 10-40 min) of time several particles are no longer able to rotate. The presence of defects (see Figure 3.1 for examples of the various types of defects that occur) on the surface can also impede the rotational behavior as it can entrap the glass rods. These defects occur in all LC phases since the orientational ordering is not perfect. However, these are most common in thicker LC layers (no exact quantification is possible, however, from the microscope it is possible to determine that these layers have various focuses of the texture, which is not possible in many of the previously conducted experiments). An additional problem is that during the rotational reorganization, these defects seem to dissipate into the surroundings accompanied by the generation of Brownian motion (observed by

translational motion of the particles) seems to govern the motion of the particles rather than the rotational behavior observed at this point in time. This dissolution of these defects generally occurs near infinite pitch (the surface lacks any visible modulation). As the defects fall apart the particles start to drift sideways. Their motion is governed by the induced turbulence. Though after several irradiation cycles fewer defects are observed, these samples were never used to determine the number of rotations as the starting point would never be purely the *P* isomer of the molecular motor.

However, despite all these influences, when looking just at two rather similarly sized particles, in the same concentration LC phase, far from defects, the rotational behavior will still vary greatly (Graph 3.6). A possible reason for this is that the height of the glass rods cannot be determined. As the previous section has confirmed, the "homogeneity" of the glass rod sizes leaves something to be desired. Therefore as the width and length of these particles vary greatly, the height/thickness could also vary dramatically. Thus, depending on the exact thickness of the layer of the LC phase the particles will sink more easily (heavier than other thinner glass rods of similar dimensions) or never rotate at all as these might reach the bottom (the polyimide substrate) directly.

3.4 Conclusions on rotational behavior of glass particles

During the study of the rotary behavior of the LC phase it was observed that the thermal cycle times are always slower than UV-irradiation induced cycle times. This is in agreement with the kinetics of the thermal isomerization processes for both **1** and **2** which are slower than the kinetics of the photoisomerization. The rotation of the phase is faster in the case of E7 doped with **2** than **1** upon UV irradiation. The photoisomerization of **2** is faster in solution than that for **1**. Varying the structure of the dopant had relatively little effect upon the number of rotations observed for the phase. Varying the type of liquid crystal mesogen did not influence the number of rotations of the phase observed, however, the LC which contained no aromatic moieties was the slowest. Upon rotation the glass particles appear to slow down with time. At very high dopant concentration, particles deposited upon the phase did not rotate at all owing to the large number of defects. In general defects are able to restrain the glass rods, only upon dissolution of the defects are the glass rods released giving way to Brownian motion. With time most particles sink through the phase. Sadly no discernable trend can be ascribed to the dimensions of the particle and its rotational behavior, as in some cases larger particles rotated longer and faster and in other cases smaller ones. Thus the rotation of the rod is not an accurate measure for rotation of the phase though the error in measuring it is less than that of a phase with no particle deposited on it.

3.5 The anchoring of a phase

The cholesteric textures observed by optical microscopy under crossed polarizers reflect the transmittance of the film. These depend on the direction of the director within it, and can be influenced by the interactions with the surface (Scheme 3.4).[11] When the director of the cholesteric LC phase is anchored according to planar boundary conditions at both interfaces (P-P anchoring), the long molecular axis is parallel to the substrate. As a result the cholesteric helix is oriented perpendicular to the surface. Planar-planar anchoring can be characterized by "oily streak" textures.[11] In the case of homeotropic boundary conditions at both interfaces, the cholesteric helix orients parallel to the substrate. The typical fingerprint texture is observed in this case. The effect of hybrid anchoring (planar anchoring on one surface and homeotropic anchoring at the other surface) on cholesteric LC systems has been far less studied. Hybrid anchoring also results in fingerprint textures.[12]

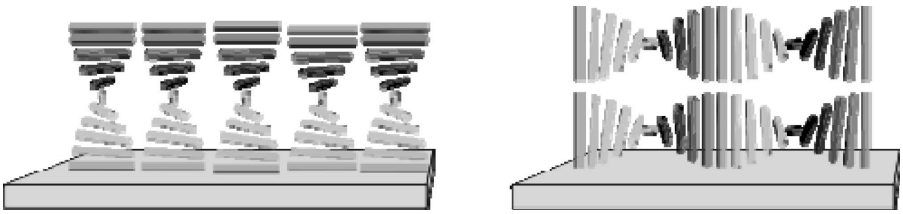

Scheme 3.4 Anchoring of a cholesteric liquid crystal on a surface: planar (P), on the left, and homeotropic (H), on the right. The rods represent the orientation of the director.

In the setup used in our group for the previous rotational reorganization experiments, a rubbed polyimide functionalized glass slide was used as one surface and air as the other surface.[8] Rubbed polyimide surfaces are known to induce planar anchoring. However, under the microscope with cross-polarizers, fingerprint textures could be observed rather than the expected oily streaks. Therefore it became clear that in our semi-free system we were dealing with two different types of anchoring having an influence on each other.[13] Owing to the lack of information in the literature as to the interactions between the mesogens and air, it became crucial to discover whether or not these semi-free (the sample is sandwiched between a surface and air) samples undergo hybrid anchoring. To support this hypothesis a molecular motor (**1**)/LC system was used with different anchoring situations.

Semi-free anchoring

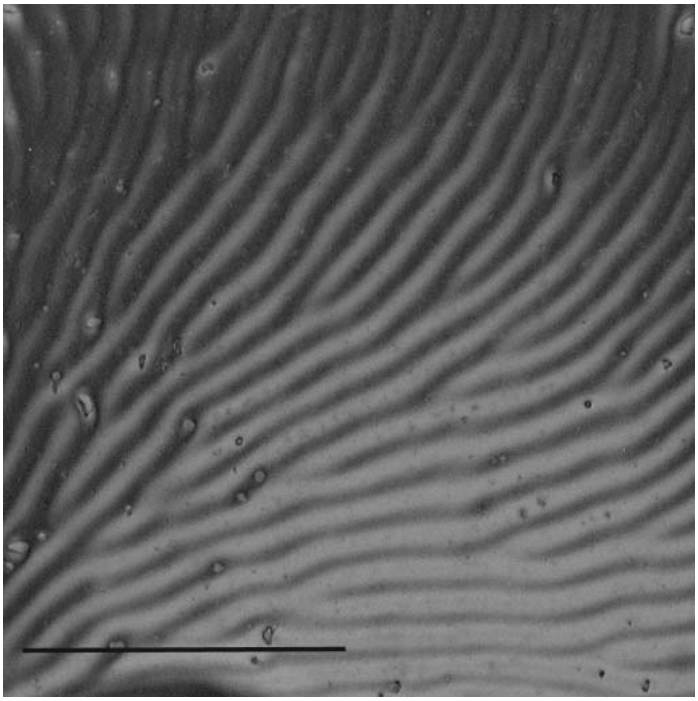

Figure 3.2 Optical micrograph of an E7 phase doped with 1 wt% of molecular motor **1** sandwiched between a rubbed polyimide functionalized slide (rubbing alignment from north to south on the image) and air. The scale bar represents 200 μm.

In the case of semi-free anchoring, the LC phase is deposited on a planar anchoring slide (functionalized with polyimide and rubbed in one direction) and left free to the air (the second anchoring surface). In all cases the phenyl-functionalized molecular motor (**1**) was used as it has the highest HTP in E7. A cholesteric fingerprint texture can be observed. However, when determining the pitch length from the periodicity of the surface fingerprint texture a value which was approximately twice as large as the pitch that was determined using the Grandjean-Cano method was obtained. When looking at larger domains arch textures could be observed. The frequency of these arches increases towards the rims of the cholesteric film.

Upon irradiation with UV (365 nm) light the phase rotates. The observed texture periodicity decreases (length between ridges increases) until an optically nematic phase is reached. The ridges reappear and move closer together until PSS is reached. The phase rotates throughout this cycle. The process is thermally reversible.

3.5.1 Planar-planar (P-P) anchoring

In the case of P-P anchoring, the LC phase was deposited between two planar anchoring slides (functionalized with polyimide and rubbed in one direction). The slides were aligned so that the rubbing directions matched. The phenyl-functionalized molecular motor (**1**) was used as it has the highest HTP in E7. In the case of P-P anchoring a typical oily streak texture is observed. Upon irradiation no rotation was observed. There were some minor changes observed such as color changes. However, these changes were not significant compared to those previously reported.

3.5.2 Homeotropic-homeotropic (H-H) anchoring

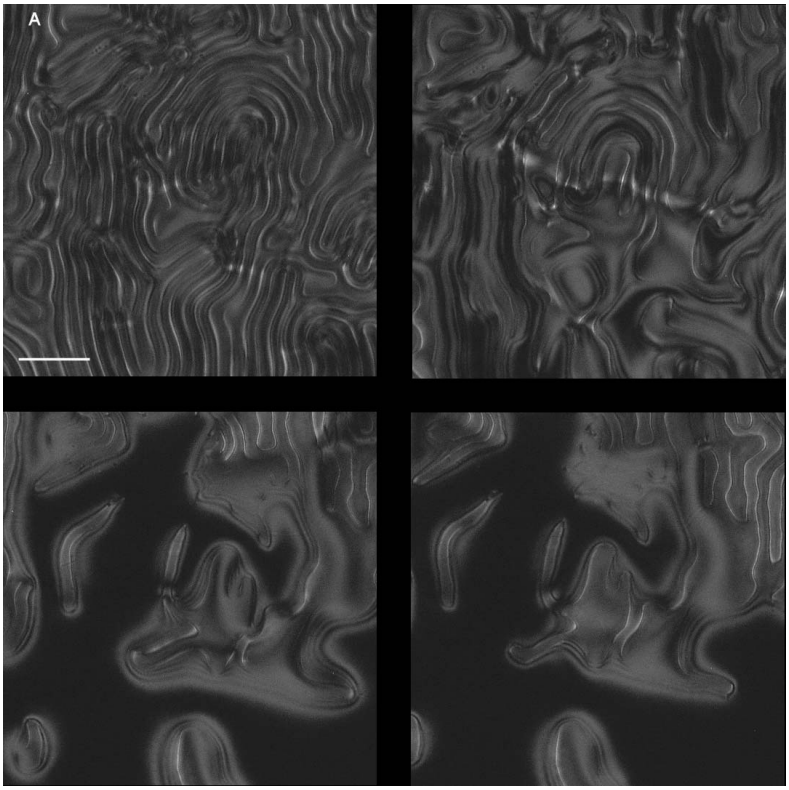

Figure 3.3 Optical micrograph of the UV irradiation cycle of an E7 phase doped with 1 wt% of **1** sandwiched between two OTS[§] functionalized slides with a Teflon spacer with a thickness of 25 μm. The scale bar represents 50 μm. A) t = 0 B) 3 min C) 6 min D) 9 min.

[§] OTS functionalization is known to generate homeotropic surfaces. See for instance ref 38.

In the case of H-H anchoring, the LC phase is deposited between two homeotropic anchoring slides (functionalized with OTS (*n*-octyltrichlorosilane)). In all cases the phenyl-functionalized molecular motor (**1**) was used as it has the highest HTP in E7. The typical fingerprint pattern associated with a cholesteric phase was observed. The phase appeared rather chaotic as neither of the surfaces offers any directional orientation (no pre-alignment owing to rubbing). Upon irradiation (Figure 3.3c) no rotational behavior was observed. However, upon irradiation with UV light a lengthening of the pitch could be observed (pitch determined from period of the fingerprint texture). Upon continued irradiation the period of the surface pattern decreases until eventually the entire image appeared black (this might indicate alignment of the LCs corresponding to the orientation of the polarizers). Once the irradiation was stopped no further changes were observed within the system. Thus the process was no longer reversible. A plausible reason for this, is that in fact the lack of color observed through the crossed-polarizers indicates the presence of air. As the LC is irradiated, the mesogen molecules might seep out through the Teflon spacer slowly, causing an air-filled pocket to remain.

3.5.3 Planar- Homeotropic (P-H) hybrid anchoring

The hybrid system was generated between a planar and a homeotropic anchoring slide (bottom slide is polyimide functionalized (rubbed in one direction) and the top slide is OTS-functionalized). The phenyl-functionalized molecular motor (**1**) was used as it has the highest HTP in E7, still shows the characteristic fingerprint textures observed for an H-H system (Figure 3.3). However, when looking at larger areas an arch-texture (the fingerprint texture is arched/curved) can be observed as was observed in the case of the semi-free anchoring (see Figure 3.2).

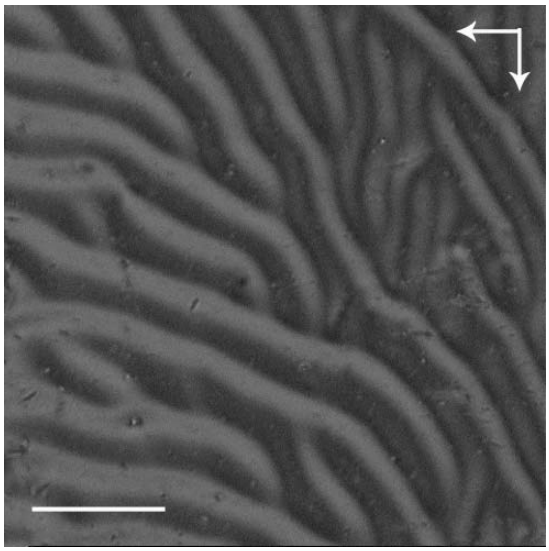

Figure 3.4 Optical microgram of an E7 phase doped with 1 wt% of molecular motor **1** in a cell of rubbed polyimide functionalized slide (rubbing alignment from north to south on the image) and a silane functionalized upper slide. The cell has a spacing thickness of 10 μm. The scale bar represents 50 μm. The arrows represent the orientation of the crossed polarizers in this image.

Only the hybrid system shows the change in pitch length and the rotational behavior as observed for the semi-free system. These changes are accompanied by a change in color observed through the crossed polarizers (from green to yellow). The rotational speed seems slightly decreased compared to that of the sample with semi-free anchoring conditions. As was the case for the H-H system, the sandwiched hybrid system reaches infinite pitch but seems unable to pass this point despite extended irradiation times. After the irradiation is stopped, and the thermal isomerization of the molecular motor occurs, the system remains unchanged. This is contrary to the semi-free system where an opposite direction of rotation is observed and a returning of the fingerprint texture. Thus in the closed system the rotation is no longer reversible.

3.5.3.1 Variation of LC layer thickness

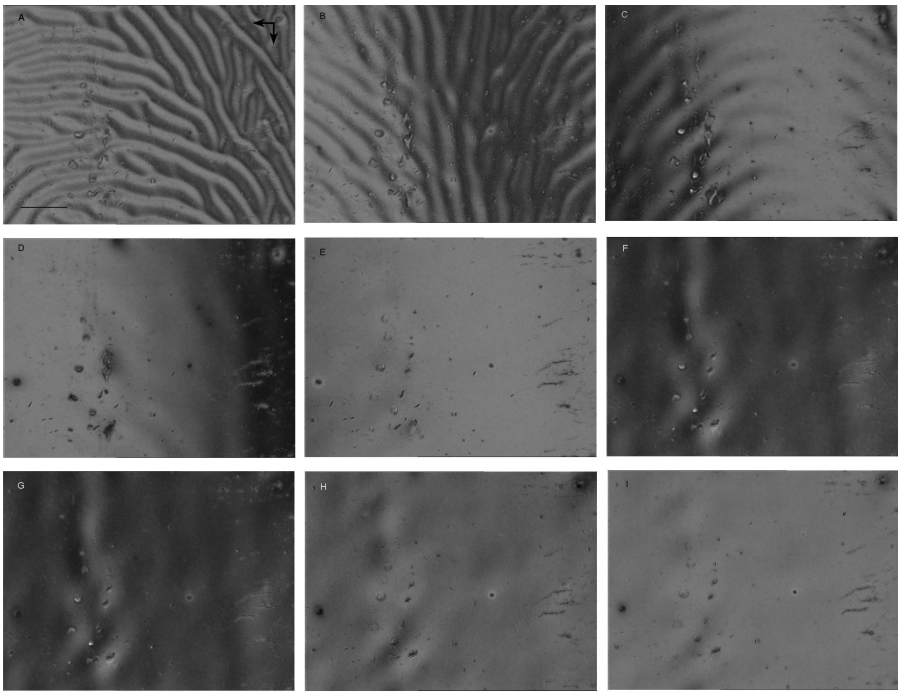

Figure 3.5 Optical micrographs of the rotational reorganization of the LC film upon irradiation with UV light of a hybrid anchoring cell with a layer thickness of 25 μm containing a sample of molecular motor **1** in E7 (0.96 wt%). A) t = 0 B) 1 min C) 2 min D) 3 min E) 4 min F) 9 min G) 15 min H) 34 min I) 49 min. The arrows represent the direction of the crossed polarizers. The scale bar equals 50 μm.

Figure 3.5 shows the rotational reorganization of the hybrid system LC phase. Full alignment of the liquid crystals along the axis of the crossed polarizers (black image) is achieved after five hours and fifteen minutes. No reformation of the fingerprint texture is observed. The observed infinite pitch (apparently no changes in the finger print texture) is reached within minutes. It is assumed that the longer reorganization times recorded are owing to the fact that the presence of a second surface on the top induces pressure on the system, which is not present in the semi-free system. In addition, the complete disappearance of the surface texture does not equate exactly to what is happening below as there is some disparity in the elastic boundary layer. Also, as was the case with the H-H system, the black area observed through the crossed polarizers, other than indicating alignment, could indicate seepage of the LC matrix through the Teflon. Interestingly, when a layer thickness of 10 μm was used barely one full rotation was observed (contrary to the four rotations for 25 μm thickness layer). Thus, the duration and number of rotations observed is dictated by the layer thickness used.

3.6 Theoretical study

In conjunction with our experimental data computer simulations were carried out in an attempt to clarify the exact mechanism for the observed rotational reorganization of the LC phase. This study focuses on the phenyl-substituted molecular motor **1** in Scheme 3.5 as the kinetic behavior of this molecular motor in solution is well precedented.[15] As previously described in chapter 2, irradiation with UV light (λ = 365 nm) and subsequent thermal isomerzation allows for the unidirectional rotation of the upper rotor part of the molecular motor relative to the lower stator part around the central double bond (the axis of rotation). As this molecular motor has a symmetrical lower half both **1a** and **1c** are degenerate.

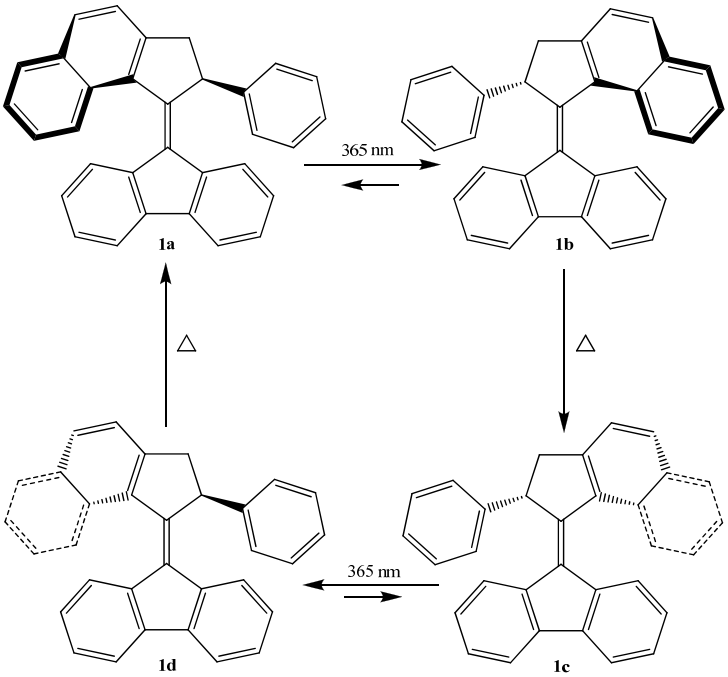

Scheme 3.5 Unidirectional rotary cycle for the phenyl-substituted molecular motor **1**.

The liquid crystal of choice in this study is the blend E7 (for the exact composition, see Scheme 3.5). This nematic achiral LC has shown high compatibility with molecular motor **1** (see chapter 2 for high HTPs). Its elastic constants and behavior with respect to temperature are well precedented.[21]

As stated previously, the helical twisting power (HTP) is a measure of the ability of a chiral molecule to induce a twist in the nematic host. In this case we are studying the LC system under irradiation of the molecular motor

molecule resulting in the isomerization from **1a** to **1b.** Therefore throughout the irradiation there are varying ratios of these two isomers within the LC matrix. The resulting HTP at any given time is thus a sum of the individual contributions of each isomer:

$$\mathrm{HTP} = \sum_i x_i \ \mathrm{HTP}_i \qquad 1$$

where HTP_i is the HTP value of isomer *i* and x_i is the fraction of isomer *i* $(\sum_i x_i = 1)$.

It is well precedented that the molecular motor **1a** (Scheme 3.5) induces a HTP of +90 μm^{-1}. For **1b** the HTP is -90 μm^{-1}. However, when irradiating the motor/LC system the interconversion between **1a** and **1b** is not complete. At the PSS the HTP measured is -59 μm^{-1}. The exact isomer population is known in solution,[15] however, it is not known in the liquid crystalline matrix.

In this section we will look at the effect of the anchoring, and the isomerization of **1** on the rotational behavior of the LC phase as predicted by calculation and comparison with experimental data.

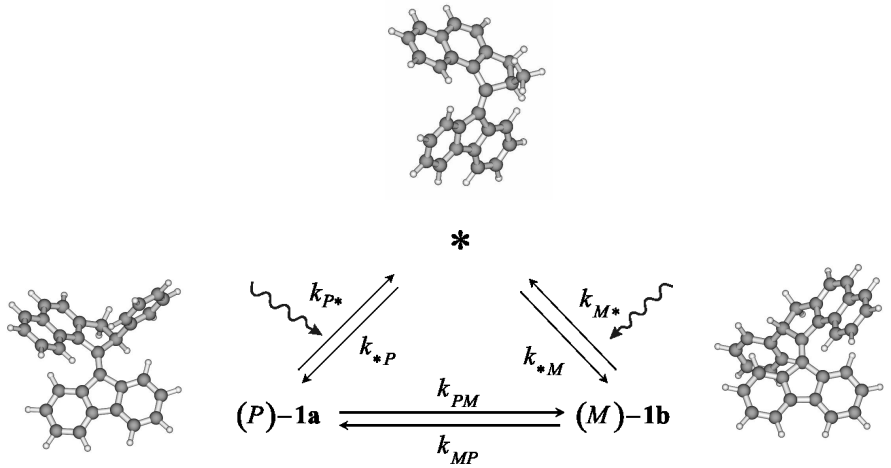

Figure 3.6 Schematic representation of the kinetics of the molecular motor during irradiation with UV light, showing the optimized geometry of the stable (***P***) and unstable (***M***) isomers and the excited state. The geometry was determined using DFT, B3LYP/6-31g** level.

Upon irradiation with UV light molecular motor **1** undergoes photoisomerization of the central double bond. This process is shown schematically in Figure 3.6. The geometries of **1a** and **1b** (Figure 3.6) were obtained using DFT calculations at the B3LYP/6-31g** level. [14] To ascertain the accuracy of the calculations the obtained molecular geometry of **1a** was compared to the X-ray structure.[15] The isomers **1a** and **1b** are almost exact mirror images of each other when looking at the naphthyl and

fluorene moieties. The naphthyl moieties are twisted on opposite sides of the central double bond. The quantum mechanical analysis of the saddle point of the isomerization pathway was also calculated using DFT at the B3LYP/6-31g** level. These calculations show that the isomerization process involves the concerted displacement of several atoms.

Throughout the irradiation experiment, the rate of the photoisomerization will determine the ratios between the *P* and *M* isomers at various stages throughout the system. In order to determine the kinetics of this system and the subsequent effects of these upon the LC phase rotation several assumptions were made.

At any time the LC system is in equilibrium as the reorganization time of the phase is negligible compared to the characteristic times required for the isomerization of the molecular motor. The presence of the liquid crystalline blend E7 can affect the photoisomerization either by affecting the number of photons reaching the molecular motor, or through friction. However, the viscosity effects of E7 are not expected to be dramatic.[16] The estimated ratio is $\eta^{300}/\eta^{345} \sim 4$ (E7 is nematic at 300 K and isotropic at 345 K). Considering that the viscosity of isotropic E7 at 345 K is likely to be higher than that of *n*-hexane at room temperature (0.3 cP)[17], a decrease of the rate constant by at least an order of magnitude in E7 could be expected.

After applying the assumptions indicated, the molar fraction $x_{M,PSS} \sim 0.8$ can then be estimated[14], and compared with the value $x_{M,PSS} = 0.86$ obtained from ^{1}H-NMR experiments in liquid toluene at -40 °C. As the conditions of the UV irradiation source (i.e. wattage and exact amount of light reaching the sample) are not consistent, the similarity between these values can be taken as a check of the kinetic parameters assumed.

As the kinetics of the system are modeled the next step is to attempt to determine the interaction that either conformer might have on an LC host such as E7. Most properties of liquid crystals are described in terms of a director field which is locally defined by the average orientation of the molecules. The director introduces a relevant intermediate length-scale, between the molecular and the macroscopic levels, whose behavior can be described by the continuum theory: the director deformation, over distances much longer than the dimensions, is opposed by elastic restoring torques, as described by the Frank expression:[18]

$$a_{el} = K_t q + \frac{1}{2} K_{11} s^2 + \frac{1}{2} K_{22} q^2 + \frac{1}{2} K_{33} b^2 \qquad 2$$

where a_{el} is the Helmholtz free energy density, and *s*, *q*, *b* denote the three deformation nodes of an LC, $s = \nabla \cdot \mathbf{n}$ (splay), $q = -\mathbf{n} \cdot (\nabla \times \mathbf{n})$ (twist),

$b = \mathbf{n} \times (\nabla \times \mathbf{n})$ (bend). The K_{ii}'s are the corresponding *elastic constants* and K_t is the so-called *chiral strength*, which disappears in an achiral sample. The equilibrium configuration of the director in the bulk corresponds to the minimum of the elastic free energy. A cholesteric LC is characterized by a twisted director (thus twist elastic constants are used), with wave number:

$$q = 2\pi/p = - K_t/ K_{22} \qquad 3$$

In doped cholesteric LCs the chiral strength K_t depends on the concentration and the nature of the chiral dopant present. At low dopant concentration K_t can be assumed to be proportional to the concentration of the dopant and K_{22} equal to that of the nematic LC host. Thus eq. 1 can be used to determine the HTP. During the irradiation with UV light of the sample a changing ratio of the two isomers **1a** and **1b** are present. As a consequence $K_t = x_P\ K_{t,P} + x_M\ K_{t,M}$ where $K_{t,P(M)}$ is the chiral strength contribution from either the *P* or *M* isomer; it follows that the HTP of the mixture is given by eq. 2.

The *surface interaction* model was first developed by A. Ferrarini to emulate the chiral induction of azobenzenes. It provides an expression connecting the chiral strength to the structure of the chiral dopant; the following expression is obtained for the HTP:[19]

$$\mathrm{HTP} = AQ \qquad 4$$

where Q is the so called surface chirality parameter, specific for the chiral dopant used, and A is a quantity which depends on the nematic LC host being used; it is defined as $A = N_A\xi\ /2\pi K_{22} v_m$, with N_A being Avogadro's number, v_m the molar volume of the LC host, and the parameter ξ the orienting strength, which is related to the degree of order of the LC host. It follows from the definition that the value of A for a particular LC host is a function of temperature and depends on the structure of the LC host, mainly through the twist elastic constant. It can simply be taken as a scaling parameter when comparing calculated and experimental HTP values for different chiral dopants in the same LC host.[20]

The key property accounting for the twisting ability of a given dopant is the surface chirality parameter Q, which is proportional to the average helicity of the molecular surface in the nematic environment. Labeling as x and y the molecular directions which tend to lie perpendicular to the director we can write:[18]

$$Q = - 6^{1/2} (Q_{xx} + Q_{yy})S_{\perp} \ + \ 6^{-1/2} (Q_{yy} - Q_{xx})\ \Delta S_{\perp} \qquad 5$$

where Q_{ii} is the helicity of the molecular surface along the *i*-th axis and $S_{\perp} = (S_{xx} + S_{yy})/2$ and $\Delta S_{\perp} = (S_{xx} - S_{yy})$, with S_{ii} being the order parameters which specify the degree of alignment of the *i*-th molecular axis tot the local director in the cholesteric phase. The S_{ii}'s are the principal values of the Saupe matrix,[21] with $-0.5 \leq S_{ii} \leq 1$; the molecular axes (*i*) are parallel to the principle alignment directions in the molecule. Positive and negative S_{ii} values mean that the corresponding axes tend to lie parallel or perpendicular to the director, respectively. The order parameters are identical for the mirror images of a molecule while the Q_{ii}'s, thus the chirality parameter *Q*, take opposite values for enantiomeric pairs. Due to the fluid nature of the liquid crystal mesogen, dopants can sample all orientations, with certain preferences described by the order parameters; differently oriented dopants promote twist of the nematic director of different magnitude and handedness and the resulting twist is a weighted average over all possible orientations.

The Saupe matrix and chirality parameter have been calculated for the *P* and *M* isomers assuming the geometries obtained from the DFT calculations[14] and the X-ray data in the case of the *P* isomer[15]. The results are shown in Table 3.2. Figure 3.8 shows the principal alignment directions for the isomer **1a**. As the order parameters are similar for **1a** and **1b** the orientational behavior in the LC host is essentially the same. This behavior can be classified as disc-like: the *y* axis (perpendicular to the fluorene plane) is predicted to preferentially orient normal to the local director; the large difference between S_{yy} and S_{zz} shows significant anisotropy in the alignment to the director of the fluorene plane. The S_{yy} value indicates a significant degree of order in the system.

		S_{ii}	Q_{ii} (Å^3)	Q (Å^3)	HTP exp (μm^{-1})
1a[§]	x	0.06	-17	+36	+90
	y	-0.28	95		
	z	0.22	-77		
1a[‡]	x	0.05	-19	+30	
	y	-0.27	79		
	z	0.23	-59		
1b[§]	x	0.05	20	-37	Not available
	y	-0.28	-96		
	z	0.23	76		

Table 3.2 Order parameters of **1** (obtained giving the orienting strength the value $\xi = 0.025$ Å^{-2}), corresponding diagonal elements of the chirality tensor (***Q***), chirality parameter *Q* and measured HTP values.[8] *x, y, z* are the principal axes of the Saupe matrix. [§] Geometry from DFT calculations[14], experimental HTP not available as measured at PSS and not pure **1b** isomer. [‡] X-ray geometry[15].

Linear dichroism measurements give the order parameter of the electronic transition dipole as $S_{\mu\mu} = (A_{//} - A_{\perp}) / (A_{//} + 2A_{\perp})$ where $A_{//}$ and $A_{\perp}$ are the absorbances parallel and perpendicular to the director.[22] The value obtained for $S_{\mu\mu} = 0.07$ for a racemic mixture of **1** in K18 at room temperature.[23] If we assume that the transition dipole is close to the central double bond $S_{\mu\mu} \sim S_{xx}$, (Table 3.2). The high and positive value for Q_{yy} of isomer **1a** indicates a strong induction of right-handed helicity which explains the induced right-handed cholesteric helix. The calculated Q_{ii} values for **1b** are similar in magnitude to **1a** but of opposite sign. Thus the calculations predict $HTP_P \sim -HTP_M$. This can be explained by the fact that the fluorene and naphthalene moieties are twisted at approximately the same angle with respect to each other but in opposite sense. The phenyl substituent which changes from the pseudoaxial to pseudoequatorial orientation appears to have little affect on the isomer's twisting capability.[24] The contributions of the different molecular groups on the HTP for both isomers are illustrated in Figure 3.8: the darker the color[25] the stronger the chiral induction amongst the mesogens. It can be seen that **1a** has a strongly positive effect while **1b** is strongly negative (explanation for the differently induced helicities). In both cases the phenyl is almost colorless, indicating no particularly strong inductive preference for either orientation.

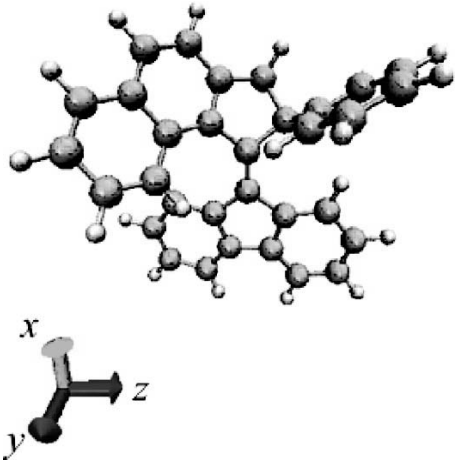

Figure 3.7 Principal alignment axes of the stable isomer (*P*) of **1** in a nematic environment.

Using the results $HTP_M \sim -HTP_P$ in eq 2, the isomer population in the PSS state in the cholesteric film can be calculated, given the HTP values measured with the Grandjean-Cano technique for the isomers **1a** (+90 μm^{-1}) and **1b** at PSS (-59 μm^{-1}). The value $x_{M,PSS} = 0.83$ is close to that derived from ^{1}H-NMR experiments in toluene at -40 ºC, $x_{M,PSS} = 0.86$.[15] This suggests that the isomerization rates should not be dramatically altered on going from isotropic to the LC mesophase.

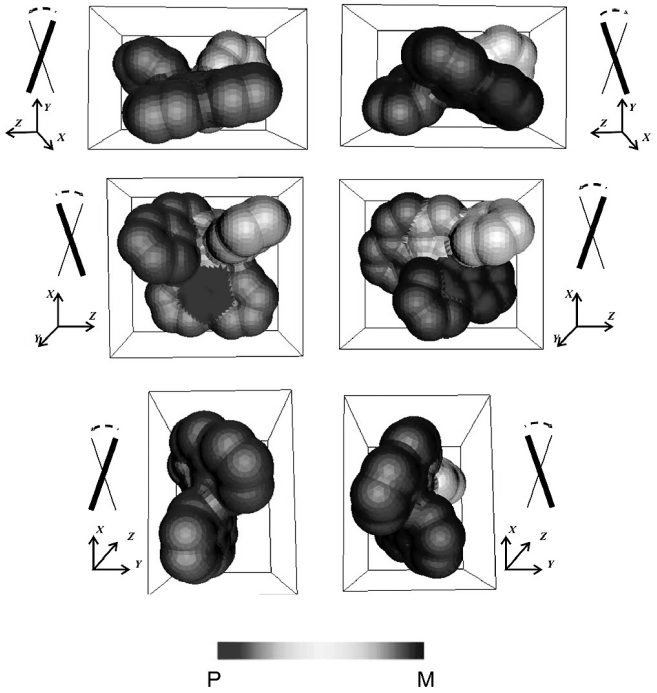

Figure 3.8 Views of the molecular surface of **1** along the principal alignment axes (left: **P** isomer, right: **M** isomer). The color code indicates the contribution to HTP of each functional group. At the side of each figure, the helicity along the view axis is schematized. The molecular surfaces are generated with MSMS[26] and visualized with Geomview[27].

The analysis presented in the previous section establishes a quantitative connection between the structure of the two isomers of molecular motor **1** and the director twist they induce in the cholesteric mesophase. This is, however, insufficient to explain the observed macroscopic rotation observed. A further insight into the director configuration in the semi-free film of cholesteric LC is needed.

As mentioned in section 3.6 (Scheme 3.4), depending on the type of anchoring induced by the substrate, the mesogen will orient differently. Hence the cholesteric helix orientation is altered depending on the interactions with the surface. In the case of cyanobiphenyl-based molecules, such as the main constituents of E7, which have a dipole of approximately 5 D, these tend to orient with their main axis perpendicular to the interface.[28] The actual interactions in the case of semi-free cholesteric mesophases,is poorly understood. They are assumed to be dependent on a sublte interplay between elastic forces and surface tension.[29]

In the case of the chirally doped E7 films in a semi-free environment (thus the top substrate is air), arch textures are visible in areas of varying thickness. This has previously been observed for wedge cells with hybrid anchoring.[12] The period of the fingerprint texture and the orientation of the stripes with respect to the alignment were found to vary with cell thickness. The thickness dependence explains the resulting arch texture in continuously varying layer thickness systems.[12] Locally, in areas of constant thickness, parallel stripes are observed. As the sample is irradiated with UV light these features rotate and the period of the stripes is altered. As the semi-free system shows many similarities to the hybrid system (see section 3.6 for experimental data supporting this) it can be assumed that our system is likewise subjected to hybrid boundary conditions. As described in section 3.6, an increase of pitch is observed in the hybrid systems along with the rotational behavior. The number of rotations observed was dependent on the layer thickness.[30]

A theoretical analysis based on minimization of the elastic free energy of the system, shows that under hybrid (P-H) anchoring two regions can be distinguished in a cholesteric layer of thickness D, larger than a few times the natural pitch p (defined in eq. 3). In most of the sample a cholesteric helix with pitch $p' \sim p$ is present (the "helical layer") and only in a thin elastic boundary layer (of thickness d), close to homeotropic boundary, the director is forced to undergo a strong deformation, to comply with the anchoring conditions.[12] The deformation within this layer is characterized by a periodicity Λ, which corresponds to the period of the stripes as observed by optical microscopy. A pictorial representation is given in Figure 3.9.

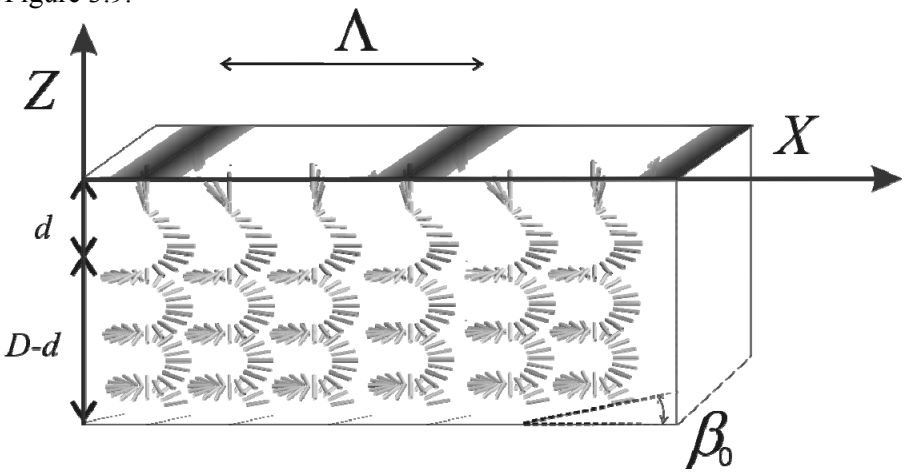

Figure 3.9 Schematic representation of the alignment of the LC director throughout the matrix: where d is the elastic boundary layer ($d \sim p/2$), D is the thickness of the layer, Λ is the period of the stripes in the fingerprint texture, and β_0 is the angle between the normal to the stripes and the orientation of the director on the substrate. Bottom substrate gives planar anchoring, top substrate gives homeotropic anchoring.

The parameters characterizing the director configuration across the doped E7 film, like the periodicity Λ of the stripes in the texture, the pitch *p*'and the thickness *d*, by minimizing the elastic free energy of the system, eq. 11, under the hybrid boundary conditions, according to the model presented in ref. 11 were calculated. The elastic constants reported for pure E7 are K_{11} = 10.3 pN, K_{22} = 7.4 pN, K_{33} = 16.5 pN at room temperature.[32]

Figure 3.10 shows the periodicity Λ of the texture modulation and the angle β_0 between such modulation and the director orientation on the substrate as a function of the ratio *D*/*p*. We can see that for the explored range, the periodicity Λ is roughly twice as big as the natural pitch, Λ ~2.16 *p* (derived from eq. 2) .[31] The predicted thickness of the elastic layer *d* is about 0.47 *p* and starts increasing only when the thickness *D* becomes comparable with the natural pitch *p*; the ratio *p'*/*p* in the helical layer is very close to unity and exhibits a smooth decrease with decreasing *p*. Figure 3.10 shows that the angle β_0 changes roughly linearly with the natural pitch *p,* for a given film thickness: $\beta_0 \sim -\pi + 2\pi\, D/p$. This reflects the director organization in the helical layer, starting from a fixed orientation on the substrate defined by the polyimide orientation: the bottom being fixed, the number of turns in the helical layer, which is proportional to (*D*-*d*)/*p*, imposes the value of β_0.

The rotational behavior is general; however, the numeric results differ depending on the elastic constants being used in the calculation. For instance, in the literature the values K_{11} = 30 pN, K_{22} = 8.5 pN, K_{33} = 46 pN have also been found at room temperature for E7.[32] When using these values with particularly high resistance to splay and bend deformations, a thicker elastic boundary layer is predicted of *d*/*p* ~ 0.6. The texture periodicity increases and an increase in the helical layer *p'* occurs especially in the case of a low *D*/*p* ratio. The increased cost of splay and bend deformations would make higher twist contribution become favored.

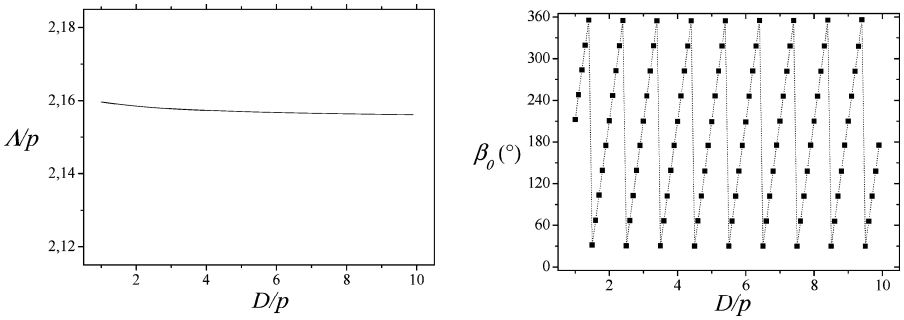

Figure 3.10 Periodicity Λ of the stripes in the fingerprint texture (left) and angle β_0 between the director orientation on the substrate and the normal to the stripes (right), calculated for a cholesteric film of thickness *D* and natural pitch *p*. The elastic constants reported for E7 in ref. 33 have been assumed.

The mechanism proposed for the director reorganization in the cholesteric film of E7 doped with **1** is presented here. The lowest energy configuration of the cholesteric film under hybrid anchoring is helical, with the helix axis perpendicular to the substrate across the whole thickness of the layer, excepting a thin layer at the air interface. In the absence of UV light the presence of **1b** in the LC film is negligible. According to eq 1 (with ee = 1) the pitch can be expressed as $p \sim c\ HTP_P$, where HTP_P is the helical twisting power of the *P* isomer (**1a**). Upon irradiation with UV light the chiral dopant undergoes photoisomerization to the *M* isomer (**1b**). The measured positive HTP_P and the calculated $HTP_{M'}$ are of opposite sign but are of similar magnitude. As a result of the interconversion the helix is expected to unwind and rewind with opposite handedness until reaching the pitch $p \sim c\ HTP_{PSS}$ upon reaching the PSS. HTP_{PSS} is determined by the contribution of both isomers according to eq. 1. As p increases during irradiation the number of turns in the helical layer decreases and so β_0, the modulation orientation with respect to the rubbed surface changes as shown in Figure 3.10. A clockwise rotation is predicted in agreement with experimental results.[34]

For a complete understanding of the phenomenon, the dynamics of the reorganization process must be considered. This involves slow collective variables and the methods of nematodynamics should be used to describe the coupling between time evolution of the director and flux of matter in the film. [35] When looking at a simplified system, i.e. neglecting the elastic boundary layer, the orientation is only determined by internal torques which depend on the chiral strength K_t and the twist elastic constant K_{22}. In the case of the isomerization of the molecular motor the chiral strength of the system changes with time. Thus the director configuration within the LC film changes with time as well. The time-scale of the rotational isomerization is affected by the isomerization process of the selected molecular motor **1**, and by the inherent properties of the liquid crystal being used (i.e. viscosity coefficient).[36] If the isomerization process is far slower than the influence of the liquid crystal, it can be assumed that the rotational reorganization is controlled by the isomerization process. In the case of hybrid anchoring it was observed that $\Lambda \sim 2.16\ p$. Thus when looking at the time dependence of the rotation of the phase we can write:

$$\Lambda(t) \approx 2.16\frac{2\pi}{q(t)} = \frac{4.32\pi}{q_{PSS} + (q_P - q_{Pss})} e^{-t/\tau_{photo}} \qquad 6$$

As the pitch length p and the angle β_0 are inversely proportional the equation can be rewritten as:

$$\beta_0(t) = -\pi + D\left[q_{PSS} + (q_p - q_{PSS}) e^{-t/\tau_{photo}} \right] \qquad 7$$

These theoretical assumptions were used to attempt to fit the experimental results.

Experimental data on areas of constant thickness have been analyzed to generate the two curves $\Lambda(t)$ and $\beta_0(t)$. These two curves were compared to equations 6 and 7 with the wavenumbers in the absence of light q_P and in the photostationary state q_{PSS}, calculated from the measured HTP values, $HTP_P = +90\ \mu m^{-1}$ and $HTP_{PSS} = -59\ \mu m^{-1}$ given the dopant concentration equal to 1 wt%.[37] The film thickness D and time τ_{photo}, were derived from comparison between experiment and theoretical predictions. The results can be seen in Figure 3.12. The measured periodicity in the absence of light (t = 0) is approximately 20% higher than the theoretical prediction of $\Lambda(0) \sim 2.16\ p_P$. The origin of this discrepancy is rather difficult to asses. There is an error in the manual determination of the pitch using the Grandjean-Cano technique, usually in the order of 5 to 10%. Also, as expressed previously, literature provides varying values for the elastic constants for a film of pure E7. In this study the values in ref 27 were used rather than those in ref 26, however, this does cause uncertainty about the parameters used in eq 6. However, the error margin may also be due to the limitations of the model being used, as it excludes the corrugation[38] of the LC film at the air interface. Figure 3.11 shows the curves calculated using eq. 6 for τ_{photo} equal to 160, 180, and 220 s. These values are obtained by assuming the 60 s lower limit estimated from the kinetic analysis. A general underestimate of the texture periodicity is obtained with τ_{photo} = 180 s, which reproduces the slope of the experimental curve.

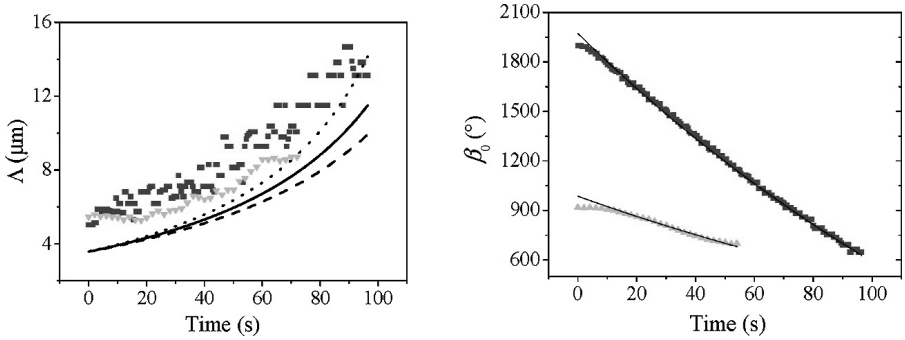

Figure 3.11 Left: Periodicity of the stripes in the texture Λ, as a function of time, as obtained by UV irradiation of a semi-free cholesteric film of E7 doped with **1** (1 wt%), deposited on rubbed polyimide and calculated according to eq. (6), with τ_{photo} = 180 s (solid line), τ_{photo} = 220 s (dashed line) and τ_{photo} = 160 s (dotted line). Right: On the same sample, time dependence of the angle β_0 between the normal to the stripes and the anchoring direction on the substrate. The theoretical curve (solid line) has been obtained from eq. (7), with τ_{photo} = 180 s and D = 8.7 μm; a phase factor has been introduced, to account for the arbitrariness in the choice of the laboratory axis taken as a reference for the measure of β_0.

The right-hand plot of figure 3.11 shows that if the initial short transient is neglected the angle $\beta_0(t)$ exhibits a monotonic decrease with time in analogy with the prediction of the model presented above for the reorganization of the director under the control of the isomerization kinetics. The theoretical curve has been calculated using eq. 7 with τ_{photo} = 180 s, and giving the thickness D the value of 8.7 μm. Different values of the thickness, D = 8.7 ± 0.5 μm, would yield a change of the angle of about 100º in 100 s. For a dopant concentration of 1 wt%, the calculated thickness is approximately five times the cholesteric pitch in the absence of UV irradiation. It corresponds to approximately one and a half pitch after 100 s of UV irradiation.
The recovery of the thermal equilibrium state, after irradiation is stopped, was found to be between three to four times slower than the photo-chemically induced process. Lacking an estimate of the thermal isomerization time τ_{therm}, in E7, the value τ_{therm} = 850 s obtained from measurements in *n*-hexane at -40 ºC was used. The measured decrease of rate is compatible $\tau_{therm} > \tau_{photo}$ = 180 s.

The partial agreement between the experimental and theoretical results may be related to the fact that the model assumes a flat surface at the air interface. However, from previous experiment it has been shown using AFM (non-contact mode) that there is a topographic modulation present at the air interface. The model may thus be too simple. Future investigation would be needed to address the influence of this modulation on the elastic calculations.

3.7 Conclusions Calculations

The theoretical study, in conjunction with the experimental data proves that rotation of the LC phase is only observed in the case of hybrid (P-H) anchoring. Fully reversible rotation of the phase is only observed in the case of a semi-free liquid crystalline film. The texture observed by optical microscopy studies under crossed polarizers is consistent with that expected for hybrid anchoring. The cholesteric helix is perpendicular to the substrate surface; however, this is strongly deformed in close proximity to the air interface in order to undergo homeotropic (helix axis parallel to the surface) anchoring. The deformation can be determined by the difference between the measured helical pitch using the Grandjean-Cano method and the period of the topographic modulation.
The model devised to attempt to rationalize the rotational behavior has shown that the rotational reorganization derives from the unwinding of the cholesteric helix which is produced by the photoisomerization of the molecular motor **1** under UV irradiation. Both isomers have equivalent, but opposite, HTP values. Upon irradiation with UV light (365 nm) the respective concentrations of the two isomers within the LC phase change

and as a result the director rotates, to adjust the pitch in such a way that the elastic free energy is minimized. The direction of rotation depends on the HTP differences between the two isomers. Starting with a dopant of M helicity (-HTP) an anticlockwise rotation is observed. As the cholesteric helix unwinds the periodicity and the rotation of the texture modulation is altered. Defects in the phase do not seem to affect the rotational behavior significantly. The rotational behavior is dependent on the thickness (*D*) of the layer and the elastic boundary layer. With larger thicknesses more rotations are observed.
The kinetics of the molecular motor determines the kinetics of the rotational reorganization. Thus as is the case in solution the rate for the photoisomerization is faster than the thermal back reaction. The rotational reorganization has a thermodynamic origin: owing to the change in HTP upon isomerization the phase must adapt to minimize the elastic free energy within the system. This is the driving force for this reorganization. The rotational behavior is affected by the kinetics and exact structure of the dopant i.e. for optimal interactions with the chosen LC host. The choice of host will also have an effect owing to the structure and exact viscosity i.e. through friction opposing the molecular motion.[39] As was shown previously (chapter 2) subtle changes in the molecular motor structure greatly influence the HTP and isomerization times. This analysis shows that by fine-tuning the interactions between the LC and molecular motor the rotational behavior can be optimized.

3.8 Acknowledgements

The theoretical study into the mechanism of rotation of the LC phase was carried out in collaboration with Alessandro Bosco and Prof. Alberta Ferrarini (Padova), Emmanuelle Lacaze (Paris) and Nathalie Katsonis who are gratefully acknowledged for their contributions and the analysis of data.

3.9 Experimental

Materials

In all of the experiments carried out in this chapter three liquid crystals were used: E7 (Merck; average weight 274.244), MLC-6815 (gift from Merck; average weight 288.38) and Felix R&D (96322/EoiD, Hoechst, weight 253.374). The molecular motors **1** and **2** were synthesized according to the procedure developed by J. Vicario.[15] All solvents used were distilled before use. All experiments were carried out at ambient temperature.

LC detection

Color optical micrographs and movies of the liquid crystalline phase were recorded in transmission using an Olympus BX 60 microscope, equipped

with polarizers and a Sony 3CCD DXC 950P digital camera, attached to a personal computer with Matrox Inspector 8.0 imaging software.

Photochemistry

For irradiation a Spectroline model ENB-280C/FE lamp was used at: 365 nm, ± 5 nm. This lamp has a peak intensity (365 nm) at 15 cm equal to 470 >W/cm². The lamp was held at an angle of approximately 45° with respect to the sample plane, to allow irradiation under the microscope. The distance between the lamp and the sample was approximately 15 cm.

Sample preparation

For the generation of the planar anchoring a microscope glass slide was thoroughly cleaned, spin-coated with a commercially available polyimide (Optmer AL1051, JSR, Belgium) and allowed to harden overnight in a vacuum oven (170 °C, 200 mbar). The surface was then rubbed with a polyester fabric to induce parallel alignment in the liquid crystalline samples. For the preparation of the homeotropic sample, the glass slide was octyltrichlorosilane (OTS)-coated according to a literature procedure.[40]
For the sections 3.1-3.5 1 wt% solutions were prepared with freshly distilled toluene and the LC blend of choice. For sections 3.6 onwards a solution consisting of 0.70 mg of **1** was mixed with 71.72 mg of E7. The mixture was dissolved in 80 µl of freshly distilled toluene. For each experiment 5 µl of sample were dropcasted on the appropriate surface, between the spacer. Then the appropriate top slide was used to cover the sample.

Automated Picture Processing

The rotation was recorded during UV irradiation, for areas of fingerprint texture which were flat enough to visualize parallel lines. Both the angular speed and the period modification were digitized by a Matlab routine based on decomposing the movie in frames. For each frame, the polar coordinates of the point having the maximum intensity on the Fourier transform of the image provided both the period and the angle of the parallel lines. The dispersion of the points on the curves obtained by this procedure depends on the number of frames in each movie and on the flatness and the size of the chosen area.

3.10 References

[1] a) S. Chandrasekhar, *Liquid Crystals*, II ed. (Cambridge University Press, Cambridge, 1992); b) P. Oswald, P. Pieranski, *Nematic and Cholesteric Liquid Crystals* (Taylor & Francis Ltd., London, 2005)
[2] O. Lehmann, *Ann. Phys*. (Leipzig) **1900**, *2*, 649-705

[3] N.V. Madhusudana, R. Pratibha, *Mol. Cryst. Liq. Cryst. Lett*. **1987**, 5, 43-51; N.V. Madhusudana, R. Pratibha; H.P. Padmini, *Mol. Liq. Cryst*. **1991**, 202, 35-49
[4] I. Gvozdovskyy, I. Terenetskaya, *Liq. Cryst. Today* **2002**, 11, 8
[5] H.R. Brand, H. Pleiner in *Encyclopedia of Materials: Science and Technology*, (K.H.J. Buschow, R.W. Cahn, MCB Ilschner, E.J. Kramer, S. Mahajan, eds.) (Elsevier, Amsterdam, 2001)
[6] For reviews on LC dopants see e.g: G.P. Spada, G. Proni, *Enantiomer* **1998**, 3, 301-314; R. Eelkema, B.L. Feringa, *Org. Biomol. Chem*. **2006**, 465, 3729-3745
[7] a) S. Pieraccini, G. Gottarelli, R. Labruto, S. Masiero, O. Pandoli, G.P. Spada, *Chem. Eur. J*. **2004**, *10*, 5632; b) N. Tamaoki, *Adv. Mater*. **2001**, *13*, 1135; c) R.A. van Delden, T, Mecca, C. Rosini, B.L. Feringa, *Chem*. *Eur. J*. **2004**, *10*, 61-70
[8] a) R. Eelkema, J. Vicario, N.H. Katsonis, B.S. Ramon, C.W.M. Bastiaansen, D.J. Broer, B.L. Feringa, *Nature* **2006**, 440, 163; b)R. Eelkema, M.M. Pollard, N. Katsonis, J. Vicario, D.J. Broer, B.L. Feringa, *J. Am. Chem. Soc*. **2006**, 128, 14397-14407
[9] See Chapter 2 of this thesis for examples of substituent effects on molecular motor molecules.
[10] See chapter 2 for HTP values, $t_{1/2}$ = 587 s for **1** vs. 190 s for **2** see ref 15b for all kinetic data.
[11] I. Dierking, *Textures of Liquid Crystals* (Wiley-VCH, Weinheim, 2003); P. Oswald, P. Pieranski, *Nematic and Cholesteric Liquid Crystals* (Taylor & Francis LTD., London, 2005)
[12] Baudry, J.; Brazovskaia, M.; Lejcek, L.; Oswald, P.; Pirkl, S. *Liq. Cryst.* **1996**, *21*, 893
[13] The anchoring at the air interface has not been described in the literature
[14] As can be seen in the supporting information in paper: A. Bosco, M.G.M. Jongejan, R. Eelkema, N. Katsonis, E. Lacaze, A. Ferrarini, B.L. Feringa. *J. Am. Chem. Soc.* **2008**, *130*, 14615-14624
[15]a) J. Vicario, A. Meetsma, B.L. Feringa *Chem. Commun.* **2005**, 5910 b) J. Vicario, M. Walko, A. Meetsma, B.L. Feringa *J. Am. Chem. Soc.* **2006**, *128*,5127-5135
[16] ESR spectra of TEMPONE in E7 have shown to dramatic changes on going from the isotropic to the nematic phase. See A. Ferrarini, P.L. Nordio, *J. Am. Soc. Faraday Trans*. **1992**, 88, 1733
[17] D.R. Lide, ed. *Handbook of Chemistry and Physics* (CRC, Cleveland, 2003)
[18] a) F.C. Frank, *Discuss. Faraday Soc*. **1958**, 25, 19; b) C.W. Oseen, *Trans. Faraday Soc*. **1933**, 29, 883
[19] a) A. Ferrarini, G.J. Moro, P.L. Nordio, *Phys. Rev. E* **1996**, 53, 681; b) A. Ferrarini, G.J. Moro, P.L. Nordio, *Molec. Phys*. **1996**, 87, 485
[20] Common values are of the order of unity if HTP is given in μm^{-1}, and Q in $Å^{-3}$. See S. Pieraccini, A. Ferrarini, G.P. Spada *Chirality*, **2008**, *20*, 749-759
[21] A. Saupe, *Mol. Cryst. Liq. Cryst*. **1973**, 21, 211
[22] D. Dunmur, K. Toriyama, in *Handbook of Liquid Crystals*, D. Demus, J. Goodby, G.W. Gray, H.-W, Spiess, V. Vill, eds. (Wiley-VCH, Weinheim, 1998)
[23] TD-DFT calculations show that the transition dipole is close to the central double bond. Thus the data achieved for K18 are comparable to DFT. See ref 14
[24] This behaviour is analogous for binaphthyl, see ref 25
[25] S.M. Todd, A. Ferrarini, G.J. Morro, *Phys. Chem. Chem. Phys*. **2001**, *3*, 5535
[26] M.F. Sanner, J.-C. Spehner, A. Olson, *Biopolymers* **1996**, 38, 305
[27] http://www.geom.uiuc.edu/software/download/geomview.html

[28] H. Yokoyama, S. Kobayashi, H. Kamei, *Mol. Cryst. Liq. Cryst*. **1983**, 99, 39; V.N. Matveenko, E.A. Kirsanov, *Russ. Chem. Rev*. **1986**, 55, 743; B. Jêrome in *Handbook of Liquid Crystals*, D. Demus, J. Goodby, G.W. Gray, H.-W. Spiess, V. Vill, eds. (Wiley-VCH, Weinheim, 1998)
[29] R. Meister, H. Dumoulin, M.-A. Hallé, P. Pieranski, *J. Phys. II France* **1996**, *6*, 827; and ref 27
[30] P. Oswald, P. Pieranski, *Nematic and Cholesteric Liquid Crystals* (Taylor & Francis Ltd. London 2005)
[31] As mentioned previously in the chapter, is section 3.6, the pitch determined from the corrugation on the surface was approximately 2 times as large as the pitch determined using the Grandjean-Cano method.
[32] J.F Strömer, E.P. Raynes, C.V. Brown, *Appl. Phys. Lett*. **2006**, 88, 051915/1
[33] R. Meister, H. Dumoulin, M.-A. Hallé, Pi. Pieranski, *J. Phys. II France* **1996**, 6, 827; A. Saupe, *Mol. Cryst. Liq. Cryst*. **1973**, 21, 211
[34] See contents of chapter 2 of this thesis and section 3.6 of this chapter along with published data in reference 8.
[35] F.M. Leslie, *Quart. J. Mech. Appl. Math.* **1966**, *19*, 357; J.L. Ericksen, *Arch. Ration. Mech. Analysis* **1960**, *4*, 231
[36] $\tau_{nem} = D^2\gamma_1/K_{22}$ is in the order of of seconds for a layer thickness D in the order of micrometers. K_{22} is the twist elastic constant of the LC and γ_1 is the viscosity coefficient opposing the director of rotation.
[37] For experimental data, see chapter 2 of this thesis.
[38] See AFM image (non contact mode) in ref 8a for proof of corrugation on the surface
[39] According to Kramers theory for activated processes.
[40] J-S. Park, C-H. Jang, M.L. Tingey, A.M. Lowe, N.L. Abott, *J. Colloid Iterf. Sci*. **2006**, 304, 459-473

Chapter 4

The Liquid Crystalline Behavior of a Polyisocyanate Functionalized with a Molecular Motor and a Chiroptical Switch

Achiral polyisocyanates generate non-chiral lyotropic liquid crystalline phases. By functionalizing the polyisocyanate with a single chiral molecular motor or chiroptical switch at the terminus a preferred helicity could be induced in the polymer chain. As a result the generated liquid crystalline phase in toluene was also chiral. The chiroptical switch-functionalized polyisocyanate formed the better cholesteric phase. Subsequent irradiations with UV and visible light demonstrated that the switch-functionalized polyisocyanate can be isomerized within the LC matrix and as a result the expected pitch elongation and subsequent shortening could be observed.

Part of this chapter has been published: D. Pijper, M.G.M. Jongejan, A. Meetsma, B.L. Feringa, *J.Am. Chem. Soc*., **2008**, *130*, 4541-4552

4.1 Introduction

Transferring chiral information from the molecular to the macro- or supra-molecular level is a topic of intense contemporary interest.[1] Of particular importance are asymmetric autocatalysis, attempting to explain the origin of homochirality in nature,[2] and the sensing of chiral compounds.[3] This amplification of chirality has previously been shown in dynamic systems such as chiral aggregates and gels,[4] synthetic helical foldamers[5] and polymers.[6] Liquid crystals (LC's) are especially suitable as a host material owing to their sensitivity to small chiral molecular perturbations.[7] The presence of small chiral dopant molecules can also affect the macroscopic organization within an LC phase.[8]

It has been demonstrated that by using a chiral dopant which is bi-stable in nature and addressable using external stimuli (heat or light), the two states have a different effect on the LC phase owing to their different configurations.[9] This behavior has been well precedented in the literature, especially for lower molecular weight, thermotropic, rigid, rod-like mesogens. However, LC phases can also be generated using rigid rod-like polymers in the presence of a solvent.[10] One well documented class of compounds are the polyisocyanates,[11] which are stiff helical polymers which adopt both *P* and *M* helical conformations. The two helical structures exist in rapid dynamic equilibrium.[12] A strong preference for one handedness can be biased via a subtle chiral influence owing to the large cooperativity throughout the chain, resulting in infrequent helix reversals along the polymer chain. This amplification of chirality throughout the polymer chain has been observed for "sergeant-and-soldiers"[13]and in the case of "majority-rules"[14] systems. The most impressive amplification of chirality has been observed in the case where a chiral bias is generated at each stereocenter of every monomeric unit through the substitution of one hydrogen atom for a deuterium.[15] These appendages can also be photo-switchable units introduced in the polymer side chains.[16] One example involves the incorporation of an azobenzene photo-switch containing two stereocenters in the side chains of the copolymer which upon inversion of the molecular chirality induced a transition of *M* to *P* helicity in the polyisocyanate chain.[17] Thus an alteration at the molecular level has a macromolecular effect. Through the use of an optically active initiator for polymerization one chiral unit at the terminus of the polymer chain can be introduced which induces a preferred helical twist sense along the polymer backbone.[18] Here the measure of the chiral influence on the polymer is determined by the persistence length: thus the chiral information is transferred along the chain until a helix reversal is encountered at which point the chiral influence of the terminus is lost. When the chiral induction is dependent on the presence of a single chiral molecule at the terminus, the extent of induction varies greatly with the length of the polymer chain (molecular weight) and the temperature.[18]

The photo-induced *trans*-to-*cis* isomerization of photochromic azobenzene groups introduced in the side-chains of these polymers generally causes a disruption of the nematic LC phase, leading to a large change in birefringence.[19] Recently, it was reported that upon irradiation with circularly polarized light, these polymeric LC's display a chiral organization.[20] The origin of the supramolecular chiral organization in the LC systems is not clear, however, since it could also be induced in amorphous polymer films.[21] A series of polymeric LC's with photochromic switch units bearing a chiral pendant group, either covalently attached to the polymer side-chains or seeded as a dopant in the LC, were used to induce a change in the cholesteric pitch upon irradiation.[22] Therefore it was decided to examine whether it would be possible to use a molecular motor or a chiroptical switch as initiators for a polymer synthesis of (*n*-hexyl polyisocyanate (PHIC)), and still be able to affect the chirality of the polymer chain upon photoisomerization of the central double bond in these overcrowded alkene units at the polymer terminus. In this way an attempt is made to go from the molecular to the macroscopic level. It became apparent that in solution these systems showed inversion of the helicity upon inversion of the intrinsic helicity of the molecular motor or the chiroptical switch.[23]

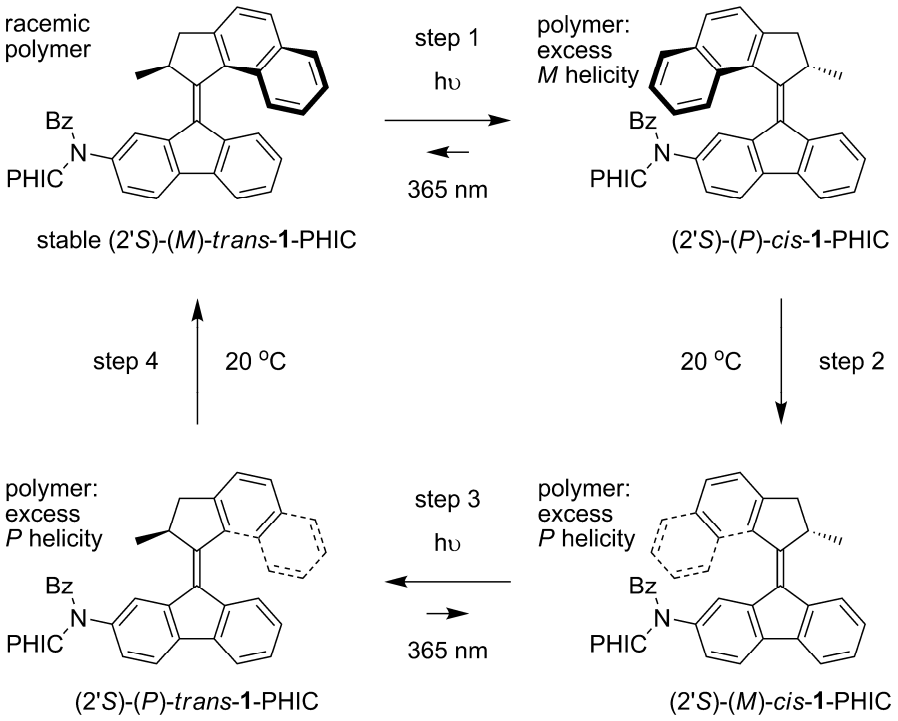

Scheme 4.1. Representation of the photochemical and thermal isomerizations[24] of (2'*S*)-(*M*)-*trans*-**1**-PHIC.

As was mentioned in previous chapters, when the molecular motor undergoes photochemical isomerization (UV light irradiation) the intrinsic helicity of the molecule changes from *M* to *P* (Scheme 4.1, step 1). Upon thermal isomerization the intrinsic helicity is changed from *P* to *M* (step 2, Scheme 4.1). However, in the case presented in Scheme 4.1 the polymeric chain is attached to the lower half (desymmeterizing the molecular motor). Therefore, though both structures (stable (2'*S*)-(*M*)-*trans*-**1**-PHIC versus (2'*S*)-(*M*)-*cis*-**1**-PHIC) have the same intrinsic helicity (*M*) they are *trans* and *cis*, ergo not the same.

In the previous chapters of this thesis the liquid crystalline studies have all been focused on thermotropic liquid crystals. These LC mesogens generate an LC phase without the assistance of other molecules. However, LC phases can also be generated using lyotropic systems.[25] These mesogen molecules are not capable of generating an LC phase on their own. The formation of an LC phase requires the presence of a solvent in large quantities (usually more than 50 wt%). The presence of the solvent ensures that the temperature at which liquid crystallinity is observed is lowered.

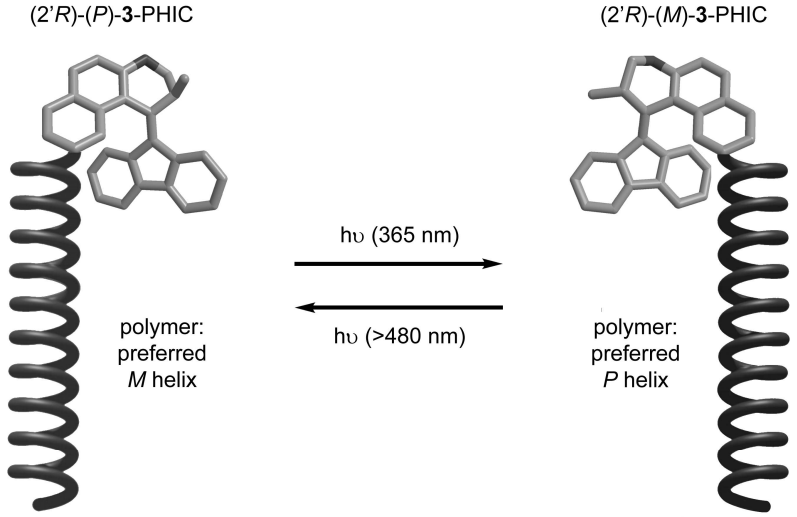

Scheme 4.2 Schematic illustration of the reversible inversion of the preferred helical twist sense of a polymer backbone by a chiroptical molecular switch at the terminus. The initial isomer of the molecular switch unit, (2'*R*)-(*P*)-**3**-PHIC, induces a preferred *M* helical twist of the polymer backbone. UV irradiation inverts the intrinsic helicity of the photochromic switch, yielding (2'*R*)-(*M*)-**3**-PHIC, which as a consequence now induces a preferred *P* twist sense of the polymer chain. Subsequent irradiation with visible light reverts the system to (2'*R*)-(*P*)-**3**-PHIC with a preferred *M* helicity of the polymer. Image from ref 30.

In the case of the switch-functionalized system the polymer chain is connected via the upper half to the chiroptical switch: Thus the lower (stator)

half remains symmetrical. As a result the system is simplified, and rather than having four states only two can be addressed.

It is well known that polyisocyanates can generate lyotropic liquid crystalline phases in toluene. In this chapter we analyze the ability of these two functionalized polyisocyanates (Schemes 4.1 and 4.2) to influence the polyisocyanate chain to generate an LC phase and to determine whether or not it would be possible to affect the phase upon irradiation as has been previously shown for these types of overcrowded alkenes in thermotropic LC systems. In succeeding, a system would be developed in which hierarchical transmission of chiral information from the chiroptical switch or motor (molecular level, Scheme 4.3), via the macromolecular level of the polyisocyanate chain to the supramolecular level of a cholesteric LC phase occurs.

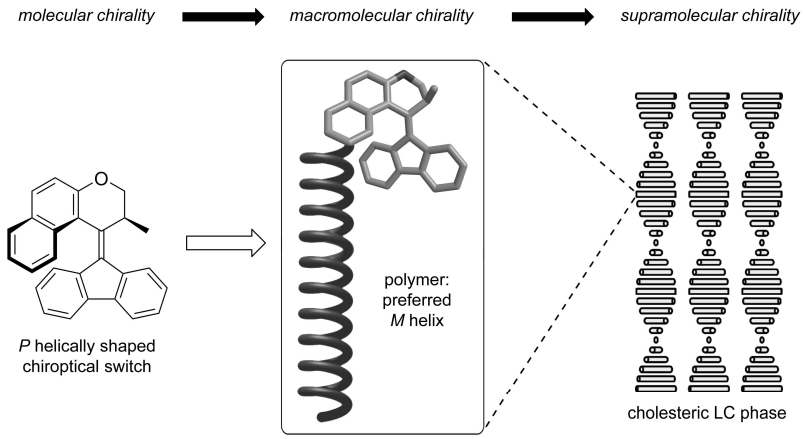

Scheme 4.3 Schematic representation of the transmission of chiral information from the molecular level (chiroptical switch) to the macromolecular level (polyisocyanate chain) to the supramolecular level (cholesteric LC phase). Image from ref 30.

4.2 Lyotropic Liquid Crystalline setup

4.2.1 The lyotropic LC system

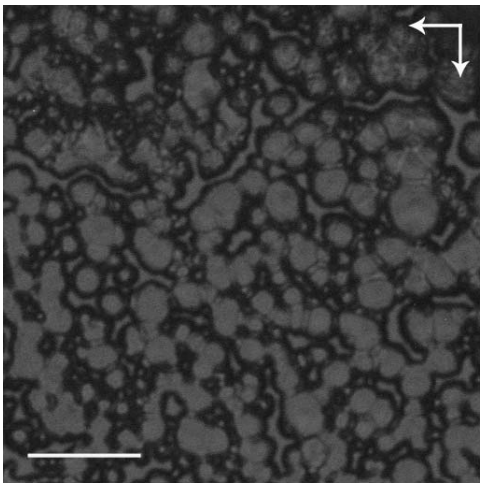

Figure 4.1: Optical micrograph representing the result of a solution of 20 wt% unfunctionalized PHIC in toluene which is left open to the air on a polyimide surface. The scale bar represents 50 μm.

A lyotropic liquid crystalline phase contains both a solvent and a potentially liquid crystalline molecule. The addition of the solvent lowers the temperature at which liquid crystallinity is observed. However, as the solvent evaporates from the mixture the mesogen molecules will form crystalline domains (Figure 4.1). Therefore a setup was required which would contain the solvent vapor. Typically, in the literature[26], 1 mm quartz cuvets are used to study lyotropic LC phases. However, the volume required to fill these with enantiopure material entirely would be cost prohibitive. Even attempts with unfunctionalized PHIC in these cuvets, however, still showed crystallization. Partial filling resulted in very messy phases which crystallized rapidly. Figure 4.2 shows some of the many homemade sample holders which were designed to overcome this problem but were later discarded owing to low efficiency.

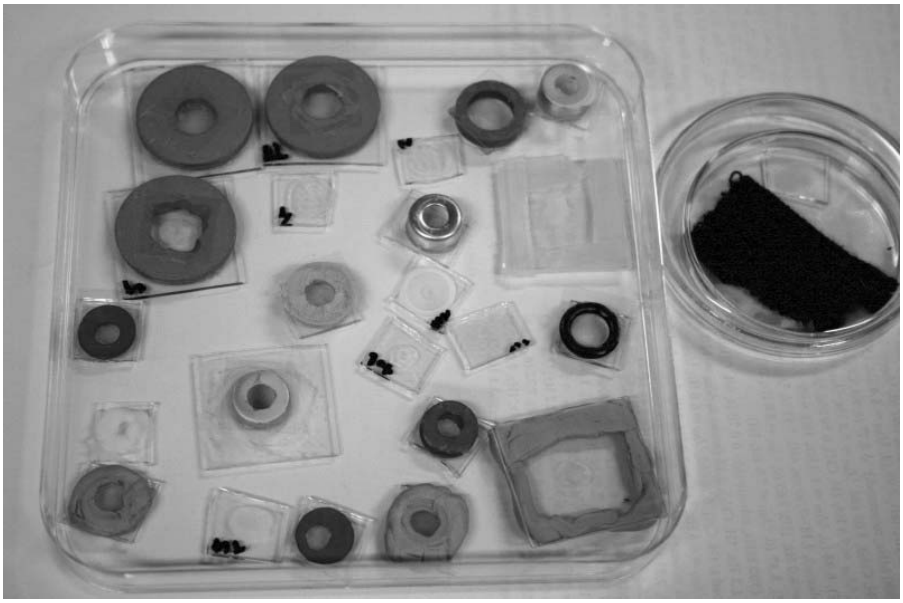

Figure 4.2: An example of the wide variety of sample holders that were designed in order to attempt to make visualization of the lyotropic LC phases under the microscope possible for prolonged periods of time. The samples on the left are all based on two slide systems which are kept on top of each other using various techniques such as rubber ring with glue and Blue Tack. The right sample is contained in a Petri-dish with a constant toluene environment.

As can be seen from Figure 4.3, despite enclosure of the sample, as long as the sample holder is not fully air tight the solvent evaporates rapidly. Though toluene has a high boiling point, within 8 min, enough of the solvent has evaporated at the rims to induce crystallization. Within another 10 min the entire phase is dried out. Upon addition of solvent the polymer can be rewetted, but only partially. Strange defects remain on the surface as the polymer does not fully dissolve after crystalline deposition.

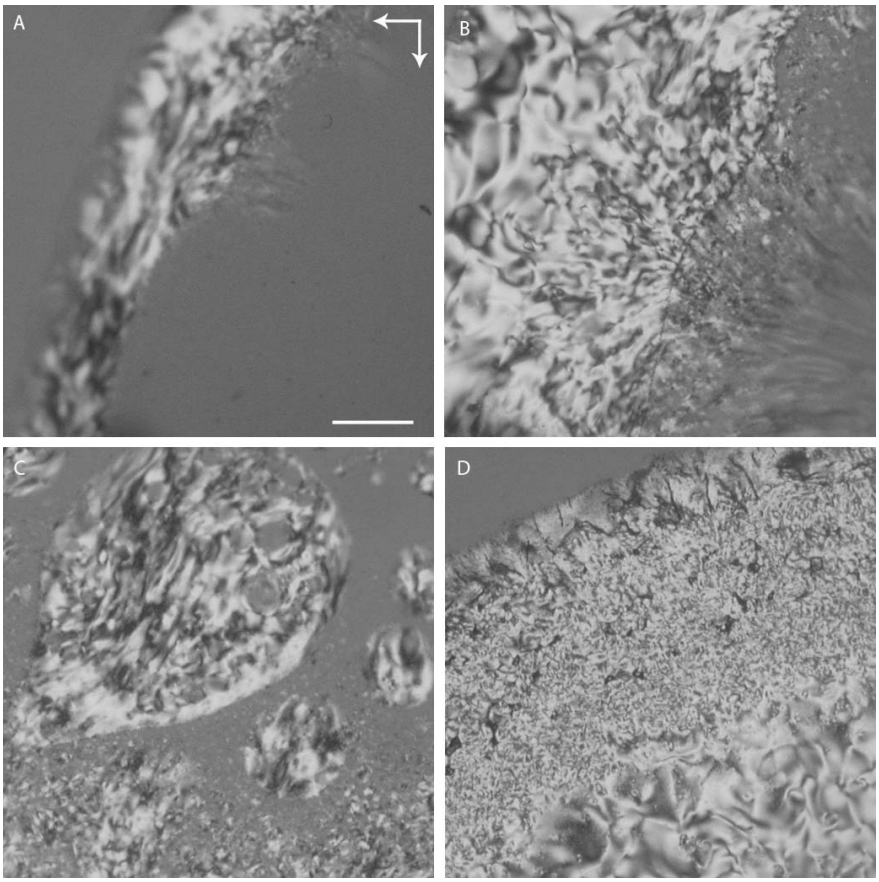

Figure 4.3 Optical micrographs of a sample of polyisocyanate in toluene (20 wt%) enclosed using Blue Tack at different times a) t = 0 b) 3 min c) 6 min d) 8 min. scale bar represents 200 μm.

Using the constant toluene vapor system (Figure 4.2, small crystallization dish) it was possible to keep the sample in the liquid crystalline state. Typical nematic phases could be observed for longer periods of time without crystallization. It allowed for the analysis of different substrates to examine the effect that an induced director might have on the lyotropic LC system.

4.2.2 Surface effects

Changing the surface properties can alter the alignment of LC phases (chapter 3). Unfunctionalized glass does not give preferential ordering, while polyimde-functionalized glass can be rubbed in one direction in order to orient the mesogens along one director.

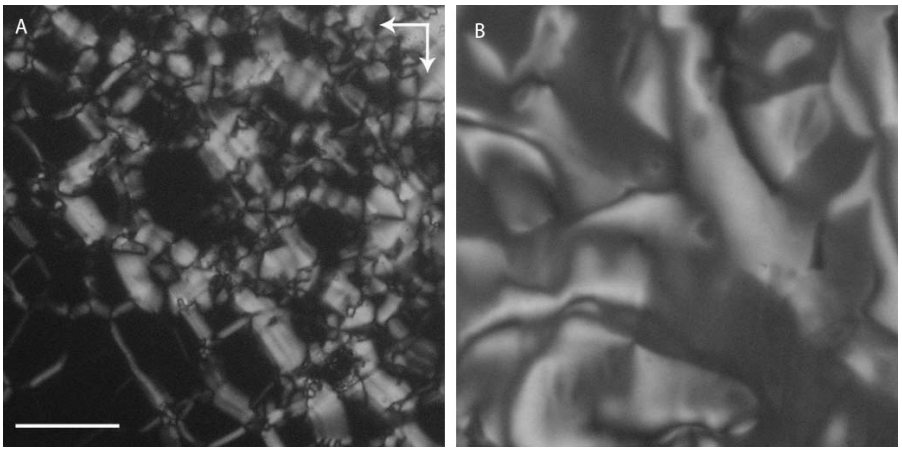

Figure 4.4: Optical micrographs of racemic **1**- PHIC 20 wt% solution in toluene on various surfaces: a) glass b) rubbed polyimide. The scale bar represents 100 μm.

As can be seen from the optical micrographs in Figure 4.4, depending on whether a unfunctionalized glass or a rubbed polyimide coated slide was used as the anchoring surface, the appearance of the phase altered. The polyimide-rubbed system resulted in a phase which appeared to be more homogeneous in nature. The appearance of the glass slide sample looked more like the typical oily streak textures. Thus ideally the setup should include a rubbed polyimide substrate.

4.2.3 The effect of solvent

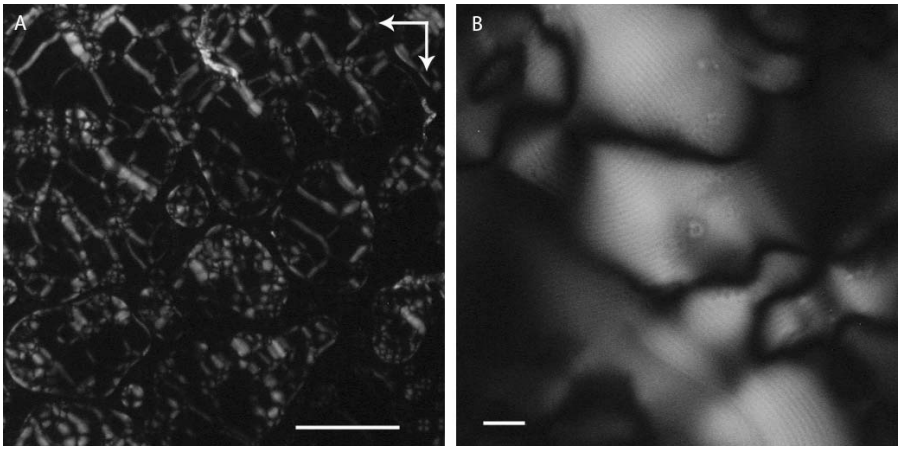

Figure 4.5: Optical micrographs of the chiral phase observed for a 27 wt% solution of (2'*S*)-(*M*)-*trans*-**1**-PHIC in toluene at varying magnifications. A) scale bar represents 200 μm B) scale bar represents 10 μm.

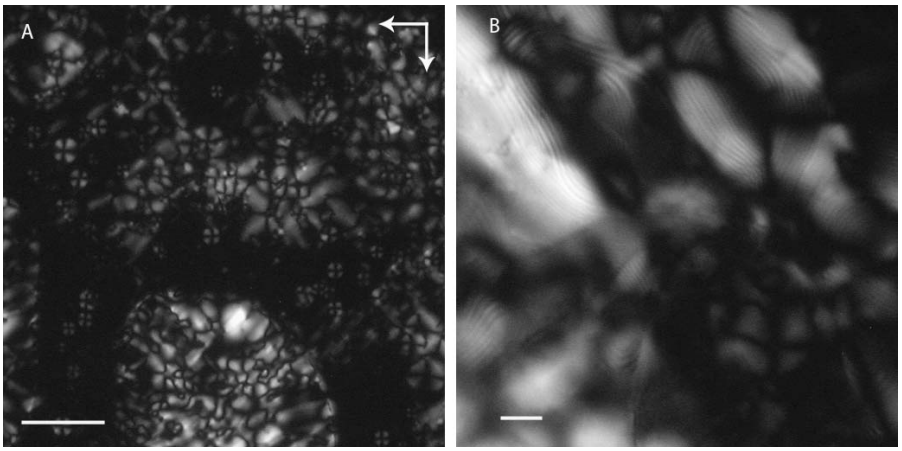

Figure 4.6: Optical micrographs of the chiral phase observed for a 20 wt% solution of (2'*S*)-(*M*)-*trans*-**1**-PHIC in trichlorobenzene at varying magnifications. A) scale bar represents 200 μm B) scale bar represents 10 μm. The arrows represent the orientation of the crossed polarizers.

Various solvents were used in the preparation of the lyotropic LC samples to determine which would provide the greatest longevity of the sample. Though the functionalized polymer is soluble in acetonitrile, the solvent was too volatile and thus the sample was already dried out before deposition on a slide could take place. Thus the remainder of the examined solvents all had boiling points above that of toluene. Though the trichlorobenzene allowed for longer preparation times, the cholesteric phase was no better than in the case of toluene (compare Figure 4.5 (toluene) and Figure 4.6 (trichlorobenzene)). In fact, the cholesteric regions within the sample appeared larger in the case of toluene as solvent. Thus toluene remained the solvent of choice for further experiments.

4.3 The use of the liquid IR cell

The initial setups (previous sections of this chapter) used for the preparation of the lyotropic LC films were affected by the quick evaporation of the solvent from the samples and thus formation of crystalline domains. Also the layer thickness achieved is fully arbitrary. The use of a liquid IR cell proved the most successful method for maintaining the LC phase for longer periods of time (i.e. the LC sample remained fluid for a month at a time within the holder provided it was kept at room temperature). The holder was mostly airtight. The KF plates can be separated using Teflon spacers of a known thickness, therefore a minimal layer thickness can be used which is consistently the same. The wells beneath the plugs were sealed using Teflon grease to prevent evaporation of solvent through this cavity. Subsequently the spacer thicknesses could be varied to determine an ideal thickness for easy analysis.

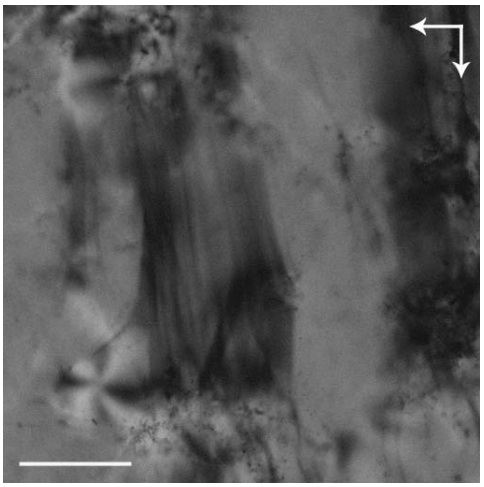

Figure 4.7: Optical micrograph of an apparent fingerprint texture of a solution of 20 wt% enantiopure (2'*S*)-(*M*)-*trans*-**1**-PHIC in toluene with a layer thickness of 0.1 mm. The scale bar represents 50 μm.

4.3.1 Concentration effects

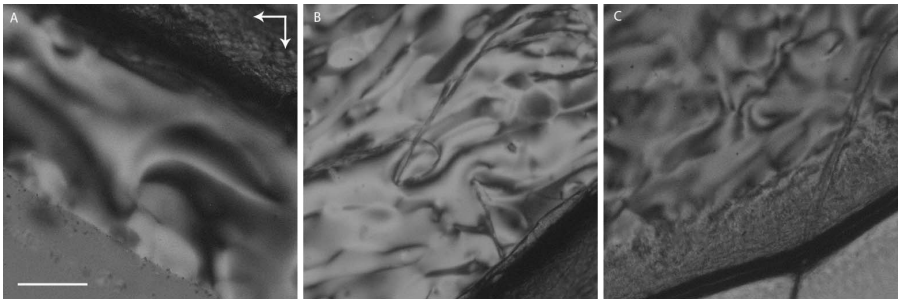

Figure 4.8: Optical micrograph of a solution of various concentrations of racemic **1**-PHIC in toluene. A) 20 wt% B) 40 wt% C) 60 wt%. The scale bar represents 100 μm.

Various ratios of polymer to solvent were used in order to determine which would give the best lyotropic phase for further studies (Figure 4.8). At 20 wt% the solution already forms an LC phase, however, the area which appears liquid crystalline under the microscope is limited (usually only at the rims). In the case of a 40 wt% solution the full area is liquid crystalline but already a bit chaotic. At 60 wt% the solution became viscous and was rather unmanageable while preparing the sample. As a result the edges showed crystallization problems again despite the use of the liquid IR cell. The generated phase also was far more chaotic than the one generated for 40 wt%. Thus it was decided to go for a concentration that was as low as possible to increase the manageability of sample preparation (lower viscosity), but still have a proper LC phase. It was opted to continue all

further experiments with mixtures containing approximately 30 wt% of polymer to solvent.

4.3.2 The cholesteric phase of (2'*S*)-(*M*)-*trans*-PHIC

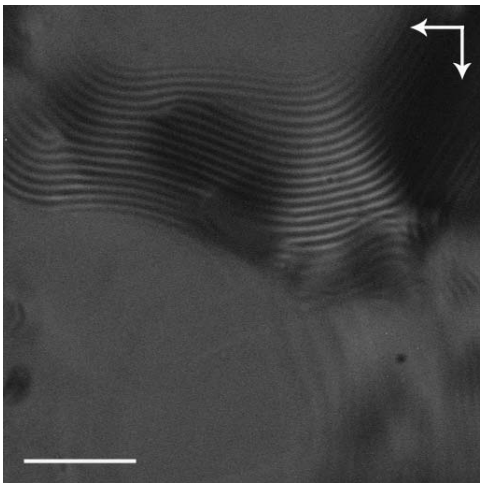

Figure 4.9: Optical micrograph of a cholesteric phase generated by 30 wt% (2'*S*)-(*M*)-*trans*-**1**-PHIC in toluene. The scale bar represents 100 μm.

As can be seen from Figure 4.9, a cholesteric fingerprint region was observed. However, the remainder of the cell containing the lyotropic LC system does not show the expected characteristic texture. Instead the LC phase appears to have "highways" of cholesteric fingerprint regions. These "highways" tend to appear near defects in the phase such as near the rim or at air bubbles (see Figure 4.10).

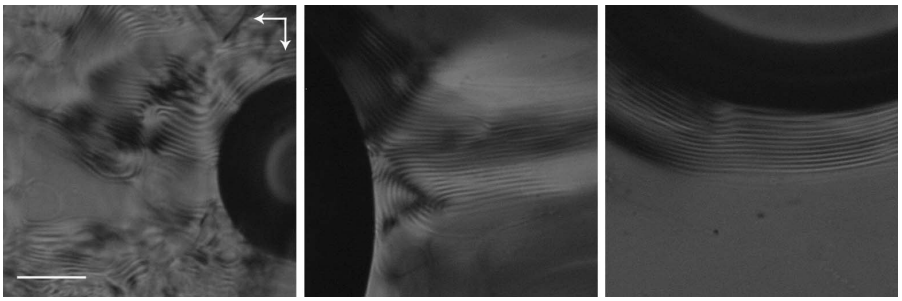

Figure 4.10: Various optical micrographs of an LC phase generated by a 30 wt% solution of (2'*S*)-(*M*)-*trans*-**1**-PHIC in toluene. The micrographs show the appearance of the cholesteric fingerprint region at various defects. The scale bar represents 100 μm.

4.3.3 Effect of UV irradiation on the cholesteric phase of (2'*S*)-(*M*)-*trans*-PHIC

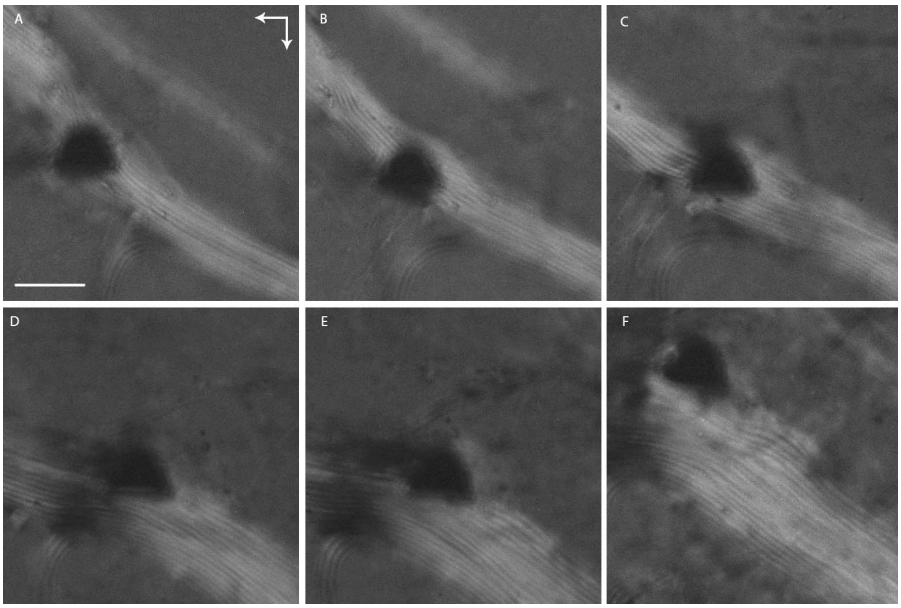

Figure 4.11: Optical micrographs of a single spot of a sample of 20 wt % of enantiopure (2'*S*)-(*M*)-*trans*-**1**-PHIC under irradiation with UV light (365 nm) at various time intervals. A) t =0 B) 30 min C) 1h D) 90 min E) 2h F) 150 min. The scale bar represents 50 μm.

Upon irradiation of the (2'*S*)-(*M*)-*trans*-**1**-PHIC lyotropic LC phase it became apparent that though the process of reorientation is far slower than that observed for the previously studied thermotropic systems (chapters 2 and 3), it is clear that the *cis*-*trans* isomerization of the central alkene moiety of the molecular motor is able to affect the phase as a whole (Figure 4.11). However, owing to the fact that the (2'*S*)-(*M*)-*trans*-**1**-PHIC molecule yields only small regions of cholesteric fingerprint surrounded by areas of optically nematic LC, very little can be concluded about whether or not rotation[27] occurs. It is quite clear from Figure 4.11a compared to Figure 4.11f, that broadening of the cholesteric domains takes place throughout the isomerization process. As the molecular motor (2'*S*)-(*M*)-*trans*-**1**-PHIC only produced small sections which appeared fingerprint like, and the system has four stages to go through during irradiation it became apparent that for simplification of the analysis of the irradiation process a chiroptical switch system would be preferred.

4.4 Layer thickness

The liquid IR cell is available with Teflon spacers, which separate the KBr plates. By changing the spacer thickness the volume of sample required could be varied. Three commercially available Teflon spacers were attempted with thicknesses of : 50, 200, and the 500 μm.

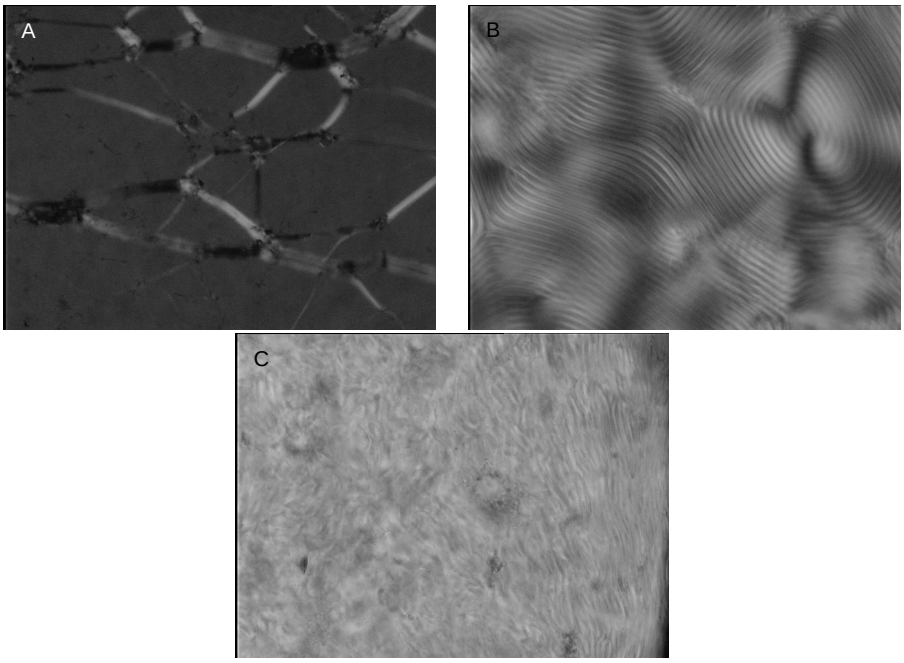

Figure 4.12: Optical micrographs of an LC phase of a sample of 30 wt% enantiopure (2'*S*)-(*P*)-**3**-PHIC in toluene at various thicknesses in the liquid IR cell. Layer thickness of A) 50 μm B) 200 μm C) 500 μm.

The layer of 50 μm thickness (see Figure 4.12, A) shows features that could be described as oily streaks. These features are characteristic of cholesteric phases with planar-planar anchoring (Scheme 4.4, left image). In this case the axis of the cholesteric helix is perpendicular to the substrate. The LC phase generated using the 200 μm layer features a typical fingerprint texture. These are characteristic of cholesteric phases with homeotropic anchoring (Scheme 4.4, right image). Interestingly, on increasing the layer thickness by a factor of 4 the apparent anchoring of the phase is totally altered: going from a helical axis which is perpendicular to the substrate to one which is parallel. In all cases the sample was placed between two unfunctionalized KBr plates, thus no preferred anchoring is expected.

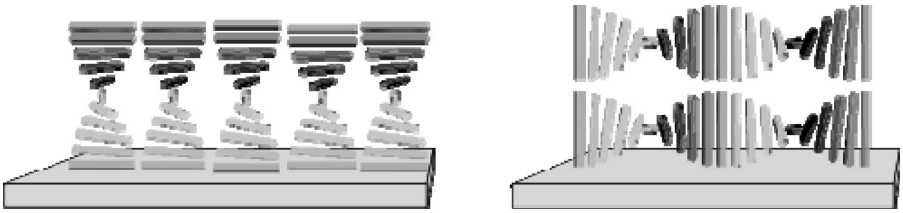

Scheme 4.4 Anchoring of a cholesteric liquid crystal on a surface: planar (P), on the left, and homeotropic (H), on the right. The rods represent the orientation of the director amongst the liquid crystalline molecules.

The 200 μm layer is, however, very well oriented. In the case of a layer thickness of 500 μm (Figure 4.12 C) the resulting phase is far more chaotic. A cholesteric fingerprint texture is present, though not as clearly defined as in the case of the thinner layer. As had been previously observed, the LC phase continues to alter with time until it reaches the thermodynamic equilibrium of the system. Time-dependent measurements were carried out for the thicker layers (Figure 4.12 B and C) which both generated cholesteric phases to determine which of the two would generate LC phases which would be easiest to study for the effects of irradiation.

4.4.1 Time dependence of sample orientation

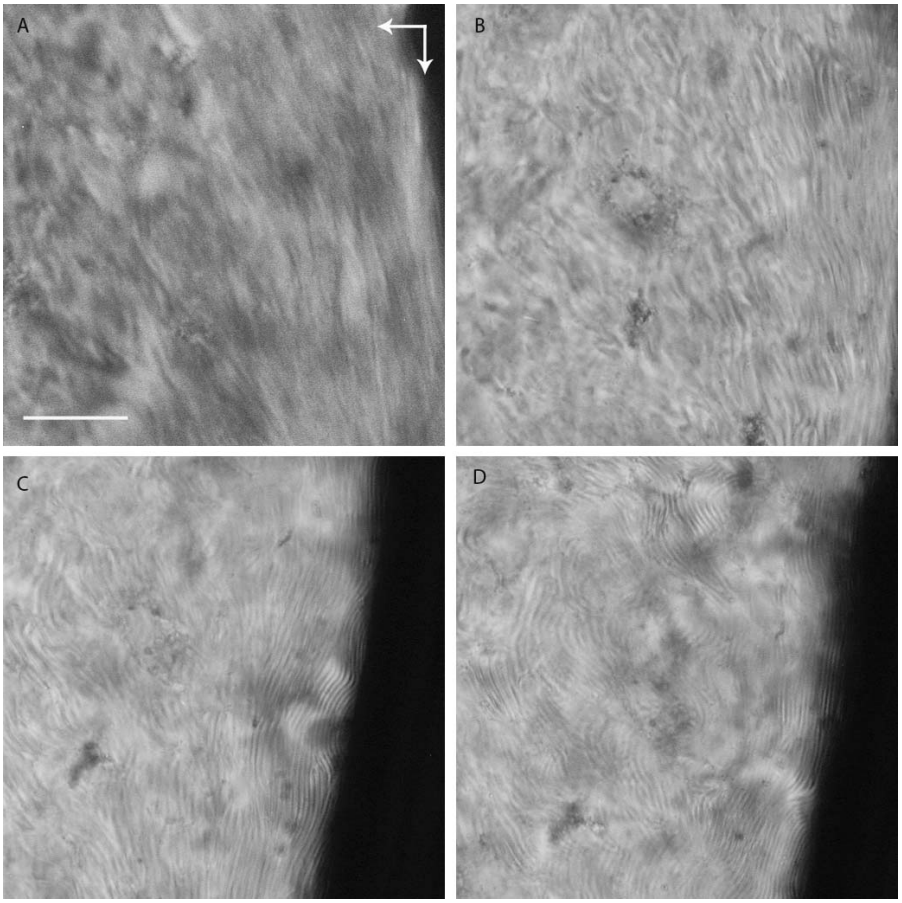

Figure 4.13: Optical Micrographs of an LC phase of a sample of 30 wt% (2'*S*)-(*P*)-**3**-PHIC in toluene with a thickness of 500 μm at various times: A) 1 h B) 2 h C) 4 h D) 5 h. The scale bar represents 50 μm.

An LC phase with a layer thickness of 500 μm was observed with time. The slowly generated cholesteric phase continues to rearrange throughout the 5 h time period. As can be seen in Figure 4.13 after 1 h no cholesteric fingerprint is visible at all, as the phase appears a smear of various colors. After 2 h the first hint of a fingerprint region is visible. After 4 h the rim of the drop clearly shows the characteristic fingerprint texture, although towards the center the LC phase is still highly disorganized. This has not improved markedly even within 5 h. As a result any potential reorganization of the phase observed during UV irradiation could be attributed to the photoisomerization process and to the general reorganization of the phase to reach an equilibrium state. Therefore it was decided that a thinner layer (200 μm) which also generated a cholesteric phase, and reorganized more quickly, would be better suited for the irradiation experiments.

4.5 Irradiation experiments

As could be seen in Scheme 4.2, (2'*S*)-(*P*)-**3**-PHIC consists of a chiroptical switch moiety and the PHIC segment. Owing to the introduction of the chiral moiety the polyisocyanate chain now has a preferred helicity. The initial isomer of the molecular switch unit, (2'*R*)-(*P*)-**3**-PHIC, induces a preferred *M* helical twist of the polymer backbone. UV irradiation (λ = 365 nm) causes photoisomerization at the central double bond resulting in the inversion of the intrinsic helicity of the photochromic switch, yielding (2'*R*)-(*M*)-**3**-PHIC. As a consequence of this inversion, the interaction with the polymer chain is altered and a preferred *P* twist sense of the polymer chain is induced. Subsequent irradiation with visible light (λ > 480 nm) reverts the system to (2'*R*)-(*P*)-**3**-PHIC with a preferred *M* helicity of the polymer.

4.5.1 UV cycles

When irradiating the (2'*S*)-(*P*)-**3**-PHIC in toluene (30 wt%) sample with UV light the chiroptical switch in (2'*S*)-(*P*)-**3**-PHIC changes its intrinsic helicity from *P* generating (2'*S*)-(*M*)-**3**-PHIC (chiroptical switch has *M* helicity). The helicity of the polymer chain is also inverted from *M'*[*] in the case of (2'*S*)-(*P*)-**3**-PHIC to *P'* in the case of (2'*S*)-(*M*)-**3**-PHIC. As a mixture of isomers is present within the LC phase, upon irradiation the pitch length (length for 360 º rotation within the helix) increases until visually no pitch can be observed (50:50 mixture of both isomers at infinite pitch). Upon continued irradiation (Figure 4.14) the fingerprint texture is restored with a tighter pitch than measured for pure (2'*S*)-(*P*)-**3**-PHIC (p = 6.0 μm before irradiation and after leaving the irradiated sample in the dark overnight p = 4.5 μm). The UV irradiation experiment was conducted placing a cutoff filter of λ > 520 nm over the microscope light source in order to prevent the visible light to induce the reverse reaction as the isomer (2'*S*)-(*M*)-**3**-PHIC does not absorb above this wavelength. The pitch was determined from measurements of the periodicity of the observed fingerprint texture. Several measurements were carried out on each micrograph. The reported pitch values are an average of 10 measurements with an error of ± 5%. The error comes from the slight variation in the pitch throughout the sample. For example, in the case of the appearance of circular patterns (Figure 4.14 d) the edges of the sample have longer pitch lengths than the centers.[28]

[*] *M'* and *P'* refer to the intrinsic helicity of the polymer helix whereas *M* and *P* refer to the intrinsic helicity of the switch functionality.

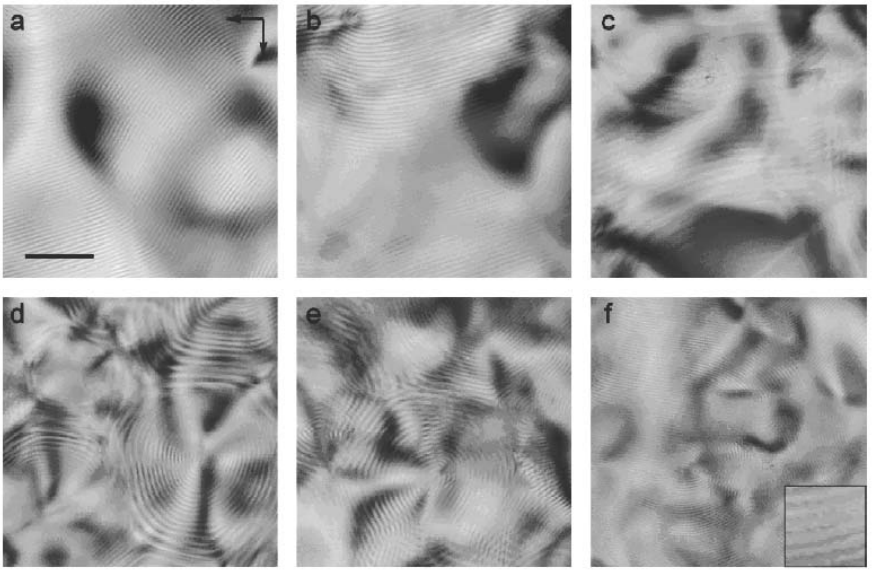

Figure 4.14. Optical micrographs of a thin film (thickness: 200 μm) of (2'*S*)-(*P*)-**3**-PHIC in toluene (30 wt%) using a 520 nm cutoff filter a) before irradiation (p = 6.0 μm), b) after 15 min (p = 6.2 μm), c) 45 min, d) 90 min and e) 150 min of UV irradiation (λ = 365 nm), after which a PSS mixture (no further changes were observed upon irradiation) is obtained that consists of a large excess of (2'*S*)-(*M*)-**3**-PHIC over (2'*S*)-(*P*)-**3**-PHIC and f) after leaving the irradiated sample in the dark overnight (p = 4.5 μm) (inset shows an enlargement of five times). The scale bar represents 50 μm. The arrows indicate the direction of the crossed polarizers.

4.5.2 VIS cycles

When irradiating the sample with visible light (λ > 480 nm) the chiroptical switch system is reversibly addressed (figure 4.15). Therefore the switch segment in (2'*S*)-(*M*)-**3**-PHIC changes its intrinsic helicity from *M* to *P* generating (2'*S*)-(*P*)-**3**-PHIC. The alteration in the pitch length which was observed upon UV irradiation is observed again for the visible light irradiation, however, starting with the opposite enantiomer. As a mixture of enantiomers is present within the LC phase, upon irradiation the pitch length (length for 360 º rotation within the helix) increases until visually no pitch can be observed (50:50 mixture of both enantiomers at infinite pitch). Upon continued irradiation the fingerprint texture is restored with a tighter pitch than originally reported for pure (2'*S*)-(*P*)-**3**-PHIC. This would suggest that the initial measurement on the sample of pure (2'*S*)-(*P*)-**3**-PHIC was actually conducted on a sample which had partially switched during preparation. The UV irradiation cycle was completed far more quickly than the visible light irradiated cycle (150 min versus 24 h). As previously mentioned it appeared that in the initial phase did not purely consist of (2'*S*)-(*P*)-**3**-PHIC, thus a short irradiation time would be required to reach PSS. However, this difference in initial (2'*S*)-(*P*)-**3**-PHIC

concentration cannot account for the large difference in observed isomerization time. The largest difference is the variation in the intensity of the light source at a given wavelength used for the irradiation step. For the UV irradiation a lamp with irradiation wavelength 365 nm ± 5 nm was used directly on the sample. For the reverse process the light source of the optical microscope was used with a cutoff filter. Thus the microscope light source was irradiating the sample with a range of wavelengths above 480 nm. A large spread of wavelengths which are not compatible with switching would be included. The intensity of wavelengths for optimal switching is therefore far better during the UV irradiation than during the visible light irradiation cycle.

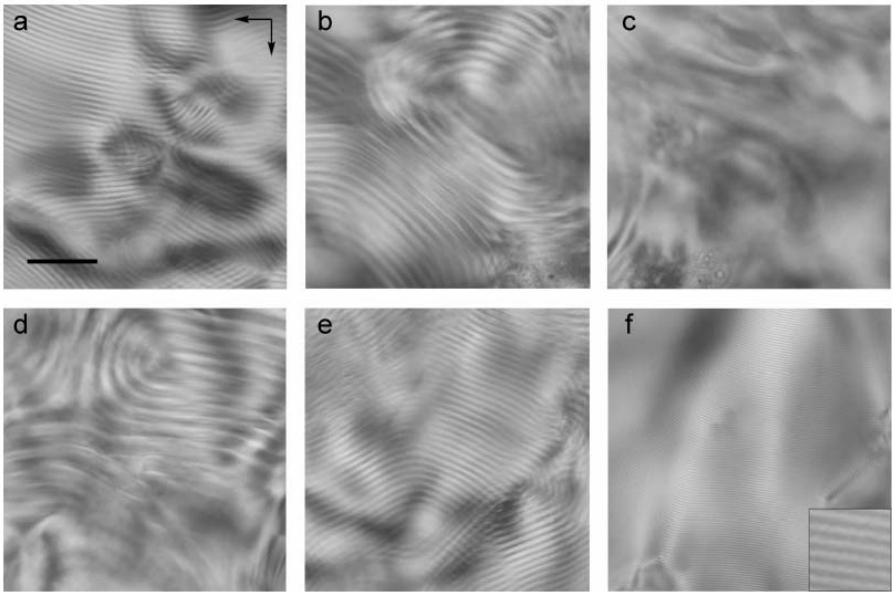

Figure 4.15. Optical micrographs of a thin film (thickness: 200 μm) of the PSS mixture obtained upon UV irradiation which consists of a large excess of (2'*S*)-(*M*)-PHIC over (2'*S*)-(*P*)-PHIC in toluene (30 wt%), after a) 5 h (p = 7.8 μm), b) 6 h (p = 13 μm), c) 7h, d) 8 h (p = 22 μm) e) 10 h (p = 9.0 μm) f) 24 h of irradiation with visible light (λ > 480 nm), after which a PSS mixture is obtained that consists of a large excess of (2'*S*)-(*P*)-PHIC over (2'*S*)-(*M*)-PHIC (p = 3.7 μm) (inset shows an amplification of five times). The scale bar represents 50 μm. The arrows indicate the direction of the crossed polarizers.

The occurance of full photocontrol of the magnitude and sign of the supramolecular helical pitch of a cholesteric LC phase generated by a polyisocyanate with a single chiroptical molecular switch covalently attached to the polymer's terminus can be easily understood from the schematic representation in figure 4.16. Initially pure (2'*S*)-(*P*)-**3**-PHIC adopts an M helical cholesteric LC phase[29] with a tight pitch. Upon UV irradiation (λ = 365 nm) the switchable moiety is interconverted between intrinsic *P* and *M* helicity resulting in the generation of polymer (2'*S*)-(*M*)-

3-PHIC. The presence of a mixture (2'*S*)-(*P*)-**3**-PHIC and (2'*S*)-(*M*)-**3**-PHIC leads to an elongation of the cholesteric pitch. When equal amounts of (2'*S*)-(*P*)-**3**-PHIC and (2'*S*)-(M)-**3**-PHIC are present in the LC mixture the cholesteric pitch has an infinite pitch length, which appears optically nematic. After prolonged UV irradiation an excess of (2'*S*)-(*M*)-**3**-PHIC will be present in the mixture resulting in the returning of the cholesteric helix and the fingerprint texture, however now with opposite helicity (*P*). At PSS the LC phase predominantly consists of (2'*S*)-(*M*)-**3**-PHIC, resulting in a cholesteric helix of *P* helicity with a tight pitch. This process is fully reversible upon irradiation with visible light (λ > 480 nm).

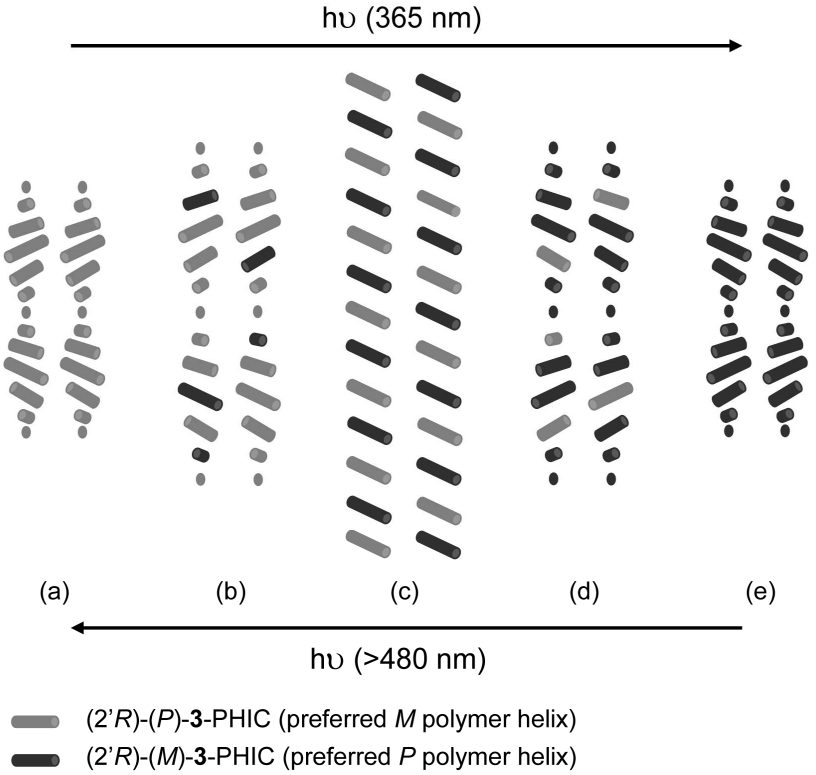

Figure 4.16 Schematic representation of the full photocontrol of the magnitude and sign of the supramolecular helical pitch of a cholesteric LC phase generated by a polyisocyanate with a single chiroptical molecular switch covalently attached to the polymer's terminus. a) Initially (2'*S*)-(*P*)-**3**-PHIC adopts an M helical cholesteric LC phase with a tight pitch. b) UV irradiation (λ = 365 nm) converts the switchable moiety from intrinsic *P* to *M* helicity resulting in the generation of polymer (2'*S*)-(*M*)-**3**-PHIC, leading to an elongated cholesteric pitch. c) Equal amounts of (2'*S*)-(*P*)-**3**-PHIC and (2'*S*)-(M)-**3**-PHIC are present in the mixture resulting in an infinite pitch of the cholesteric helix, which appears optically nematic. d) After prolonged UV irradiation an excess of (2'*S*)-(*M*)-**3**-PHIC will be present in the mixture resulting in the returning of the cholesteric helix, however, now with opposite helicity (*P*). e) PSS is reached, predominantly consisting of (2'*S*)-(*M*)-**3**-PHIC, resulting in a cholesteric helix of *P* helicity with a tight pitch. This is a reversible process (λ > 480 nm). From ref 32.

4.5.3 Thermal control experiment

The irradiation cycles of the cholesteric LC phase doped with (2'*S*)-(*P*)-**3**-PHIC are accompanied by long irradiation times. Therefore it is also possible that the heat generated by the irradiation source during this time might be responsible for the observed effect. Therefore, as a control, a cell containing the cholesteric LC phase was allowed to settle overnight (as with the irradiation experiments) and then the pitch was determined. Afterwards the sample was irradiated with $\lambda > 540$ nm for a period of 8 h (Figure 4.17).

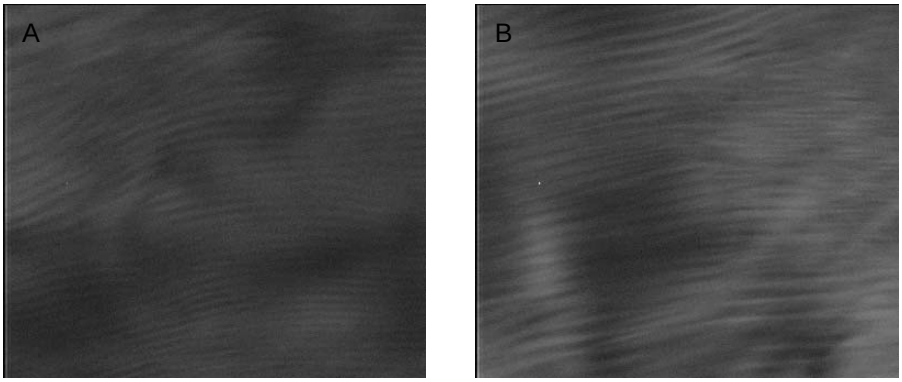

Figure 4.17 Optical micrographs of a thin film (thickness: 200 μm) of (2'*S*)-(*P*)-**3**-PHIC in toluene (30 wt%). a) before irradiation b) after 8 h of irradiation $\lambda > 540$ nm.

The pitch length upon long irradiation times remains the same within error margins, though the polygonal structure is less well defined for the optical micrograph taken after the 8 h irradiation period. Therefore the period varies slightly throughout the micrograph.

During the irradiation cycles it became apparent that upon undergoing an irradiation cycle the pitch tightened. The pitch was 6.0 μm before irradiation and after UV and Vis irradiation the pitch was 3.7 μm. The difference in magnitude is outside of the error margin. It was necessary to determine whether or not this change was caused by a continual loss of solvent owing to sample heating (though no crystallization was observed). Though longer irradiation times (8 h, Figure 4.17) seemed to have little effect, the entire cycle requires days of exposure to a light source. Therefore it was decided to attempt to repeat the cycle several times and to ascertain what would happen to the pitch length upon sequential irradiation cycles (Figure 4.18).

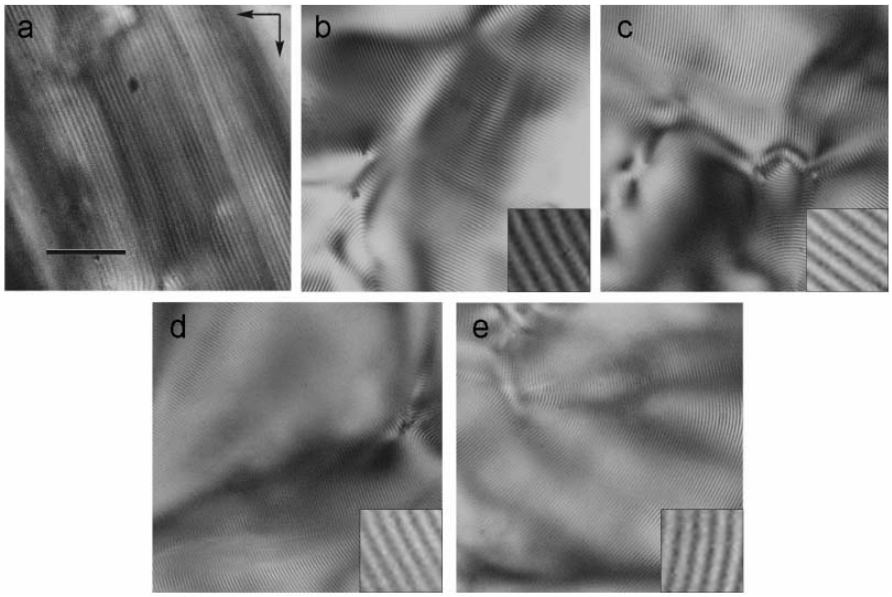

Figure 4.18 Optical micrographs of a thin film (thickness: 200 μm) of a) (2'*S*)-(*P*)-**3**-PHIC in toluene (~30 wt%, p = 6.9 μm), b) after a first cycle of 1 h of UV (λ = 365 nm) and 20 h of visible light (λ >480 nm) irradiation (p = 4.4 μm), c) after a second (p = 4.1 μm), d) a third (p = 4.0 μm) and e) a fourth irradiation cycle (p = 4.2 μm). Scalebar is equal to 50 μm. The arrows indicate the directions of the crossed polarizers. Insets show enlarged sections under 5x higher magnification.

The initial pitch length of the sample, before irradiation was applied, was 6.9 µm (Figure 4.18 a). This pitch is somewhat longer than the 6.0 μm observed for the previous sample (Figure 4.14) before irradiation, which is assumed to be caused by a slight difference in the exact sample concentration between the two experiments (both were prepared as 30 wt%, however, miscibility issues may have varied the actual amounts in solution). After the first irradiation cycle, the pitch had decreased to a value of 4.4 µm (Figure 4.18 b), a similar decrease in pitch length over one switch cycle as observed before (Figures 4.14 and 4.15: 6.0 µm to 3.7 µm). Three subsequent switching cycles, however, did not result in a further decrease in pitch length: similar pitch values, varying between 4.0 µm and 4.4 µm, were obtained (Figure 4.18 c-e). It is therefore highly unlikely that the observed decrease in pitch length after irradiation is caused by continual solvent evaporation due to heating of the sample under the irradiation conditions applied, as a gradual further decrease in pitch length over subsequent irradiation cycles would be expected. We propose that the observed tightening of the pitch is actually the result of the photo-induced switching of the polymer's helicity causing an overall improvement in the packing of the polymers in the helical organization of the LC phase.

4.5.4 CD spectra

In solution (2'*S*)-(*P*)-**3**-PHIC generates an *M* helicity in the polymer chain, whereas in the case of (2'*S*)-(*M*)-**3**-PHIC a *P* helicity is generated. To ascertain whether or not this is still the case in the liquid crystalline phase CD spectroscopy was used to determine whether or not inversion of the helicity could be observed after irradiation.

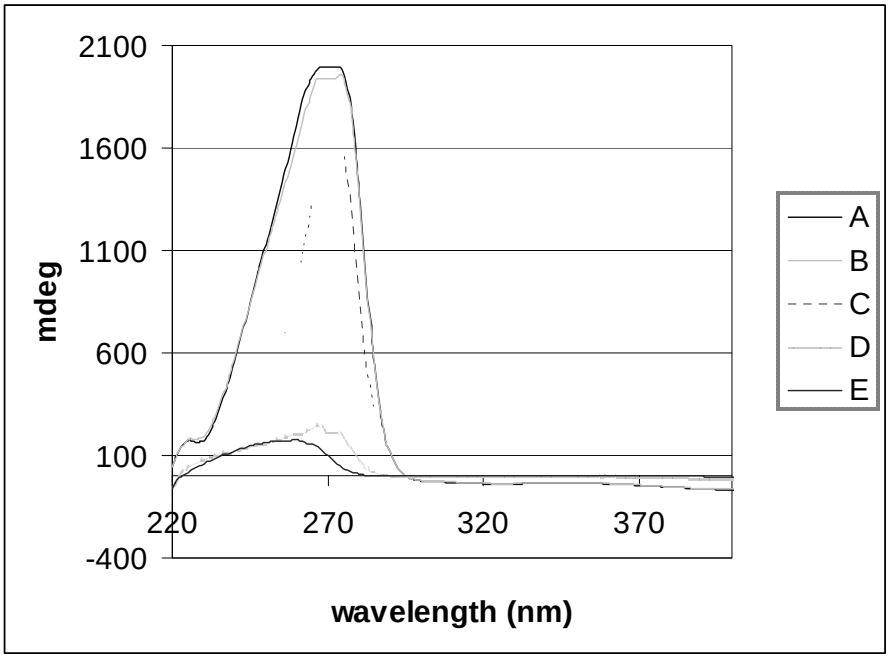

Figure 4.19 CD spectra of a cholesteric liquid crystalline phase of 30 wt% of (2'*S*)-(*P*)-**3**-PHIC in toluene in the liquid IR cell with a layer thickness of 200 μm. Spectrum A was taken before irradiation. All sequential spectra are achieved after varying irradiation times: B = 15 min; C = 5 h; D = 48 h; E = after 72 h.

The CD spectra generated from the liquid crystalline cell are different from those of the same material in solution. In solution both a positive and negative Cotton effect can be observed. However, that is not the case in the matrix. This alteration in the spectral shape can be attributed to potential interference of LD. The molecules are aligned in the LC matrix and this alignment can cause interference with the circularly polarized light. Initial experiments showed that by changing the position of the LC sample with respect to the light source the signal was altered dramatically. Thus exactly the same position would be required for all measurements to determine if irradiation had any effects as the LD effect should remain similar.
The sample was kept in the same position in order to minimize the effects of changing LD. Upon irradiation it could be observed that the maximum intensity was decreasing. For a noticeable decrease, however, extensive

irradiation times were required: 5 h versus the 150 min required for full conversion according to the microscopy studies. An explanation for this could be the layer thickness being used. In the case of a sample thickness of 200 μm, there are many layers of the polymeric system present. The upper layer can be addressed easily and observed under the microscope. However, there may still have been lower layers which were not organized within the 150 min period. Using more intense and direct irradiation the sample could be altered more deeply than is the case with the microscope sample. As CD spectroscopy measures the sample throughout a remainder of polymer with opposite helicity will affect the cumulative CD signal. No inversion of the signal was ever observed as after 72 h crystallization occured. This may have started earlier, causing the maximum to undergo a sudden blue shift while previously it was red shifting. Also as the helices unwind and rewind in the opposite fashion the LD effect could change making the actual shape of the observed CD spectra change. However, the fact that a change can be observed implies that the switching is still occurring and inducing opposite helicity, though the sample is not stable enough to undergo full inversion owing to drying out phenomena.

4.6 Conclusions

It has been demonstrated that, using either (2'*S*)-(*M*)-*trans*-**1**-PHIC or (2'*S*)-(*P*)-**3**-PHIC, a lyotropic LC phase can be generated in toluene. The clearest cholesteric phases were generated using toluene as the solvent and a concentration of approximately 30 wt% of the functionalized-PHIC systems. The liquid IR cell proved the best sample holder for these systems and a layer thickness of 200 μm gave the best results for analysis under the optical microscope.

As (2'*S*)-(*P*)-**3**-PHIC is better than (2'*S*)-(*M*)-*trans*-**1**-PHIC at inducing a preferred helicity throughout the polymer chain and has a simplified irradiation cycle, (2'*S*)-(*P*)-**3**-PHIC was the system of choice for the irradiation experiments. It was shown that the cholesteric phase generated could be altered upon irradiation with UV light. The continuing reorganization in the dark after stopping irradiation proved that the reorganization of the LC phase as a whole is a slower process than the photoisomerization of the chiroptical switch moiety. A similar slow reorganization over a period of hours has been reported in the case of a polymeric LC based on a polymer with chiral photo-switchable groups introduced in the side chains.[30] This could be attributed to the fact that the irradiation source only accesses the top layer of the system, however there are 200 μm worth of polymer units in toluene which need to reorient. Therefore it would potentially be better to use thinner layers as long as a fingerprint region could still be observed (N.B. in our case thinner layers resulted in oily streaks rather than fingerprint textures). The process of interconversion between (2'*S*)-(*P*)-**3**-PHIC and (2'*S*)-(*M*)-**3**-PHIC with UV irradiation is fully reversible using visible light irradiation. The long

irradiation times, and heat do not affect the pitch of the cholesteric phase. CD spectroscopy shows that the helicity of the polymer chain is probably inverted upon irradiation in the LC matrix, though actual inversion was never observed owing to both LD and sample crystallization problems.

4.7 Acknowledgements

Dr. D. Pijper is kindly acknowledged for synthesizing the two functionalized-PHIC systems and for his collaboration on the work described in this chapter.

4.8 Experimental section

General remarks

The molecular motor [31] and chiroptical switch [32] functionalized polyisocyanate were synthesized according to literature procedures. All solvents used throughout the experiments were freshly distilled before use.

Equipment

The optical micrographs were recorded using an Olympus BX 60 microscope equipped with crossed polarizers and a Sony 3CCD DXC 950 P digital camera attached to a PC running Matrox Inspector 8.0 imaging software. The samples were prepared in demountable liquid IR cell (Sigma-Aldrich Z112003-1KT). The thickness of the LC layer was controlled by using various different Teflon spacers between two KBR plates. Irradiation at 365 nm was carried out using a Spectroline ENB-280C/FE UV lamp. A 200 W Oriel Xe-lamp adapted with a 480 nm cut-off filter was used for the reverse reaction.

Preparation of the samples

A mixture of 15 mg of the functionalized polyisocyanate and 35 mg of freshly distilled toluene were mixed rigorously to generate a homogeneous phase. Owing to drying out and viscosity problems the mixture had to be used directly to generate a layer in the IR cell containing a Teflon spacer of desired thickness (200 μm for the irradiation experiments). The optical micrographs could then be taken. For irradiation experiments the sample was allowed to orient itself within the IR sample holder over night. For the experimental set-up, see Figure 4.20; it shows the IR cell positioned on the microscope table under the lens with the position of the UV irradiation source.

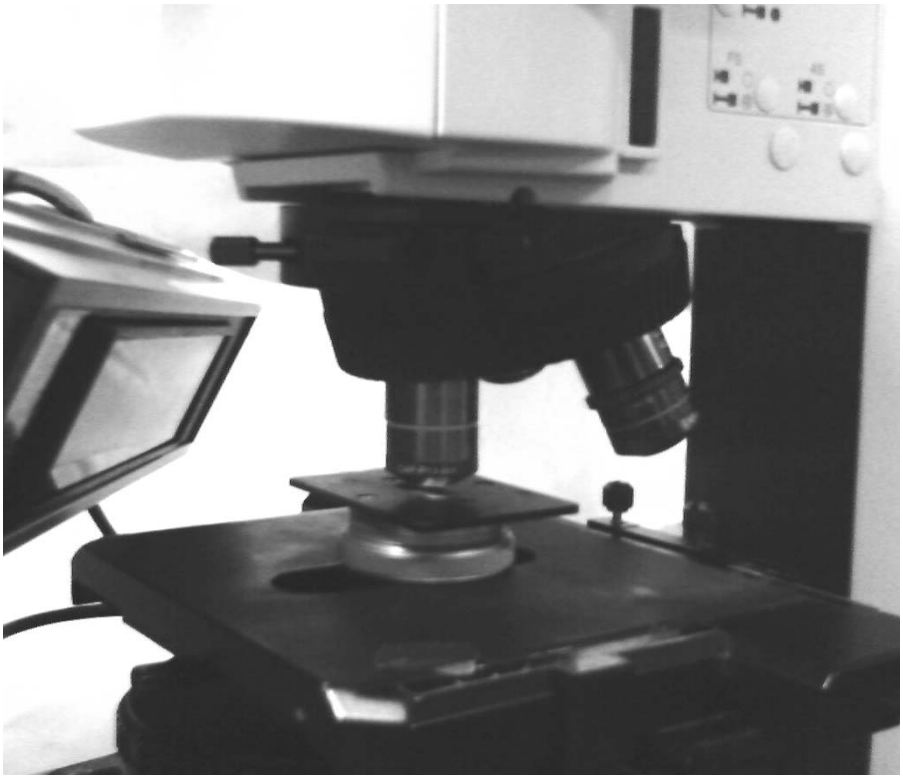

Figure 4.20: The experimental set-up used for irradiation experiments of the IR cell.

CD Spectral measurements

The CD spectra were measured on a Jasco J-715 instrument using a horizontal attachment (especially manufactured). The attachment is screwed on externally to the spectrometer where the detector is normally located. The detector is screwed onto the top of the attachment so that it is at right angles with respect to the light source. The liquid IR cell slides in horizontally in a fixed holder in the attachment, the CD light source is passed through the sample by use of mirrors.
The horizontal attachment allows a sample in the liquid IR cell to be placed horizontally and then be sampled, thus preventing drift and gravity issues that would occur when placing the LC sample vertically. Owing to the very high intensity of signal coming from the LC sample the intensity of the light source was lowered (ten fold) to prevent problems with the high tension (overloading of detector and thus making the measured data unreliable).

4.9 References

[1] a) B. L. Feringa, R. A. van Delden, *Angew. Chem. Int. Ed.* **1999**, *38*, 3418-3438. b) *Materials-Chirality* (Eds.: M. M. Green, R. J. M. Nolte, E. W. Meijer), *Top.*

Stereochem. **2004**, *24*. c) *Supramolecular Chirality* (Eds.: M. Crego-Calama, D. N. Reinhoudt), *Top. Curr. Chem.* **2006**, *265*. See also chapter 1 of this thesis.
[2] a) I. Sato, H. Urabe, S. Ishiguro, T. Shibata, K. Soai, *Angew. Chem. Int. Ed.* **2003**, *42*, 315-317. b) D. G. Blackmond, *Proc. Nat. Ac. Sci. USA* **2004**, *101*, 5732-5736.
[3] a) R. A. van Delden, B. L. Feringa, *Angew. Chem. Int. Ed.* **2001**, *40*, 3198. b) R. Eelkema, R. A. van Delden and B. L. Feringa, *Angew. Chem., Int. Ed.*, **2004**, *43*, 5013-5016. c) Yashima E.; Maeda K.; Nishimura T. *Chem. Eur. J.* **2004**, *10*, 42-51.
[4] a) Engelkamp, H.; Middelbeek S.; Nolte R. J. M. *Science* **1999**, *284*, 785-788. b) Hirschberg J. H. K. K.; Brunsveld L.; Ramzi A.; Vekemans J. A. J. M.; Sijbesma R. P.; Meijer E. W. *Nature* **2000**, *407*, 167-170. c) H. Fenniri, B.-L. Deng, A. E. Ribbe, *J. Am. Chem. Soc.* **2002**, *124*, 11064. d) De Jong J. J. D.; Lucas L. N.; Kellogg R. M.; Van Esch J. H.; Feringa B. L. *Science* **2004**, *304*, 278-281. e) R. Eelkema, B. L. Feringa, *J. Am. Chem. Soc.* **2005**, *127*, 13480-13481. f) R. Eelkema, B. L. Feringa, *Org. Lett.* **2006**, *8*, 1331-1334.
[5] Hill D. J.; Mio M. J.; Prince R. B.; Hughes T. S.; Moore J. S. *Chem. Rev.* **2001**, *101*, 3893-4011.
[6] a) Yashima E.; Maeda K.; Okamoto Y. *Nature* **1999**, *399*, 449-451. b) Cornelissen J. J. L. M.; Rowan A. E.; Nolte R. J. M.; Sommerdijk N. A. J. M. *Chem. Rev.* **2001**, *101*, 4039-4070. c) Pijper D.; Feringa B. L. *Angew. Chem. Int. Ed.* **2007**, *46*, 3693-3696.
[7] a) *Handbook of Liquid Crystal Research* (Ed.: Collins P. J. and Patel J. S.), Oxford University Press, New York, Oxford, **1997**. b) *Chirality in Liquid Crystals*, (Ed.: Kitzerowand H.-S. and Bahr C.), Springer-Verlag, New York, **2001**. c) Eelkema R.; Feringa B. L. *Org. Biomol. Chem.* **2006**, *4*, 3729-3745.
[8] For reviews see: a) G.P. Spada, G. Proni, *Enantiomer* **1998**, *3*, 301-314; b) R. Eelkema, B.L. Feringa, *Org. Biomol. Chem.* **2006**, *4*, 3729-3745.
[9] a) N.P.M. Huck, W.F. Jager, B. de Lange, B.L. Feringa, *Science* **1996**, *273*, 1686-1688; b) T. Ikeda, A. Kanazawa in *Molecular Swit*ches (Ed. B.L. Feringa), Wiley-VCH, Weinheim, **2001**, Ch. 12; c) S. Pieraccini, S. Masiero, G.P. Spada, G. Gottarelli, *Chem. Commun*. **2003**, 598-599; d) T. Ikeda, *J. Mater. Chem*. **2003**, *13*, 2037-2057; e) R. Eelkema, B.L. Feringa, *Chem. Asian J.* **2006**, *1*, 367-369.
[10] G. Solladié, R.G. Zimmermann, *Angew. Chem., Int. Ed.* **1984**, *23*, 348-362.
[11] i.e. M. M. Green, N. C. Peterson, T. Sato, A. Teramoto, R. Cook, S. Lifson, *Science* **1995**, *268*, 1860-1865.
[12] M.M. Green, J.-W. Park, T. Sato, A. Teramoto, S. Lifson, R.L.B. Selinger, J.V. Selinger, *Angew. Chem., Int. Ed*. **1999**, *38*, 3138-3154.
[13] M.M. Green, M.P. Reidy, R.D. Johnson, G. Darling, D.J. O'Leary, G. Willson, *J. Am. Chem. Soc*. **1989**, *111*, 6452-6454.
[14] M.M. Green, B.A. Garetz, B. Muñoz, H. Chang, S. Hoke, R.G. Cooks, *J. Am. Chem. Soc*. **1995**, *117*, 4181-4182.
[15] M.M. Green, C. Andreola, B. Muñoz, M.P. Reidy, K. Zero, *J. Am. Chem. Soc*. **1988**, *110*, 4063-4065.
[16] a) M. Brehmer, J. Lub, P. v.d. Witte, *Adv. Mater*. **1998**, *10*, 1438-1441; b)R. Mruk, R. Zentel, *Macromol*. **2002**, *35*, 185-192; c) V. Shibaev, A. Bobrovsky, N. Boiko, *Prog. Polym. Sci*. **2003**, *28*, 729-836.
[17] G. Maxein, R. Zentel, *Macromolecules*, **1995**, *28*, 8438-8440. In the case of CPL-induced helical changes, see: J. Li, G.B. Schuster, K.-S. Cheon, M.M. Green, J.V. selinger, *J. Am. Chem. Soc*. **2000**, *122*, 2603-2612.

[18] a) Y. Okamoto, M. Matsuda, T. Nakano, E. Yashima, *Polymer J.* **1993**, *25*, 391-396; b) Y. Okamoto, M. Matsuda, T. Nakano, E. Yashima, *J. Polym. Sci. A, Polym. Chem.* **1994**, *32*, 309-315.
[19] a) Natansohn A.; Rochon P. *Chem. Rev.* **2002**, *102*, 4139-4175. b) Ikeda T. *J. Mater. Chem.* **2003**, *13*, 2037-2057.
[20] Iftime G.; Labarthet F. L.; Natansohn A.; Rochon P. *J. Am. Chem. Soc.* **2000**, *122*, 12646-12650.
[21] The effect likely originates from a long-range helical arrangement of the azobenzenes, see: Kim M.-J.; Yoo S.-J.; Kim D.-Y. *Adv. Funct. Mater.* **2006**, *16*, 2089-2094.
[22] a) Campbell S.; Lin Y.; Muller U.; Chien L.-C. *Chem. Mater.* **1998**, *10*, 1652-1652. b) Bobrovsky A. Y.; Boiko N. I.; Shibaev V. P.; Springer J. *Adv. Mater.* **2000**, *12*, 1180-1183. c) Mruk R. Zentel R. *Macromolecules* **2002**, *35*, 185-192. d) Shibaev V.; Bobrovsky A.; Boiko N. *Prog. Polym. Sci.* **2003**, *28*, 729-836.
[23] D.Pijper, *Ph.D. Thesis*, University of Groningen, **2008**, CD data in chapters 5 and 6.
[24] The half-lifes of the thermal steps for the molecular motor used in (2'*S*)-(*M*)-*trans*-PHIC are in the order of only 5 min.
[25] High Molecular Weight Liquid Crystals.
[26] See references above by Green et. al or A.M. Schoevaars, *Ph.D. Thesis*, University of Groningen, **1998**.
[27] Rotation was observed for the thermotropic systems with molecular motors, see chapters 2 and 3 of this thesis.
[28] The circular patterns observed (Figures 4.14d and e) have been previously described as defects for other cholesteric liquid crystalline systems: Bouligand Y. *Le Journal de Physique*, *34*, **1973**, 603. The defects seem to originate from an ensemble of pseudo-ellipses, which result in several hyperbolic segments (see especially Figure 1d in the Bouligand paper).
[29] For a study on the relation between the helicity of the polyisocyanate and the helicity of the cholesteric LC formed by these polymers, see: M.M. Green, N.C. Peterson, T. Sato, A. Teramoto, R. Cook, S. Lifson, *Science*, **1995**, *268*, 1860-1865.
[30] N. Tamaoki, *Adv. Mater*. **2001**, *13*, 1135-1147.
[31] D.Pijper, B.L. Feringa, *Angew. Chem., Int. Ed*. **2007**, *46*, 3693-3696.
[32] D.Pijper, M.G.M. Jongejan, A. Meetsma, B.L. Feringa, *J. Am. Chem. Soc*. **2008**, *130*, 4541-4552.

Chapter 5

Surface Phenomena of a Functionalized Polyisocyanate

Functionalized polyisocyanates generate toroidal structures when drop-cast onto a surface. These doughnut-shaped aggregates can be generated on various substrate types (gold, mica, and glass) and from various solvent systems. Depending on the solvent used for drop-casting the exact dimensions are slightly altered. Therefore depending on the application appropriate dimensions can be selected. Unique to this system is that large arrays of ordered toroids (more than 100 x 100 µm) are generated.

Part of this chapter has been published: G. T. Carroll, M.G.M. Jongejan, D. Pijper, B.L. Feringa, *Chem. Sci*., **2010**, *1*, 469–472

5.1 Introduction

Many biological macromolecules are known to be globules in their native state. Controlling the condensation of such biomolecules has drawn much attention in the potential of using these as a form of non-viral gene therapy.[1] Therefore there is a large interest in stiff, single-chained macromolecules which can form similar globular structures.

Toroidal shapes are one possible globular structure that can be generated. These types of structures can be generated by DNA, [2] porphyrin derivatives,[3] charged molecules such as polyelectrolytes,[4] or doughnut-like aragonite particles.[5] Similar structures have also been observed for various other polymeric systems as well.[6] In the case of flexible amphiphilic polymer chains, cylindrical globules are formed which generate nearly spherical globules (based on spherical micellar aggregation). In the case of stiffer chains, the globules tend towards more elongated cylindrical shapes (cylindrical micelles). If there is an even further increase in the degree of stiffness, a collagen-like structure is obtained. Owing to the chains folding in upon themselves and winding around each other, collagen-like and toroidal structures are formed.[7] Therefore transition of a globule to a torus is achieved as a function of the increased stiffness of the polymer chain.[8]

These toroidal morphologies could be useful in applications such as templates for stable nano- and micro-meter scale patterning.[9] These patterns could then be used to control the condensation of large biomolecules in non-viral gene therapy [10], nanoreactors [11] and selective cellular translocation [12]. For optimal use of a substrate, monodisperse and well ordered arrays of these toroids are required[13]. The most uniform nano-scale toroidal structures thus far have been achieved by Chang *et al.* in the case of diblock copolymers.[14] Though the structures are uniform in size and shape, they are distributed over the surface in a non-uniform fashion. The structures are occasionally found in bunches, or entirely alone rather than in uniformly ordered arrays.

Lateral order in molecular and polymeric assemblies has often been generated by self assembly and dewetting and drying processes,[15] airflow,[16] or through shear induction[17]. The phenomenon of a drying droplet has been studied for over 200 years.[18] However, its behavior is still not fully understood. Upon drying such features as wormlike clusters,[19] saw-tooth patterns and lamellar structures can be observed.[20] It is not a typical feature to find arrays of toroids in an ordered pattern as a result of dewetting.

Poly(*n*-hexyl isocyanate) (PHIC) is a polymer known for its helical configuration. In solution it exists as a dynamic equilibrium between left- and right-handed helices. PHIC behaves as a rod-like polymer owing to the

fact that its contour length is less than its persistence length.[21] The persistence length of a polymer quantifies its stiffness. In the case of semiflexible polymer chains, it is equal to one half the Kuhn length (theoretical value which can be thought of as if they are freely jointed with each other). The contour length of a polymer is the length of the entire polymer chain at the maximum physically possible extension. The chain dimensions of PHIC are solvent dependent.[22] As the molecular weight of the polymer changes, so do its interfacial properties.[23] It was demonstrated previously by several groups that functionalizing a PHIC with chiral[24] groups, potentially switchable,[25] affects the persistence length of the molecule. PHIC has previously been functionalized with either a molecular motor[26] or chiroptical switch[27] increasing the persistence length as well as being able to induce both helicities depending on the chirality of the switch or motor segments. In this study we focus on the effects of molecular motor functionalized PHIC macromolecules (Scheme 5.1 and 5.2) and their interfacial behavior compared to its switch- and non-functionalized counterparts. Various solvents, substrates, temperatures and aging effects of the sample stock solution were studied.

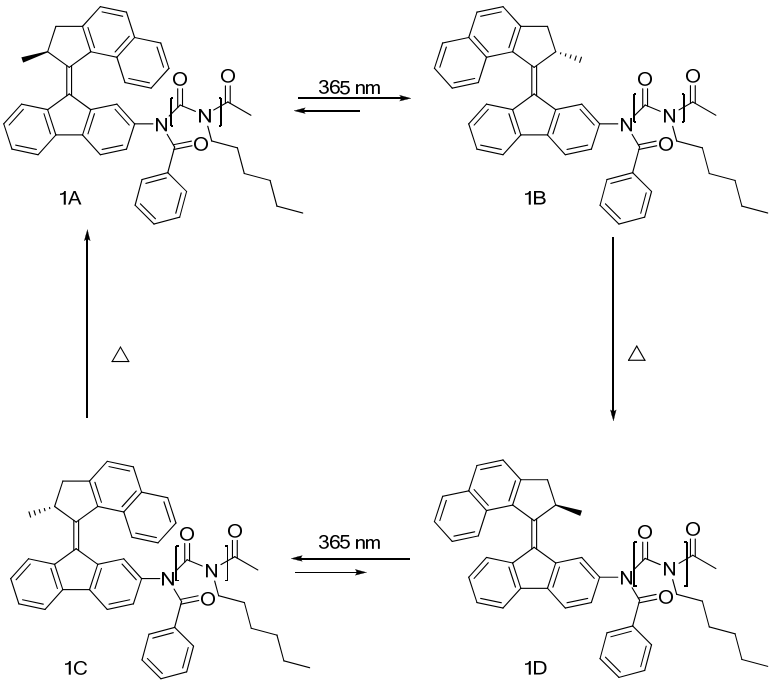

GPC = (for *cis* compound) M_w =28,700

Scheme 5.1 The molecular motor functionalized PHIC (referred to as (2'*S*)-(*P*)-**1**-PHIC) structure and the irradiation cycle. Partially adapted from ref 26.

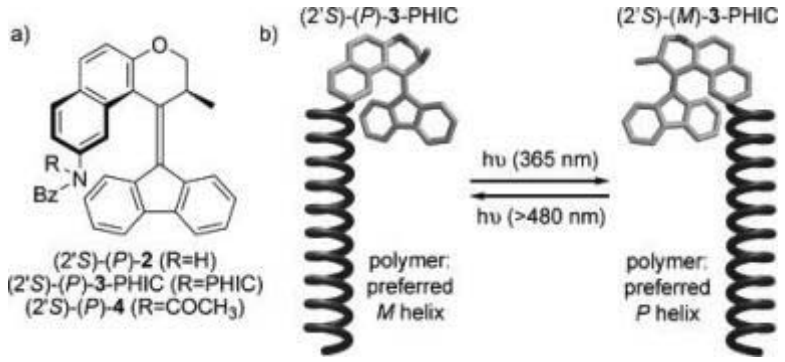

GPC: M_n) 25 850, M_w) 32 650, D) 1.26.

Scheme 5.2 The chiroptical switch functionalized PHIC (referred to as (2'*S*)-(*P*)-**3**-PHIC) structure and the irradiation cycle. Partially adapted from ref 26.

The main differences between the switch- and motor- functionalized PHIC are the number of addressable states and the helical induction. In the case of the motor system the polymerization is initiated from the lower half. Thus a de-symmeterized lower half ensues. Upon subsequent UV irradiation and heating cycles full unidirectional 360 º rotation is achievable. Therefore this structure would seem the most likely to be able to cause motion on a surface. However, the switch-functionalized PHIC ((2'*S*)-(*P*)-**3**-PHIC) has only two states which can be reached using light of different wavelengths. It was previously shown that the helical induction in this system however, is three times higher.[28] Thus it would be interesting to observe whether this increased induction can alter the morphologies observed upon a surface after deposition, and whether or not motion can be observed as a consequence of irradiation.

5.2 Aggregation Behavior in solution

It is interesting to determine whether or not aggregation[29] of the functionalized polymer is possible in solution as this will effect the type of aggregate formed and the homogeneity of the structures observed (i.e. if aggregation occurs, large aggregates might be expected at high concentrations). To ascertain whether or not the formation of the toroidal (doughnut-shaped) aggregates observed on the surface were due to pre-aggregation in solution several experiments were conducted.

5.2.1 DLS

DLS (dynamic light scattering) is a technique often used in surfactant chemistry to determine the size of aggregates such as vesicles. When studying the samples of (2'*S*)-(*P*)-**1**-PHIC in chloroform (concentration 1 x 10^{-6}M), the Z average mean was 254.5 nm with a polydispersity of 1 and a count rate (the number of aggregates registered per second) of 0.1 kCps. The sample was measured at 24 ºC and has a viscosity of 0.950 cP. The

experiments had to be conducted quickly as the chloroform dissolves the cuvet with time. Toluene has a similar effect. However, these were the solvents of choice as the polymer had to be soluble in order to conduct the experiment. Repeating the experiment occasionally yielded no Z average (owing to a too low count rate). The low count rate is a direct consequence of the low concentration of the samples being used (however, note that this is the concentration at which the solution is deposited on the surface). The polydispersity indicates that there seems to be no variation in the size of aggregate present. This would be unexpected in the case of a large number of aggregates. DLS is a very dust sensitive technique and therefore usually special filters are used to remove dust particles and prevent false positives (the DLS cannot distinguish between a dust particle, or an aggregate of the same size). However, chloroform and other organic solvents dissolve membranes used for filtering, adding more undefined materials to the system. Thus, in this case it cannot be excluded that dust caused the observed signal. This would explain why so few particles were observed. Another technique will be required to prove the pre-aggregation of these materials in solution.

5.2.2 UV-VIS and CD spectroscopy

UV/VIS spectra were measured to attempt to ascertain whether switching is still possible and whether there are aggregates in solution.

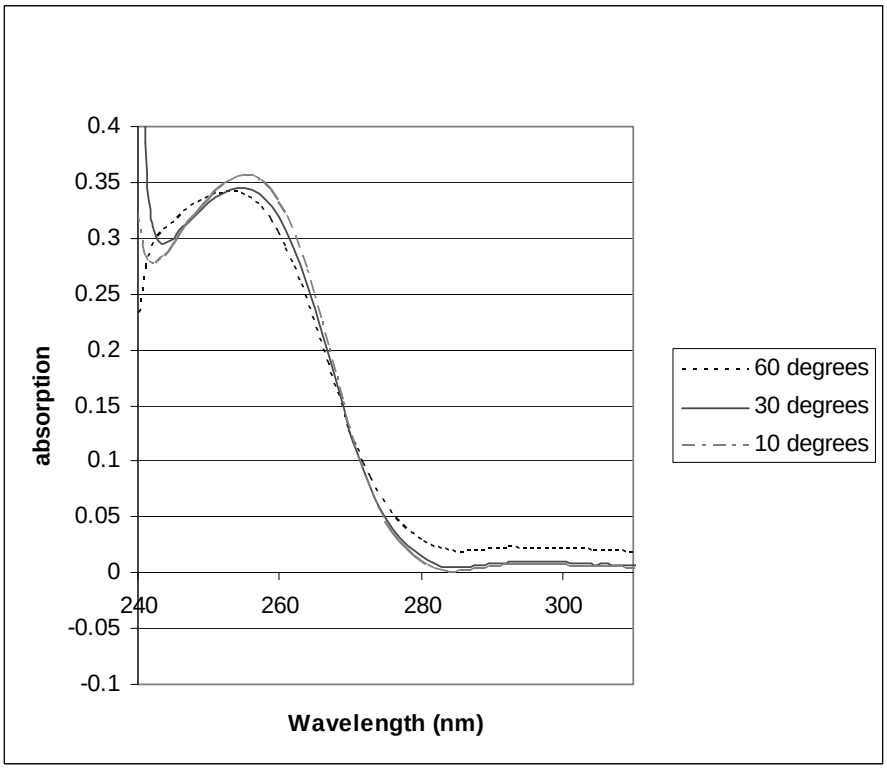

Figure 5.1 UV-VIS spectra of a solution of (2'*S*)-(*P*)-**3**-PHIC in chloroform at various temperatures (concentration $1x10^{-6}$ M). Presented are UV-VIS difference spectra, as the spectrum for the solvent at the same temperature is subtracted.

The UV-VIS spectra showed that at normal UV concentrations the region for the π-π* transition shows mostly a flat baseline (Figure 5.1). As the polymer monomer units are present in vast excess to the motor molecule, high concentrations of sample are required to see changes in the π-π* region (280-400 nm). Owing to the relatively high concentration used so that the switch moiety could be observed, the spectra were only recorded starting at 240 nm. At lower wavelengths the absorption was too large (absorption intensity in the range of 2-4) and could damage the instrument during measurement. The absorption for the polymer chain with a maximum at 258 nm shows a minor decrease with a temperature increase. This effect may be caused by the fact that the rigidity of the stiff helical structure is somewhat altered.[30] However, the effect in this case is minor. The changes in the wavelength range of the switch absorption were not possible to ascertain owing to the intensity problems caused by the polymer chain.

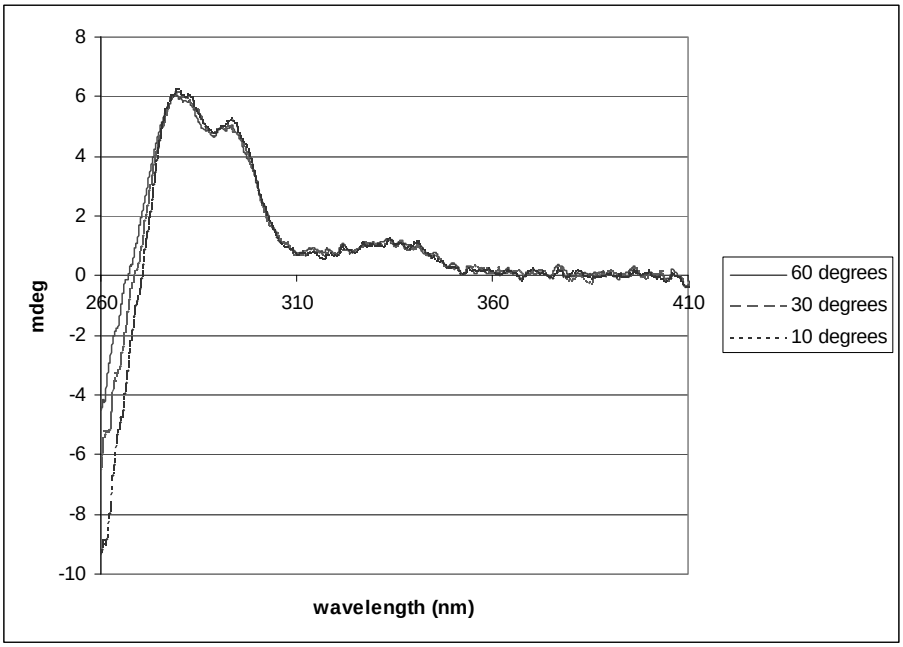

Figure 5.2 CD spectra of a solution of (2'*S*)-(*P*)-**3**-PHIC in chloroform at various temperatures (concentration $1x10^{-6}$ M).

To attempt to determine whether or not aggregation occurs in solution, CD spectra were taken at various temperatures. It can be seen from Figure 5.2 and the enlargement of part of the spectrum in Figure 5.3 that there are tiny changes in the signal in the region between 260 and 310 nm. The absorption maxima at both 280 and 295 nm decrease upon increasing the temperature. This could be interpreted as a hypochromic effect. The decrease in magnitude is only about 5 mdeg. This is a minor change and thus it is not conclusive proof of aggregation in solution.

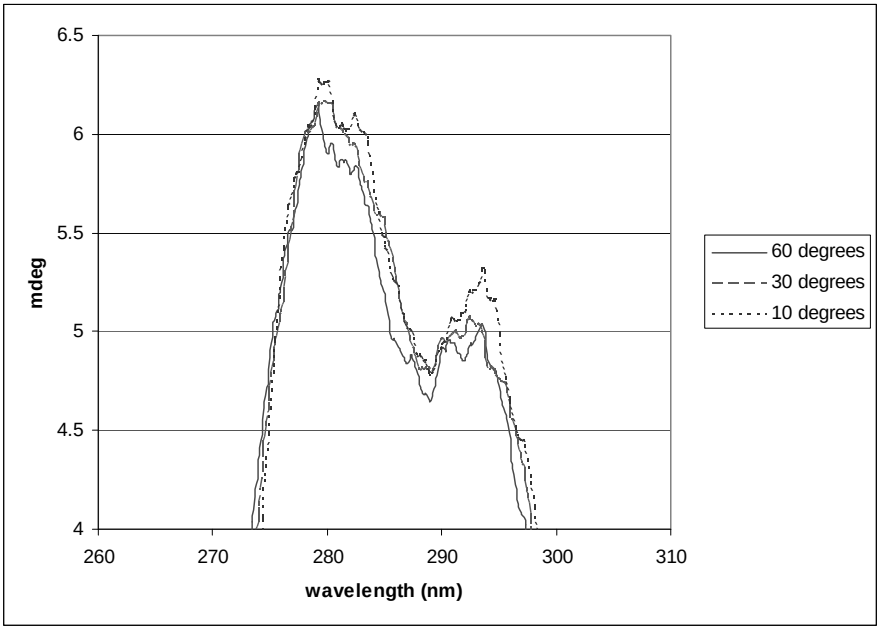

Figure 5.3 Enlargement of an area of the CD spectrum shown in Figure 5.4 where changes occurred with varying temperature.

5.2.3 DSC

In surfactant chemistry differential scanning calorimetry (DSC) is often used to determine the transition temperature at which molecules within the aggregate change from a gel-like to a liquid crystalline phase. In our case organic solvents are used. Chloroform is known for its ability to dissolve plastics and synthetic rubbers. Thus, certain standard setups used for aqueous solutions are no longer compatible with the solvent used. Therefore it was attempted to place the chloroform solution of (2'*S*)-(*P*)-**1**-PHIC in special DSC pans with rubber rings for sealing oils. Though the seals appeared to keep the solvent inside the container, the resulting DSC scans upon heating proved inconclusive. The first trial showed a transition temperature, however this proved irreproducible. Thus this technique was incapable of proving or disproving aggregation in solution.

The solid samples of the functionalized and unfunctionalized polyisocyanate were measured in the temperature range of -50 ºC to approximately 120 ºC. This upper limit was selected as it is known in the literature that heating above 120 ºC destroys the polyisocyanate. The measured glass transition temperatures were -23.6 ºC for unsubstituted PHIC and -24.1 ºC for (2'*S*)-(*P*)-**1**-PHIC.

5.2.4 Temperature-dependent NMR analysis

^{1}H-NMR spectra reveal the particular nature and surroundings of the hydrogens in a molecule. As the temperature at which the spectra are measured is changed the resulting spectra will show varying characteristics. In the case of aggregates one would expect that upon going to higher temperatures, the aggregates would dissociate and thus the signals of individual hydrogens should become apparent. In single molecules with rigid bonds coalescence is expected (rotation about a bond is rapid enough to make two signals become one). In this case we have been studying the (2'*S*)-(*P*)-**1**-PHIC system at temperatures above room temperature.

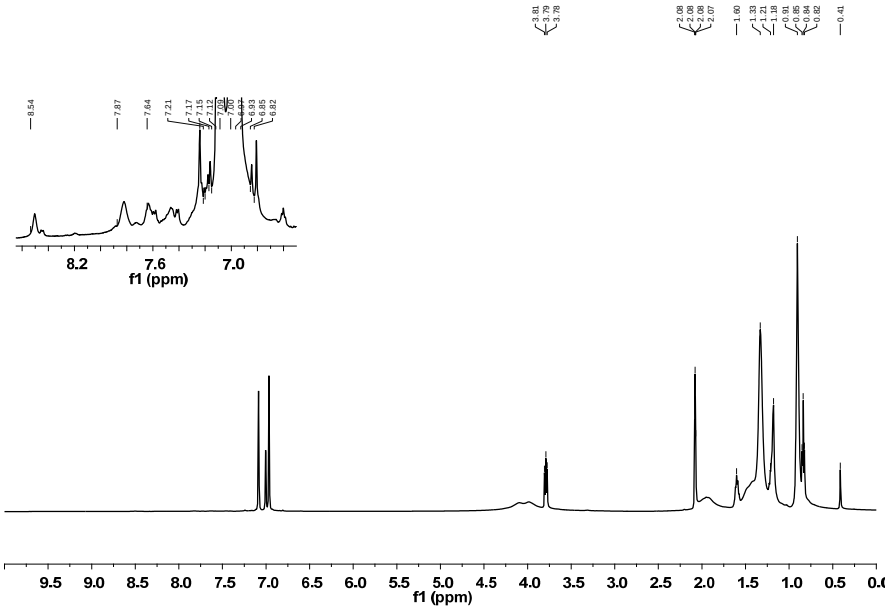

Figure 5.4 ^{1}H-NMR spectrum of a solution of (2'*S*)-(*P*)-**1**-PHIC in D_8-toluene (concentration of 15 mg/ml). The temperature was 31 ºC.

^{1}H-NMR spectra were recorded of (2'*S*)-(*P*)-**1**-PHIC in toluene owing to the larger temperature range that can be measured in order to attempt to clarify whether or not aggregation takes place in solution at different temperatures (see Figure 5.5 for an expanded aliphatic region and Figure 5.6 for the expanded aromatic region). The spectra were measured at 31 ºC, 60 ºC, 90 ºC and after the heating cycle again at 31 ºC. The spectra before and after the heating cycle were identical, thus degradation can be excluded as an explanation for any variations in the ^{1}H-NMR spectra at higher temperatures.

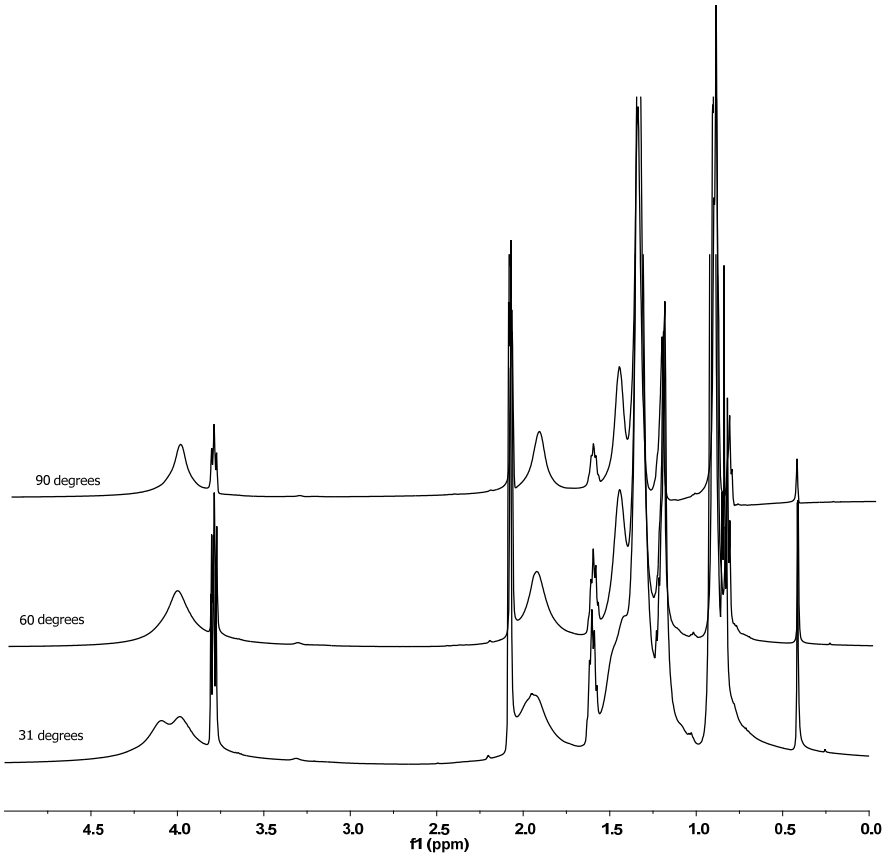

Figure 5.5 Expansions of the aliphatic region of ^{1}H-NMR spectra of the (2'*S*)-(*P*)-**1**-PHIC (15 mg in 1 ml) in toluene D_8 at various temperatures.

In the aliphatic region the ^{1}H-NMR spectra represents the polymeric segment of the molecule. This segment shows few changes upon heating. The polymer chain is helical in nature and rigid. Therefore the aggregation would have to take place amongst the *n*-hexyl side chains. Upon heating one might expect the rigidity of the polymer chain to decrease. If aggregation would occur the protons on the side chains should show more distinct signals. The doublet at 4.2 ppm coalesces (Figure 5.5) going from a subtle doublet to a singlet. This doublet represents the CH_2 directly attached to the isocyanate backbone. Coalescence is expected upon heating for rigid bonds. At higher temperatures rapid conformational interconversion along the bonds is possible and thus the separate signals merge. Two signals in the aliphatic region, however, become more defined. The broad singlet before 2.0 ppm becomes more defined, while at 1.4 ppm there is initially only a shoulder on the side of a large singlet. Upon heating this shoulder becomes a well-defined singlet. Both of these signals are related to the *n*-hexyl side chain at various positions relative to the isocyanate chain. As stated above

upon heating coalescence is expected. However, in the case of aggregated systems, upon heating the aggregates would dissociate and the spectra of the original monomer unit become visible (better resolution). This could be an explanation for the better resolution observed. It must be remembered that the polyisocyanate chain orientation is itself temperature dependent; as the helix reversals are temperature dependent[30] and determine the cooperativity in the system (optical activity alters). In our system there are relatively few helix reversals to contend with, however, improved cooperativity may also be responsible for some of the observed changes. There is no direct comparison possible, as previous measurements on temperature dependence have been based on blends or on slightly different structures (i.e. PBHIC instead of PHIC).[31] However, the mixture of coalescence and increased definition in the NMR spectra has not been reported. This is a good indication that the alterations observed are not entirely generated by the temperature dependence of the polymer and might indicate aggregation.

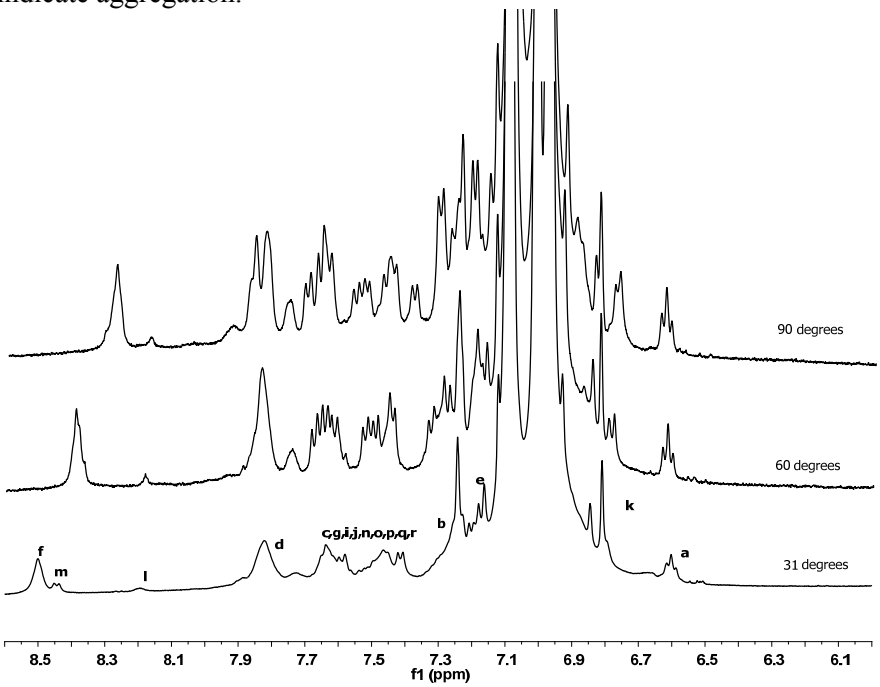

Figure 5.6 Expansions of the aromatic region of ^{1}H-NMR spectra of the (2'*S*)-(*P*)-**1**-PHIC (15 mg in 1 ml) in toluene D_8 at various temperatures.

The aromatic region of the ^{1}H-NMR spectra is more difficult to interpret.[32] Several absorptions coalesce i.e. the one at 8.4 ppm (Figure 5.6). However, simultaneously several other absorptions show improved resolution upon heating. At 31 and 60 ºC the absorption at 7.9 ppm looks like a well-defined multiplet (see Figure 5.7 for possible identities of protons). However, at 90 ºC this multiplet splits into a doublet and a triplet. This might imply that through aromatic π-π stacking the signals originally broaden, however,

upon heating the molecules disassemble and their separate absorptions become visible. The three bands of the solvent are always located in the middle of the aromatic region and overlap with bands corresponding to the polymer; however a larger temperature range could be achieved.
In the case of dominating solvent resonances in an ^{1}H-NMR spectrum, these can be suppressed. This suppression can be achieved by saturation of the solvent resonance.[33] However, solvent suppression cannot be used in this case as the area where the solvent peak resides and a section around this will be invisible in the new spectra, overlapping with even more of the signals of interest. As a result even fewer peaks will remain visible. Thus no more detailed information could be obtained from this experiment.

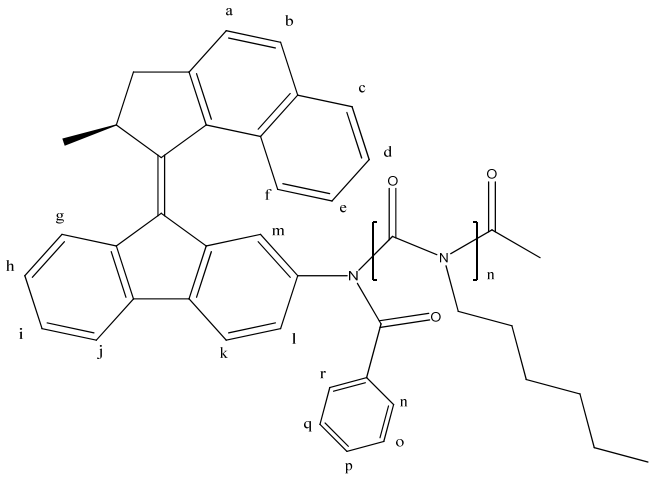

Scheme 5.7 The structure of **1** being used in the temperature dependent ^{1}H-NMR measurements with labeling for the carbons in the aromatic region used in the NMR spectra in Figure 5.8 in attempts to assign specific hydrogens.

However, it appears that in the samples based on my ^{1}H-NMR data aggregation seems to take place. However, this does not automatically imply that this is the case on the surface. The solutions used for the AFM experiments are vastly less concentrated than the solution used for the ^{1}H-NMR experiment. The high concentrations used in the ^{1}H-NMR experiment were necessary to allow a reasonable concentration of motor molecule to be present in the NMR sample so the aromatic region could be studied. Thus the functionalized PHIC does not necessarily aggregate at the concentrations used for drop casting. However, when the sample is drop-cast onto the surface, the solvent slowly evaporates allowing deposition. This solvent evaporation will cause the local concentration to increase. Thus, the aggregation may be caused on the surface as a result of local concentration changes.

5.3 Behavior on the surface

The functionalized PHIC molecules were dissolved at low concentrations and drop-cast on a freshly cleaned surface. Scheme 5.3 depicts the drop-casting and evaporation process used to study the morphologies generated by (2'*S*)-(*P*)-**1**-PHIC. This results in the observation of large concentric ring depositions reminiscent of coffee stains.[34] However, between these concentric depositions arrays of small toroidal structures were observed.
In the subsequent sections the effects of solvent, substrate dependence and structural effects will be examined in order to determine which conditions are required to generate an optimally patterned surface (i.e. largest arrays of equidistant toroids of equivalent size).

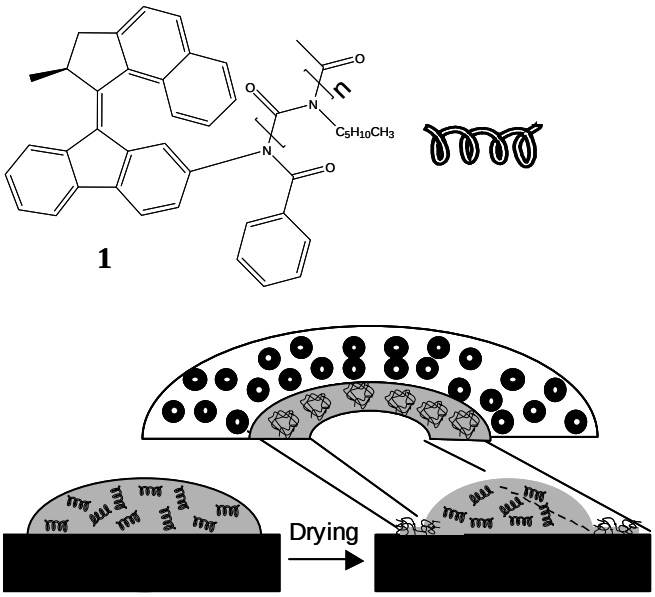

Scheme 5.3 Schematic representation of the possible mechanism of deposition of the solubilized **1**-PHIC on a surface.

5.3.1 Substrate effect

Glass, gold and mica were used as substrates for the deposition of functionalized PHIC systems. The glass surfaces were studied using optical microscopy. Large areas of droplets, which appeared to contain feature holes in the center, could be observed. However, only rather large aggregates could be observed (starting from approximately 5 μm). In the background smaller droplets could be observed, but the exact dimensions could not be ascertained. As a consequence a technique was required that would be able to examine smaller sizes.

For the AFM studies (sections 5.3.2-5.3.3 and 5.3.5-5.3.6) samples were always prepared on gold or mica surfaces. Glass was used for optical

microscopy (sections 5.3.4 and 5.3.7) as it is fully transparent and has fewer defects than mica, but its surface roughness makes it problematic for use in AFM measurements (surface roughness can affect the morphology detected by the AFM). Mica was chosen as the preferred substrate for its atomic flatness and ease of preparing a clean surface via cleavage (gold cleansing or deposition requires far more time). On mica it became apparent that there are large arrays of toroids generated on the surface.

SEM was performed on both gold and mica surfaces to ascertain what the effect of possible different surface interactions could have. Gold, a surface extensively used in electronic devices, has great malleability, corrosion resistance and is highly conductive (5.90×10^{29} cm^{-3} for free electrons). It is also atomically flat. Mica, as well as being atomically flat and easily cleavable (to generate clean surfaces) is used as an insulator as it is a poor conductor. The varying electronic and chemical properties of the two surfaces may alter the ability to generate certain types of morphologies. The results of these measurements can be seen in Figure 5.8.

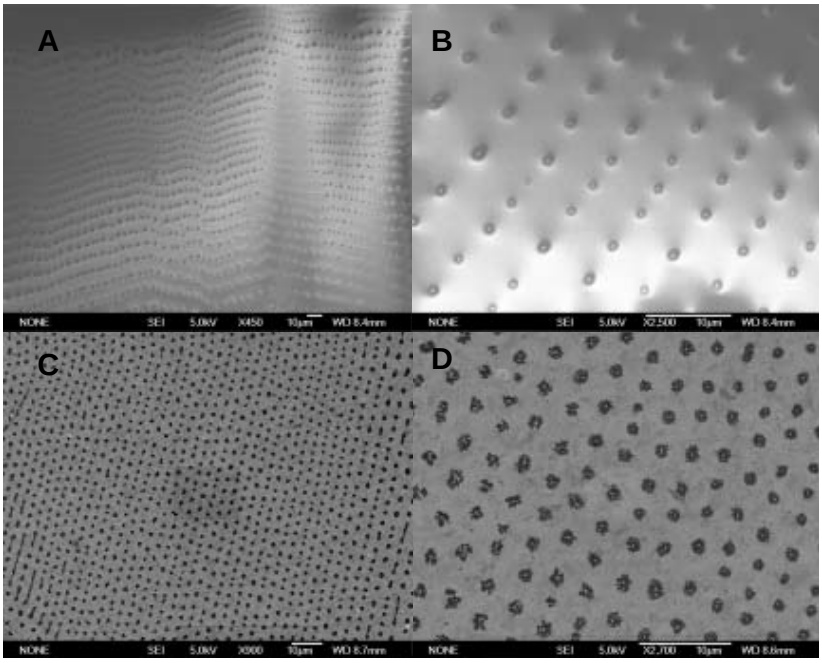

Figure 5.8 SEM images of films prepared by evaporation of a toluene solution containing (2'*S*)-(*P*)-**1**-PHIC on mica (A,B) and gold (C,D) reveal a morphology consisting of spatially aligned toroidal/semi-toroidal structures. The size of the scale bar on each image is 10 μm.

The images in Figure 5.8 show that whether the solutions are deposited on mica or gold, arrays of toroids are generated. However, the shape of these toroids is different. As can be seen from the magnifications in Figure 5.9

the toroids on the mica surface appear to be more homogeneously spherical while those on the gold surface appear to be more wreath-like

(A)

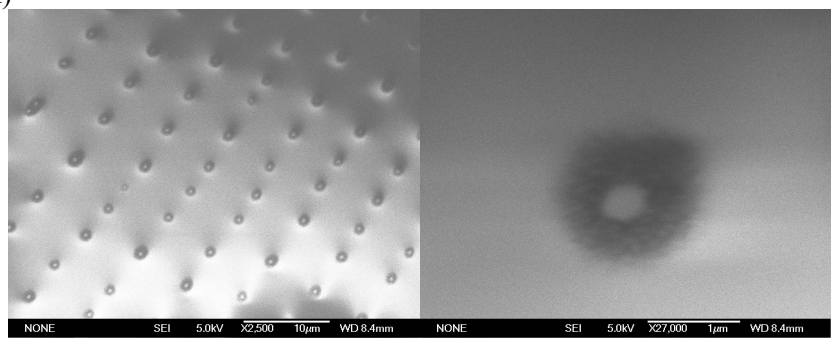

(B)

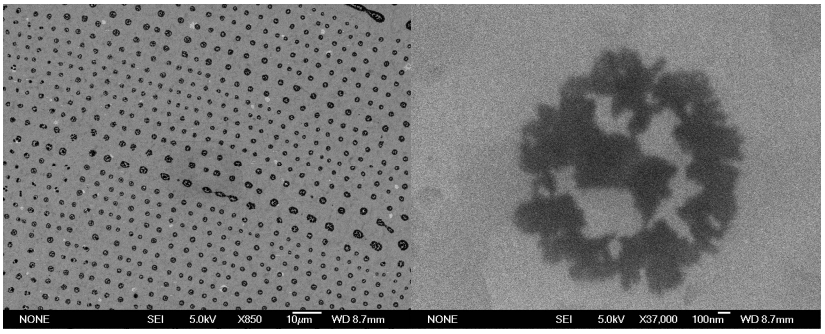

Figure 5.9 SEM images of films prepared by evaporating a toluene solution containing (2'*S*)-(*P*)-**1**-PHIC on (a) mica and (b) gold.

A problem with SEM is that while imaging, the surface is bombarded with electrons. Zooming in, the intensity of this bombardment increases. The polymer system is not very stable under these conditions. A result of this is that after having imaged a small area when zooming out a large white patch can be seen. Therefore imaging must be completed quickly and many areas must be imaged. This problem can be circumvented when using gold as a substrate (good conductor) and when placing a thin gold layer over the surface to protect the polymer morphologies. However, as a result of these deposits the definition of the aggregates becomes less. Though SEM generates clear images of the morphologies on the surface, it does not give clear indication of height variations throughout the sample. Therefore it was opted to carry out further imaging using AFM (no electron bombardment and provides a true three-dimensional surface profile).

5.3.2 Solvent effects

Polyisocyanates are well known to form liquid crystalline phases in toluene. Therefore initially it was decided to prepare all solutions for deposition on a surface in toluene (Figure 5.10). Later two other apolar solvents with different boiling points and protic/aprotic characteristics were also tested. The tested solvents were chloroform (Figure 5.11) and THF with 10% water (Figure 5.12).

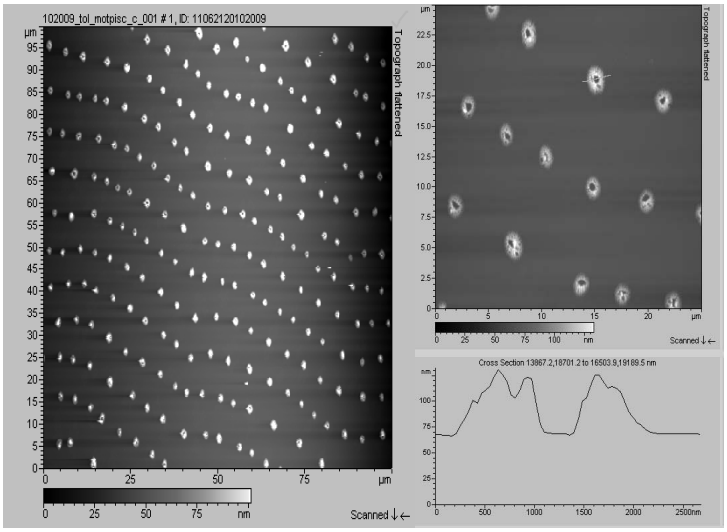

Figure 5.10 AFM images of films prepared by evaporation of (2'*S*)-(*P*)-**1**-PHIC from toluene show fields of toroids. The left image depicts a large field of toroidal structures while the right image shows the toroidal nature of these structures (there is a hole in the middle). The bottom right image shows the relief of the structures. There are clear holes in the middle with an average height of 60 nm.

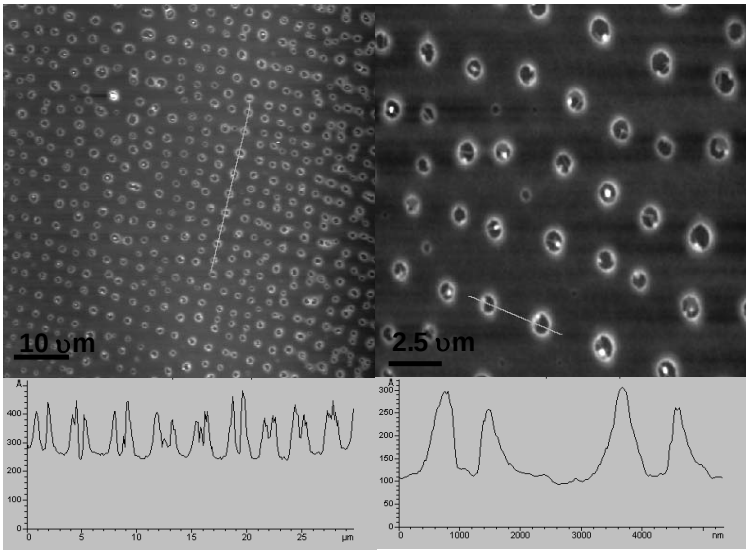

Figure 5.11 AFM images of films prepared by evaporation of (2'*S*)-(*P*)-**1**-PHIC from chloroform show fields of toroids. The left image depicts a large area of toroidal structures while the right image shows the true toroidal nature of these structures (there is a hole in the middle). The bottom images show the relief of the structures. There are clear holes in the middle with an average height of 150-200 Å.

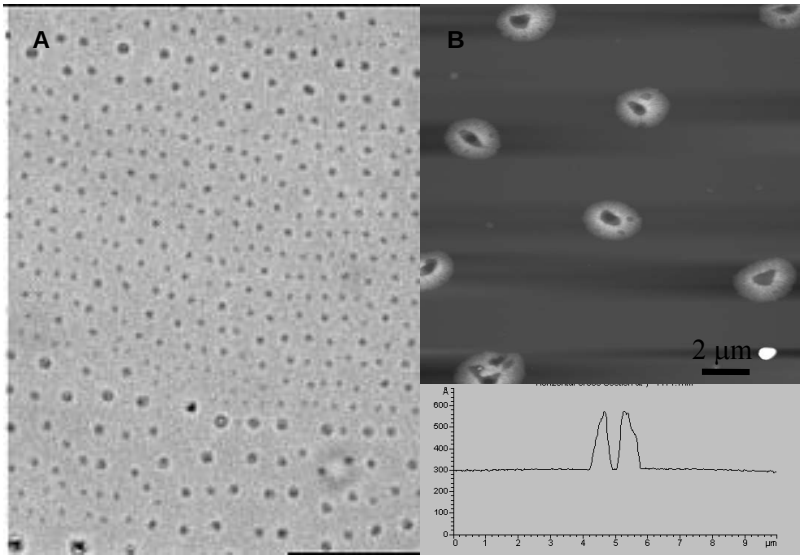

Figure 5.12 Optical microscope image (left) of a film of (2'*S*)-(*P*)-**1**-PHIC drop-cast from THF on mica. Right image is an AFM image of the same film. There are clear holes in the middle with an average height of 200-250 Å.

The different solvents seem to affect the (2'*S*)-(*P*)-**1**-PHIC system slightly. However, all of the solvents generated large domains of regular arrays. These domains were at least 100 x 100μm in size, though larger domains have been observed using optical microscopy. In theses cases the detail of the toroidal structure was lost. It was shown initially (Figure 5.10) that the toroid shapes could be generated from toluene (an aromatic apolar aprotic

solvent). The toroids have dimensions of approximately 2 μm outer diameter, and a height of 10-15 nm. The spacing between the toroids is between 2-6 microns. In this case the possible π-π interactions between the molecular motor segments and the solvent could provide an explanation for the observed toroidal structures. Therefore another apolar aprotic solvent was tested without aromatic segments. As can be seen from Figure 5.11 toroids can also be generated from chloroform (apolar aprotic solvent). In the case of chloroform the height and dimensions of the toroids formed are similar though the structures are slightly smaller in diameter. It was attempted to use a protic solvent to determine the affect of this property on this system. In the case of THF/H_2O (apolar protic) the results are less obvious (Figure 5.12). The microscope pictures suggest droplets, but the structures are too small to obtain more detail. It is clear from the AFM images that there are toroidal structures. The outer rims of the structures are much broader than is the case for the other two solvents. The height is between 20-25 nm, the toroidal diameter starts from 2 μm. The spacing in the arrays is somewhat less consistent. Thus in general the structures generated from THF are thicker and larger rimmed. In the cases of chloroform and toluene the differences in dimension were small, however, the equality of distribution of the toroids is different. The definition of the arrays appears to be dependent on the solvent cohesion, as toluene (highest b.p.) gave the most regular arrays of toroids.

Interestingly, the toroid structures could be generated in all solvents despite the fact that the exact dimensions change. Therefore depending on the exact conditions, the toroid system might be tuned by varying the solvent depending on the particular requirements.

Chloroform became the solvent of choice as more control was possible during evaporation. Controlled drop size made further analysis with AFM easier. However, the uniformity of the arrays was better in the case of toluene. A reason for this might be easier aggregation.[35] Interesting to note is the fact that these samples (when stored away from dust at room temperature) are excessively stable. The original samples were restudied a year after their preparation and the toroidal structures remained intact.

5.3.3 Structural effects

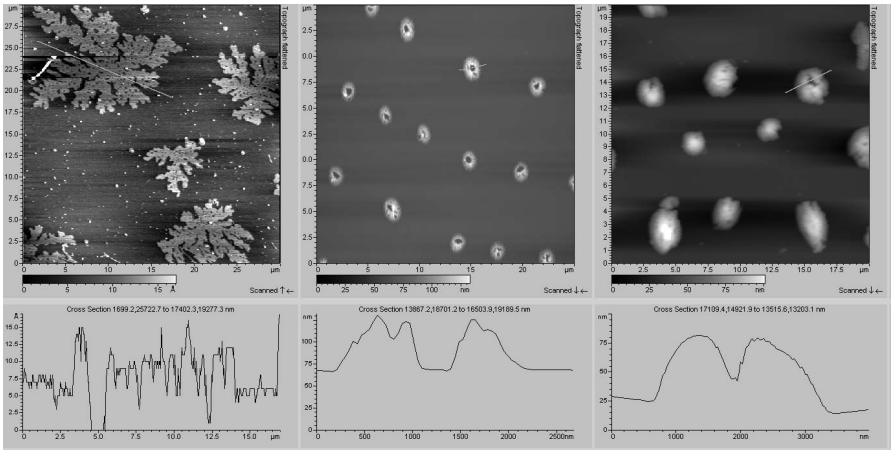

Figure 5.13 AFM images of pure polyisocyanate (left) enantiopure (2'*S*)-(*P*)-**1**-PHIC (middle) and enantiopure (2'*S*)-(*P*)-**3**-PHIC (right).

From the toluene drop-casted samples it became apparent that the sample prepared using enantiopure molecular motor-functionalized PHIC ((2'*S*)-(*P*)-**1**-PHIC) gave the most monodisperse and consistent structures (Figure 5.13, middle image). The chiroptical switch functionalized polyisocyanate ((2'*S*)-(*P*)-**3**-PHIC) mostly formed spherical droplets, though these were much more randomly scattered and less well defined. The pure polyisocyanate sample contained a mixture of structures from droplets to ribbons and the rather unusual dendritic rather flat structures as shown in Figure 5.14 (left image). The reason for these differences might be the fact that the unfunctionalized polyisocyanate has equal amounts of both helices, while in both of the functionalized systems there is a helical preference, however, the persistence length is longer in the case of the (2'*S*)-(*P*)-**3**-PHIC. Due to the conditions of the polymerization process the lengths of the polymeric chains are not equivalent for the three samples in Figure 5.13. As it is known in the literature that chain length is a determining factor, this may as well contribute to the differences observed between structures.[23]

5.3.4 Temperature effect

It was determined that polyisocyanate has a glass transition temperature T_g of -23.6 ºC. In the case of the motor-substituted polyisocyanate this is lowered to a T_g of -24.1 ºC. Therefore, the phenomena observed are independent of the current ambient temperature as these observations are made well above the transition temperature. Thus all samples are always in the glassy state during the experiments.

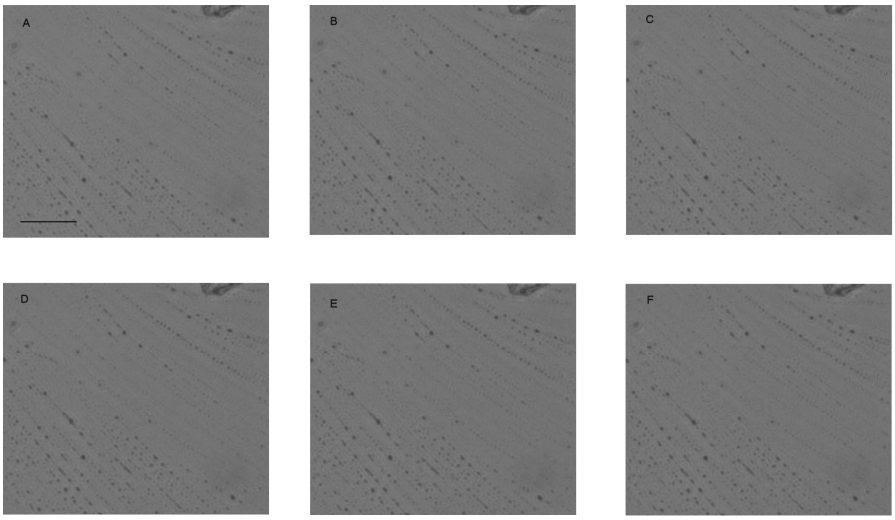

Figure 5.14 Optical micrographs of toroids formed from motor-functionalized polyisocyanate ((2'*S*)-(*P*)-**1**-PHIC) in toluene at different temperatures on glass. A) 25.6 °C B) 39.9 °C C) 50.1 °C D) 60.4 °C E) 65.0 °C F) 70.0 °C. The scale bar equals 50 μm.

A surface covered in the typical arrays of toroidal structures was placed on the heating table under the optical microscope. It was warmed to determine at what temperatures changes in the surface structures might occur. The heating cycle shows that in the case of toluene no change is observed until approximately 70 ºC (Figure 5.14). Upon further heating, the structures seemed to get smaller (Figure 5.15). The doughnuts appear "deflated". The structures have more definition than at room temperature. After cooling the sample, the system does not revert to the swollen doughnuts previously observed. This could indicate that evaporation of solvent molecules remaining entrapped within the polymer coils is taking place.

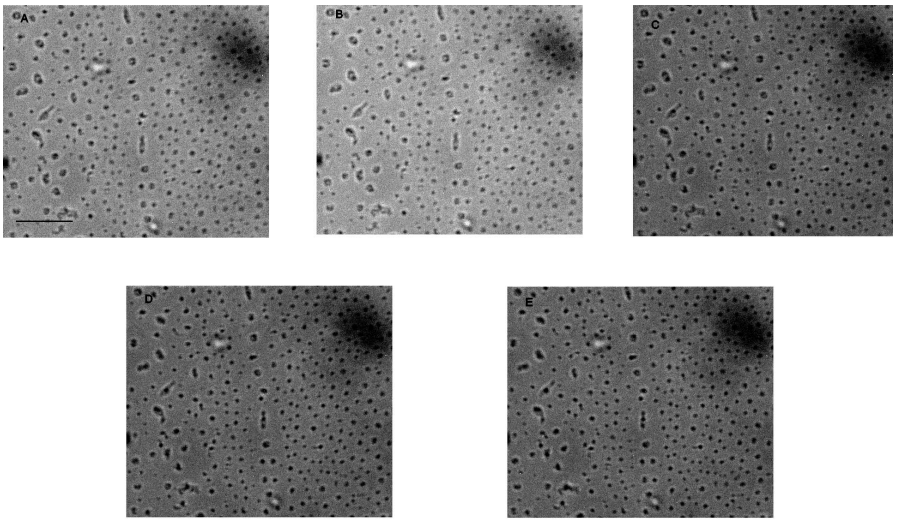

Figure 5.15 Optical micrographs of toroids formed from motor-functionalized polyisocyanate ((2'*S*)-(*P*)-**1**-PHIC) in toluene at different temperatures on glass. A) 70.0 °C B) 75.2 °C C) 80.1 °C D) 85.7 °C E) 90.0 °C. The scale bar equals 25 μm.

5.3.5 Age and concentration effect

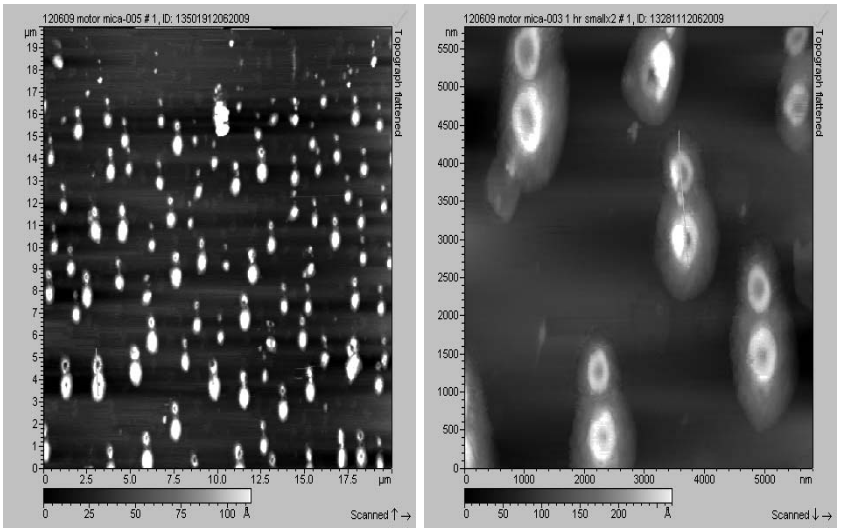

Figure 5.16 AFM images of a large field (left) and a close-up (right) of a sample of ~ 1 μM in chloroform on mica of (2'*S*)-(*P*)-**1**-PHIC. Original concentration of the stock solution was 2 μM and it was diluted to ~ 1 μM on day 5 (day of drop casting).

When preparing the samples, it became apparent that if the solution had been drop-casted directly onto a surface after preparation, toroidal structures were not observed. However, upon aging the solution for a day, large arrays of toroidal structures were observed (see Figure 5.9). It was

therefore decided to age the solutions over several days to compare whether or not with age better defined aggregates resulted. It became apparent that after five days, depending on the concentration of the sample prepared, different aggregates were observed. In the case of higher concentration sample larger well-defined aggregates were generated (Figure 5.16). The lower concentration sample formed small globule-like aggregates. These were spread more randomly over the surface (Figure 5.17). In general the images were difficult to reproduce. Therefore it was decided to continue with solutions of a maximum age of one day.

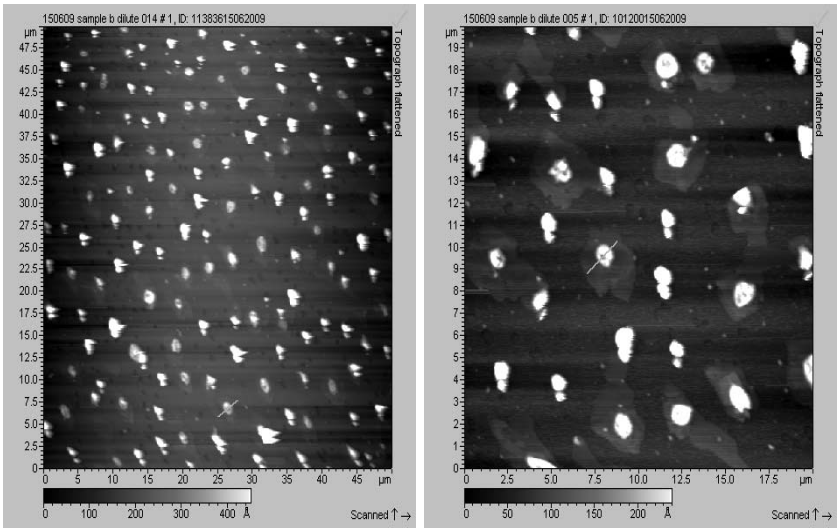

Figure 5.17 AFM images of a large area 50*50 µm (left) and a close-up (right) of a sample cast from ~ 1 µM (2'*S*)-(*P*)-**1**-PHIC in chloroform on mica after 5 d in solution (diluted on day 1, drop casting on day 5).

5.3.6 Irradiation effect

On the surface the polymeric systems form possibly rigid structures. Therefore it would be interesting to determine whether or not it is still possible to switch the molecular motor segment in spite of the tight packing within the toroidal structure on the surface. As the sample being used consists of enantiomerically pure molecular motor, CD spectroscopy could be used to determine whether or not the system is still switchable on the surface.

CD spectra were measured for the sample deposited from chloroform on a quartz surface. It could be seen that using a solution at the concentration of our stock solutions (1.5 mg in 10 ml) the polymer on the surface gave a CD signal (Figure 5.18). However, upon rotating the surface with respect to the light source, the CD signal could be inverted. This would indicate that the observed CD signal is vastly affected by the presence of a linear dichroism

(LD) signal. LD is caused by linear polarization of the light rather than the circular polarization expected. This is a result of the presence of, for instance, patterns on a surface, which will be affected differently depending on the position of the pattern relative to the circularly polarized light source. Thus the actual CD evidence presented here is irrelevant (i.e. the observed spectra are not the actual spectral shapes for the polymeric material in solution). However, the differences in the spectra when a constant position is maintained can be used as evidence of changes in the system.

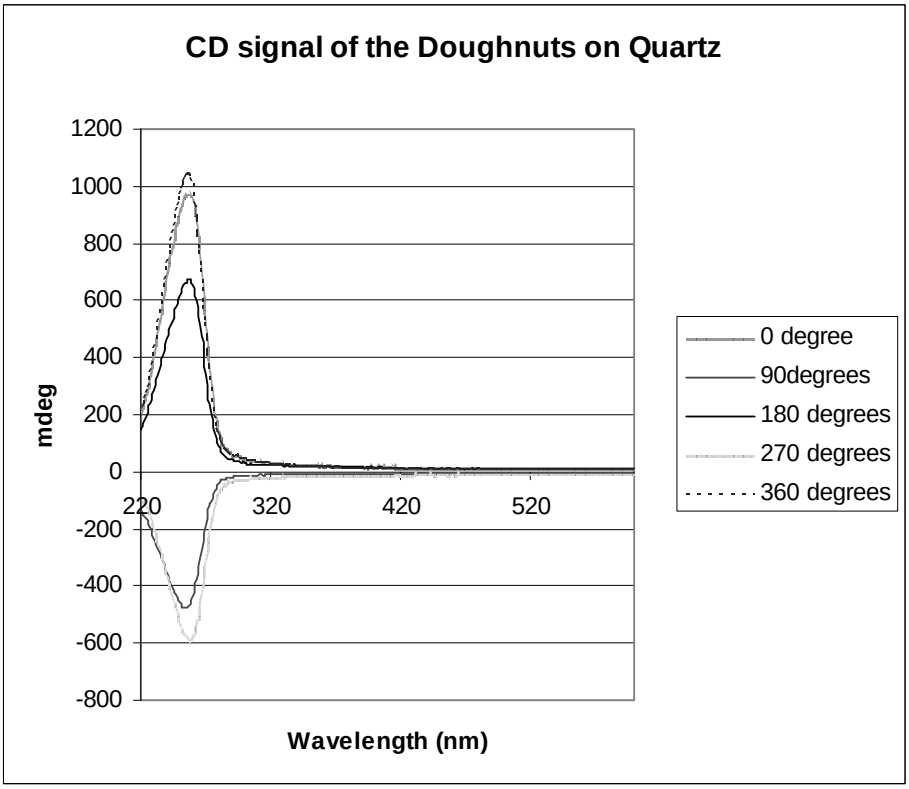

Figure 5.18 CD spectra of the switch functionalized polyisocyanate ((2'*S*)-(*P*)-**3**-PHIC) in chloroform on a quartz surface at various degrees of rotation with respect to the beam.

The CD absorptions observed at the various degrees of rotation are in the region where a signal for the polymer chain is expected. The CD spectra at 0 and 360 degrees of rotation do not overlap exactly owing to the fact that the rotations are approximate. To ascertain whether or not the sample could still be affected by irradiation with UV light in the precipitated form, the slide was fixed in one position and then the sample was irradiated. Owing to the fact that the signal of the switch segment is negligible relative to the signal of the polymer chain the region between 220 and 300 nm was studied (Figure 5.19).

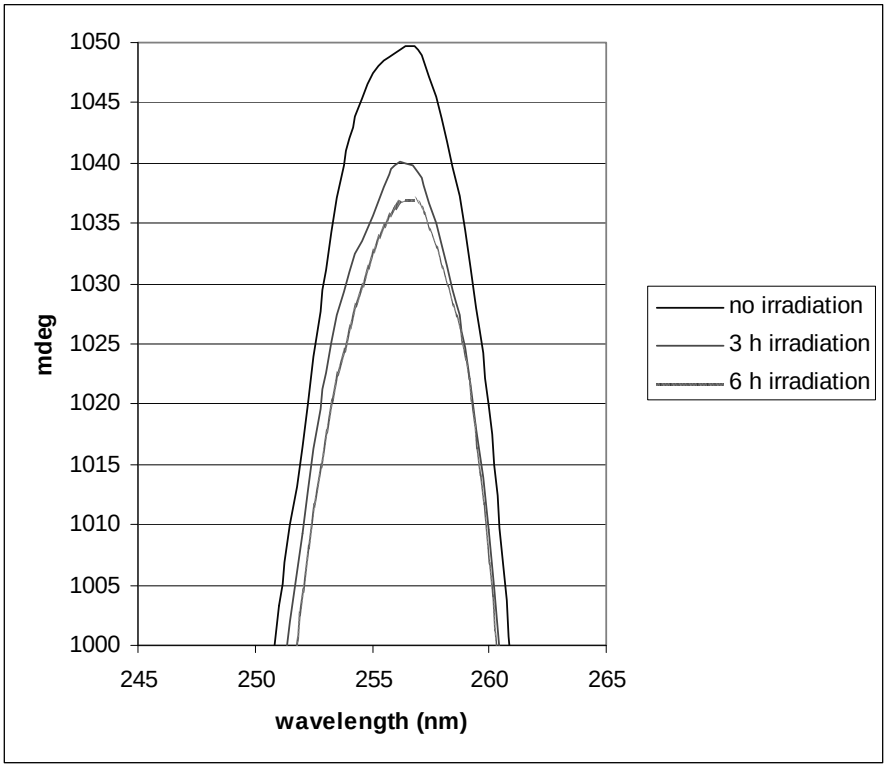

Figure 5.19 Enlargement of an area of the CD spectrum shown in Figure 5.18, of the switch-functionalized polyisocyanate ((2'*S*)-(*P*)-**3**-PHIC) in chloroform on a quartz surface at a fixed position upon irradiation with UV light (λ = 365 nm).

It can be seen that with long irradiation times a decrease in the signal at 257 nm can be observed. A lack of inversion in this region can be a result of the large artifact induced by the LD signal at this wavelength. The data do, however, suggest that switching is still possible in the toroidal shapes deposited on the surface.
As possibly the LD was a direct result of the layer thickness on the surface a lower concentration of sample was deposited on the surface before attempting CD again.

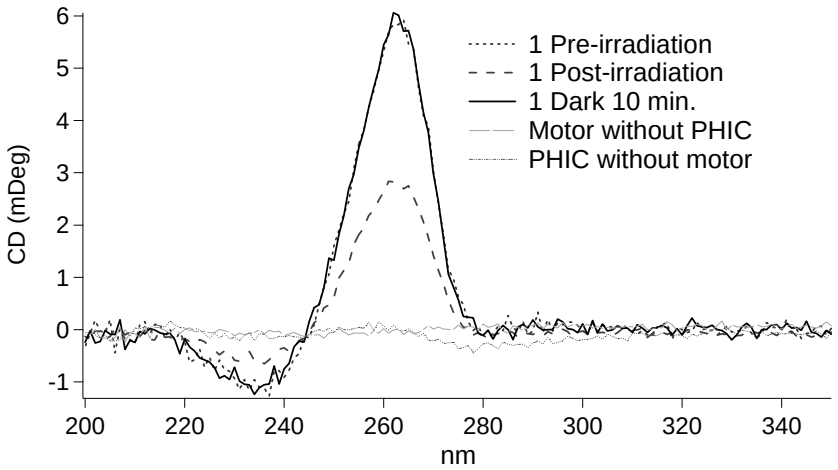

Figure 5.20 Deposition of (2'*S*)-(*P*)-**1**-PHIC from chloroform on a quartz slide produces a chiroptical film displaying a CD signal. Irradiation of the film with UV light decreases the intensity of the CD. The signal is restored after thermal isomerization in the dark. Both PHIC without the motor and the molecular motor produce a signal at the concentration employed.

The resulting film prepared by evaporation of chloroform shows a clear CD effect (Figure 5.20). Pure molecular motor and PHIC show almost no signal. This is expected. The pure PHIC is a helical structure, but, it has helix reversals and is dynamic thus on average it is racemic. The CD spectrum of the molecular motor was recorded at concentrations consistent with the amount present in the solution (there is a large excess of polymer present). Therefore the signal is negligible. Thus the observed spectrum is generated entirely by the induced preference in the polymer. It is clear that the signal after irradiation decreases largely. Upon waiting in the dark it returns to the original signal. This is unexpected since for this form of the molecule (*trans*-) no induction is expected in solution.[26] However, in the toroids the polymeric chains may be intertwined. Thus the expected zero induction might be circumvented by some residual "memory" of the previous position in the system, or incomplete isomerization. Interestingly, not all of the surfaces generated showed an attenuation of the signal or a restauration upon leaving it in the dark. The reproducibility of the data appeared very sensitive to ambient temperature[30] and position (LD[36]). This suggests that in theory the toroids could be addressed with light on the surface. It becomes a challenge to visualize this on the surface using AFM.

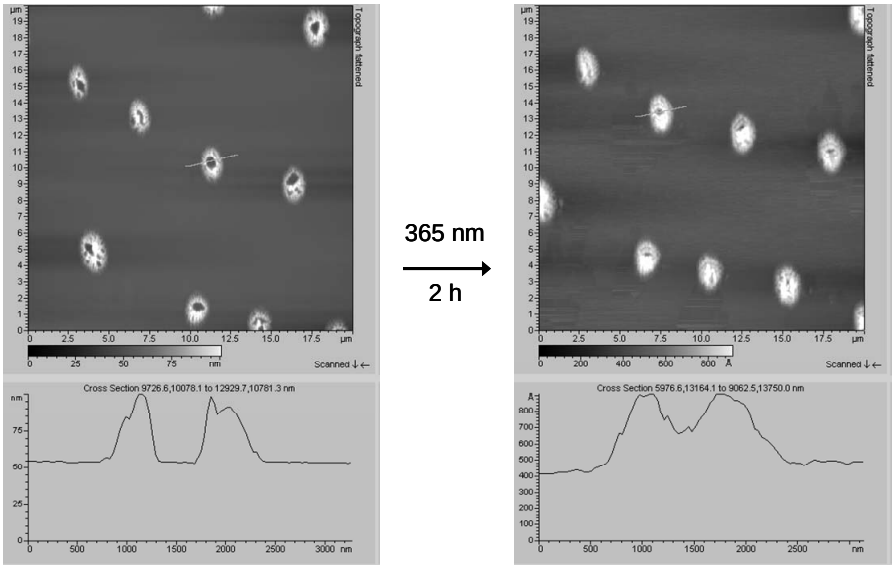

Figure 5.21 AFM images of a film prepared by drop-casting (2'*S*)-(*P*)-**1**-PHIC from toluene. The images show ordered toroidal structures (a) before irradiation with UV light and (b) after 2 h of 365 nm irradiation.

Figure 5.21 shows the changes in the observed toroidal structures after irradiation. As expected there are few dramatic changes, although the toroidal structures appear to have closed up. The potential heating of the sample via the irradiation seems unlikely to be the cause of this because heating of the sample has no effect until 70 ºC. The two-hour irradiation time does not seem long enough to cause such a temperature increase. Especially considering the fact that the toroidal shapes do not undergo the "shrinking" that would be expected at those temperatures (section 5.3.4 for details). The temperature increase could, however, affect the tip used to measure the AFM images. No changes were observed after leaving the sample overnight. This may be because no back reaction occurs or owing to the different induction capabilities of the motor at the different states in the rotary cycle. Also if the tip was physically affected by the irradiation it will continue to show the same results. Thus the results are inconclusive.

5.3.7 Effects of introduction of a thermotropic LC

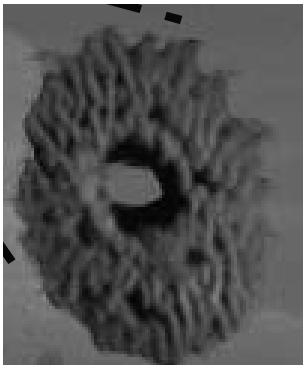

Figure 5.22 A phase contrast AFM image of an individual aggregate formed when drop-casting a toluene solution of (2'*S*)-(*P*)-**1**-PHIC on mica (1 μM).

At higher concentrations in toluene, the functionalized PHIC molecules are able to generate a chiral liquid crystalline phase (see chapter 4 for further details) which is addressable through irradiation. Interestingly, it was previously observed that the toroidal structures show a somewhat periodic undulation in the surface composition (which was more difficult to resolve with the traditional topography image), hinting that the surface aggregates may contain some orientational order induced by the packing of the helical rod-like macromolecules (Figure 5.22). This might imply that chiral induction from this surface is possible. Therefore, it was decided to add a thin layer of a commercially available liquid crystal blend (E7) which is known to respond to the chiral induction of systems previously used in our group.[37] The effects of placing a droplet of this material on the toroid-covered surface and then squashing it between two surfaces (in order to make the latter as thin as possible for optimal contact with the surface). The results of these experiments can be seen in Figures 5.23 and 5.24.

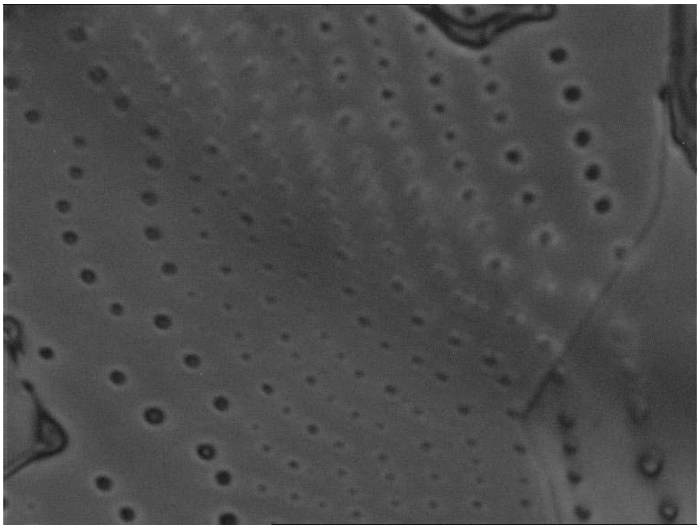

Figure 5.23 Optical micrograph of the (2'*S*)-(*P*)-**1**-PHIC toroidal surface on glass covered in E7 and a second surface (glass) with pressure* to minimize the layer of LC in contact with the toroid structures. The doughnut shaped molecules are between 5-10 μm.

As can be seen in Figure 5.23, the definition of the toroidal structures under the optical microscope is increased in the presence of the LC. The ability of the liquid crystalline molecules to reflect different colors of light through the polarizers[38] makes it easier to identify the fact that there are holes in the center. The toroidal dimensions appear to be larger than measured by AFM. This is presumed to be an effect of the surrounding LC layer.

* One drop of LC was placed onto the toroid-covered surface. A second surface was placed on top and pressure was applied in order to spread the LC as thinly as possible in order to best determine whether or not there is an induction of chirality.

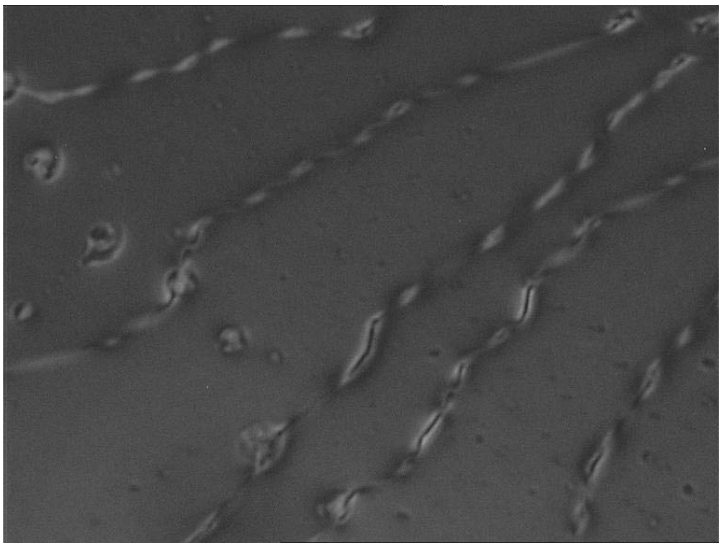

Figure 5.24 Optical micrograph of the (2'*S*)-(*P*)-**1**-PHIC toroidal surface on glass covered in E7 and a second surface (glass) with pressure to minimize the layer of LC in contact with the toroid structures. The helical structures are approximately 2-5 μm wide and 20+ μm long.

Besides the typical toroidal structures, twisted helical-type morphologies were observed (Figure 5.24). These could only be observed in the case of pressurized samples. Polymer chains often form fiber-like structures. As the polyisocyanate is a rigid helical structure, helical fibers morphologies could be possible instead of the previously addressed toroidal structures. However, these would be expected to be far smaller than those observed here. Perhaps the presence of these fibers is enhanced in the presence of LC, or may be caused by the shear forces exerted in the system during the squashing. These structures were very rare and only observed in one sample.

The results were inconclusive on helical induction from the toroids towards the LC phase. This may be for several reasons. The layer of the LC may be so thick that the chiral induction is too small to be observed using optical microscopy. Perhaps, using AFM more details could be observed. It is also possible that within the toroidal structure the helices are so intertwined that these are incapable of properly interacting with the LC present, or that the surfaces able to interact with the LC are at such angles to each other that these cause counter inductions. The pressure exerted during the squashing procedure might affect the surface relief observed of the toroids themselves, and as a consequence reduce the interactions with the surrounding LC. However, as soon as the pressure is released the toroid relief may be restored (it is metastable) and the pressure should not affect the LC.[39] Thus, at present, this is not an application for the toroidal arrays.

5.4 Conclusions

This research shows that drop-casting can be an efficient and easy way forward in patterning. The arrays of morphologies deposited on surfaces are similar regardless of the solvent being used. The motor-functionalized system yields the best homogeneous areas of evenly spaced toroids. The switch-functionalized system, though generated some toroidal structures mostly generated globules. The non-functionalized PHIC showed no toroidal structures, while the toroid structure is prevalent in the case of the motor-functionalized PHIC ((2'*S*)-(*P*)-**1**-PHIC). This difference may be purely a length issue though the varying helical inductions may also be important reasons for the homogeneity in the functionalized systems. The best arrays of toroidal structures were obtained in the case of motor-functionalized PHIC dissolved in toluene (aged for one day) deposited on freshly cleaved mica. The NMR data suggests that at higher concentrations there is aggregation in the aromatic sections. The mechanism for the formation of the toroids themselves is not clear. It may be that as the solvent evaporates the local concentration of the polymer becomes high enough to mimic the concentrations used for the NMR experiments and that aggregation is thus induced locally, causing aggregation, which forms these morphologies. However, another explanation might be dewetting. The large broad deposits observed as the concentric circles, are attributed to pinning of the contact line of the droplet followed by a flow of solvent to the contact line to replenish evaporated fluid. The solute is then delivered to the contact line where it accumulates. In the present work the toroid structures are sub-patterns found between the pinned contact lines. The regularity of the patterns presented in the present work is probably related to the above mechanism in which a flow is directed towards the perimeter of the droplet, delivering polymer which is then trapped within the confines of a thin film with a large length but small width. The length scale of the drying process delivers the polymer in laterally ordered rows.

5.5 Acknowledgements

Greg Carroll is gratefully acknowledged for his contributions to the work in this chapter. He is responsible for the SEM images, and several AFM images as well as teaching me the technique. I also wish to acknowledge Dirk Pijper for donating the remainder of the motor- and switch-functionalized PHIC that he synthesized.

5.6 Experimental

General Remarks

All solvents used in these experiments were of analytical grade. The polymeric systems were synthesized according to a literature procedure.[26,27] The liquid crystal used (E7) was purchased from Merck.

Equipment

DSC was measured on a Perkin Elmer DSC 7 equipped with a thermal analysis controller TAC71DX (and a cooler provided by VDM cool systems) connected to a PC with Pyris Series-DSC 7 software. DLS was measured on a Zetasizer 5000 (Malvern Instruments) with a laser at $\lambda = 633$ nm. CD was measured on a Jasco-815 equipped with a water circulation system (Haake DC-10 by Thermo Electron Corporation) and a temperature control unit Jasco PTC-4245/15. For the samples on quartz a horizontal attachment was employed (custom made). UV/VIS spectra were measured on a Jasco V-630 with piezo and temperature control. NMR spectra were measured on a Varian 500 MHz machine. AFM images were obtained with a PicoScan LE (Molecular Imaging) atomic force microscope in tapping mode. Tips with a force constant of 60 N/m were used. Images were scanned at rates ranging from 1-2 lines per second. SEM images were obtained with a JEOL scanning electron microscope. A voltage of 5 kV was used. Optical microscopy was carried out on an Olympus BX 60 microscope equipped with crossed polarizers, a heating table, and a Sony 3CCD DXC 950P digital camera attached to a PC running Matrox Inspector 8.0 software. Irradiation was carried out using a UV pen.

Sample preparation

Approximately 1 to 1.5 mg of polymer was dissolved in 10 ml of solvent (THF, toluene or chloroform) in a volumetric flask. This solution was subsequently diluted 1 to 1 with the solvent. A drop (volume = 2 μL) of the solution was then placed on a cleaned substrate. The substrate was enveloped with a brown glass vial to allow slow evaporation of the solvent without potential effects of irradiation or the settling of dust. Once dried these samples were then used for measurements.

Gold surfaces were cleansed under UV irradiation in the presence of ozone for a period of at least 15 min. The mica surfaces were freshly cleaved, and the glass slides were cleaned using an acidic piranha solution (70:30 H_2SO_4:H_2O_2). Caution: the piranha solution should be handled with extreme care!

LC experiments

Glass slides were cleaned using an acidic piranha solution. The 5 μl of a 1 μM solution of **1** in toluene was drop-cast onto the surface. Then, as the surface was dry, 1 μl of a commercially available LC (E7) droplet was placed onto the surface. In order to achieve optimal dispersion of the LC, the surface was covered with another cleaned glass surface and pressure was exerted. The top glass was removed and the sample was ready for examination under the optical microscope.

5.7 References

[1] Review of synthetic DNA delivery systems see: D.Luo, W.M. Saltzman, *Nat. Biotechnol*. **2000**, *18*, 33-37; For encapsulation of the condensed DNA globule see for instance: D.H. Liang, Y.K. Luu, K.S. Kim, B.S. Hsiao, M. Hadjiargyrou, B. Chu, *Nucleic Acids Res*. **2005**, 33, # E170 b) B. Chu, D.H. Liang, M. Hadjiargyrou, B.S. Hsiao, *J. Phys. Condens. Mat*., **2006**, 18, S2513-S2525

[2] S.Sankararaman, J.F. Marko, *Phys. Rev. Lett*. **2005**, *95*, 078104; b) A.Y. Grosberg, A.R. Khokholov, *Statistical Physics of Macromolecules* (American Institute of Physics, Woodbury, NY, 1994); b) K.Yoshikawa, M.Takahashi, V.V.Vasilevskaya, A.R. Khokhlov, *Phys. Rev. Lett*. **1996**, *76*, 3029; for simulations on formation see: V.Barsegov, D.Thirumalai, *J.Phys.Chem.B*, **2005**, *109*, 21979-21988; for DNA in poor solvent, see: G.G. Pereira, D.R.M. Williams *Biophys. J*. **2001**, *80*, 161-168; For aggregates on a surface see: C. Zhang, J.R.C. van der Maarel, *J.Phys. Chem. B*, **2008**, 112, 3552-3557

[3] a) A.P.H.J. Schenning, F.B.G. Benneker, H.P.M. Geurts, X.Y. Liu, R.J.M. Nolte, *J.Am. Chem. Soc*., **1996**, 118, 8549-8552 b) L.Latterini, R.Blossey, J.Hofkens, P.Vanoppen, F.C. de Schryver, A.E. Rowan, R.J.M. Nolte, *Langmuir*, **1999**, 15, 3582-3588 c) C.R.L.P.N. Jeukens, M.C. Lensen, F.J.P. Wijnen, J.A.A.W. Elemans, P.C.M. Christianen, A.E. Rowan, J.W. Gerritsen, R.J.M. Nolte, J.C. Maan, *Nano Lett*., **2004**, 4, 1401-1406

[4] T. Iwaki, *J. Chem. Phys*. **2006**, *125*, 224901

[5] M. Li, B. Lebeau, S. Mann, *Adv. Mater*, **2003**, 15, No. 23, 1032-2035

[6] For dendrimers, see a) S. Masuo, H. Yoshikawa, T. Asahi, H. Masuhara, T. Sato, D.-L. Jiang, T. Aida, *J. Phys. Chem. B*, **2001**, 105 (15), 2885-2889 b) A.J. Boydston, T.W. Holcombe, D.A. Unruh, J.M. Fréchet, R.H. Grubbs, *J. Am. Chem. Soc.* , **2009**, 131, 5388-5389; protein polymer hybrid, see. P. Foubert, J.M. Hannink, F. Köhn, R. Gronheid, N.A.J.M. Sommerdijk, R.J.M. Nolte, S. De Feyter, F.C. De Schryver, *Thin Solid Films*, **2003**, 443, 124-135

[7] V.V.Vasilevskaya, V.A. Markov, P.G. Khalatur, A.R. Khokholov J. Chem. Phys, **2006**, *124*, 144914

[8] I.R. Cooke, D.R.M. Williams, *Physica A*, **2004**, *339*, 45-52

[9] For a potential application, see p 2373 in M.H. Stenzel, C. Barner-Kowollik, T.P. Davis, *J. Polym. Sci. Part A: Polym. Chem*., **2006**, 44 where microorganisms are grown within honeycomb structures.

[10] For a review on the use of polycation-mediated DNA delivery as a non-viral gene therapy, see: M. Thomas, A.M. Klibanov, *Appl. Microbiol. Biotechnol*. **2003**, *62*, 27-34

[11] R. Djalali, J. Samson, H. Matsui, *J. Am. Chem. Soc*. **2004**, *126*, 7935-7939

[12] L. Alexander, K. Dhaliwal, J. Simpson, M. Bradley, *Chem. Comm*. **2008**, 3507-3509
[13] For a comprehensive review on the surface behaviour of highly branched molecules see: S. Peleshanko, V.V. Tsukruk. *Prog. Polym. Sci*. **2008**, 33, 523-580
[14] H.Huang, B. Chung, J.Jung, H.-W. Park, T.Chang, *Angew. Chem. Int. Ed*. **2009**, 48, 1-5 and A. J. Boydston, T. W. Holcombe, D. A. Unruh, J. M. J. Frechet, R. H. Grubbs, *J. Am. Chem. Soc.*, **2009**, *131*, 5388-5389.
[15] A) Z. Lin, S. Granick, *J. Am. Chem. Soc.*, **2005**, 127, 2816-2817 b) R. van Hameren, P. Schön, A.M. van Buul, J. Hoogboom, S.V. Lazarenko, J. W. Gerritsen, H. Engelkamp, P.C.M. Christianen, H.A.Heus, J.C. Maan, T. Rasing, S. Speller, A.E. Rowan, J.A.A.W. Elemans, R.J.M. Nolte, *Science*, **2006**, 314, 1433-1436
[16] M.H. Stenzel, C. Barner-Kowollik, T.P. Davis, *J. Polym. Sci. Part A: Polym. Chem.*, **2006**, 44, 2363-2375
[17] S.-L.Lee, C.-Y.J. Chi, M.-J. Huang, C.-H. Chen, C.-W. Li, K. Pati, R.-S. Liu, *J. Am. Chem. Soc*. **2008**, 130, 10454-10455
[18] T. Young, *Philos. Trans. R. Soc.* **1805**, 95, 65
[19] K. Mougin, H.Haidara, *Langmuir*, **2002**, 18, 9566-9569
[20] R.D.Deegan *Phys. Rev. E* **2000**, *61*, 475-485, for example see pictures p 479
[21] See chapter on PHIC 573-581 in the *Polymer Data Handbook* available online at http://www.qmc.ufsc.br/~minatti/docs/20061/polymer_data_handbook.pdf
[22] R. Cook, R.D. Johnson, C.G. Wade, D.J. O'Leary, B. Muñoz, M.M. Green, *Macromolecules*, **1990**, 23 (14), 3454-3458
[23] M. Kawaguchi, R. Ishikawa, M. Yamamoto, T. Kuki, T. Kato, *Langmuir*, **2001**, *17*, 384-387
[24] For examples of PHIC chiral inductions see: M.M. Green, M.P. Reidy, R.D. Johnson, G. Darling, D.J. O'Leary, G. Willson, *J. Am. Chem. Soc.* **1989**, 111, 6452-6454; b) M.M. Green, B.A. Garetz, B. Muñoz, H. Chang, S. Hoke, R.G. Cooks, *J. Am. Chem. Soc*. **1995**, 117, 4181-4182; In copolymerization, see: Z.-Q. Wu, K. Nagai, M. Banno, K. Okoshi, K. Onitsuka, E. Yashima, J. Am. Chem. Soc. **2009**, 131, 6708-6718 Subtle chiral induction from for instance deuterium see: M. M. Green, N.C. Peterson, T. Sato, A. Teramoto, R. Cook, S. Lifson, *Science* **1995**, *268*, 1860-1866; for a comprehensive review on the influence of chiral appendages on helical polymers, see: K. Maeda, E. Yashima, *Top. Curr. Chem*. **2006**, 265, 47-88 for a single chiral unit at the terminus, see: Y. Okamoto, M. Matsuda, T, Nakano, E. Yashima, *Polymer J*. **1993**, 25, 391-396; b) Y. Okamoto, M. Matsuda, T. Nakano, E. Yashima, *J. Polym. Sci. A Polym. Chem*. **1994**, 32, 309-315
[25] Photochemical control through azobenzenes see: G. Maxein, R. Zentel, *Macromolecules* **1995**, *28*, 8438-8440; Polymer backbone switching by CPL see: J. Li, G.B. Schuster, K.-S. Cheon, M.M. Green, J.V. Selinger, *J. Am. Chem. Soc*. **2000**, 122, 2603-2612
[26] D.Pijper, A. Meetsma, B.L. Feringa, *Angew. Chem. Int. Ed,* **2007**, 119, 3767-3770
[27] D.Pijper, M.G.M.Jongejan, A. Meetsma, B.L.Feringa, *J. Am. Chem. Soc*, **2008**, 130, 4541-4552
[28] See reference 26 versus 25
[29] Aggregation of PHIC in toluene has been studied previously, see: H.J. Coles, A.K. Gupta, E. Marchal, *Macromolecules* **1977**, *10*, 182-187
[30] For temperature-dependence PHIC, see, for instance: B.T. Muellers, J.-W. Park, M.S. Brookhart, M.M. Green, *Macromolecules*, **2001**, *34*, 572-581

[31] PBHIC temperature dependent ^{1}H-NMR only shows coalescence at higher temperatures see Figures 2,3 and 5 in: K.Ute, Y. Fukunishi, S.K. Jha, K.-S. Cheon, B. Muñoz, K. Hatada, M.M. Green, *Macromolecules*, **1999**, *32*, 1304-1307

[32] N.B. exact assignment of the protons in the aromatic region of molecular motors has not been published neither has their ^{1}H-NMR at various higher temperatures.

[33] This method is called Presaturation. For disadvantages see: A.S. Altieri, R.A. Byrd, *J. Mag. Res. Series B* **1995**, *107*, 260-266

[34] See for instance: a) R. D. Deegan, O. Bakajin, T. F. Dupont, G. Huber, S. R. Nagel, T. A. Witten, *Nature*, **1997**, *389*, 827-829; b) Z. Lin, S. Granick, *J. Am. Chem. Soc.*, **2005**, *127*, 2816-2817.

[35] Aggregation of poly(*n*-hexyl isocyanate) in toluene has been known for some time. See, for instance: H.J. Coles, A.K. Gupta, E. Marchal, *Macromolecules*, **1977**, 10, 182-187

[36] Alignment can generate linear dichroism signals which interfere with the CD spectra. CD spectra in solution are not expected to show alignment. The LD signal will alter the shape of the CD signal, and thus result in irreproducibility if no care is taken to maintain the sample in exactly the same position. For basic explanation of the LD principle, see for instance: http://en.wikipedia.org/wiki/Linear_dichroism

[37] Chapters 2 and 3 of this thesis.

[38] For more details on the characteristics of liquid crystals, see chapter 2 introduction segment (i.e. birefringence and polarization)

[39] Cholesteric LCs are capable of maintaining their corrugated nature despite the presence of slides on the top (see chapter 3 for more details).

Chapter 6

Aggregation Phenomena of a Water-Soluble Molecular Motor

The first water-soluble molecular motor was synthesized. In aqueous solution (pH = 10), these amphiphilic molecules aggregate to form micelles. Interestingly, the stable (before irradiation) and unstable (after UV irradiation) forms of the molecular motor segment of these amphiphiles have different CMC values. In the case of the stable systems the CMC is 1.1 x 10^{-3} M while in the case of the irradiated system the CMC is 5.0 x 10^{-4} M. Therefore by choosing the correct concentration a system could be made in which the irradiated molecules generate micelles, while after thermal isomerization (return to stable state) aggregation is no longer observed.

6.1 Introduction.

Amphiphilic molecules consist of two different segments: a hydrophilic segment and a hydrophobic segment. These surfactants have been used both in nature as components of biological membranes, in everyday life as soaps and in the food industry.[1] In aqueous media amphiphilic molecules will tend to assemble together either at the air water interface (hydrophilic segments in the water and the hydrophobic tails protruding in the air) or these molecules will cluster together to form aggregates (Scheme 6.1). In 1891, Traube was one of the first to observe the accumulation of molecules at the air-water interface due to hydrocarbon disaffinity with water.[2]

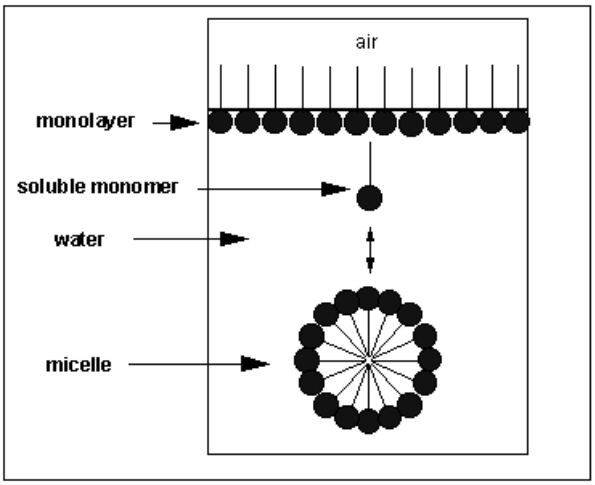

Scheme 6.1 Schematic representation of amphiphilic molecules at the air/water interface and the formation of aggregates above a critical concentration.

This occurs owing to the hydrophobic effect.[3] Hartley describes this process by referring to "the strong tendency of the water to expel the paraffin-chain itself from solution".[4] This effect is related to the unique properties of water: water molecules are small and posses two hydrogen-bond donor and two hydrogen-bond acceptor sites. This results in a highly defined three-dimensional hydrogen-bonding network throughout the aqueous phase. This causes water to have such a high heat capacity. Adding apolar molecules to an aqueous solution is unfavorable as these molecules are incapable of forming hydrogen bonds with the present water molecules, thus disrupting the network. The attractive tail-tail hydrophobic interactions, the "steric hindrance" between tails that are too closely packed (the Pauli exclusion principle[5]), the electrostatic repulsion between the hydrophilic headgroups and the gain of entropy through the release of hydration water of the hydrophobic tails into the bulk solution, are the forces taken into account for aggregation.[3] Therefore, in order to minimize this disruption of the "water structure" the apolar segments will bunch together so that the tails

avoid contact with water and as little of the network is affected as possible.[6] In the case of amphiphilic molecules aggregates are generated above a certain critical concentration (CAC or critical aggregation concentration), below this the amphiphiles will remain at the air/water interface or as monomers in the solution.

6.1.1 Aggregate types

The types of aggregates observed in aqueous solution depend on the actual size and shape of the amphiphilic molecule being used. The packing parameter developed by Ninham[7] is a good measure for the type of aggregate observed in solution (See table 6.1 and equation 1).

$$P = \frac{V}{a_o \times l} \qquad 1$$

Herein P is the packing parameter, V is the volume of the hydrophobic chains, a_o is the cross-sectional surface area of the headgroup including the hydration shell and l is the length of the hydrophobic tails in the all *trans* conformation. The packing parameter is difficult to predict with great precision as the parameters are somewhat interdependent.[8] Nevertheless P represents a powerful tool to predict amphiphile aggregation.

Packing Parameter	<1/3	1/3 – 1/2	1/2 – 1	>1
Molecular shape	cone	trapezoid	cylinder	Inverted cone
Phase type	micellar	micellar	lamellar	cubic† + hexagonal† + lamellar† + bicontinuous cubic†
	Cubic micellar	hexagonal	Bicontinuous cubic	
Aggregate type	micelle	Worm-like micelle	Vesicle or flat bilayer	

Table 6.1 Schematic presentation of the relation between the packing parameter and the type of phase generate in solution. † Represent inverted phases.[7]

Each different packing parameter corresponds to a different phase being generated in solution. For small packing parameters micelles are observed. These are small spherical aggregates with simply the tails pointing towards each other and the headgroups pointing towards the water (Scheme 6.2). It must be emphasized that these aggregates are not rigid structures; these are dynamic in solution (assembly and disassembly continuously occur). As the conical shape of the molecule narrows at the top or widens at the hydrophobic part, worm-like micelles are observed. When the packing

parameter increases above ½ a lamellar phase is observed. The aggregates generated are bilayers (such as in biological membranes) or spherical bilayers called vesicles or liposomes (Scheme 6.3). In a bilayer the amphiphilic molecules are located directly across from one another with the hydrophobic segments facing each other in the inside of the bilayer and the hydrophilic headgroups pointing towards the water. In the case of vesicles an aqueous "vacuole" is generated. In this case a bilayer is folded generating a spherical aggregate which contains some of the surrounding water in the center. As the packing parameter increases above one the inverted phases will be observed. For some examples of their appearance, see Scheme 6.4.

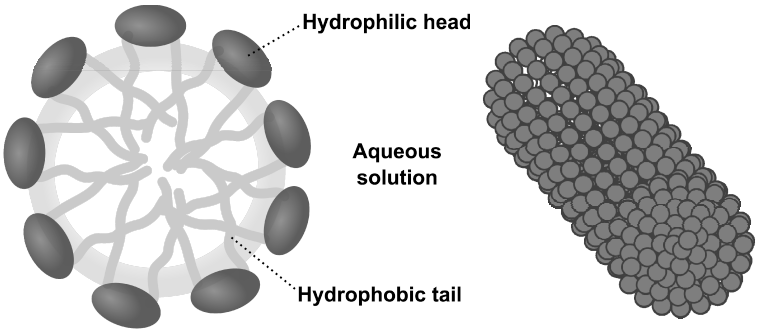

Scheme 6.2 Schematic representation of the micellar phase: left a micelle and right a worm-like micelle. Adapted from ref 9.

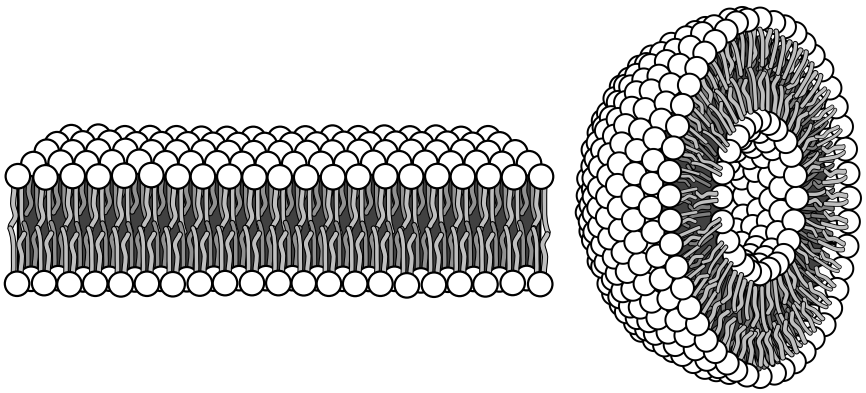

Scheme 6.3 Schematic representation of the lamellar phase: left a bilayer and right a vesicle. Adapted from ref 9.

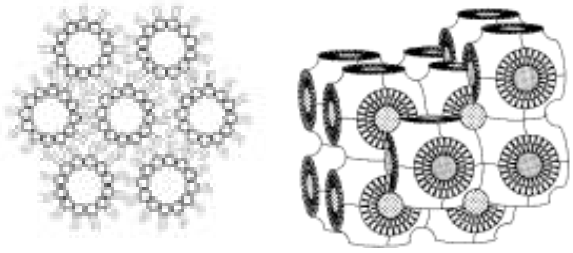

Scheme 6.4 Schematic representation of examples of phases generated with a packing parameter larger than one: inverted hexagonal- (left) and the bicontinuous cubic- phase (right). Adapted from ref 9.

As mentioned previously, amphiphilic molecules will initially be at the air water interface. At high enough concentrations (usually in the order of 10^{-6} to 10^{-2} M)[10] aggregates can be formed. Depending on the amphiphilic molecule this CAC (critical aggregation concentration) will vary. The CAC can be determined in different ways: surface tension, electric conductivity and fluorescence spectroscopy. In this study fluorescence spectroscopy will be the method of choice.

Aggregates have been looked into as potential drug delivery systems, owing to their dynamic nature. For a successful carrier lack of cytotoxicity and timely release of the drugs within the human body are essential. Therefore being able to address the type of aggregate formed or by switching between assembly and disassembly the release could be controlled. The switching between aggregates can be achieved using various different external stimuli. For example: electrochemistry[11], change in counterion[12], shear force[13] or temperature dependence[14,15] can be used to switch these systems. Considerable research has concentrated on the use of variable pH[16] and irradiation with a light source[17,18].

6.1.2 A Switchable Amphiphilic Molecular Motor

In our group many molecular motor molecules have been designed which show rotation along their central axis (central double bond) unidirectionally under subsequent irradiation with UV light (λ = 365 nm) and thermal isomerization.[19] However, none of these have been water soluble. Therefore it was decided to examine whether or not a molecular motor could be successfully combined with amphiphilic behavior to generate aggregates that can be addressed upon UV/VIS irradiation.

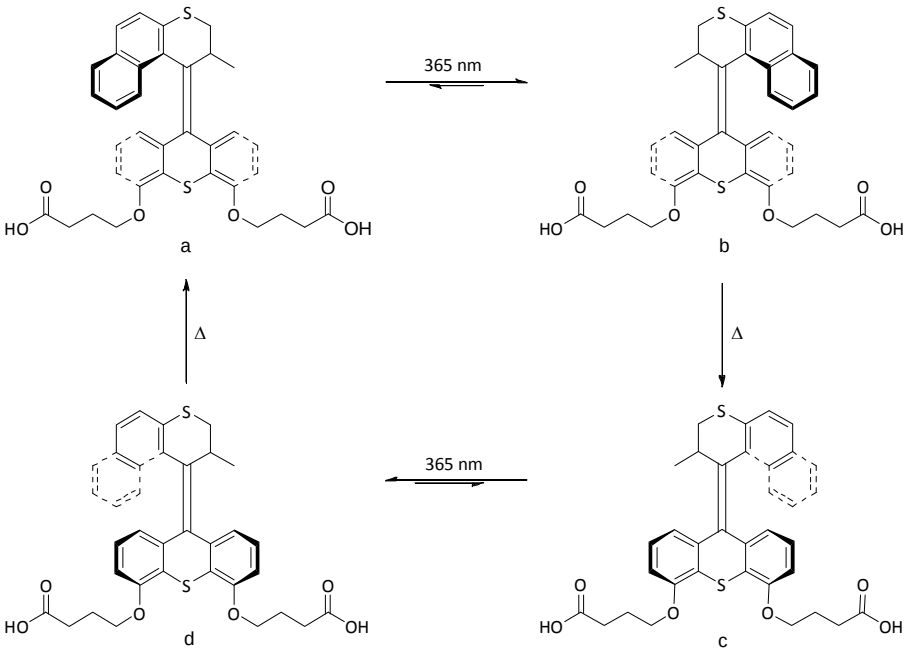

Scheme 6.5 The expected unidirectional rotary cycle induced by consecutive UV/VIS irradiation and thermal isomerization steps of a water soluble molecular motor (**A**).

In this study a second generation (symmetrical lower half), relatively slow molecular motor[20] was functionalized with potentially water-soluble carboxylic legs (Scheme 6.5). The general methodology to generate the central double bond is to couple the upper and lower half via a Barton-Kellogg reaction.[21] Thus it was decided to first functionalize the lower half with two legs and then to couple this segment to the upper half.

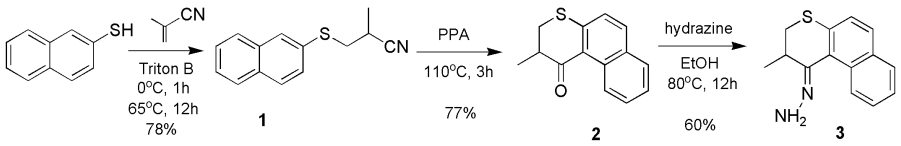

Scheme 6.6 Synthetic route followed to construct the upper half of the molecular motor.

In the synthesis of the upper half (Scheme 6.6), thionaphthol was reacted with methacrylonitrile to form thioether **1**. This compound was then cyclized using polyphosphoric acid (PPA). The final hydrazone was obtained after reacting with hydrazine.

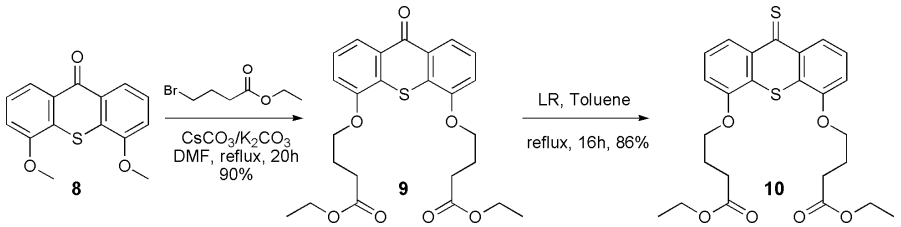

Scheme 6.7 Synthetic route followed to construct the functionalized lower half of the molecular motor.

The methoxy functionalized lower-half ketone **8**, was synthesized according to a literature procedure.[22] Subsequently the methoxy groups were deprotected using boron tribromide (Scheme 6.7), after which the ester tails were attached. Compound **10** was then converted into the thioketone using Lawesson's reagent.

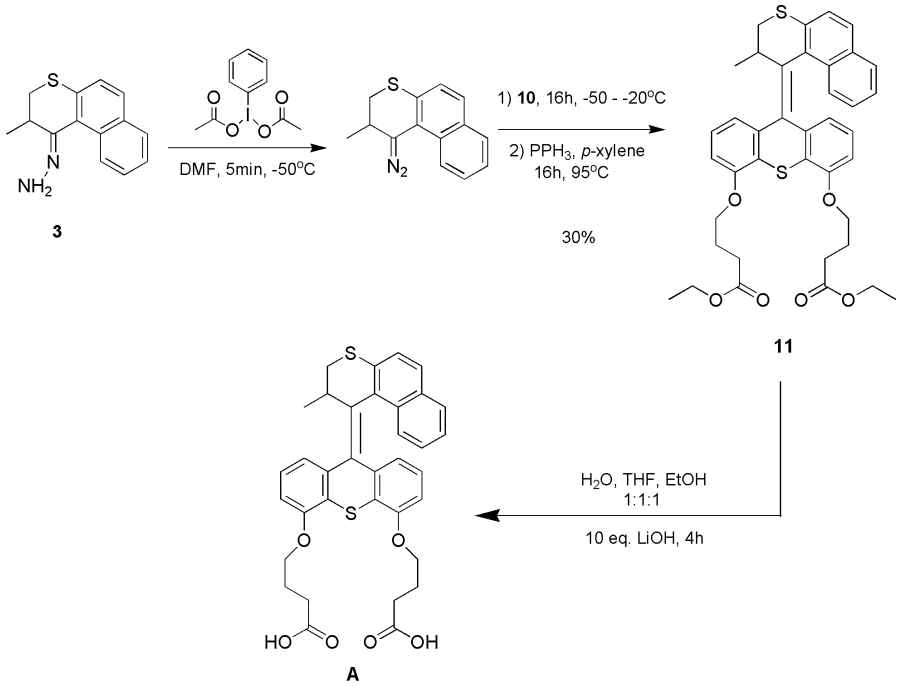

Scheme 6.8 Schematic representation of the synthetic route followed for the coupling of the upper and lower half to prepare the molecular motor **A**.

After converting the hydrazone of the previously synthesized upper-half into the corresponding diazo-compound, using hypervalent iodine, the thioketone lower half was added and coupled to the upper half via the Barton-Kellogg reaction (Scheme 6.8). The resulting episulfide was then desulphurized using triphenylphosphine. Subsequently, the ester moieties were deprotected quantitatively using a large excess of lithium hydroxide to yield the final molecule **A**. The purity of the compound **A** was determined using ^{1}H-NMR, ^{13}C-NMR and HRMS (experimental section 6.6).

6.2 Results and discussion

The carboxylic groups of **A**, when protonated, are only slightly hydrophilic, but upon a pH increase one or both groups can be deprotonated. This will result in a highly hydrophillic head group. Together with the motor part which is hydrophobic an amphiphile is generated. The pKa of carboxylic acids is around 4, but upon an increase of the hydrophobic domain this pKa increases dramatically, as was shown for a series of linear soaps.[23] When amphiphiles aggregate into micelles or vesicles the ionic groups start to repel each other and deprotonation becomes more difficult. Therefore most experiments were performed at pH 10.

6.2.1 Photochemical and Thermal Isomerization

Most of the fast second generation (symmetrical lower half) molecular motors constructed in our group consist of rigid five-membered rings separated by a central double bond functioning as an axis of rotation.[24] Upon irradiation with UV light, and photoisomerization of the double bond, these always show a bathochromic effect (red shift) in their UV/VIS spectra. In the case of sulfur six-membered rings such as our water-soluble molecular motor (**A**), the inherent photochemistry is different. In fact, upon irradiation a hypsochromic (blue shift) is observed with very few details in the spectrum. However, an isosbestic point is observed (λ = 322 nm, Figure 6.1). Thus a singular process is found here. This behavior is characteristic for all sulphur-sulphur systems studied thus far,[25] and is probably caused by a change in the electronic effect compared to the non-sulfur containing molecular motors (the sulphur atoms donate electron density).

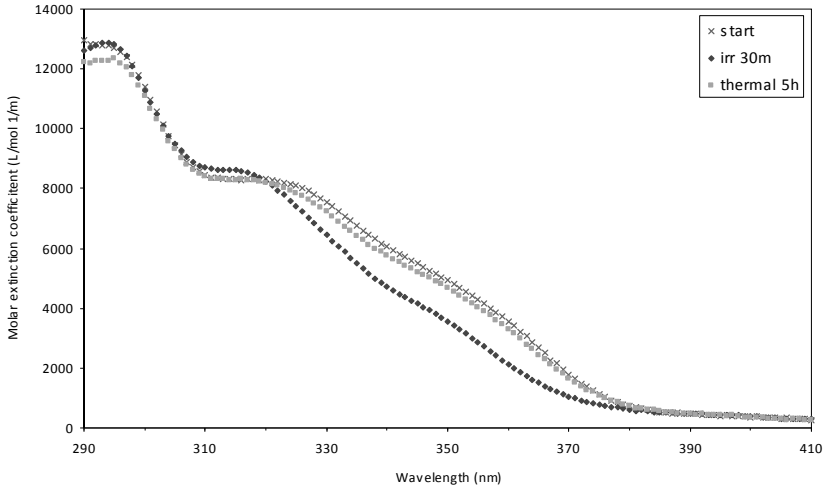

Figure 6.1 UV/VIS spectra of the molecular motor **A** (Scheme 6.5) before irradiation (crosses), after irradiation with 365 nm light (diamonds), and after 5 h of heating at 80°C (grey squares). The spectra were recorded of a solution of **A** ($1*10^{-6}$ M) in water at pH 10.

Main conclusion drawn from these results is that the molecular motor still shows the same behavior in aqueous environment as the molecular motor without the legs in chloroform. The thermal isomerization step was studied for molecular motor **A**, by irradiating the sample until full conversion (Figure 6.1) and than following the increase in absorbance at 350 nm at various temperatures. This was done for two different concentrations (one at normal UV concentrations and one above the concentration required for aggregation[*]) in an aqueous solution at pH 10 in a temperature range between 20 and 80 °C. The calculated[26] data for both concentrations are presented in table 6.2.

Concentration molecular motor	$\Delta G^{\ddagger}$ (kJ/mol)	$\Delta H^{\ddagger}$ (kJ/mol)	$\Delta S^{\ddagger}$ (kJ/mol)	$t_{1/2}$ (h)
3.5×10^{-5} M No micelles	104.0	91.1	-44.0	53
1.3×10^{-3} M Micelles	102.2	73.4	-98.1	26

Table 6.2 Energies of activation and the half life for the thermal isomerization of molecular motor **A** in water at pH 10.

[*] This concentration was determined using fluorescence see section 6.2.2.

Both of the half-life times presented in table 6.2 are in the region of tens of hours. Thus, at regular UV concentrations this particular molecular motor is considered to be relatively slow (there are systems known with half-life times in the microsecond region)[20]. The largest difference between the two solutions of varying concentration, can be seen in the far larger negative contribution of ΔS in the case of the aggregated system. Interesting to note is that the half-life time for the thermal isomerization process is halved at the higher concentration at which aggregation is observed. This suggests a cooperative system, as a solvent effect for motor molecules this large has not been observed. As the thermal isomerization step is unidirectional (Scheme 6.5), once one molecule undergoes the thermal isomerization process the packing in the aggregate is disrupted which is energetically unfavorable. Thus the surrounding molecules must undergo the same process to diminish the unfavorable interactions within the aggregate. Therefore the close packing increases the ability of the molecular motor **6** to undergo a thermal helix inversion. The measured rate for isomerization in the micellar system is probably somewhat lower than it would be in actuality, as the UV/VIS measures an average over the entire system. As micelles are highly dynamic systems[27] these are constantly reforming, meaning that there will be motor molecules just spread around in solution which would be expected to have a similar isomerization rate as that observed for the system at a concentration of 3.5×10^{-5} M. Thus the isomerization rates within the micellar aggregate or its interior cavity should be higher than the predicted half life of 26 h. It was attempted to measure the thermal isomerization of the amphiphile within a vesicular system using scattering diffuse reflectance spectroscopy.[28] However, these results were inconclusive, as heating is impossible within the sample holder, removal of the sample causes base-line shifts too large to ignore, runs are not possible for periods longer than an hour, and the sample at pH 10 at room temperature was too instable for any conclusions to be drawn.

6.2.2 CMC determination

The hydrophobic fluorescent probe Nile Red is sensitive to polarity[29] of the medium or the aggregate in which it resides. In water Nile Red is poorly soluble and hardly fluorescent with a maximum emission at 660 nm. If hydrophobic domains are present, such as in micelles or bilayers, Nile Red will reside in these hydrophobic domains, which shows up as an increase in the fluorescent intensity and a blue shift in the emission maximum. Depending on the location of the probe with respect to the aggregate the probe will sense a different polarity: near the outer rim the environment will be more polar than in the core between all the hydrophobic moieties. As a result the Nile Red in the varying positions can be excited differently and as a result produce a different emission spectrum. Thus, if an aggregate is present an excitation dependent emission is observed.

In Figures 6.2 and 6.3 it can be seen that at low concentrations (below CMC) there seems to be barely any exitation dependent emission maximum (i.e. at all excitation wavelengths the emission maximum is approximately the same). Above the CMC there is a clear dependence. The data show that in the case of the non irradiated system the CMC is below 1.55 x 10^{-3} and far above 3.9 x 10^{-4} M; In the case of the irradiated sample the CMC lies between 7.8 x 10^{-4} and 9.8 x 10^{-5} M (this first experiment does not show the exact CMC). This indicates that the two isomers (stable and unstable) have different CMCs.

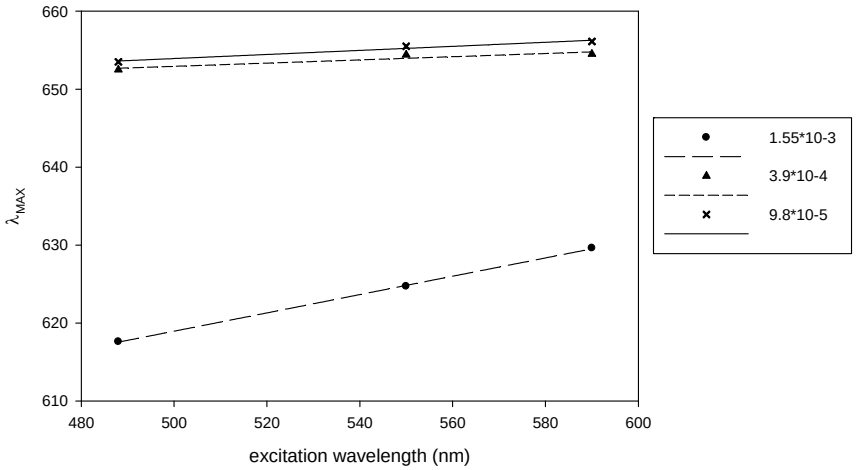

Figure 6.2 Plot of the excitation wavelength versus the maximum emission wavelength for the molecular motor before irradiation at various concentrations.

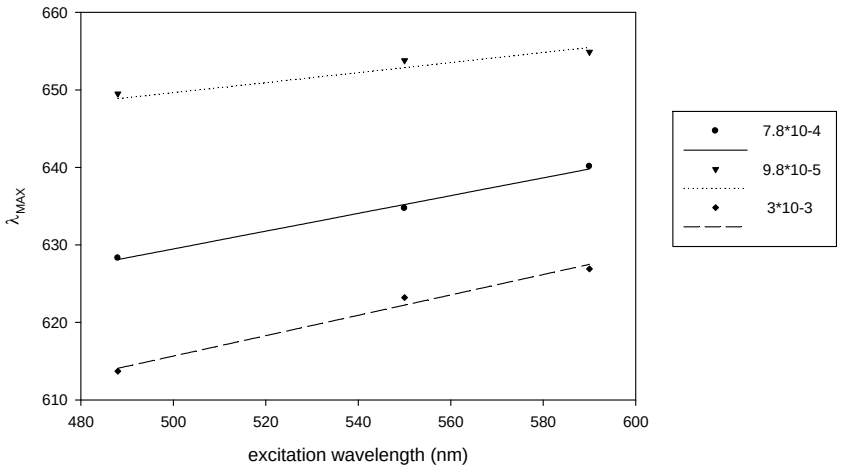

Figure 6.3 Plot of the excitation wavelength versus the maximum emission wavelength for the molecular motor after irradiation (20 minutes at 365 nm) at various concentrations.

From the fluorescence measurements for concentrations varying between 10^{-3} and 10^{-5} M for both the irradiated samples, measured at PSS (a in Scheme 6.5) and non-irradiated (b in Scheme 6.5) molecular motor **A** it became apparent that there is indeed a difference in the CMC between the two forms (Figure 6.4). In the case of the non-irradiated sample the CMC is at 1.1 x 10^{-3} M. In the case of the irradiated sample, the CMC is at a lower concentration of 5.0 x 10^{-4} M. This is a factor of two smaller. Control of the system is possible by choosing a concentration at which only the irradiated form will aggregate. With heat, unstable **A** will undergo thermal isomerization resulting in the stable isomer, which does not generate aggregates at this concentration, and thus slowly disassembles. In the case of the stable isomer the emission maximum can be found at a more blue shifted wavelength (λ= 655 nm), suggesting a more apolar environment compared to the irradiated sample. However, the difference between initial and final wavelengths above and below the CMC of the two isomers is the same.

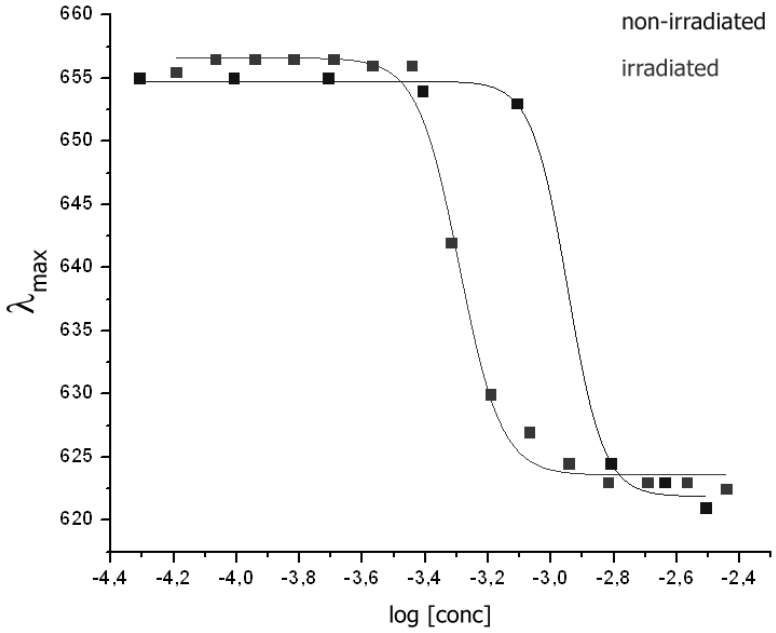

Figure 6.4 Plot showing the emission maxima of Nile Red in a solution of both the irradiated (stable) and non irradiated (unstable at PSS[†]) sample in water at pH 10. The excitation wavelength is 550 nm and the concentration of Nile Red used per measured data point is 1.22 μM.

[†] PSS was determined using UV/VIS on comparable samples. It was determined that 20 minutes of irradiation was enough to complete isomerization in these systems.

6.2.3 Langmuir-Blodgett measurements

A solution of **A** in chloroform was deposited on a Langmuir-Blodgett trough containing water at pH 5.5. Nevertheless evaporation of the solvent containing the molecules forms a monolayer at the air-water interface (based on the LB data). Apparently the protonated state is sufficiently hydrated to form a stable monolayer at the air water interface. In a Langmuir-Blodgett measurement the surface area containing the monolayer is slowly decreased in order to determine which area is required to generate a monolayer and as the concentration is known, the headgroup area per molecule can be determined. The result of the determination of the surface area of the headgroup is shown in the plot in Figure 6.5. Figure 6.6 shows the corresponding Brewster Angle Microscopy (BAM)- images determining at which stages monolayers and multilayers are observed.

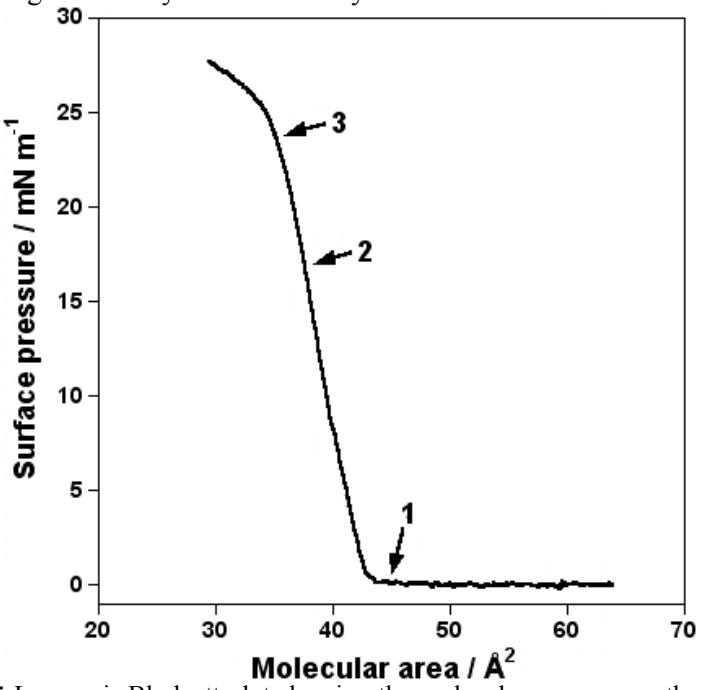

Figure 6.5 Langmuir-Blodgett plot showing the molecular area versus the surface pressure for the molecular motor before irradiation at room temperature. The numbered arrows correspond to the BAM images taken and shown in figure 6.6.

The Langmuir-Blodgett experiments show that in the region up to 45 $Å^2$ no complete monolayers are observed, as can be seen from the BAM image (Figure 6.6, left). The black stripes represent areas where no molecules are

present. Decreasing the surface area further shows that monolayers are formed. An area for the hydrated headgroup of the molecular motor in the protonated state is approximately 43 $Å^2$. At areas below 38 $Å^2$ the monolayers formed collapse upon themselves generating multilayers (Figure 6.6 right image). In our fluorescence experiments (section 6.2.2) the pH was always 10. This means that the headgroup is deprotonated and a counterion is present: in our case sodium. Thus in reality one would expect that the average headgroup area would be larger. Langmuir-Blodgett experiments were not conducted at pH 10 owing to instability of the monolayer. Thus it can be concluded that our headgroup has a minimal area of 43 $Å^2$.

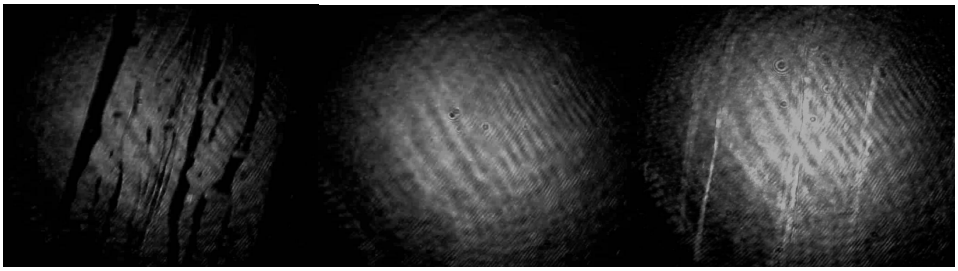

Figure 6.6 Brewster Angle microscopy images that correspond to the numbered arrows of the Langmuir-Blodgett image presented in figure 6.5. The images show left: an incomplete monolayer; middle: a monolayer; right: the formation of multilayers (the bright lines).

6.2.4 DSC measurements

In differential scanning calorimetry (DSC)[30] the heat capacity of a sample and a reference cell are compared. In the case of amphiphiles we expect these to go from a gel like more rigid state to a liquid crystalline state upon heating.[30] As this is an endothermic process a positive peak is expected. For the return wave (which is endothermic) the inverse is expected. The peaks should indicate exactly the same phase transition temperature. As our amphiphilic molecules are rather small these are expected not to have a phase transition that can be registered in water (below 0ºC). Thus a mixed vesicle approach was used. In a mixed vesicle approach an amphiphile which is known to generate a vesicle with a known phase transition temperature and the desired molecule is added in a ratio of between 1 and 10wt% (weight of **A** relative to vesicle-forming surfactant). The addition of the other molecule will affect the packing of the vesicle. Depending on the structure of the additive the packing will be more or less disrupted. In the case of large disruption the phase transition temperature will be drastically lowered.

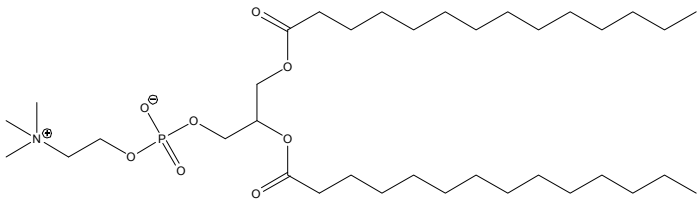

Figure 6.7 Structure of the vesicle-forming surfactant DMPC (di-myristoyl-phosphatidylcholine).

Initially a curve of pure DMPC (for its structure, see Figure 6.7) was measured. The T_m was observed at 23.8 ºC in accordance with literature.[31] Then 10% by weight of the motor amphiphile **A** was added. The DSC runs changed dramatically (Figure 6.8). Rather than a sharp transition a broad peak was observed for both the irradiated and non-irradiated molecular motor sample. The peaks were so broad that no exact transition temperature could be assigned. Therefore, it was difficult to determine whether or not there was any difference caused in the packing between the two isomers.

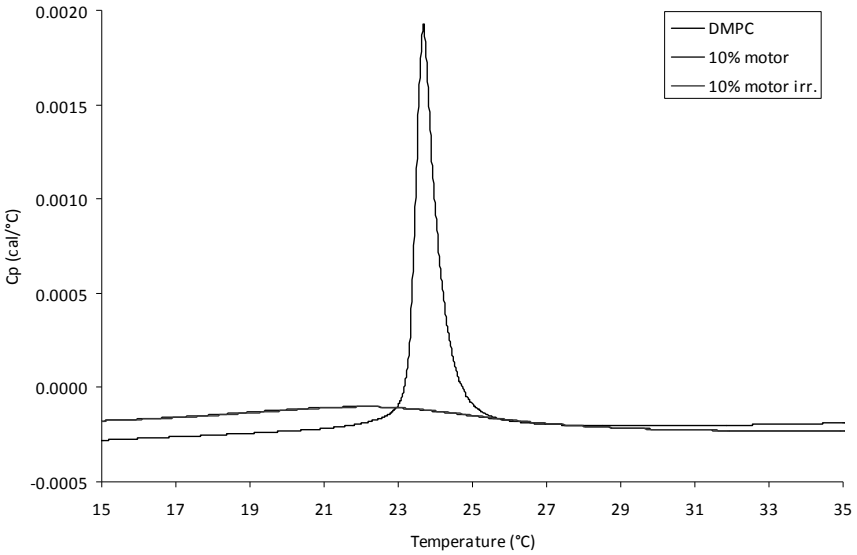

Figure 6.8 DSC scans of a 10 wt% solution of molecular motor in DMPC in aqueous solution (neutral pH). The concentration of DMPC was 0.5 mg per ml tridistilled water. The scans of the irradiated and non irradiated **A**/DMPC mixed vesicles are overlaying.

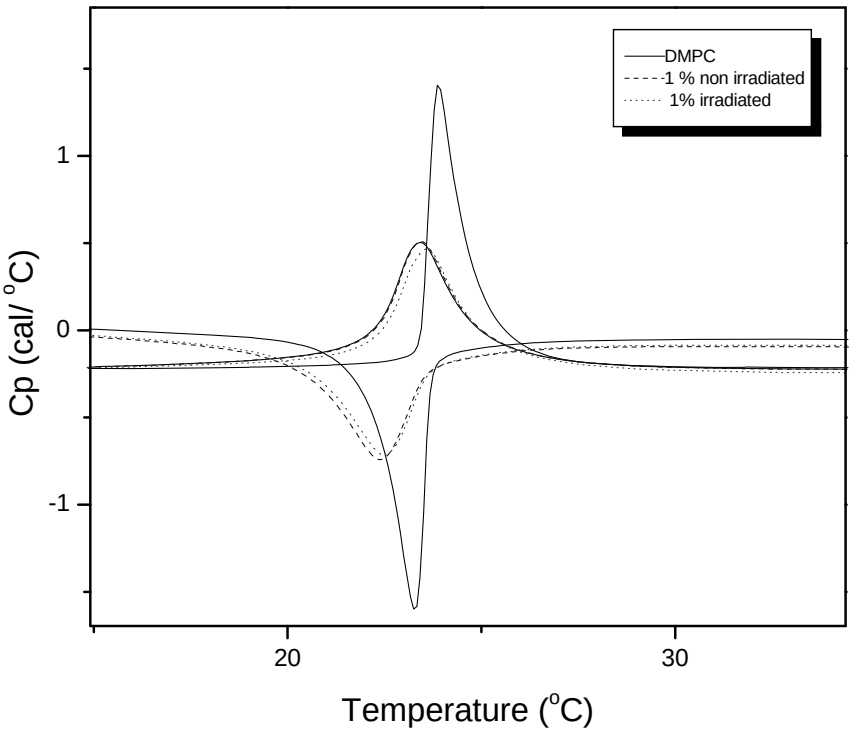

Figure 6.9 DSC scans of a 1 wt% solution of molecular motor in DMPC in aqueous solution (neutral pH). The concentration of DMPC used was 0.5 mg per ml tridistilled water.

Thus a lower concentration of amphiphilic molecular motor was examined. In the case of the pure DMPC the transition temperature was found at 23.9 °C (similar to that found in Figure 6.8). Upon inclusion of 1 wt% of motor amphiphile **A** it was apparent that relative to the higher concentration sample (10% **A**, Figure 6.8) the transition temperature is more defined and the transition temperatures of the irradiated and non irradiated systems are not superimposable anymore. Despite several heating and cooling cycles the phase transition temperatures for all **A**/DMPC mixed vesicles remain unaffected. Thus, the irradiated sample had not undergone any thermal isomerization within the period of these measurements (4 h). The observed phase transition temperature decreases to 23.4 °C. There is a decrease of 0.5 °C. It seems that the additive **A** is slightly disrupting the packing of the DMPC vesicle. Interestingly there appears to be a slight difference between the disruption induced by the irradiated and non-irradiated systems. The difference observed in the T_m, however, is only 0.1 °C. The difference between the two systems is reproducible per run, however falls within the error margin. As the experiments are carried out at neutral pH the molecular

motor molecules are not deprotonated. Thus these will reside within the DMPC bilayer.

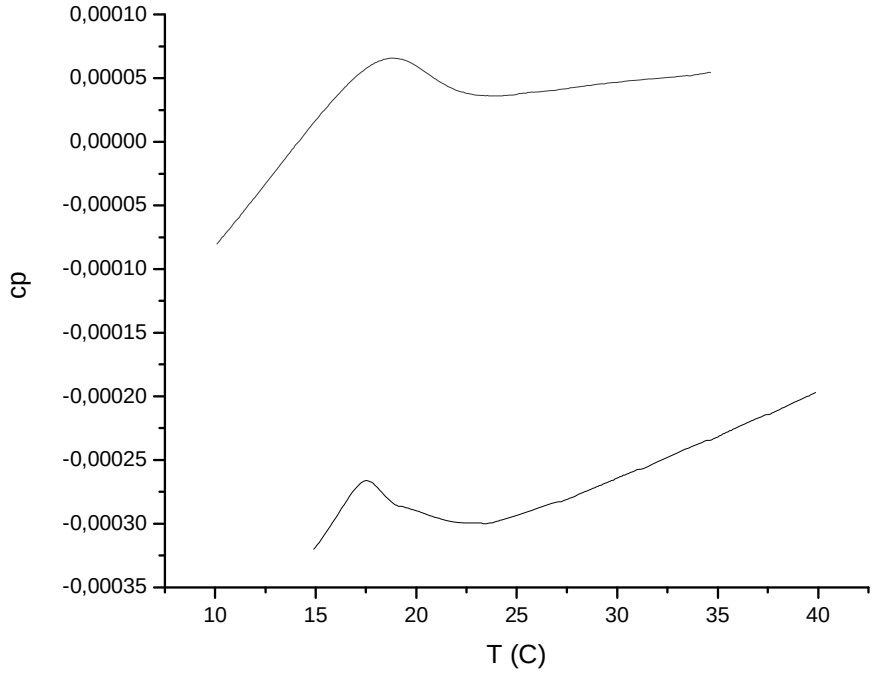

Figure 6.10 DSC scans of a 1 wt% solution of molecular motor in DMPC in aqueous solution at pH 7 and pH 10, respectively. The concentration of DMPC used was 0.5 mg per ml tridistilled water.

To determine the difference in perturbation effects, a sample measured at pH 7 was remeasured at pH 10 (Figure 6.10). The transition temperature of the sample decreases from 18.8 to 17.5 ºC. Therefore there is a clear further perturbation possible with the **A**/ DMPC mixed vesicles when measured at pH 10. It is interesting to note though that the pH 7 system with age (one week) also has an altered transition temperature compared with a fresh sample, 18.8 versus 23.9 ºC. The sample itself appeared visually unaltered (no flocculation or change in transparency). A possible explanation for this is that only after a week the thermodynamically most stable vesicle is formed containing the motor amphiphile.[32] At pH 10, the systems proved more unstable. Infact, no two DSC runs ever gave the exact same transition temperature (Figure 6.11).

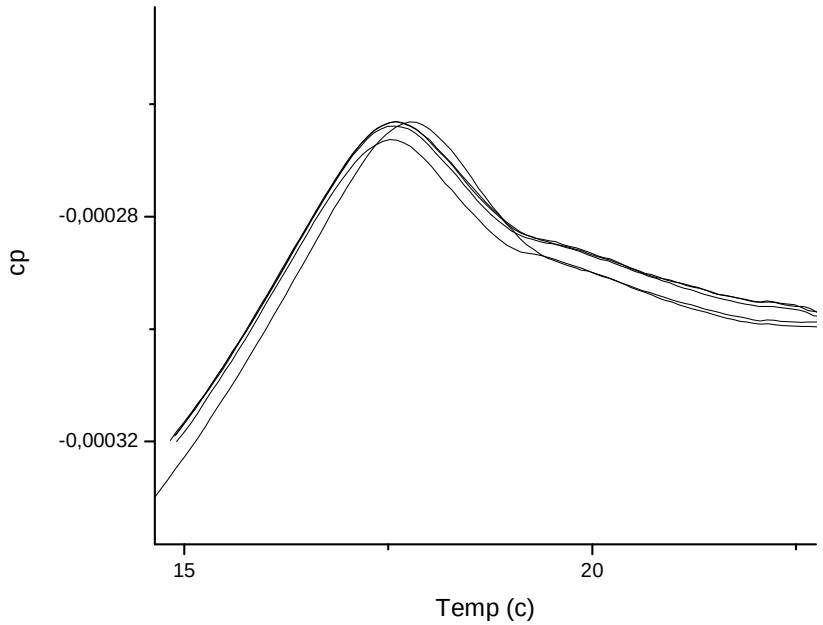

Figure 6.11 DSC scans of a 1 wt% solution of molecular motor in DMPC in aqueous solution at pH 10. Sequential scans taken at a rate of 1ºC/ min, and a stabilization time of 30 min between runs at 10ºC. The concentration of DMPC used was 0.5 mg per ml tridistilled water.

The various sequential runs usually differ by approximately 0.5 ºC. However, this was not observed for pure DMPC vesicles. These produced super imposable sequential scans showing the same transition temperature at both pH 7 and 10.The instability of the sample could be a result of the possible generation of motor amphiphile micelles in solution. The expected transition temperature is far too low for these aggregates to be observed in water. However, by having changing ratios of the motor amphiphile within the vesicular structure the reported transition temperature varies. Changing the measuring parameters (allowing more time to stabilize at a given temperature) only made the instability more prominent.

In conclusion, the pH 10 samples perturb the DMPC packing further than the pH 7 sample and there is a slight difference in observed transition temperature between the non-irradiated and irradiated samples.

6.2.5 UV/VIS of molecular motor in vesicles

A UV/VIS spectrum was taken of the pH 7 sample (1 wt%) used for DSC measurements (section 6.2.4) to determine whether or not the irradiated DMPC/molecular motor sample does indeed switch. Owing to the fact that DMPC forms vesicles, regular UV/VIS spectroscopy cannot be used as the aggregates will cause changing interference with the light beam being used. To avoid this scattering diffuse reflectance spectroscopy was used. The resulting spectrum is even more undefined than those reported in section 6.2.1 and the change between the irradiated form and the un-irradiated form is quite small, as can be seen in Figure 2:

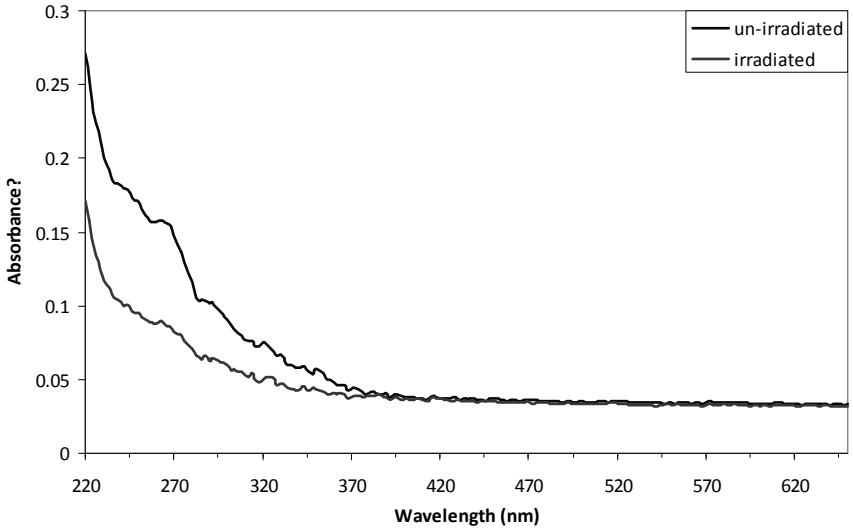

Figure 6.12 UV/VIS spectrum of a 1wt% of molecular motor **A** mixed with DMPC, at pH 7 in tridistilled water. Sample before and after irradiation.

Even though the change is small, there is a difference in the two spectra. This is further proof that the molecular motors still undergo photoisomerization when they are inside the vesicles. However, in the UV/VIS measurements, no isosbestic point can be observed. This indicates that there is no clean one-to-one conversion of one isomer to the other. The reason behind this might be that the molecular motor can be at different positions within the vesicles. A molecule in the tail region of DMPC might behave differently from a molecule close to the DMPC head groups. In this way, multiple processes can be going on, causing the non-existence of an isosbestic point.
All facts considered, it is clear that the molecular motors switch while being inside the DMPC vesicles. The DSC measurements for the samples before

and after irradiation indicate the presence of the two isomers (Scheme 6.5). However, the difference in the UV/VIS spectrum is small.

6.2.6 Cryo-TEM

The TEM images (Figure 6.13) make it apparent that the aggregates present in solution represent micelles. The micelles have an average size of between 5 and 12 nm. The fluorescence data suggested that there is a small difference in the environment sensed by Nile Red. However, as the aggregates are too small, TEM is unable to show a discernable difference for an irradiated or non-irradiated sample.

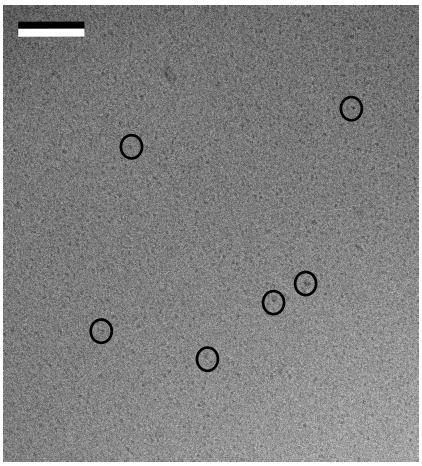

Figure 6.13 Cryo-TEM images of the stable isomer molecular motor at a concentration of 1.3 x 10^{-3} M in water at pH 10. The bar represents 100 nm.

6.3 Conclusions and Outlook

The newly synthesized molecular motor **A** is the first water-soluble motor amphiphile at pH 10**.** UV/VIS spectroscopy showed that the thermal isomerization process of **6** has a long enough half-life for easy study, which is decreased by half once the concentration used is high enough for aggregation to take place. It became apparent that **A** generates aggregates of both the stable and unstable isomers as proved by fluorescence spectroscopy and TEM imaging. Owing to the high thermal barrier, the experiments upon heating (DSC) could be carried out without affecting the aggregates. It became clear that the stable and unstable sample behave somewhat differently. The stable sample has a lower CMC value than the unstable sample. Using a concentration of 5.0 x 10^{-4} M of the irradiated sample would generate micelles. Through thermal isomerization this system would revert to the stable form (equivalent to that before irradiation) which does not aggregate at this concentration. Thus disassembly would occur. However, as the thermal isomerization is very slow at room temperature this motor could only be used when very slow delivery is required. The fact

that **A** generates micelles means that the dynamics would cause quick release. Therefore currently the system would be inappropriate for use in drug delivery.
To further develop this system towards applications, several new designs of the molecular motor amphiphile would be required. For the use in drug delivery systems it would be necessary to have a vesicle rather than a micelle, as micelles are so dynamic that these are constantly reforming. Thus targeting specific cells becomes very difficult. In order to have vesicle formation, the P parameter should be altered. The use of more hydrophilic head groups would be essential as the current system works best at pH 10 which is incompatible with the human body. To tweak delivery times varying molecular motor structures could be used.

6.4 Acknowledgments

Sander de Jong is acknowledged for carrying out part of this work as part of his master's research. Dr. Bea Maciá-Ruiz is acknowledged for her help with the synthesis section. Dr. Edzard Geertsema and Dr. Davide Pantarotto are acknowledged for their previous work on this project. Dr. Marc Stuart is acknowledged for his cro-TEM measurements. Dr. Luminita Toma is acknowledged for the Langmuir-Blodgett measurements.

6.5 Experimental

Water used was always bidistilled or milliq for the DSC measurements. Kinetic (UV/VIS) measurements were performed on a Hewlett-Packard HP 8453 FT spectrophotometer equipped with a Huber Polystat cc1 and a Quantum Northwest temperature control, running an Agilent UV-Visible ChemStation. Fluorescence was measured on a Jasco FP-6200 spectrofluorimeter at 20 °C using an excitation wavelength between 488 and 590 nm. Fluorescent emission was measured between 600 and 700 nm at 1 nm intervals. Nile Red emission maxima were calculated using a 4-parameter lognormal fit using SigmaPlot 11.0 and Microcal Origin 7. Irradiation experiments were performed using a Spectroline lamp model ENB-280C/FE (λ = 365 nm). DSC measurements were carried out on a MicroCal VP-DSC at 1.7 bar running VPViewer and MicroCal Origin 4.1. Diffuse reflectance UV-vis spectroscopy was carried out on a Jasco V-570 spectrophotometer equipped with a Jasco ISN-470 integrating sphere apparatus. Langmuir-Blodgett experiments were performed on a Nima LB Deposition Extra-Large trough and analysed using Nima TR620 software. BAM measurements were performed using a 660 nm laser.

Cryo-electron microscopy

A sample (2 µl) was placed on a holy carbon coated grid (Quantifoil 3.5/1) in a controlled environment of a Vitrobot (FEI, Eindhoven, The Netherlands). The sample was automatically blotted and vitrified in liquid ethane. Frozen hydrated grids were mounted in a Gatan (model 626) cryo-stage and examined in a Philips CM120 cryo-electron microscope at 120 kV. Images were recorded under low-dose conditions.

Fluorescence

A stock solution of Nile Red (NR) in ethanol (2.5mM) was prepared, a range of concentrations of the molecular motor, 70 eq of NaOH and water were prepared. The NR was diluted into the fluorescence cuvette containing the molecular motor solution to 1.25 µM. The sample was then measured using an excitation wavelength of 550 nm for the CMC determination. The λ_{MAX} was determined using a fit in Sigmaplot.

Kinetics

A solution of the molecular motor with 70 eq. of NaOH in water was prepared at two different concentrations (below and above the CMC). The sample was irradiated until full conversion[‡] to the unstable isomer was achieved. Subsequently the solution was placed in the UV/VIS spectrometer, and three wavelengths were monitored over time. The wavelengths selected include the one which yields the largest change between the irradiated and non-irradiated forms of the compound (~350 nm), and two which should remain unaffected (in the region above 450 nm as the compound itself here does not absorb) to monitor potential baseline shifting. The kinetics were followed until no increase in the signal could be observed anymore. This process was repeated for at least four different temperatures.

Calculations of kinetic data

Using the method of initial rate, the rate constant of conversion (*k*) at a certain temperature can be determined by plotting the natural logarithm of the relative absorption against the time, where the relative absorption is given as:

$$A_{relative} = \frac{A_{stable} - A_{current}}{A_{stable} - A_{initial}} \qquad (1.1)$$

The slope of this plot directly gives the rate constant. The experiment was run at different temperatures. The rate constant at room temperature was determined from the Arrhenius equation:

[‡] PSS was determined using UV/VIS.

$$k = Ae^{-E_a/RT} \qquad (1.2)$$

or rewritten as:

$$\ln(k) = \ln(A) - \frac{E_a}{RT} \qquad (1.3)$$

where
k = rate constant of conversion
A = pre-exponential factor (s^{-1} for a first-order process)
E_a = energy of activation
R = gas constant
T = temperature (K)

The pre-exponential factor (A) and the energy of activation (E_a) were calculated from an Arrhenius plot. In such a plot ln(k) is plotted against 1/T to give a straight line whose slope is equal to E_a. The value at the y-intercept (x=0) gives ln(A). Using these values in equation 1.3, the ln(k) and thus the k at room temperature can be calculated.
From the rate constant, the half-life of the isomerization reaction can be calculated using the following equation:

$$t_{½} = \frac{\ln(2)}{\ln(2k)} \qquad (1.4)$$

with
$t_{½}$ = half-life time

To calculate the enthalpy of activation ($\Delta H^{‡}$) and entropy of activation ($\Delta S^{‡}$) the Eyring equation is used:

$$\ln(\frac{k}{T}) = \ln(\frac{k_B}{h}) + \frac{\Delta S^{‡}}{R} - \frac{\Delta H^{‡}}{RT} \qquad (1.5)$$

where
k = rate constant of conversion
h = Planck's constant
k_B = Boltzmann constant
R = gas constant
T = temperature (K)

To determine these parameters an Eyring plot is constructed where ln(k/T) is plotted against 1/T. Thus, the y-intercept gives the value of $\Delta S^{‡}/R$ + ln(k_B/h) while the slope gives the value of $\Delta H^{‡}/R$.

Now that the enthalpy of activation ($\Delta H^{\ddagger}$) and entropy of activation ($\Delta S^{\ddagger}$) are known, the Gibbs free energy of activation ($\Delta G^{\ddagger}$) at a specific temperature can be calculated using equation 1.6:

$$\Delta G^{\ddagger} = \Delta H^{\ddagger} - T\Delta S^{\ddagger} \qquad (1.6)$$

DSC

DSC samples were prepared based on a concentration of 0.5 mg of DMPC per ml H_2O. The percentage of molecular motor added was based on weight. The two amphiphiles were each dissolved in chloroform and then mixed. The solvent of the sample was slowly evaporated under reduced pressure generating a thin film. Water was then added and the sample was placed in a freeze drier. Then 2 ml of milliq water was added. The sample was degassed for a minimum of 5 min prior to injection into the DSC. The samples followed the same heating and cooling trajectory 5 times between 10 and 40°C. Each intervening equilibrating period lasted 20 min (unless specified otherwise). The temperature was allowed to increase at a rate of 1 $^{o}C\ min^{-1}$.

Synthesis

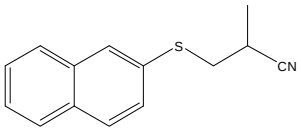

2-Methyl-3-(2-naphthylthio)propiononitrile (1)

Methacrylonitrile (5 mL) was kept at 0 °C under a nitrogen atmosphere and 2-thionaphthol (779 mg, 4.87 mmol) was added. A Triton B solution (0.1 mL, 40% in methanol) was slowly added and the mixture was stirred for one hour. The mixture was then heated to 65 °C and kept stirring overnight at this temperature.
After cooling the solution, an aqueous saturated solution of NH_4Cl (3 mL) was added. The water layer was extracted twice with ether. The combined organic layers were washed twice with brine and dried using Na_2SO_4. The solvent was then evaporated *in vacuo* and the resulting orange oil was purified using column chromatography using silica and *n*-heptane:ethyl acetate 10:1. This yielded a light-yellow oil (652 mg, 59%)
^{1}H NMR (300 MHz, $CDCl_3$): δ 7.89 (s, 1H); 7.77-7.84 (m, 3H); 7.46-7.55 (m, 3H); 3.17 (dd, J=13.9, 7.1 Hz, 2H); 2.79 (m, 1H); 1.43 (d, J=6.9 Hz, 3H)
^{13}C NMR (50 MHz, $CDCl_3$): δ 17.6; 26.4; 38.3; 121.8; 126.7; 127.1; 127.6; 128.0; 128.6; 129.3; 130.1; 131.4; 132.6; 133.9

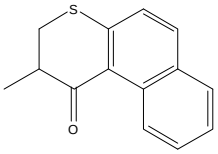

2,3-Dihydro-2-methyl-1H-naphtho[2,1-b]thiopyran-1-one (2)

Polyphosphoric acid (30 mL) was stirred mechanically at 70 °C. Propiononitrile **1** (767 mg, 3.38 mmol) was added and the temperature was raised to 110 °C. This mixture was stirred for three hours. The mixture was then allowed to cool to approximately 70 °C and it was poured over ice (150 g), and the resulting mixture was stirred overnight. The water layer was extracted with ether and the combined organic layers were washed with brine. This was dried using Na_2SO_4 and the solvent was evaporated *in vacuo*. The product was purified by column chromatography using silica and *n*-pentane:ethyl acetate 12:1 to yield an orange-yellow oil (479 mg, 62%)

^{1}H NMR (200 MHz, $CDCl_3$): δ 9.08 (d, J=7.2 Hz, 1H); 7.76 (t, J= 8.1 Hz, 2H); 7.59 (t, J= 8.1 Hz, 1H); 7.44 (t, J= 7.8 Hz, 1H); 7.25 (d, J=9.3 Hz, 1H); 3.09-3.29 (m, 3H); 1.40 (d, J=6.3 Hz, 3H)

^{13}C NMR (50 MHz, $CDCl_3$): δ 199.5; 144.2; 133.5; 132.7; 131.9; 129.2; 128.7; 126.0; 125.8; 125.6; 125.3; 43.1; 33.1; 15.6

HRMS calcd for $C_{14}H_{11}OS$: 228.061; found: 228.062.

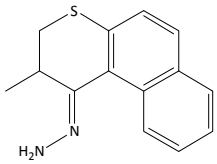

2,3-Dihydro-2-methyl-1H-naphtho[2,1-b]thiopyran-1-onehydrazone (3)

Ketone **2** (479 mg, 2.10 mmol) was added to absolute ethanol (5 mL) under a nitrogen atmosphere. Hydrazine monohydrate (2 mL) was added and the mixture was refluxed for 20 h. To the hot mixture, water (5 mL) was added and the flask was wrapped in cotton wool. This was allowed to reach room temperature and then stored in the freezer for 4 h. The organic layers were washed with water and brine and dried on Na_2SO_4. The solvent was then evaporated to yield a yellow-orange solid (305 mg, 60%)

^{1}H NMR (400 MHz, $CDCl_3$): δ 8.42 (d, J=8.0 Hz, 1H); 7.76 (d, J=8.0 Hz, 1H); 7.65 (d, J=8.0 Hz, 1H); 7.49 (t, J=8.0 Hz, 1H); 7.41 (t, J=8.0 Hz, 1H); 7.34 (d, J=8.0 Hz, 1H); 5.7-5.5 (br, 2H); 3.59-3.49 (m, 1H); 3.20 (dd, J=7.2 Hz, 6.4 Hz, 1H); 2.71 (dd, J=12.8 Hz, 9.6 Hz, 1H); 1.33 (d, J=6.8 Hz, 3H)

^{13}C NMR (75 MHz, $CDCl_3$): δ 149.3; 135.7; 133.0; 132.1; 130.8; 128.0; 127.7; 126.7; 126.1; 125.9; 125.1; 36.4; 34.0; 14.7

HRMS calcd for $C_{14}H_{14}N_2S$: 242.088; found: 242.087.

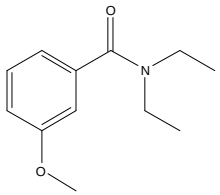

N,N-Diethyl-3-methoxy-benzamide (4)

3-Methoxybenzoic acid (756 mg, 5 mmol) was dissolved in dichloromethane (5 mL). Thionyl chloride (0.9 mL, 12.5 mmol) and a drop of dimethylformamide were added. The mixture was refluxed for 2 h after which the solvent and excess thionyl chloride were evaporated. The resulting acid chloride was again dissolved in dichloromethane and cooled to 0 °C. Diethylamine (0.8 mL, 15 mmol) was slowly added and the mixture was allowed to reach room temperature overnight. Dichloromethane (5 mL) was added and the organic layers were washed with a saturated aq. $NaHCO_3$ solution and with brine. The solution was then dried using Na_2SO_4 and the solvent was evaporated to yield a yellow oil. (738 mg, 72%)
^{1}H NMR (300 MHz, $CDCl_3$): δ 7.31-7.26 (m, 1H); 6.93-6.90 (m, 3H); 3.81 (s, 3H); 3.54 (br s, 2H); 3.26 (br s, 2H); 1.24 (br s, 3H); 1.11 (br s, 3H)
^{13}C NMR (75 MHz, $CDCl_3$): δ 13.2; 14.5; 39.5; 43.5; 55.5; 111.9; 115.2; 118.6; 129.8; 138.7; 159.7; 171.2
HRMS calcd for $C_{12}H_{17}NO_2$: 207.126; found: 207.127.

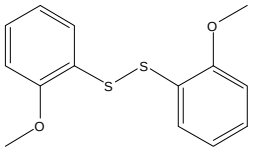

Di-(2-methoxyphenyl)disulfide (5)

2-Methoxybenzenethiol (1.0 g, 7.1 mmol) was added to dichloromethane (35 mL) at room temperature. Copper sulfate pentahydrate (2.5 g, 10 mmol) and potassium permanganate (2.5 g, 16 mmol) were added and the mixture was stirred for 3 h. The resulting solution was filtrated over celite, the solvent was removed under vacuum. Purified using flash column chromatography (silica, *n*-heptane:ethyl acetate 10:1) the product was obtained as a white to slightly yellowish powder (572 mg, 29%) m.p. 119.4-119.8 °C
^{1}H NMR (200 MHz, $CDCl_3$): δ 7.53 (dd, J=7.7, 1.6 Hz, 1H); 7.23-7.15 (m, 1H); 6.95-6.84 (m, 2H); 3.90 (s, 3H)
^{13}C NMR (50 MHz, $CDCl_3$): δ 156.4; 127.6; 127.5; 124.5; 121.2; 110.4; 55.8

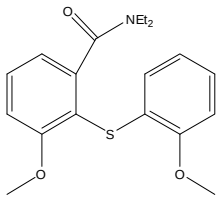

N,N-Diethyl-3-methoxy-2-(2-methoxy-phenylsulfanyl)-benzamide (6)

Dry THF (25 mL) was cooled to -80 °C and TMEDA (0.6 mL) and sec-butyl lithium (3.0 mL of a 1.6M solution in *n*-hexane) were added. After 15 min, a solution of amide **4** (738 mg, 3.56 mmol) in THF was added dropwise. Stirring was continued for 2 h at -80 °C, after which disulfide **5** (980 mg, 3.56 mmol) dissolved in THF (2 mL) was added. The mixture was kept stirring overnight. Diethyl ether (100 mL) was added and the mixture was washed twice with an aq. NaOH solution. After drying of the organic solution on Na_2SO_4, the solvent was evaporated. The resulting brownish solid was purified by chromatography on an automated silica column using a *n*-pentane:ethyl acetate gradient to yield a slightly yellow oil (711 mg, 58%)

^{1}H NMR (300 MHz, $CDCl_3$): δ 7.46-7.41 (m, 1H); 7.06 (t, J=7.2 Hz, 1H); 6.96 (d, J=7.2 Hz, 2H); 6.84-6.67 (m, 3H); 3.89 (d, J=2.2 Hz, 3H); 3.76 (d, J=2.2 Hz, 3H); 3.71 (m, 1H); 3.37 (m, 1H); 3.20-2.95 (m, 2H); 1.20 (t, J=6.9 Hz, 3H); 1.00 (t, J=7.0 Hz, 3H)

^{13}C NMR (75 MHz, $CDCl_3$): δ 168.4; 160.3; 155.3; 144.8; 130.9; 126.5; 125.5; 125.1; 120.6; 118.3; 115.6; 111.0; 109.9; 55.8; 55.4; 42.4; 38.2; 13.6; 12.1

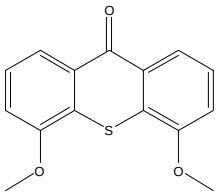

4,5-Dimethoxy-9H-thioxanthen-9-one (7)

A fresh batch of lithium di-isopropyl amine was prepared from di-isopropyl amine (0.2 mL) in dry THF under a nitrogen atmosphere. *n*-Butyl lithium (0.9 mL of a 1.6M solution in *n*-hexane) was added at -78 °C and the mixture was stirred for 5 min. It was then allowed to warm to 0 °C and a solution of amide **6** (711 mg, 2.06 mmol) in THF was added dropwise. The ice bath was removed and the solution was stirred for one hour. A saturated aq. NH_4Cl solution (25 mL) was added, after which the aqueous layer was extracted three times with 25 mL of diethyl ether. The solvent was then evaporated to give a yellow oil. This was purified on an automated silica

column using a *n*-pentane:ethyl acetate gradient to yield a yellow solid (364 mg, 65%)
^{1}H NMR (300 MHz, $CDCl_3$): δ 8.25 (dd, J=8.1, 0.9 Hz, 2H); 7.47 (t, J=8.1 Hz; 2H); 7.14 (d, J=7.5 Hz; 2H); 4.06 (s, 6H)
^{13}C NMR (75 MHz, $CDCl_3$): δ 180.2; 154.8; 129.9; 127.6; 125.9; 121.4; 112.1; 56.4

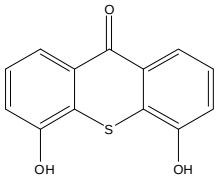

4,5-Dihydroxy-9H-thioxanthen-9-one (8)

Ketone **7** (607 mg, 2.23 mmol) was dissolved in dry dichloromethane under a nitrogen atmosphere. Tribromoborane (5 eq.) was added at 0 °C and the mixture was allowed to reach room temperature while stirring overnight. After bringing the reaction mixture back to 0 °C, ice was slowly added. The water layer was extracted five times with ethyl acetate, after which the organic layers were dried and the solvent removed under vacuum to yield **8** (186 mg, 76%)
^{1}H NMR (300 MHz, DMSO): δ 10.98 (s, 2H, OH); 7.94 (d, J=7.7 Hz, 2H); 7.38 (dd, J=7.7, 7.7 Hz, 2H); 7.20 (d, J=7.7 Hz, 2H)
^{13}C NMR (50 MHz, DMSO): δ 180.0; 153.7; 130.0; 127.0; 126.0; 119.9; 117.2

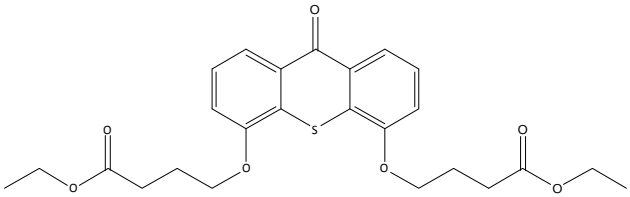

Diethyl 4,4'-((9-oxo-9H-thioxanthene-4,5-diyl)bis(oxy))dibutanoate (9)

Ketone **12** (244 mg, 1.0 mmol) was dissolved in dimethylformamide, together with ethyl 4-bromobutanoate (513 mg, 2.5 mmol), potassium carbonate (2 g), and cesium carbonate (0.5 g). This mixture was heated at reflux for 20 h. Purification on a silica column (*n*-pentane:ethyl acetate gradient up to 1:1) yielded **9** as a solid (425 mg, 90%).
^{1}H NMR (400 MHz, $CDCL_3$) δ 8.24 (dd, J=8.1, 0.9 Hz, 2H); 7.42 (t, J=8.0 Hz, 2H); 7.14 (d, J=7.9, 2H); 4.26 (t, J=6.1 Hz, 4H); 4.16 (q, J=7.1 Hz, 4H); 2.66 (t, J=7.2 Hz, 4H); 2.39-2.06 (m, 4H); 1.26 (t, 7.0 Hz, 6H)
^{13}C NMR (50 MHz, $CDCl_3$): δ 173.1; 154.0; 130.0; 128.1; 125.9; 121.6; 113.2; 68.2; 60.5; 30.5; 24.4; 14.2

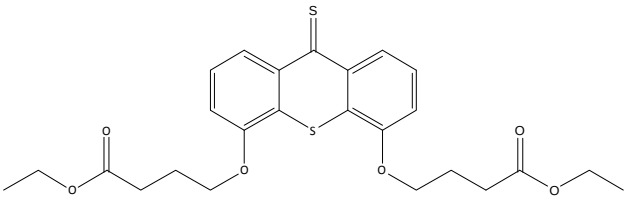

Diethyl 4,4'-((9-oxo-9H-thioxanthene-4,5-diyl)bis(oxy))dibutanoate (10)

A mixture of ketone **13** (150 mg, 0.32 mmol) and 3 equivalents of Lawesson's Reagent were heated at reflux in toluene for 16 h under an argon atmosphere. This mixture was then filtered and dichloromethane was added. The solvents were evaporated *in vacuo*. The resulting dark green solid was purified using column chromatography (*n*-pentane:ethyl acetate gradient up to 1:1) and the product was recrystallised to yield a dark green solid (131 mg, 86 %)

^{1}H NMR (400 MHz, $CDCL_3$) δ 8.64 (d, J=8.4, 2H); 8.27-7.96 (m, 2H); 7.34 (t, J=8.0, 2H); 7.10 (d, J=7.7, 2H); 7.05-6.91 (m, 2H); 4.25 (t, J=5.7 Hz, 2H); 4.16 (dd, J=13.8, 6.8 Hz, 2H); 3.86 (d, J=7.9 Hz, 2H); 2.66 (t, J=6.9 Hz, 2H); 2.27 (t, J=7.0 Hz, 2H); 2.04 (s, 2H); 1.26 (t, J=6.9 Hz, 6H)

^{13}C NMR (50 MHz, $CDCl_3$): δ 208.2; 170.5; 151.6; 135.8; 123.9; 122.9; 121.1; 109.8; 65.9; 58.0; 28.1; 22.0; 11.7

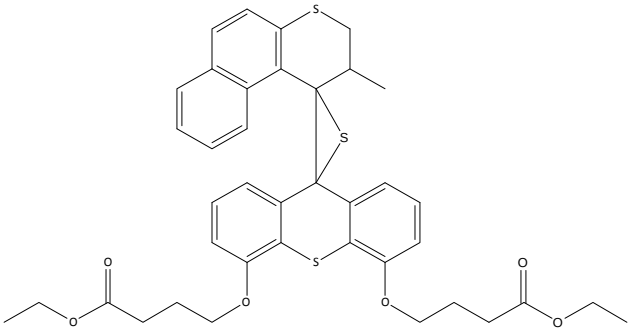

Episulfide (precursor for 11)

Hydrazone **3** (65 mg, 0.27 mmol) was dissolved in dry dimethylformamide. The solution was cooled to -50 °C and bis(trifluoro acetate) iodobenzene (88 mg, 0.27 mmol) was added. The mixture was stirred for 5 min after which thioketone **14** was added (131 mg, 0.27 mmol). The mixture was kept at -50 °C for 1 h after which it was allowed to reach room temperature, and was kept stirring for 16 h. The solvent was evaporated *in vacuo* and the solid was purified using column chromatography (*n*-pentane:ethyl acetate gradient up to 1:1) to yield the episulfide (61 mg, 30%)

^{1}H NMR (400 MHz, $CDCL_3$) δ 8.78 (d, J=8.8 Hz, 1H); 7.69 (d, J=8.2 Hz, 1H); 7.60 (d, J=8.1 Hz, 1H); 7.48 (t, J=7.7 Hz, 1H); 7.38-7.11 (m, 3H); 6.97

(d, J=8.2 Hz, 1H); 6.88 (d, J=8.2 Hz, 1H); 6.36 (dd, J=27.1, 7.9 Hz, 2H); 6.14 (t, J=7.7 Hz, 1H); 4.28-4.03 (m, 4H); 3.90 (d, J=7.3, 1H); 3.04 (s, 1H); 2.75–2.45 (m, 4H); 2.25-2.05 (m, 3H); 1.59 (s, 3H); 1.27 (t, J=6.5 Hz, 6H); 1.16 (d, J=5.6 Hz, 6H)
^{13}C NMR (50 MHz, $CDCl_3$): δ 173.6; 154.2; 153.3; 140.4; 135.0; 132.4; 131.8; 131.6; 128.4; 128.3; 127.03; 126.98; 126.0; 125.3; 124.4; 124.2; 123.5; 122.6; 110.4; 110.2; 110.1; 68.5; 68.4; 65.6; 62.0; 60.62; 60.59; 41.0; 35.8; 31.0; 29.9; 24.9; 24.8; 21.2; 14.5

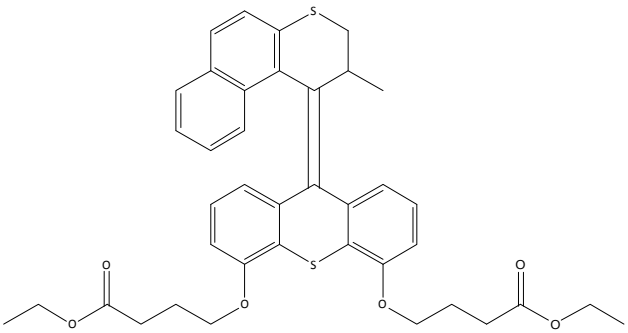

Diethyl 4,4'-(9-(2-methyl-2,3-dihydro-1H-benzo[f]thiochromen-1-ylidene)-9H-thioxanthene-4,5-diyl)bis(oxy)dibutanoate (11)

Episulfide **11** (27 mg, 0.023 mmol) and triphenyl phosphine (34 mg, 0.12 mmol) were dissolved in p-xylene. This mixture was heated at 95 °C for 16 h. The product was purified on a silica column (*n*-pentane:ethyl acetate gradient up to 2:1) to yield **11** (15 mg, 95%).
^{1}H NMR (300 MHz, DMSO): δ 7,59-7.49 (m, 3H); 7.35 (d, J=8.4 Hz, 1H); 7.30-7.21 (m, 3H); 7.10 (dd, J=7.3, 7.0 Hz, 1H); 6.99 (dd, J=8.4, 7.0 Hz, 1H); 6.86 (d, J=8.1 Hz, 1H); 6.35 (dd, J=7.7, 7.7 Hz, 1H); 6.30 (dd, J=8.1, 7.0 Hz, 1H); 6.03 (d, J=7.7 Hz, 1H); 4.29-4.02 (m, 8H); 3.98-3.90 (m, 1H); 3.70 (dd, J=11.4, 7.3 Hz, 1H); 3.07 (dd, J=11.4, 2.6 Hz, 1H); 2.77-2.55 (m, 8H); 2.27 (q, J=6.7 Hz, 2H); 2.15 (q, J=6.7 Hz, 2H); 1.28 (t, J=7.3 Hz, 6H); 0.75 (d, J=6.6 Hz, 3H)
^{13}C NMR (50 MHz, DMSO): δ 173.27; 173.23; 155.2; 154.2; 138.7; 136.4; 136,1; 134.6; 132.1; 131.4; 131.2; 130.7; 127.4; 127.3; 126.3; 125.5; 125.4; 125.3; 124.9; 124.4; 124.2; 123.6; 121.8; 119.9; 109.4; 109.2; 67.8; 67.7; 60.3; 37.1; 31.7; 30.7 (2x); 24.6; 24.5; 19.0; 14.2 (2x)

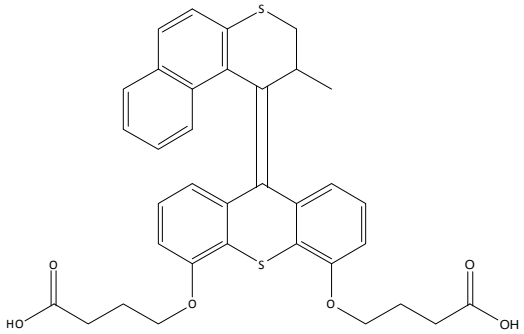

4,4'-(9-(2-Methyl-2,3-dihydro-1H-benzo[f]thiochromen-1-ylidene)-9H-thioxanthene-4,5-diyl)bis(oxy)dibutanoic acid (A)

Diester **11** (92 mg, 0.08 mmol) was dissolved in a mixture of 2mL ethanol, 2 mL water and 2 mL THF. Lithium hydroxide (20 mg, 0.8 mmol) was added and the mixture was refluxed for 4 h. A concentrated HCl solution (1 mL) was added and the mixture was stirred for another 90 min. The mixture was then filtered and the solid was washed with cold methanol and ethanol. Recrystallisation from methanol yielded pure **A** (30 mg, 0.05 mmol, 63 %)
^{1}H NMR (300 MHz, DMSO-d_6): δ 12.16 (b, OH, 2H); 7.65 (d, J=8.4 Hz, 1H); 7.60 (d, J=8.1 Hz, 1H); 7.41-7.35 (m, 3H); 7.26 (d, J=7.3 Hz, 1H); 7.10 (dd, J=7.7, 7.3 Hz, 1H); 7.05 (d, J=8.1 Hz, 1H); 6.94 (dd, J=7.7, 7.0 Hz, 1H); 6.46 (d, J=8.4 Hz, 1H); 6.38 (dd, J=8.1, 7.7 Hz, 1H); 5.88 (d, J=7.0 Hz, 1H); 4.23-3.77 (m, 6H); 3.08 (d, J=11.4 Hz, 1H); 2.02 (dd, J=7.0, 6.6 Hz, 2H); 1.89 (dd, J=7.0, 6.6 Hz, 2H); 0.59 (d, J=6.6 Hz, 3H); 4 proton signals hidden under the DMSO peak.
^{13}C NMR (50 MHz, DMSO-d_6): δ 174.83; 174.80; 155.5; 154.7; 139.1; 136.5; 136.3; 135.2; 132.1; 131.5; 131.3; 130.9; 128.3; 128.2; 127.8; 126.5; 126.0; 125.0; 124.3; 124.2; 123.7; 121.6; 120.5; 110.8; 110.4; 68.3; 31.6; 30.7; 30.6; 25.0; 24.8; 19.3; one quartenary aromatic carbon signal was not observed.
HRMS calcd for $C_{35}H_{32}O_6S_2$: 612.16403; found: 612.16353

6.6 References

[1] T.F. Tadros, *Applied Surfactants*; Wiley-VCH: Weinheim, **2005.**
[2] Traube, *Ann. Chem*. **1891**, *265*, 27-55.
[3] Review: W. Blokzijn, J.B.F.N. Engberts, *Angew. Chem. Int. Ed*. **1993**, *32*, 1545-1579
[4] G.S. Hartley, B. Collie, C.S. Samis, *Trans. Faraday Soc*. **1936**, *32*, 795-815
[5] P.W. Atkins, *Physical Chemistry*, Sixth ed. Oxford University Press: Oxford **1998**; p 362
[6] P.H.K. de Jong, J. E. Wilson, G.W. Neilson, A.D. Buckingham, *Mol. Phys*. **1997**, *91*, 99-103.
[7] J.N. Israelachvili, D J. Mitchell, B. W. Ninham, J. Chem. Soc. Faraday Trans. 2, 1976, 72, 1525-1568.

[8] For instance, the cross-sectional area of the headgroup depends on the volume occupied by the tails. See ref. R. Nagarajan, Langmuir, **2002**, *18*, 31-38.
[9] M. Scarzello, *Ph.D. Thesis*, University of Groningen, **2006.**
[10] M.J. Rosen, Surfactants and Interfacial Phenomena; Wiley, Hoboken, **2004**, 122-137.
[11] For some examples of redox chemistry see: a) S, Munoz, G.W. Gokel, *Inorg. Chim. Acta*, **1996**, *250*, 59-67; b) Y. Kakizawa, H. Sakai, A. Yamaguchi, Y. Kondo, N. Yoshino, M. Abe, *Langmuir*, **2001**, *17*, 8044-8048; c)H. Sakai, H. Imamura, Y. Kondo, N. Yoshino, M. Abe, *Colloid. Surf. A: Physicochem. Eng*. **2004**, *232*, 221-228.
[12] For an example of ion and pH dependence, see: A.F. Dexter, A.S. Malcolm, A.P.J. Middelberg, *Nature Mat.* **2006**, *5*, 502-506.
[13] For shear-induced vesicles see: B. Medronho, S. Fuiji, W. Richtering, M.G. Miguel, U. Olsson, *Coll. Polym. Sci*. **2005**, *284*, 317-321.
[14] For examples of only temperature dependence, see: a) I.F. Uchegbu, A. Schatzlein, G. Vanlerberghe, N. Morgatini, A.T. Florence, *J. Pharm. Phamacology*, **1997**, *49*, 606-610; b) I.S. Kim, Y.I. Jeong, C.S. Cho, S.H. Kim, *Int. J. Pharma*. **2000**, *205*, 167-172; c)E. Di Cola, C. Lefebre, A. Deffieux, T. Narayanan, R. Borsali, *Soft Matt*. **2009**, *5*, 1081-1090; d) Z. Yang, J.D. Xie, W. Zhou, W.F. Shi, J. *Biomed. Mater. Res. A*. **2009**, *89A*, 988-1000 .
[15] For an example of temperature and pH dependence, see: J. Huang, L.X. Ren, Y.M. Chen, *Polym. Int*. **2008**, *57*, 714-721.
[16] For some examples of pH dependence, see: a) H. Kawasaki, M. Souda, S. Tanaka, N. Nemoto, G. Karlsson, M. Almgren, H. Maeda, *J. Phys. Chem. B*, **2002**, *106*, 1524-1527; b) M. Johnsson, A. Wagenaar, M.C.A. Stuart, J.B.F.N. Engberts, *Langmuir*, **2003**, *19*, 4609-4618; c) M.H. Chung, Y.C. Chung, B.C. Chun, *Coll. Surf. B- Biointerfaces*, **2003**, *29*, 75-80 d) J.E. Klijn, M.C.A. Stuart, M. Scarzello, A. Wagenaar, J.B.F.N. Engberts, *J. Phys. Chem. B*. **2007**, *111*, 5204-5211; e) F. Versluis, I. Tomatsu, S. Kehr, C. Fregonese, A. W.J.W. Tepper, M.C.A. Stuart, B.J. Ravoo, R.I. Koning, A. Kros. *J. Am. Chem. Soc.* **2009**, *131*, 13186-13187.
[17] For examples of amphiphiles based on azobenzenes see: a) H. Sakai, A. Matsumura, S. Yokoyama, T. Saji, M. Abe, *J. Phys. Chem. B*. **1999**, *103*, 10737-10740; b) J.M. Kuiper, J.B.F.N. Engberts, *Langmuir*, **2004**, *20*, 1152-1160; c) J. Ruchmann, S. Fouilloux, C. Tribet, *Soft. Matt*. **2008**, *4*, 2098-2108.
[18] For other switchable surfactants see: a) T.M. Fyles, B. Zeng, *J. Org. Chem*. **1998**, *63*, 8337-8345; b) Y.G. Jiang, Y.P. Wang, N. Ma, Z.Q. Wang, M. Smet, X. Zhang, *Langmuir*, **2007**, *23*, 4029-4034; c) J. Zou, F. Tao, M. Jiang, *Langmuir* **2007**, *23*, 12791-12794.
[19] a) R. A. van Delden, B. L. Feringa, *Angew. Chem. Int. Ed.* **2001**, *40*, 3198. b) R. Eelkema, R. A. van Delden and B. L. Feringa, *Angew. Chem., Int. Ed.*, **2004**, *43*, 5013-5016. c) J. Vicario, M. Walko, A. Meetsma, B.L. Feringa, *J. Am. Chem. Soc*. **2006**, *128*, 5127-5135
[20] See ref 17 for kinetic data and for instance: M. Klok, *Ph.D. Thesis*, University of Groningen, **2009**, 133 and compare to E.M. Geertsema, *Ph.D. Thesis*, University of Groningen, **2003**, 125-126 (half-life = 215h in toluene for the thermal isomerization). For comparative studies, see: J. Vicario, M. Walko, A. Meetsma, B.L. Feringa, *J. Am. Chem. Soc*, **2006**, *128*, 5127-5135 and T. Fernández Landaluce, G. London, M.M. Pollard, P. Rudolf, B.L. Feringa, *J.Org. Chem*. **2010**, *75*, 5323-5325

[21] For an example of a typical molecular motor synthesis see for instance: N. Koumura, E.G. Geertsema, M.B. van Gelder, A. Meetsma, B.L. Feringa, *J. Am. Chem. Soc.* **2002**, *124*, 5037.
[22] M.K.J. ter Wiel, *Ph.D. Thesis*, University of Groningen, **2004**, 245 (the synthetic data (NMR are available for the synthesis of **8** in the experimental section **4**-**8**)
[23] pKa increases with chain length in linear fatty acids. For example: J.K. Kanicky, A.F. Poniatowski, N.R. Mehta, D.O. Shah, *Langmuir*, **2000**, *16*, 172; J.K. Kanicky, D.O. Shah, *Langmuir*, **2003**, *19*, 2034-2038.
[24] See for instance chapter 2 of this thesis or ref 17 c.
[25] S. de Jong, *Master Thesis*, University of Groningen, **2009** and E. Geertsema, *PhD Thesis*, University of Groningen , **2003**
[26] For detailed explanation on method for calculations see experimental section.
[27] For surfactants it is well known that micelles exist in the order of milliseconds and that surfactants reside at most between 5-10 seconds in the aggregate.
[28] Scattering diffuse reflectance spectroscopy is a technique used as it analyses the diffused reflected light of samples. This is necessary in this case as vesicles are present and in a normal set up vesicles will pass in and out of the beam yielding different results will the system as a whole has not changed.
[29] P. Greenspan, S.D. Fowler, *J. Lipids Res*. **1985**, 781 for specific information on the effect of polarity, see for example: J.F. Deve, T.A. Berger, A.G. Anderson, *Anal. Chem*. **1990**, 615-622
[30] J.A. Dean, *The Analytical Chemistry Handbook*; McGraw Hill: New York **1995**; pp. 15.1-15.5
[31] T_m is 23.8 ºC see: G.T. Barnes, G.A. Lawrie, B.J. Battersby, S.M. Sarge, H.K. Cammenga, P.B. Schneider, *Thin Solid Films*, **1994**, 201-207.
[32] It has been previously observed that vesicles can take long period of time before becoming "stable". It can take up to a month in the case of SDS + DDAD see reference: E.F. Marques, *Langmuir*, **2000**, *16*, 4798-4807.

Nederlandse Samenvatting

Het onderzoek beschreven in dit proefschrift draait om meerdere complexe systemen rond een chiraal molecuul wiens eigenschappen door omliggende moleculen versterkt kunnen worden (amplificatie).

Schema 1 Demonstratie van chiraliteit. De twee kurkentrekker spiralen gaan in tegenovergestelde richting, tegenovergestelde heliciteit (linksom en rechtsom).

De term *chiraal* komt van het Griekse χειρ (cheir), dat *hand* betekent. De handen zijn ook een van de beste alledaagse voorbeelden van chiraliteit, de linker- en rechterhand, die elkaars spiegelbeeld zijn en niet door draaien in elkaar omgezet kunnen worden (Schema 1). Chiraliteit komt veelvuldig voor op moleculaire schaal. Deze eigenschap is essentieel in vele chemische en fysische processen. In de natuur komen vele chirale verbindingen maar in één spiegelbeeldvorm voor, zoals suikers en de aminozuren waar eiwitten uit zijn opgebouwd. Dit is bepalend voor de uiteindelijke vorm van het eiwit, en is essentieel voor de interactie tussen deze eiwitten en andere chirale moleculen.
Een interactie tussen twee chirale moleculen is afhankelijk van de respectievelijke pasvormen (de juiste sleutel voor het juiste slot). Het passen van de twee moleculen luistert heel precies. In het verleden werd het medicijn Softenon (thalidomide) als mengsel van zijn twee spiegelbeelden toegediend bij zwangere vrouwen tegen ochtendmisselijkheid. Van het toegediende mengsel van spiegelbeelden (racemaat) had maar een van de twee spiegelbeeld vormen (enantiomeer) de gewenste werking. Het andere enantiomeer bleek aangeboren afwijkingen bij baby's te veroorzaken. Het werd dus duidelijk aan de hand van dit voorbeeld dat bij het toedienen van racematen (wat tot dus ver veel voorkwam) problemen kunnen worden voorkomen. Op dat moment werd besloten dat medicijnen alleen nog maar toegediend mogen worden bestaande uit het werkende enantiomeer (enantiomeer zuiver).

Een eiwit vouwt zich als het ware om een chiraal molecuul. Andere moleculen vormen zich hier weer naar, dit is zogenaamde versterking, of amplificatie van chiraliteit. In dit proefschrift kijken we naar verschillende vormen van amplificatie van chiraliteit.

De moleculaire motor (in 1999 ontwikkeld) is een molecuul bestaande uit twee helften dat draait om een centrale as (Schema 2). Onder invloed van UV licht zal de bovenste helft in stabiele vorm **1a** een kwart slag draaien ten opzicht van de onderste helft. De ontstane vorm (**1b**) is minder stabiel en zal bij hogere temperatuur verder draaien. Het molecuul **1a'** is gelijk aan **1a** (stabieler dan **1b**) maar de boven helft is 180 graden gedraaid ten opzicht van de onderkant. De draaiing van deze moleculaire motor gaat altijd in één richting (unidirectional rotation). De richting wordt bepaald door de exacte structuur van het uitgangsmolecuul. Door UV bestraling en verwarming afwisselend toe te passen kan de ene helft van het molecuul voortdurend roteren ten opzichte van de andere helft.

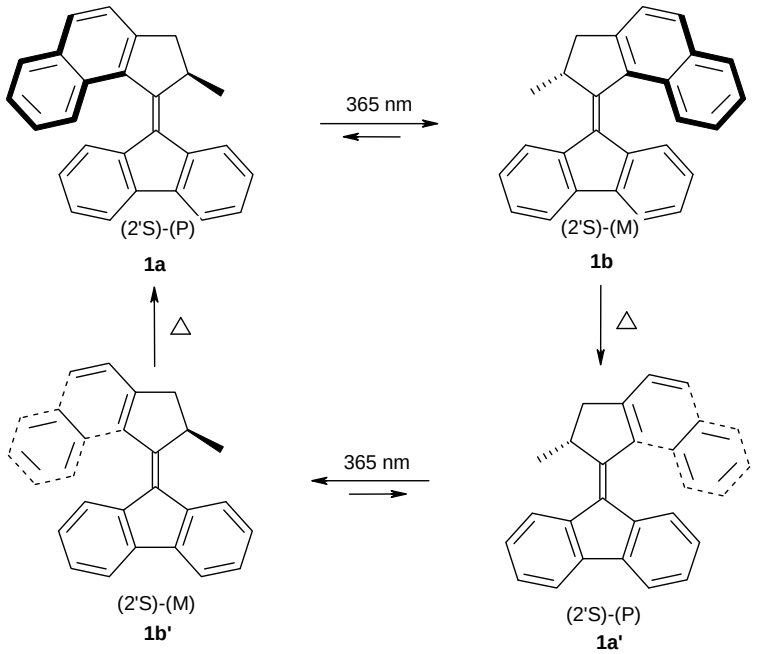

Schema 2 Rotatie rond de centrale dubbele binding in de moleculaire motor.

Belangrijk voor dit onderzoek is dat molecuul **1a** en **1b** niet gelijk zijn in drie dimensies. Moleculen **1a** en **1b** hebben van boven af bekeken verschillende heliciteiten ("schroefdraad") waardoor zij omliggende moleculen anders kunnen beïnvloeden.

In hoofdstuk twee tot en met vier wordt er gekeken naar de amplificatie van chirale verbindingen in niet-chirale vloeibare kristallen (bekend van LCD schermen).

De vloeibaar kristallijne fase wordt vaak ook de vierde fase genoemd. Dit omdat de eigenschappen van een vloeibaar kristallijn materiaal ergens

tussen de vaste en de vloeibare fase inzitten. De moleculen bevinden zich niet in een vaste ordening in drie richtingen zoals in een kristal. Maar, de moleculen kunnen zich onderling wel ordenen door verschillen in polariteit[*]. De ordening is meestal maar in één richting langs een richter (zie Schema 3). Voor staafvormige moleculen heet dit de nematische fase. Door deze ordening en versterkte interacties tussen de moleculen is een vloeibaar kristal viskeuzer[†] dan een normale vloeistof, en heeft het twee smeltpunten.

Schema 3 Ordening van VK moleculen in een nematische fase (ordening verticaal ten opzichte van het plaatje).

Een achiraal mesogeen (molecuul dat een vloeibaar kristallijne fase vormt) genereert een achirale VK fase. Door toevoeging van een chiraal molecuul wordt de ordening tussen deze mesogenen veranderd. Deze mesogenen ordenen zich nu in de vorm van helixen (zie Schema 4). Deze fase wordt de cholesterische fase genoemd. Onder een microscoop ziet deze fase eruit als een vingerafdruk (Schema 4).

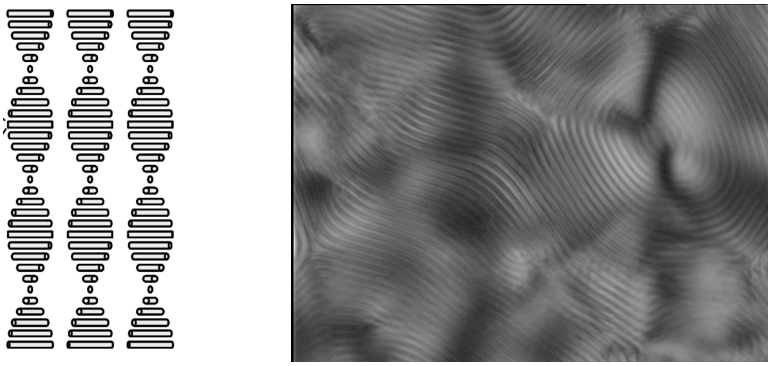

Schema 4 Links) de helix ordening in een cholesterische fase. Rechts) de cholesterische fase zoals te zien onder de microscoop.

[*] kan optreden bij twee atomen/ segmenten van een molekuul waarvan de ene harder aan de elektronenwolk trekt dan het andere. Hierdoor zijn de bindingselektronen niet gelijkmatig verdeelt.

[†] Viscositeit is een fysische eigenschap die de traagvloeibaarheid weergeeft. Bijvoorbeeld: ketchup is veel traag vloeiender dan water en dus viskeuzer.

Moleculaire motoren met kleine structurele variaties (Schema 5) werden als chirale gast toegevoegd aan mesogenen om te zien of er verschillen zijn in de inductie van chiraliteit.

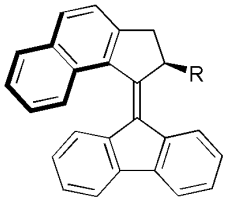

Schema 5 Een voorbeeld van de verschillende moleculaire motoren die gebruikt zijn als gast, waarbij R verschillende substituenten (grote/aard) voorstellen.

Uit dit onderzoek blijkt dat mesogenen erg gevoelig zijn voor kleine veranderingen in een gast-molecuul. Het veranderen van de R groep in de structuur van de motor in Schema 5 verandert niet veel aan de vorm van het molecuul maar in sommige gevallen bleek dat zelfs de gehele chirale inductie wegvalt. Hiernaast werd ook gekeken naar de invloed van het bestralen (de moleculaire motor verandert van vorm **1a** naar **1b**) van het mengsel. Het bleek dat tijdens de bestraling de gehele VK fase lijkt te roteren. In hoofdstuk 3 is uitgebreid onderzoek gedaan naar de reden voor deze rotatie. Een computer model is geconstrueerd dat de geobserveerde roterende fase voorspelde.

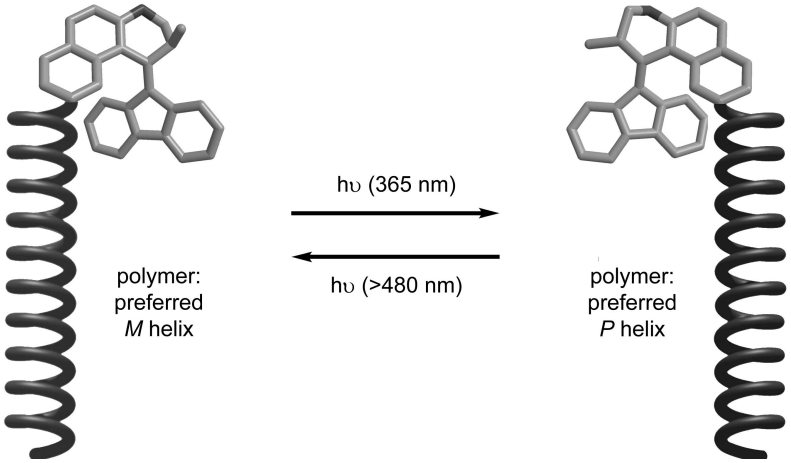

Schema 6 Moleculaire motor aan polymeerketen. De “schroefdraad” van de polymeerketen veranderd met bestraling.

Ook werd er gekeken naar het effect dat optreedt als de moleculaire motor deel uitmaakt van een polymeerketen (Schema 6) dat op zichzelf ook VK fasen genereert. Het blijkt dat zelfs in het geval van een polymeer keten die veel groter is dan het motor molecuul, de cholesterische fase nog steeds

wordt waar genomen en dat onder bestraling veel van dezelfde veranderingen waargenomen werden.
In hoofdstuk vijf wordt er gekeken naar de amplificatie van chirale verbindingen op een oppervlak.

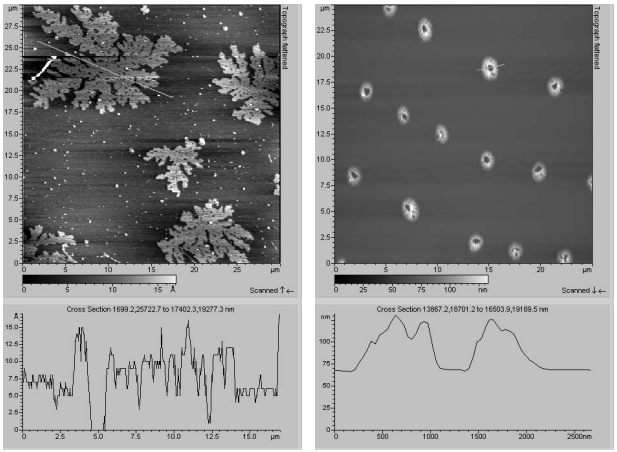

Schema 7 Plaatjes van de verschillende architecturen op een oppervlak. Links) alleen polymeerketen. Rechts) de polymeerketen met moleculaire motor.

Chiraliteit is niet alleen waarneembaar in vloeistoffen maar ook op oppervlakken. In dit hoofdstuk werden de polymeer ketens aan moleculaire motoren vast gezet (eerder gebruikt in hoofdstuk 4) en op een oppervlak ingedroogd om te zien of de aanwezigheid van deze kleine moleculaire motoren aan veel langer ketens (100 keer zo groot) invloed zouden hebben op het gedrag van de polymeer keten op een oppervlak. Het resultaat waren kleine ringvormige formaties in een geordend patroon. Dit was niet het geval voor dezelfde polymeerketen zonder de moleculaire motor functionaliteit (Schema 7).

In hoofdstuk zes is onderzoek gedaan naar de eerste water oplosbare moleculaire motor.

In zeepachtige moleculen is er een waterliefhebbende (hydrofiel) en een waterafstotend (hydrofoob) segment van het molecuul. Door deze moleculen in water te brengen zullen de hydrofobe segmenten bij elkaar gaan zitten en worden er kleine bolletjes genaamd micellen in het water gevormd.

In dit hoofdstuk werd er gekeken naar de eerste water oplosbare moleculaire motor. Deze vormt micellen in water. Heel interessant is het feit dat de concentratie moleculaire motor die nodig is om deze micellen te vormen varieert voor de stabiele en instabiele vormen van de moleculaire motor. Er is twee keer zoveel nodig van de stabiele water oplosbare motor als van de instabiele vorm van de motor om micellen te vormen.

Acknowledgements

Het is alweer 5 jaar geleden dat ik als promovendus binnenstapte om aan mijn promotie onderzoek te beginnen. Ik heb in die tijd veel geleerd over onderzoek maar ook over mijzelf.
Ten eerste wilde ik graag diegenen bedanken die mij geïnspireerd hebben in de chemie om mij zo enthousiast te maken dat ik besloot een promotie onderzoek aan te gaan. Beste Jan, bedankt dat ik bij jou mijn masters onderzoek mocht doen. Jij hebt mij veel geleerd over meetfouten, reproducibility en de juiste vragen stellen, maar ook dat men toch vele interesses naast scheikunde kan hebben. Het is geweldig dat de cirkel nu rond is en jij deel kan uitmaken van mijn beoordelingscommissie. Bedankt! Dear Larry, thank you for allowing me to be an intern in your group for five months. The period I spent with you taught me a lot about self reliance and my ability to try something completely new, and developing my true enthusiasm for a Ph.D. position. I had a ball!

Graag wilde ik mijn promotor Ben Feringa bedanken. Ben bedankt voor de mogelijkheid om een onderzoek te doen waar weinig gesynthetiseerd wordt maar veel gemeten. Het onderwerp was iets waar ik niets van af wist maar je had vertrouwen in mijn kunnen. Bedankt voor al jouw enthousiasme, opbouwende kritiek en ondersteuning gedurende deze promotie. Ik wilde de leden van de leescommissie, Prof. Dr. D.J. Broer, Prof. Dr. J.B.F.N. Engberts, en Prof. Dr. E.J.R. Sudhölter bedanken voor het lezen en de correcties van mijn proefschrift.

Voor goede data heb je soms wat hulp nodig. Bedankt Hans van der Velde voor het mogen gebruiken van jouw zeer accurate balans en de andere apparatuur (DSC, DLS). Theodora, je hebt vele uren met mij doorgebracht achter de prep HPLC om alles in goede banen te lijden; bedankt hiervoor. Thank you Syuzi en Wim Kruizinga for your help with my temperature-dependent NMR measurements. Lumi, thank you for your in-depth explanations of Langmuir-Blodgett and the beautiful data.

Dear Mike, though you are no longer with us, I would like to thank you for taking on the role of a day-to-day supervisor, asking me the tough questions and forcing me to look at everything from a different point of view. When not discussing chemistry you always tried to make me think of the bigger picture during our dinners. You were crucial to my finding my way as a Ph.D.

I've had the privilege of collaborating with many different people of different nationalities. Dirk, ik heb erg genoten van onze samenwerking. Ik heb veel bewondering voor jouw oog voor detail. Bedankt! Nathalie, you taught me STM, and helped me during our collaboration with Alberta. You were essential in helping me learn to communicate with physicists (and teach me the differing nomenclature) and helping me analyze our data and ask the right/tough questions. Thank you for everything. Greg, you taught me how to clean various surfaces and use an AFM. The hours we spent imaging our samples and listening to your explanations of wrestling moves and cartoons were always lots of fun, but you always got the perfect images. A plethora of thankyous! Marc, bedankt, voor jouw mooie cryo-TEM plaatjes maar ook voor jouw analytische kracht. Je hebt mij vele tips en ideeën gegeven die uiteindelijk allen in hoofdstuk 6 terecht gekomen zijn. Wes, helping you with maintaining the measuring labs has taught me a lot about maintaining equipment and making myself at home in techniques I did not always use a lot myself. Thank you for your help with all the little instrumental hiccups,

the nasty questions and especially for arranging the special horizontal attachment for the CD spectrometer. You're a crack person.

Gedurende mijn onderzoeksperiode heb ik het voorrecht gehad om twee bachelor, en een masters project met veel plezier te begeleiden. Jos, je kunt koppig zijn, maar je hebt goede innovatieve ideeën en bent niet bang om iets te proberen. Ik wens je veel succes met je promotie in de toekomst. Sander, jouw onderzoek heeft bijgedragen aan hoofdstuk 6. Je bachelor onderzoek bij mij liep gesmeerd, maar je hoofdvak had wat haken en ogen. Voornamelijk de synthese liep erg zwaar. Toch heb je altijd de moed erin gehouden. Bedankt voor onze gezellige en leuke samenwerking.

During a period of 5 years many people come and go. I spent them all in lab 16.238N with many very friendly neighbors. Thank you: Tibor for your wise lessons on Tokaj making; Fletcher for your cowboy chemistry and musical education (Johnny Cash rocks!); Fred for being the worlds only chemist ballerina; Lubi, Tatiana, Robert (chemist poet), Alex, Jos, Sander, Lorena, Gabor, opera Santi and Arjen for all the fun and laughs during the serious chemistry. At coffee times the entire wing (+ others) would get together. Thank you Nopje, Eričko, Jort, Thom, Tom, Steve x2, Koen, Johan, Hans, Jochem, Pat, Hella, Heloise, Jiaobing, Jurica, Lumi, Tatiana, Nuria, Barbara, Chris and Giuseppe for all the support and friendship. It's always good to be able to share frustrations. Thank you all!

Thom, bedankt voor al je computer hulp. Ook bedankt voor de salsa. Peter bedankt voor het omtoveren van mijn proefschrift in een PDF waarin alles klopt.

I would especially like to thank those people who I am honored to not only refer to as colleagues but life long friends. Barbara, Tatiana, Lubi, the four of us were quite a group running around together at the university. Sadly we all live far away from each other now but we still find the time to meet. Little one, the fact that you are coming for my promotion from the Czech Republic means so much to me. Sestry navždy! Tatibeestje our holidays together were a blast and they were just what I needed to round off my promotion. Muchas gracias por todo tu cariño y amor. Besotes y un abrazo. Barbarelli thank you for our many dinners, alternative movie nights and the ability to vent now and then. You're the best! Arjen en Jacqueline, bedankt voor de vriendschap, de choco-pauzes en het heerlijke sarcasme. Het heeft me overeind gehouden. Eričko d'akujem for agreeing to support me on my big day by being my photographer. Reinou en Arjen, jullie hebben toegezegd mijn paranimfen te zijn en mij te ondersteunen bij de promotie. Ik dank jullie voor jullie vriendschap en het aannemen van deze post.

Cinewin bedankt voor onze al 16 jaar durende vriendschap! Jij staat altijd klaar voor me en ik kan niet goed genoeg aangeven hoeveel dat voor mij betekent. Boefiline, Paaihaai en Nintha jullie kracht en doorzettingsvermogen zijn altijd een voorbeeld geweest. Não posso les agradecer sufficiente por toda sua ajuda en seu amor. Eu amo vocês. Katerline there are no words other than thank you!

Mahthild